APPLIED COMPUTATIONAL ELECTROMAGNETICS SOCIETY JOURNAL

January 2014
Vol. 29 No. 1
ISSN 1054-4887

The ACES Journal is abstracted in INSPEC, in Engineering Index, DTIC, Science Citation Index Expanded, the Research Alert, and to Current Contents/Engineering, Computing & Technology.

The illustrations on the front cover have been obtained from the research groups at the Department of Electrical Engineering, The University of Mississippi.

JANUARY 2014 REVIEWERS

Md Rezwaul Ahsan
Ayman Al-Zayed
Marco Arjona
Zhipeng Cao
Alistar Duffy
Khaled Elmahgoub
Amir Hajiaboli
Mang He
Mourad Ibrahim
Peyman Jahanshahi
Shan Jiang
Ahmed Kishk
Michiko Kuroda
David Lautru
Yang Lin
Xin Liu
Maryam Majidzadeh
Senem Makal Yucedag
Zah
Kurt Oughstun
Nitin Saluja
Michael Schneider
Seyyed Sedighy
Apirat Siritaratiwat
Abhay Srivastava
Quanquan Wang
Joshua Wilson
Qianyin Xiang
Run Xiong
Guomin Yang
Muhammad Zubair

THE APPLIED COMPUTATIONAL ELECTROMAGNETICS SOCIETY

JOURNAL

Vol. 29 No. 1 January 2014

TABLE OF CONTENTS

Finite Difference Time Domain Modeling of Sub-Wavelength Structured Anti-Reflective Coatings

K. Han[1, 2], H.-Y. Han[3], J. Stack Jr.[4], and C.-H. Chang[1, 2]

[1] School of Chemical, Biological, and Environmental Engineering
Oregon State University, Corvallis, OR 97331, USA
vanwormk@onid.orst.edu, chih-hung.chang@oregonstate.edu

[2] Oregon Process Innovation Center, Microproduct Breakthrough Institute
Oregon State University, Corvallis, OR 97330, USA

[3] Inspired Light, Llc., Corvallis, OR, 97330, USA
haiyuehan@gmail.com

[4] Remcom, Inc., State College, PA, 16801, USA
jim.stack@remcom.com

Abstract **–** The finite difference time domain (FDTD) method was used to model anti-reflective properties of a variety of sub-wavelength structures for 300 nm to 1300 nm input light. Light hitting non-tapered nanostructures exhibited interference patterns similar to thin film anti-reflective coatings (ARCs), increasing the anti-reflective effect at several wavelengths. The lowest reflectance was observed with conical and pyramidal nanostructures with bases of 100 nm or 200 nm and heights of 400 nm or 800 nm.

Index Terms **–** Anti-reflective, FDTD, modeling, nanostructure, and sub-wavelength.

I. INTRODUCTION

Improvements in solar module efficiency have been a popular topic of research these past few decades, usually focusing on either decreasing costs or increasing efficiency. One method to increase efficiency is by reducing reflections off solar module lamination materials. Reflections occur when light travels between media with two different refractive indices (RI). The amount of light reflected at a normal incidence can be described by,

$$R \equiv \left(\frac{n_1 - n_2}{n_1 + n_2} \right)^2 \quad (1)$$

where n_1 is the index of refraction of the low RI material (usually air) and n_2 is the index for the high RI material. One technique to reduce reflection is to gradually increase the index of refraction from that of air to that of the surface so that there are little to no abrupt changes in RI that would induce reflections. This can be done by creating a sub-wavelength structured anti-reflective coating (ARC) at the reflective interface. Sub-wavelength sized structures (SWS) are perceived by light as a material with an intermediate index of refraction between that of air and that of the surface.

Advances in computing resources have made it possible to quickly and accurately model the anti-reflective properties of 3-dimensional sub-wavelength structures. The FDTD method performs numerical time-stepping of Maxwell's curl equations to describe the behavior of electric and magnetic fields. The FDTD method has been used to model ARCsin2 and 3 dimensions of pillars [1], pyramids [2-5], slots [6], cones [3, 4, 7, 8], conical cylinders [9], triangles [10], spheres [11], hemispheres [5], nanoholes [12], thin films [13], nanoporous films [14], and nanowires [15].

Submitted On: June 14, 2013
Accepted On: March 2, 2014

Experimental photonic nanostructures are reviewed by Chattopadhyay*et al* [16].

To date FDTD has been used primarily to compare modeling ARC results for a small number of SWS. This paper will model a variety of shapes and sizes in three dimensions to quantify the reflectivity of AR sub-wavelength structures (ARSWSs), compare this calculated reflectivity to results from transfer matrix method modeling, describe trends in the effects of shape and size of the ARSWSs, and provide a direction for future experimental research.

II. METHODS

Remcom's XF 7.3.1 was used to model the behavior of light reflections from anti-reflective coatings (ARCs). All simulations were performed on a NVIDIA M1060 Tesla GPU. The geometry was drawn using the XF CAD GUI to produce an area of air on the +Z end of the simulation, an SWS in the middle, and a solid bulk material on the –Z end (see Fig. 1). In all cases the SWS and solid material were assigned the same RI, n = 1.5, except the thin film ARC, which was 1.22. To simulate solar input, a polarized plane wave with an automatic waveform with a Gaussian distribution of frequencies between 300 nm - 1300 nm was input at the eighth cell from the +Z boundary toward the –Z direction (see Fig. 1 parts B and D). Boundary conditions in the +Z and –Z directions were perfectly matched layer (PML) with 7 cells of padding and in the X and Y directions were periodic. Electric field sensors were placed to the +Z side of the plane wave generation plane (reflected light sensor; see Fig. 1 A) and just inside the bulk material (transmitted light sensor; see Fig. 1 C). Cell sizes were 5 nm for short or non-tapered structures and 2.5 nm for the cone and pyramid sweeps. The bulk material was 2,000 nm × 2,000 nm × 1,000 nm, resulting in 400 × 400 points output for each sensor at each time point. Hollow spheres were drawn in a hexagonal closest packed structure with one modeling unit consisting of 4 sphere diameters on one axis and 4 rows of closest packed spheres on the other axis. All hollow spheres were constructed with 5 nm shell thickness and the grid sizing was 1/200th of the overall modeling dimension in question for X and Y axes, keeping the mesh size between 0.866 nm and 3 nm. These small mesh sizes are required to resolve the shell thickness features of the hollow spheres with the FDTD method.

Hollow spheres were modeled with *s*- and *p*-polarized plane waves and the results were averaged to report unpolarized results. This is a requirement due to their non-square packing. For many semi-analytical methods *p*-polarized light is complicated to simulate [17], but FDTD handles either polarization naturally.

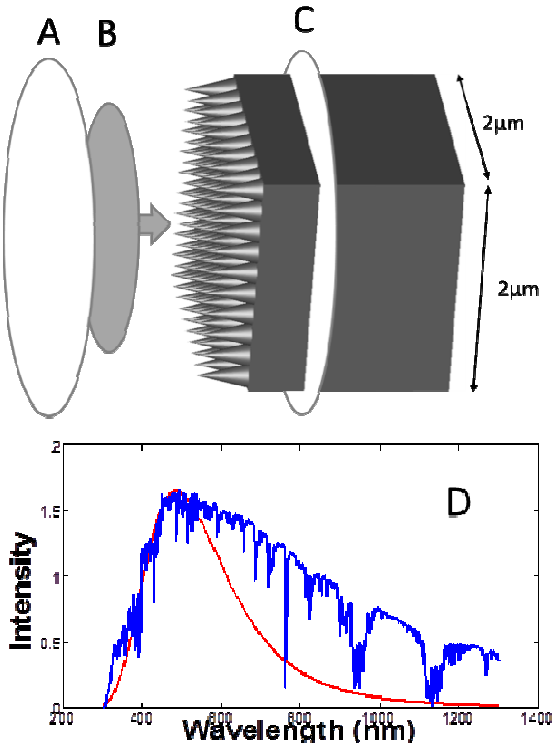

Fig. 1. Schematic of modeling domain with reflected light plane sensor (A), light source (B) and transmitted light plane sensor (C), the shape of the input waveform (D, red line) and the intensity of solar input (D, blue line).

Electric field data was post-processed using Matlab R2012a. A discrete fast Fourier transform (DFT) was performed for each space point for each of Ex, Ey, and Ez in both the transmitted and reflected planes. The absolute value squared of the FFT result at each point in the plane of the sensor was multiplied by the index of refraction and the values for Ex, Ey, and Ez were added together, resulting in the light intensity at each frequency. Intensities for each frequency were averaged over the area of the sensor. The reflected and

transmitted light intensities were then added and compared to the input wave light intensities to determine the error of the simulation; only simulations with < 2% error are reported. Reported reflection values are an average of the percent reflection weighted over the solar input spectrum as shown in equation (2),

$$\%R = \frac{\sum \%R_\lambda * AM1.5Intensity_\lambda}{\sum AM1.5Intensity_\lambda}. \quad (2)$$

Transfer matrix method simulations were performed on the Luxpop software (luxpop.com). The Lorentz approximation [18] was used to determine an effective index of refraction for the pyramids and nanorods. For pyramids approximations were calculated for each 1 nm slice.

III. RESULTS

In this experiment all sub-wavelength structures, as well as thin film ARCs with intermediate RI values, resulted in lower reflectance than a simple flat surface of glass (4.0%). Overall, ARSWSs that have full or nearly full coverage at the substrate and taper to a point with higher aspect ratios (2 to 8) exhibited the lowest reflection. Structures with widths larger than 200 nm required prohibitively long calculation times due to the multiple reflectionsinduced by the higher frequency input wavelengths.

To investigate the anti-reflective effects of well-oriented nanorods on a surface, a series of cylinders of the same material as the substrate (n=1.5) were simulated (see Fig. 2). All cylinders in this sweep were 375 nm in length and they ranged in fill factors of 20%, 50%, and 79%. For each density, the distance between cylinders was modeled to be 50 nm, 100 nm, or 200 nm. The fill factor of the cylinders was the most important determining factor in reducing reflections; cylinders covering about 20% of the area reflected 2.3% to 3.9% of the light, cylinders covering 50% of the area reflected 2.0% to 2.1%, and the 79% fill factor cylinders had reflectances of 2.8% to 3.1%. The reflectance spectrum of the 375 nm cylindrical ARSWSs with characteristic of that of thin films with intermediate indexes of refraction; both ARC types exhibit interference patterns, as seen in Fig. 2, and the lowest reflection was seen in the 50% fill factor cylinders and the thin film, both of which had an effective index of refraction of 1.22.

FDTD-predicted reflection characteristics for nanorods matched FDTD results for thin films will have the same effective refractive index as well as TMM results for effective medium-approximated nanorods (see Fig. 2, red and light blue lines for FDTD results and circles for TMM results).

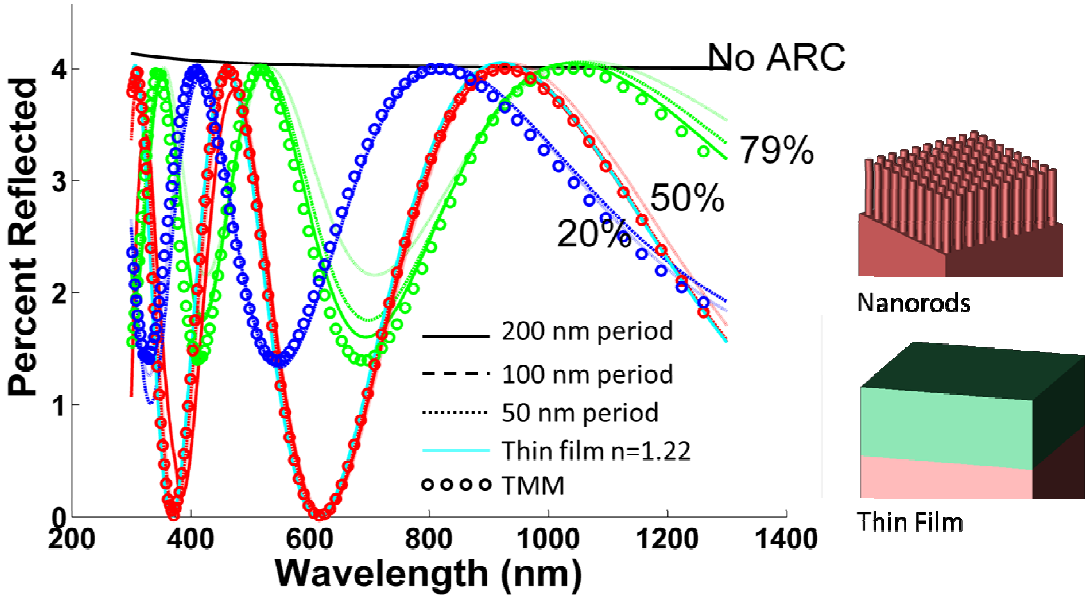

Fig. 2. Reflectancespectra of nanorods of 375 nm length. Volumetric fill factors are indicated by color.

The sub-wavelength structures with the best anti-reflective properties were tapered structures with high aspect ratios. Pyramids with lengths of 800 nm or 400 nm had the lowest reflectance (<0.1%; see Fig. 3). Cones, which were modeled here in a grid array with their bases of each touching its four closest neighbors had reflectances of < 0.25% for the same lengths (see Fig. 4). For both shapes, the configurations with the lowest reflectance (< 0.25%) were 100 nm to 200 nm across at the base and 400 nm to 800 nm long. The pyramids with the worst AR properties had a length of 100 nm (1.7%–1.9%). Cones of length 100 nm reflected between 1.6% and 1.75% of light. Thus the height of the tapered structure was more important to anti-reflective properties than was base width or shape. The main difference between the reflectivity behavior of the cones and pyramids is that cones had a slightly higher reflection due to the step change in effective medium where the cone base meets the substrate.

Comparison of FDTD with TMM simulation results for pyramidal ARSWS structures indicates a consistently lower predicted reflectance from TMM for all heights below 800 nm. For the 800 nm structures the TMM and FDTD simulations matched closely. Upon close examination of Fig. 3 it appears that the TMM results are not shifted down, but are shifted toward longer wavelengths.

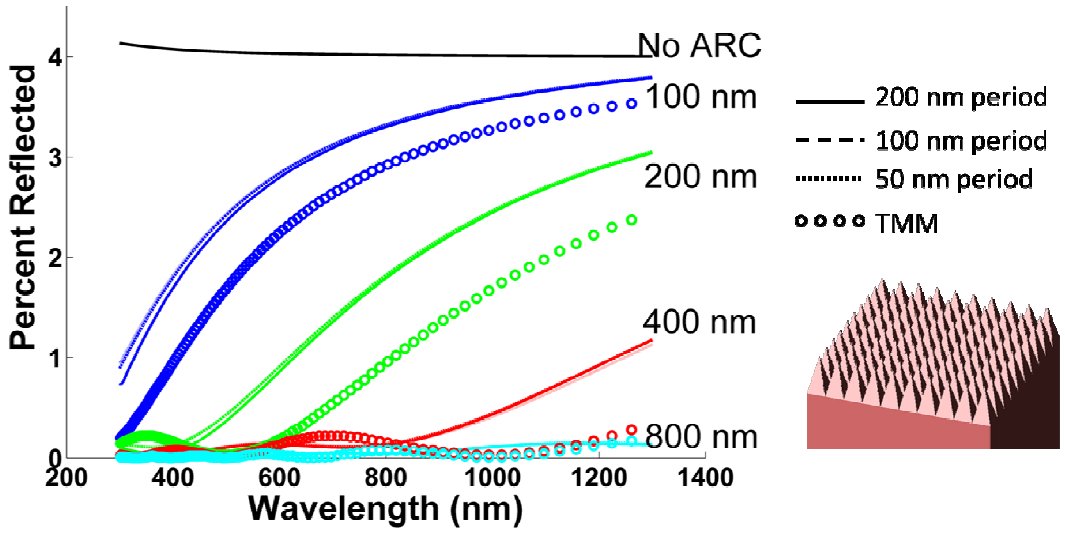

Fig. 3. Reflectance of four-sided pyramid-shaped ARSWSs. Line color indicates pyramid height.

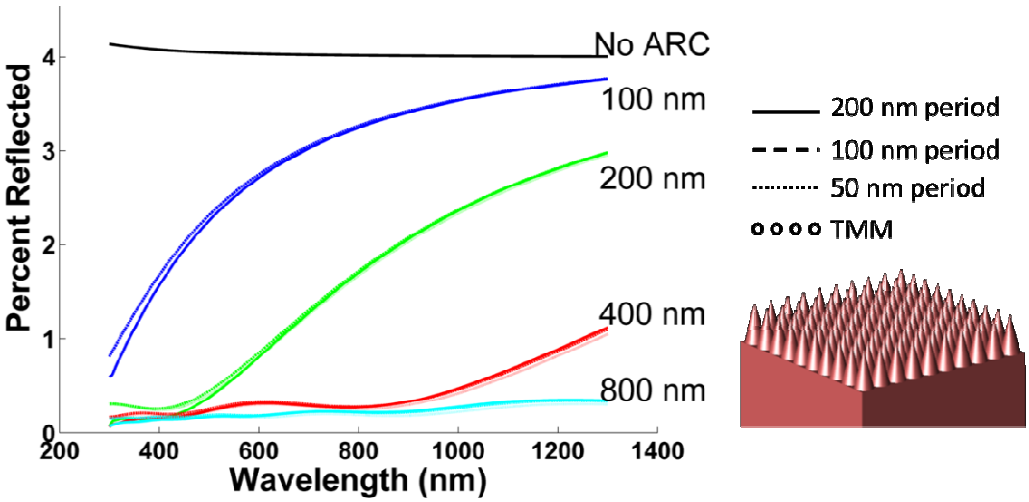

Fig. 4. Reflectance of cone-shaped ARSWSs. Line color indicates cone height.

Several structures with aspect ratios of approximately one were investigated. These structures include densely packed hemispheres, cubes (checkerboard pattern), and cylinders (see Fig. 5) as well as sparsely packed hemispheres, cubes, and cylinders (see Fig. 6). All except the hemispheres had an aspect ratio of one, while hemispheres have, by definition, an aspect ratio of one half. The sparsely packed structures were arranged in a grid with the space between each structure equal to the width of that structure (Fig. 6, right side), while the densely packed structures were arranged in a grid pattern with each structure touching its four nearest neighbors (see Fig. 5, right side). Overall, these smaller aspect ratio structures did not have as low of reflectance as did the taller cones and pyramids, with the lowest reflectance coming from densely packed hemispheres of 200 nm at 0.9% reflectance. Overall, the checkerboard configuration (dotted lines in Fig. 5) presented the lowest reflection between 1.1% and 1.6%. Larger structures exhibited less reflectance for both sparse and dense structures and the cylinders and cubes both exhibited mild interference patterns at sizes larger than 50 nm.

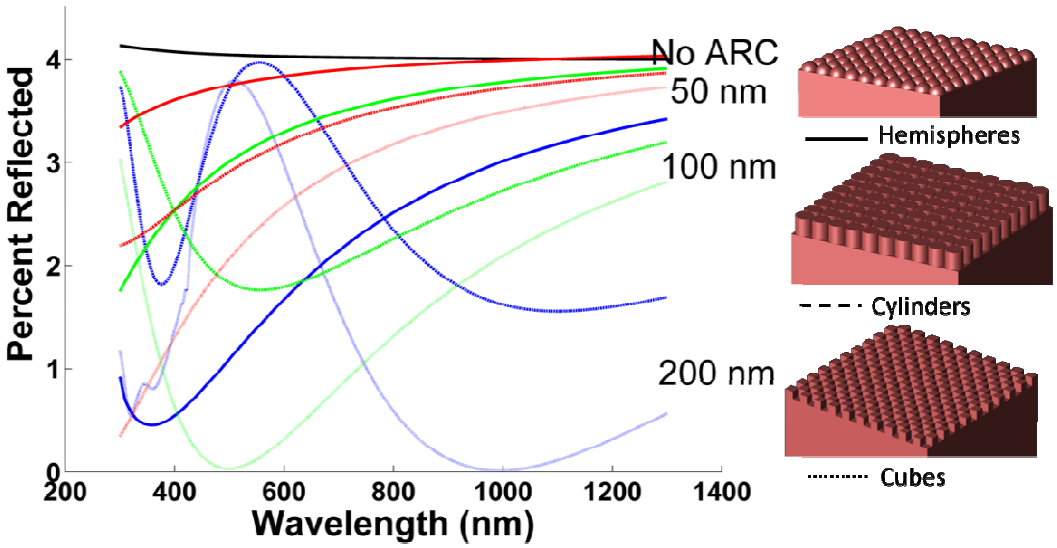

Fig. 5. Reflectance spectra ARSWSs of aspect ratio one. Colors indicate feature size.

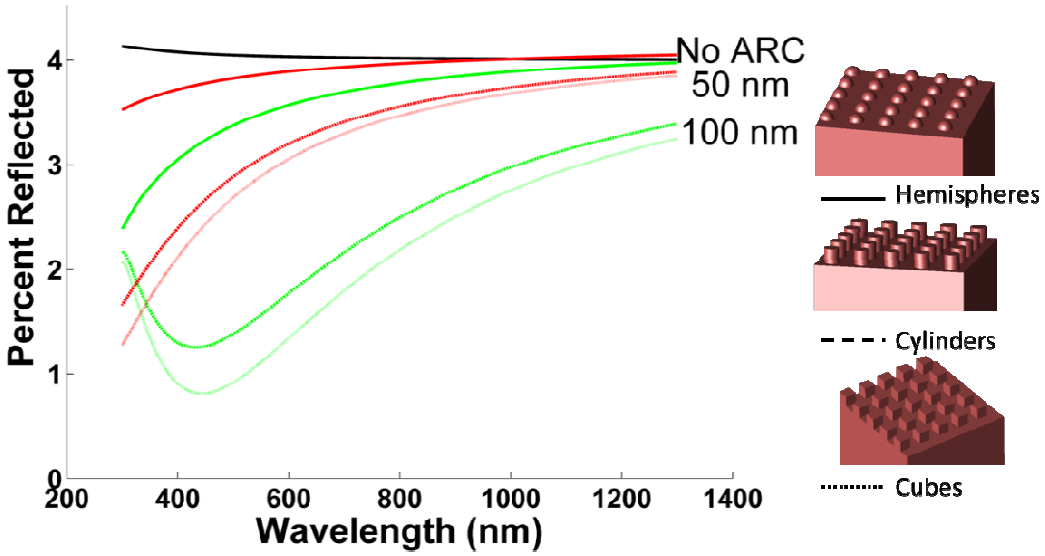

Fig. 6. Reflectance spectra of sparsely packed ARSWSs. Colors indicate feature sizes.

Hexaganol closest packed hollow spheres were modeled for their anti-reflective properties (see Fig. 7). One, two, or four layers of spheres were modeled for spheres of 50 nm, 100 nm, and 150 nm diameters, all of which had shell thicknesses of 5 nm. In general the smaller spheres, 50 nm in diameter, exhibited the lowest reflectances; the structures of two layers of hollow spheres of 50 nm in diameter had 0.7% reflectance. The next best ARC in this group was one layer of 100 nm hollow spheres at 1.4% reflectance. These values were followed by the other 50 nm hollow spheres, then the rest of the 100 nm hollow spheres, with the 150 nm hollow spheres making the worst ARCs of this subset between 3.1% (1 layer) and 3.8% (4 layers).

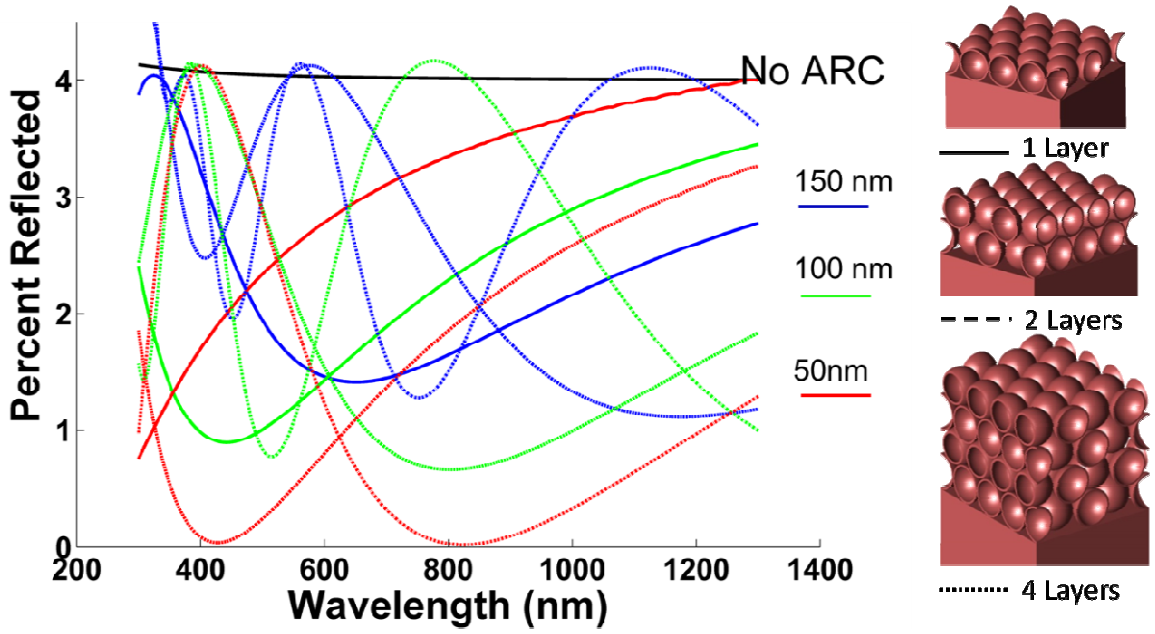

Fig. 7. Reflectance spectra of hollow spheres layered in a hexaganol closest packed structure with shell thicknesses of 5 nm. Diameter is indicated by color and number of layers is indicated by line type.

IV. CONCLUSION

Optical simulations of a variety of sub-wavelength structures were performed using the finite difference time domain method and confirmed using the transfer matrix method. The goal of this study was to provide a quantitative comparison of a variety of ARSWSs that can aid in further design of ARCs.

Nanostructures with non-tapered shapes reflected more electromagnetic radiation than did tapered structures. This is due to difference in reflective behavior between gradient index materials and the interference properties of thin film and thin film-like ARCs. Thin film-like ARCs consist of a layer of material that has the same fill factor and RI at every level of cross section normal to the travel of the light. These films, consisting of both air and nanostructure materials, have an intermediate "effective" n, which is between that of the air and the bulk solid. As light hits the top of these layers it encounters an abrupt change in n and a portion of light reflects, dictated by equation (1). The same event occurs at the bottom of the layer as the light enters the bulk substrate. When the film thickness is an odd multiple of a quarter wavelength, the reflected light from the two interfaces cause interference, resulting in reduced reflection. This periodic interference effect results in what appears to be wavelength dependent oscillations in the reflectance spectrum for these materials.

Tapered nanostructures resulted in more broadband anti-reflective properties than did non-tapered nanostructures. This occurs because the effective n of the ARSWS layer is continuously increasing from that of air to that of the substrate material over the length of the structures, so the incident light does not detect an abrupt interface

that would induce reflections. Of the structures studied, the minimum reflection was through conical and pyramidal structures with bases of 200 nm and heights of 800 nm or 400 nm. These results are in accordance with the theory that optimal textured surface ARCs have structures with diameters smaller than heights that are at least a significant fraction of the wavelengths.

Hollow nanospheres were modeled for their anti-reflective properties as a real world example of a nanostructure that can be easily created in the laboratory. Hollow nanospheres were modeled in a hexaganol closest packed structure with a variety of number of layers. These results indicate a recommendation for two layers of smaller (50 nm) nanospheres for best AR properties. These simulation results indicate that, like the non-tapered structures investigated in this paper, hollow nanospheres exhibit interference-like patterns in their reflectance spectra. This can likely be explained by an effective media theory, where the hollow nanospheres and the non-tapered nanostructures interact with light in a similar manner as a thin film of intermediate index of refraction.

The transfer matrix method was used to confirm the FDTD methods reported here. Very good correlation was found between the two methods for non-tapered nanorod structures. However, some discrepancy was found for the tapered pyramidal structures. This can be explained in part by the methods used to discretize the two simulations. While the TMM simulation was smoothly discretized every 1 nm of height of the pyramids, the FDTD method was meshed at 2.5 nm. This would affect the description of the tip of the structure, making the effective height of the structure shorter, which would target a shorter wavelength. This effect is seen in the apparent shift of the TMM data toward a longer wavelength. Discretizing the FDTD simulations further becomes very computationally intensive.

Models in this study covered feature widths between 50 nm and 200 nm, which are appropriate sub-wavelength widths for 300 nm to 1300 nm light. Attempts were made to investigate the anti-reflective properties of features larger than 200 nm, but multiple reflections in the structures not only made modeling times prohibitively long, but also resulted in regions of the spectrum that erroneously reported much higher than 100% transmission. For these simulations, error averaged over the spectrum was between 2% and 7%, while for all reported simulations the error was well below 2% and usually below 0.4%.

Future work will investigate the effects of angle of incidence and index of refraction on the anti-reflective properties of ARSWSs. The index of refraction of real materials is wavelength-dependent. A thorough study of ARSWSs within a range of indexes of refraction that is reasonable for the materials used to make those structures could provide researchers with more realistic modeling capabilities.

ACKNOWLEDGEMENT

The authors like to acknowledge the support from NSF STTR Phase II, Oregon Process Innovation Center/Microproduct Breakthrough Institute, ONAMI, Oregon BEST, and Remcom, Inc. The authors would like to thank Yujuan He for her contributions to the design of sizing and configurations of the hollow spheres simulations.

REFERENCES

[1] S. Boden and D. Bagnall, "Tunable reflection minima of nanostructured antireflective surfaces," *Applied Physics Letters*, vol. 93, Sep. 2008.

[2] H. L. Chen, S. Y. Chuang, C. H. Lin, and Y. H. Lin, "Using colloidal lithography to fabricate and optimize sub-wavelength pyramidal and honeycomb structures in solar cells," *Optics Express*, vol. 15, pp. 14793-14803, Oct. 2007.

[3] C. J. Ting, C. F. Chen, and C. P. Chou, "Antireflection subwavelength structures analyzed by using the finite difference time domain method," *Optik*, vol. 120, pp. 814-817, 2009.

[4] C. J. Ting, C. F. Chen, and C. J. Hsu, "Subwavelength structured surfaces with a broadband antireflection function analyzed by using a finite difference time domain method," *Optik*, vol. 121, pp. 1069-1074, 2010.

[5] H. Y. Tsai, "Finite difference time domain analysis of three-dimensional sub-wavelength structured arrays," *Japanese Journal of Applied Physics*, vol. 47, pp. 5007-5009, June 2008.

[6] Z. F. Li, E. Ozbay, H. B. Chen, J. J. Chen, F. H. Yang, and H. Z. Zheng, "Resonant cavity based compact efficient antireflection structures for photonic crystals," *Journal of Physics D-Applied Physics*, vol. 40, pp. 5873-5877, Oct. 2007.

[7] C. Ting, C. Chen, and C. Chou, "Subwavelength structures for broadband antireflection

application," *Optics Comm.*, vol. 282, pp. 434-438, Feb. 2009.

[8] A. Deinega, I. V. Konistyapina, M. V. Bogdanova, I. A. Valuev, Y. E. Lozovik, and B. V. Potapkin, "Optimization of an anti-reflective layer of solar panels based on ab initio calculations," *Russian Physics Journal*, vol. 52, pp. 1128-1134, Nov. 2009.

[9] C. J. Ting, F. Y. Chang, C. F. Chen, and C. P. Chou, "Fabrication of an antireflective polymer optical film with subwavelength structures using a roll-to-roll micro-replication process," *Journal of Micromech. and Microeng.*, vol. 18, July 2008.

[10] H. Ichikawa, "Subwavelength triangular random gratings," *Journal of Modern Optics*, vol. 49, pp. 1893-1906, Sep. 2002.

[11] J. R. Nagel and M. A. Scarpulla, "Enhanced absorption in optically thin solar cells by scattering from embedded dielectric nanoparticles," *Optics Express*, vol. 18, pp. A139-A146, June 2010.

[12] N. Wang, Y. Zhu, W. Wei, J. J. Chen, P. Li, and Y. M. Wen, "Conversion efficiency enhanced photovoltaic device with nanohole arrays in antireflection coating layer," *Optics Comm.*, vol. 284, pp. 4773-4777, Sep. 2011.

[13] J. Yamauchi, M. Mita, S. Aoki, and H. Nakano, "Analysis of antireflection coatings using the FD-TD method with the PML absorbing boundary condition," *IEEE Photonics Technology Letters*, vol. 8, pp. 239-241, Feb. 1996.

[14] Z. Y. Yang, D. Q. Zhu, M. Zhao, and M. C. Cao, "The study of a nano-porous optical film with the finite difference time domain method," *Journal of Optics a-Pure and Applied Optics*, vol. 6, pp. 564-568, June 2004.

[15] J. Yi, D. H. Lee, and W. I. Park, "Site-specific design of cone-shaped Si nanowires by exploiting nanoscale surface diffusion for optimal photoabsorption," *Chemistry of Materials*, vol. 23, pp. 3902-3906, Sep. 2011.

[16] S. Chattopadhyay, Y. F. Huang, Y. J. Jen, A. Ganguly, K. H. Chen, and L. C. Chen, "Anti-reflecting and photonic nanostructures," *Materials Science and Engineering R-Reports*, vol. 69, pp. 1-35, June 2010.

[17] A. Kildishev, X. Ni, L. Prokopeva, T. Knyazyan, and H. Baghdasaryan, "Non-linear modeling of active or passive optical lamellar nanostructures," *27th Annual Review of Progress in Applied Computational Electromagnetics*, Williamsburg, Virginia, USA, 2011.

[18] D. Aspnes, "Local-field effects and effective-medium theory: A microscopic perspective," *American Journal of Physics*, vol. 50, p. 704, 1982.

Katherine Han is a Ph.D. student in the School of Chemical, Biological, and Environmental Engineering. She is a co-founder of the OSU Solar Vehicle Team and has served as graduate student president in her department. Kat is the lab manager for the Oregon Process Innovation Center.

Hai-Yue Han received his Ph.D. in Electrical Engineering at Oregon State University. He is a co-founder of the Oregon State University Solar Vehicle Team and has built three solar powered cars at OSU. He currently works as the lead balance of systems engineer at Inspired Light.

James F. Stack, Jr. received a B.Sc. degree in Electrical Engineering in 2001 and an M.Eng. degree in Systems Engineering in 2010 from the Pennsylvania State University. He has worked for Remcom, Inc. since 2000 where he currently manages the applications engineering department. His research interests include high performance computing (SSE/AVX vectorization, GPGPU, MPI and threading) and using optimization techniques to achieve novel RF structures.

Chih-hung (Alex) Chang is a Professor in the School of Chemical, Biological, and Environmental Engineering. His group has studied solution based thin film deposition processes, ink jet printing, microreaction technology, and X-ray absorption fine structure. He has more than 80 refereed publications, 8 issued patents, and 4 pending patents in these areas. Chih-hung is a SHARP Labs of America scholar, an Intel Faculty Fellow, and a recipient of AVS Graduate Research award, National Science Foundation's CAREER award, and awardees of W.M. Keck Foundation. He is the founder and Director of Oregon Process Innovation Center an Oregon BEST signature research lab. He is the founder of a start-up venture, CSD Nano Inc.

Incorporation of The Nihility Medium to Improve The Cylindrical Invisibility Cloak

A. Shahzad[1], S. Ahmed[1], A. Ghaffar[2],and Q. A. Naqvi[1]

[1]Department of Electronics, Quaid-i-Azam University, Islamabad, Pakistan (45320)
gondalanjum@yahoo.com, snfawan@yahoo.com, nqaisar@yahoo.com

[2] Department of Electrical Engineering, King Saud University, Saudi Arabia
chabdulghaffar@yahoo.com

Abstract ─ Two dimensional cylindrical wave expansion method is used to analyze the cylindrical invisible nihility cloak. Ideal model of the cloak is set up to solve the problem and it is observed that a perfect equivalence with the ideal situation of the cloak can be achieved by using nihility medium at perturbed void region of the geometry. Also it is observed that the use of nihility medium at δ, the convergence rate is independent of the type of incident field. Both the transverse electric (TE) and transverse magnetic (TM) cases have been discussed.

Index Terms – Convergence, nihility, transverse electric, transverse magnetic, and wave expansion.

I. INTRODUCTION

Cloaks have attracted attentions of many researchers in the scientific community due to its amazing characteristics. Scientists have already developed such devices, which can render things invisible to electromagnetic waves. Metamaterials used for making such devices are required to have negative refraction index and are known as left-handed (LH) metamaterials. Metamaterials are a class of artificially engineered composite materials having extraordinary electromagnetic properties. Negative refraction index material has been discussed by many scientists [1-4]. Pendry is pioneer of the cloaking concept and Pendry et al., [5] first illustrated through theoretical simulations, that an object can be cloaked from electromagnetic fields by exploiting coordinate transformation in inhomogeneous and anisotropic metamaterials. Cummer et al., analyzed the full-wave simulations of electromagnetic cloaking structures [6]. They worked on the electromagnetic simulations of the cylindrical version of this cloaking structure using ideal and non-ideal electromagnetic parameters. They showed that the low reflections and power flow banding properties of electromagnetic cloaking structures are not especially sensible to modest permittivity and permeability variation. Schuring et al., described metamaterial electromagnetic cloak at microwave frequencies [7], which was the first practical realization of such a cloak. Ruan et al., [8] confirmed that a cloak with ideal material parameters in a perfect invisibility cloak by symmetrically studying the scattering coefficient from the near ideal case to the ideal one. Yan et al., explored important scattering characteristics of cylindrical invisibility cloak [9-12]. They described that cylindrical cloak having simplified material parameter inherently allowing the zeroth-order cylindrical wave to pass through the cloak as if the cloak is made of a homogenous isotropic medium and thus visible to all higher-order cylindrical waves. Their numerical simulation suggests that the simplified cloak inherits some properties of the ideal cloak, but some scattering exist. Greenleaf et al., worked on the improvement of cylindrical cloak with soft and hard surfaces (SHS) lining [13]. They showed that the cloak is significantly improved by the use of SHS lining with both the far field of the scattering wave significantly reduced and the blow up of electric field density and magnetic field density prevented. Leonhardt discussed optical conformal mapping in [14]. Shahzad et al., analyzed the cylindrical invisibility cloak incorporating PEMC

Submitted On: April 20, 2013
Accepted On: Jan. 26, 2014

at perturbed void region in [15]. A Green's function approach to calculate scattering width for cylindrical cloaks has been discussed by J. S. McGuirk [16].

The idea of nihility medium is given by Lakhtakia [17], and has received a lot of interest within the electromagnetic community. Nihility medium is a medium in which both relative permittivity and permeability are null-valued. This idea engaged many researchers in studying problem related to electromagnetics [18-24]. Due to this fact the medium does not allow the electromagnetic energy to propagate in it. For nihility condition Maxwell's equations have the form as,

$$\nabla \times \mathbf{E} = 0 \quad (1)$$

$$\nabla \times \mathbf{H} = 0. \quad (2)$$

Metamaterial with both negative permittivity and permeability, also known as backward (BW) medium or double negative (DNG) medium has been extensively studied. Scattering of electromagnetic plane waves by a nihility cylinder coated with different types of metamaterials is investigated by Ahmed et al., [23-24].

In the current work an invisibility cloak termed as cylindrical invisibility cloak incorporating nihility as core is discussed. Our main focus is to explore the scattering characteristics of the cylindrical invisible nihility cloak and to improve the convergence rate of the scattered fields in free space because in nihility case the zeroth-order contribution of Bessel functions changes to first-order for n = 0, thus decreasing the scattered fields.

The next sections deal with the formulation of the problem. Using the properties of the nihility medium, conclusions about the better cloak are drawn analytically. We have used e^{-jwt} time dependence, which is suppressed throughout the analysis.

II. ANALYTICAL FORMULATION

The geometry of 2-D cylindrical nihility cloak is shown in Figure 1. Invisibility cloak has been constructed to compress electromagnetic fields in a cylindrical region r' < b into concentric cylindrical shell a < r < b. The region outside radius b is termed as region 0, which is free space with k_0 as wave number and η_0 as impedance, which are given by

$$k_0 = w\sqrt{\mu_0\epsilon_0} \ , \eta_0 = \sqrt{\frac{\mu_0}{\epsilon_0}} \ .$$

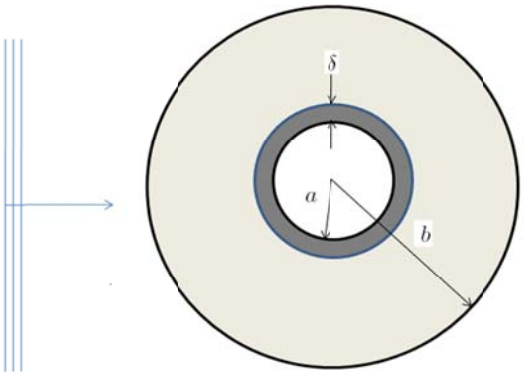

Figure1. Geometry of an invisible nihility cloak.

The region between a + δ < r < b is termed as region 1, which is composed of unknown medium. Radii of inner and outer cylinders are 'a' and 'b' respectively. 'δ' is the tiny perturbation. The region inside radius r < a + δ is region 2, which is assumed to be a dielectric medium at first instance with k_2 as wave number and η_2 as impedance, which are given as

$$k_2 = w\sqrt{\mu_2\epsilon_2} \ , \eta_2 = \sqrt{\frac{\mu_2}{\epsilon_2}} \ .$$

Consider the coordinate transformation in cylindrical coordinates [5] as,

$$f(r) = r' = a + \frac{r(b-a)}{b} \ ,$$

with the characteristics f (a) = 0 and f (b) =b, while θ and z are kept unchanged. Following the above coordinate transformation method [5], the permittivity and permeability of the cloak region may be obtained as,

$$\epsilon_r = \mu_r = \frac{f(r)}{rf'(r)}$$

$$\epsilon_z = \mu_z = \frac{f(r)f'(r)}{r},$$

$$\epsilon_\theta = \mu_\theta = \frac{f(r)f'(r)}{f(r)},$$

where the superscript ' denotes differentiation with respect to argument.

A. TE case

Consider the case when a TE wave is incident on the cloak from free space and it is assumed that the core of the cloak is composed of dielectric medium. The total electromagnetic field for the region r > b can be written as,

$$H_z = \sum_{n=-\infty}^{\infty} J_n(k_0 r) e^{jn(\theta)} + a_n H_n(k_0 r) e^{jn(\theta)} \quad (3)$$

$$E_\theta = \frac{k_0}{jw\epsilon_0} \sum_{n=-\infty}^{\infty} J_n'(k_0 r) e^{jn(\theta)} + a_n H_n'(k_0 r) e^{jn(\theta)}, \quad (4)$$

with $J_n(.)$, $H_n(.)$ are the Bessel and Hankel functions, respectively and a_n is the scattering coefficient in the region r>b. The scattering coefficients are required to be considered because region 1 is a dielectric medium at first instance and at the boundary of region 0 and region 1 some part of the fields should be reflected and some should be transmitted. The cloak having no scattering is termed as ideal one and the cloak having small scattering is nearest to ideal situation. That is the reason of considering these scattering coefficients. The total electromagnetic fields for region a<r< b are given as,

$$H_z = \sum_{n=-\infty}^{\infty} b_n J_n(k_1(r-a)) e^{jn(\theta)} + c_n H_n(k_1(r-a)) e^{jn(\theta)} \quad (5)$$

$$E_\theta = \frac{k_1}{jw\epsilon_\theta(r)} \sum_{n=-\infty}^{\infty} b_n J_n'(k_1(r-a)) e^{jn(\theta)} + c_n H_n'(k_1(r-a)) e^{jn(\theta)}, \quad (6)$$

with $k_1 = k_0 b/(b-a)$ and b_n, c_n as transmission and reflection coefficients, respectively.The fields in the region r<a are,

$$H_z = \sum_{n=-\infty}^{\infty} d_n J_n(k_2 r) e^{jn(\theta)} \quad (7)$$

$$E_\theta = \frac{k_2}{jw\epsilon_2} \sum_{n=-\infty}^{\infty} d_n J_n'(k_2 r) e^{jn(\theta)}, \quad (8)$$

where d_n is the transmission coefficient and k_2 is the wave number for region r<a.

The boundary conditions require that the tangential components of **E** and **H** fields to be continues across the interfaces at r = b and r = a + δ. After the application of the boundary conditions and utilizing the concept of impedance matching discussed in [11,15], we can find the unknown scattering coefficient a_n in free space and is given below,

$$a_n = \frac{k_2 J_n(k_1\delta) - \frac{k_1}{\epsilon_\theta(a+\delta)} L_n\big(k_0(a+\delta)\big) J_n'(k_0(a+\delta))}{\frac{k_1}{\epsilon_\theta(a+\delta)} L_n\big(k_0(a+\delta)\big) H_n'\big(k_0(a+\delta)\big) - k_2 H_n(k_1\delta)} \quad (9)$$

where

$$L_n(\chi) = \frac{J_n(\chi)}{J_n'(\chi)}. \quad (10)$$

B. TM case

Now considering the case where a TM wave is incident on the cloak from free space. The total electromagnetic field for the region r > b can be written as,

$$E_z = \sum_{n=-\infty}^{\infty} J_n(k_0 r) e^{jn(\theta)} + a_n' H_n(k_0 r) e^{jn(\theta)} \quad (11)$$

$$H_\theta = \frac{-k_0}{jw\mu_0} \sum_{n=-\infty}^{\infty} J_n'(k_0 r) e^{jn(\theta)} + a_n' H_n'(k_0 r) e^{jn(\theta)}. \quad (12)$$

The total electromagnetic field for the region a<r < b are given as,

$$E_z = \sum_{n=-\infty}^{\infty} b_n' J_n(k_1(r-a)) e^{jn(\theta)} + c_n' H_n(k_1(r-a)) e^{jn(\theta)} \quad (13)$$

$$H_\theta = \frac{-k_1}{jw\mu_\theta(r)} \sum_{n=-\infty}^{\infty} b_n' J_n'\big(k_1(r-a)\big) e^{jn(\theta)} + c_n' H_n'(k_1(r-a)) e^{jn(\theta)}. \quad (14)$$

The fields in the region r<a are,

$$E_z = \sum_{n=-\infty}^{\infty} d_n' J_n(k_2 r) e^{jn(\theta)} \quad (15)$$

$$H_\theta = \frac{-k_2}{jw\mu_2} \sum_{n=-\infty}^{\infty} d_n' J_n'(k_2 r) e^{jn(\theta)}, \quad (16)$$

Where a_n', b_n', c_n', and d_n' are the scattering coefficients for TM case. These coefficients can be found by applying appropriate boundary conditions at r = b and r = a + δ. The scattering coefficients a_n' in free space can be written as,

$$a_n' = \frac{k_2 J_n(k_1\delta) - A * J_n'(k_0(a+\delta))}{A * H_n'\big(k_0(a+\delta)\big) - k_2 H_n(k_1\delta)} \quad (17)$$

Where $A = \frac{k_1}{\mu_\theta(a+\delta)} L_n\big(k_0(a+\delta)\big)$.

C. Limiting procedure for nihility cloak

Now, the refractive index of nihility must benull-valuedbecause$\varepsilon_2 = \mu_2 = 0$as discussed by Lakhtahia in [17]. For the function $L_n(X)$ we have,

$$\lim_{\chi\to 0} \chi L_0(\chi) = -2, \quad n = 0 \quad (18)$$

$$\lim_{\chi\to 0} \chi^{-1} L_0(\chi) = n^{-1}, \quad n \neq 0. \quad (19)$$

Therefore, after taking the limit $k_2 \to 0$, equations (9) and (17) for a nihility cloak simplify to,

$$a_0 = a_n' = \frac{J_1(k_0(a+\delta))}{H_1\big(k_0(a+\delta)\big)}, \quad n = 0 \quad (20)$$

$$a_n = a_n' = \frac{J_{|n|}(k_0(a+\delta))}{H_{|n|}\big(k_0(a+\delta)\big)}, \; n \neq 0. \quad (21)$$

From the results given in the above equations, it is clear that the nihility core ($\varepsilon_2 = \mu_2 \to 0$) is the void region because no fields exist in this region.

III. NUMERICAL RESULTS AND DISCUSSION

In this section some numerical results based on the proposed geometry are presented for cylindrical invisible cloak with nihility layer at δ. Wave number of the free space is taken as $k_0=0.064/\pi$. The radius of the inner boundary is taken as $a=1.2\pi/k_0$ and radius of outer boundary is $b = 2\pi/k_0$, while the range of tiny perturbation δ is taken as $10^{-8}a < \delta < 10^{-2}a$.

Figure 2 shows the scattering coefficient for n = 0. The result is compared with the published literature and found to be much better. In Fig. 2 the dotted red line is the nihility case while the solid blue line is the case without PEC [12]. The scattering coefficient approaches 0.1 at $\delta = 10^{-8}$ while for the case of nihility approaches 10^{-19} at $\delta = 10^{-8}$. Hence better convergence rate is observed in case of nihility core. From the study of previous literature [9, 12, 15], it has been noted that better cloak may be achieved using PEC core for TM polarization and PMC core for TE polarization. In these combinations, for each case, zeroth scattering coefficient is function of first order cylindrical wave functions. This is due to the fact that nihility will have a better impedance matching with free space. Figure 3 shows the scattering coefficient for n = 0 and the result is compared with the case when PEC layer is incorporated at δ [12]. This result is found in good agreement with [12].

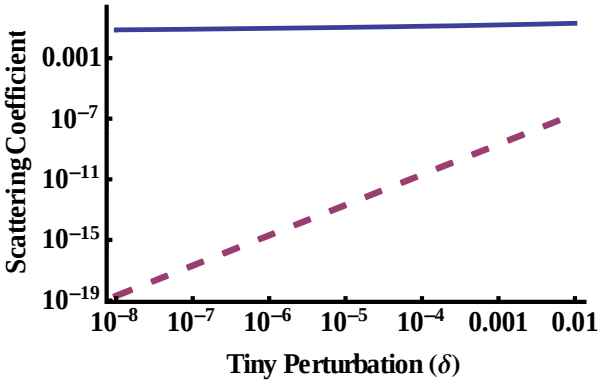

Fig. 2. Scattering coefficients for n = 0 with a=1.2π/k0 and b=2π/k0. Blue line is non PEC case [12] and dotted red line is nihility case.

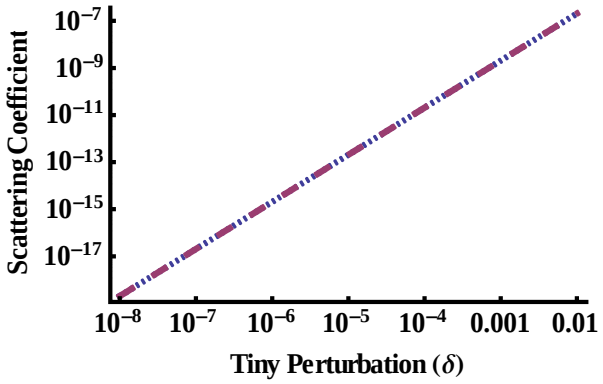

Fig. 3. Scattering coefficients for n=0 with a=1.2π/k0 and b=2π/k0. Dotted blue line is PEC case [12] and dashed red line is nihility case.

Figures 4 and 5 show the scattering coefficients for n = 1 and n = 2, respectively. These results are compared with the plots presented in [12] and found to be in good agreement.

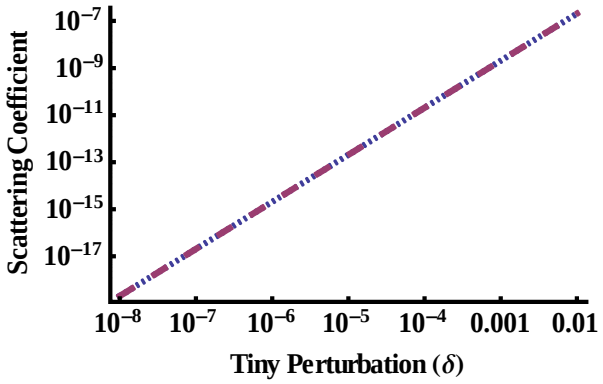

Fig. 4. Scattering coefficients for n=1 with $a=1.2\pi/k_0$ and $b=2\pi/k_0$. Dottedblue line is PEC case [12] and dashed red line is nihility case.

For the case of the nihility core, same coefficients are obtained for TE and TM case as given in equation (21). This implies that these coefficients are independent of the polarization of the incident field, which is not possible for the case when PEC or PMC are used as core reference [12]. The main advantage of using nihility is nearest ideal situation, which is very powerful characteristic of the cloak because in nihility case the zeroth-order contribution of Bessel functions changes to first-order for n = 0 (equation (20)), thus decreasing the scattered fields.

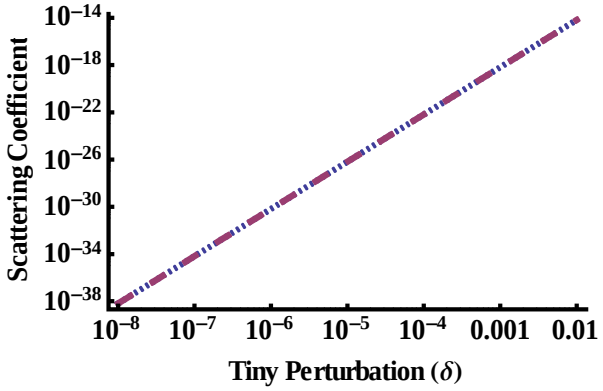

Fig. 5. Scattering coefficients for n=2 with a=1.2π/k0 and b=2π/k0. Dotted blue line is PEC case [12] and dashed red line is nihility case.

IV. CONCLUSIONS

From the analytical calculations done for both the TM and TE cases we can draw following conclusions:

i. It is shown that using nihility at δ layer o the geometry we can make cloak equal to the ideal situation.
ii. In case of nihility, the scattering coefficients are independent of the type of incident field.

ACKNOWLEDGMENT

Dr Abdul Ghaffar would like to thank, research centre, College of Engineering, Deanship of Scientific Research, King Saud University, Saudi Arabia. Authors would also appreciate the discussions with Prof. Kohei Hongo in the completion of this work with thanks.

REFERENCES

[1] D. R. Smith, J. B. Pendry, and M. C. Wiltshire, "Metamaterials and negative reflection index," *Science*, vol. 305, no. 5685, pp. 788-792, 2004.
[2] V. Shalaev, "Optical negative index metamaterials," *Nature Photonics*, vol. 1, pp. 41-48, 2006.
[3] R. Shelby, D. Smith, and S. Schults, "Experimental verification of a negative index of refraction," *Science*, vol. 292, no. 5514, pp. 77-79, 2001.
[4] J. Pendry, "Negative refraction makes a perfect lens," *Physical Review Letters*, vol. 85, no. 18, pp. 3966-3969, 2000.
[5] J. Pendry and D. Schuring, "Controlling electromagnetic fields," *Science*, vol. 312, no. 5781, pp. 1780-1782, 2006.
[6] S. Cummer, B. Popa, D. Schuring, D. Smith, and J. Pendry, "Full-wave simulations of electromagnetic cloaking structures," *Physical Review E*, vol. 74, no. 3, pp. 36621, 2006.
[7] D. Schuring, J. Mock, B. Justice, S. Cummer, A. Pendry, and D. Smith, "Metamaterial electromagnetic cloak at microwave frequencies," *Science*, vol. 314, no. 5801, pp. 977-980, 2006.
[8] Z. Ruan, M. Yan, C. Neff, and M. Qiu, "Ideal cylindrical cloak: Perfect but sensitive to tiny perturbations," *Physical Review Letters*, vol. 99, no. 11, pp. 113903, 2007.
[9] M. Yan, Z. Ruan, and M. Qiu, "Cylindrical invisibility cloak with simplified material parameters is inherently visible," *Physical Review Letters*, vol. 99, no. 23, pp. 233901, 2007.
[10] M. Yan, Z. Ruan, and M. Qiu, "Scattering characteristics of simplified cylindrical invisibility cloaks," *Optics Express*, vol. 15, no. 26, pp. 17770-17782, 2007.
[11] W. Yan, M. Yan, Z. Ruan, and M. Qiu, "Coordinate transformation make perfect invisibility cloaks with arbitrary shape," *New Journal of Physics*, vol. 10, no. 4, pp. 043040, 2008.
[12] W. Yan, M. Yan, Z. Ruan, and M. Qiu, "Influence of geometrical perturbation at inner boundaries of invisibility cloaks," *Journal of the Optical Society of America*, Series A, vol. 25, no. 4, pp. 968-973, 2008.
[13] A. Greenleaf, Y. Kurylev, M. Lassas, and G. Uhlmann, "Improvement of cylindrical cloaking with the SHS lining," *Optics Express*, vol. 15, no. 20, pp. 12717-12734, 2008.
[14] U. Leonhardt, "Optical conformal mapping," *Science*, vol. 312, no. 5781, pp. 1777-1780, 2006.
[15] A. Shahzad, F. Qasim, S. Ahmed, and Q. A. Naqvi, "Cylindrical invisibility cloak incorporating PEMC at perturbed void region," *Progress in Electromagnetics Research M*, vol. 21, pp. 6176, 2011.
[16] J. S. McGuirk, P. J. Collins, M. J. Havrilla, and A. W. Wood, "A Green's function approach to calculate scattering width for cylindrical cloaks," *Applied Computational Electromagnetics Society (ACES) Journal*, vol. 25, no. 2, pp. 108-116, Feb. 2010.
[17] A. Lakhtakia "An electromagnetic trinity from negative permittivity and negative permeability," *Int. J. of Infrared Millim. Waves*, vol. 22, pp. 1731-1734, 2001.
[18] A. Lakhtakia and J. B. Goddes, "Scattering by nihility cylinder," *Int. J. of Electron. Commun.*, (AEU) vol. 61, pp. 62-65, 2007.
[19] A. Lakhtakia, M. McCall, and W. S. "Weiglhofer brief overview of recent developments on negative phase-velocity mediums (alias left-handed

materials)," *AE Int. J. Electron. Commun.*, vol. 56, pp. 407-410, 2002.
[20] S. A. Ramakrishna, "Physics of negative refractive index materials," *Rep. Prog. Phys.*, vol. 68, pp. 449-521, 2005.
[21] A. Lakhtakia, "On perfect lenses and nihility," *Int. J. of Infrared Millim. Waves*, vol. 23, pp. 339-43, 2002.
[22] R. W. Ziolkowski, "Propagation in and scattering from a matched metamaterial having a zero index of refraction," *Phys. Rev. E*, vol. 70, pp. 046608, 2004.
[23] S. Ahmed and Q. A. Naqvi, "Electromagnetic scattering from a chiral-coated nihility cylinder," *Progress in Electromagnetics Research (PIER), Letters*, vol. 18, pp. 41-50, 2010.
[24] S. Ahmed and Q. A. Naqvi, "Scattering of electromagnetic waves from a nihility circular cylinder coated with a metamaterial," *J. of Infrared Millim. Waves*, vol. 30, pp. 1044-1052, 2009.

Anjum Shahzad was born in Malakwal Mandi Bauh-ud-Din (Pakistan) on December, 1985. He received his M.Sc and M.Phil degree in electronics from Quaid-i-Azam University in 2007 and 2010, respectively. He received Gold Medal from the Quaid-i-Azam University. He is the author of three international publications. He is currently working towards Ph.D. His current research interest includes techniques used in buried landmines detection and stealing, electromagnetic cloaks and scattering from canonical objects.

Shakeel Ahmed was born in a village Baldher (KPK), Pakistan. He received his initial education from his native town. He graduated from University of Peshawer and received PhD from Quaid-i-Azam University, Islamabad (Pakistan). He is author of over twenty (20) international journal publications. His current research interests include; electromagnetic scattering from different types of geometries and materials.

Abdul Ghaffar was born in MithaTiwana (Khushab), Sargodha (Pakistan). He got his initial education from his native town and got PhD from Quaid-i-Azam University, Pakistan. He is Assistant Professor at Agriculture University, Faisalabad (Pakistan). Currently he is working as researcher at King Saud University, SaudiArabia. His research interests are high frequency electromagnetic scattering from slabs and antennas.

Qaisar Abbas Naqvi was born in village of District Narowal (Pakistan). He got his M.Sc., M. Phil and PhD from Quaid-i-Azam University Islamabad (Pakistan). He has published over one hundred and fifty (150) papers in international journals. He also author of a book and chapters in different books. He has successfully supervised eight PhDs and more than 80 M. Phil students after his PhD in 1998. His research interests are: Kobyashi potential, Maslov's Method, GTD, Fractional electromagnetics, buried cylinders, waveguides, slits, strips, antennas and numerical electromagnetics.

A Novel WCS-SFDTD Method for Solving Oblique Incident Wave on Periodic Structures

Y.-F. Mao [1], B. Chen [2], X.-X. Yin [1], and J. Chen [1]

[1] China Satellite Maritime Tracking and Control Department, Jiangyin, 2144000, China
myf4494@163.com, yinxiaoxu@163.com, jianchen73@163.com

[2] National Key Laboratory on Electromagnetic Environment and Electro-optical Engineering
PLA University of Science and Technology, Nanjing, 210007, China
emcchen@163.com

Abstract ─ In this paper, a novel weakly conditionally stable spectral finite-difference time-domain method is proposed to solve oblique incident wave on periodic structures, namely NWCS-SFDTD. Because the stability condition is determined only by one space discretization, this new method is extremely useful for periodic problems with very fine structures in one or two directions. By using the constant transverse wave-number (CTW) wave, the fields have no delay in the transverse plane, as a result, the periodic boundary condition (PBC) can be implemented easily for oblique incident wave. Compared with the alternating-direction-implicit SFDTD (ADI-SFDTD) method this NWCS-SFDTD method has higher computational efficiency and better accuracy, especially for larger time-step size case. At each time step, it only needs to solve four implicit equations and four explicit equations, which is six implicit equations and six explicit equations in the ADI-SFDTD method. So while maintaining the same size of the time-step, the CPU time for this method can be reduced to about two-thirds of that for the ADI-SFDTD method. Numerical examples are presented to demonstrate the efficiency and accuracy of the proposed algorithm. To reduce the numerical dispersion error, the optimized procedure is applied.

Index Terms─ Finite-difference time-domain (FDTD), oblique incident, periodic structure, and weakly conditionally stable.

I. INTRODUCTION

The finite-difference time-domain (FDTD) technique is a robust analysis tool applicable to a wide variety of complex problems [1, 2]. Frequently, problems are encountered in which periodicity exists in one or more dimensions of the problem geometry, taking advantage of this periodicity can lead to greater efficiency and accuracy when solving the problem numerically. Instead of analyzing the entire structure, only a single unit cell needs to be analyzed by incorporating the periodic boundary condition (PBC) [3-5]. For a normally incident wave, the PBC is quite straightforward as there is no phase shift between each periodic cell [1]. However, when a plane-wave source is obliquely incident, there is a cell-to-cell phase variation between corresponding points in different unit cells which causes the time-domain implementation to become more difficult. To deal with this problem, several methods have been introduced, such as the Sine-Cosine method [6] and the split-field method [7]. Recently, another new formulation, named spectral FDTD (SFDTD) was proposed [8], because the constant wave-number (CTW) wave is used, there is no delay in the transverse plane and the PBC can be implemented directly in the time domain.

Aforementioned FDTD methods for periodic structures are explicit time-marching techniques that are subject to the Courant-Friedrich-Levy (CFL) stability condition [1]. As a result, a maximum time-step size is limited by the minimum cell size in a computational domain,

Submitted On: Dec. 11, 2012
Accepted On: Jan. 27, 2014

which makes this method inefficient for the problems where fine-scale structures are involved. To overcome the restriction of the CFL stability condition, an alternating-direction-implicit (ADI) FDTD solution for periodic structures is proposed [9], as well as locally-one-dimensional (LOD) FDTD [10]. Although the time-step size in the ADI-FDTD simulations is no longer bounded by the CFL criterion, the method exhibits a splitting error associated with the square of the time-step size [11], which limits the accuracy of the ADI-FDTD method. Meanwhile, in the ADI-FDTD scheme, it must solve six implicit updates and six explicit updates for one full-update cycle, which makes it computationally inefficient.

To overcome the drawbacks of the ADI-FDTD method, a hybrid implicit-explicit (HIE) FDTD method was submitted [12], and it has been introduced to solve periodic problems [13]. This method has higher accuracy and efficiency than the ADI-SFDTD method, but with confined usage, because the time-step size in this method is limited by two space discretizations, namely, $\Delta t \le 1/\left(c\sqrt{1/\Delta y^2 + 1/\Delta z^2}\right)$, which is independent of Δx. So if there are fine structures in the x-direction, the advantage of the method is obvious. However, for certain problems, if there are fine structures in two directions its efficiency is reduced. Recently, a novel weakly conditionally stable (NWCS) FDTD method, which is extremely useful for problems with very fine structures in two directions was discussed [14], namely, NWCS-FDTD. It has been introduced to the body-of-revolution FDTD [15].

In this paper, the novel weakly conditionally stable technique is applied to the SFDTD method, resulting in a NWCS-SFDTD method, which can solve periodic structures with oblique incident wave efficiently. The time-step size in this method is only determined by one spatial increment, the weakly conditional stability is presented analytically. To eliminate the time delay in transverse plane, the CTW wave [8] is applied. As a result, the FDTD code needs to be changed from real variables to complex variables, which is different from the conventional NWCS-FDTD method. Compared with the ADI-SFDTD method it only needs to solve four implicit updates, other four equations can be updated directly, which are six implicit updates and six explicit updates in the ADI-SFDTD method. The proposed method has higher computational efficiency and better accuracy than the ADI-SFDTD method. The running time can be reduced to about two-thirds of the ADI-SFDTD method. Numerical examples are conducted to verify the accuracy and the efficiency of this implementation. In order to reduce the numerical dispersion error, the optimized procedure is applied.

II. THEORY

A. Spectral FDTD implementation

In the SFDTD method, the incident wave is represented in the frequency domain. By applying an inverse Fourier transform on it, we can obtain the CTW wave in the time domain, which can be represented as [8],

$$\begin{aligned} E_t^{CTW} &= \exp\left(\tilde{j}k_x x\right)\exp\left(\tilde{j}k_y y\right)\xi^{-1}\left[\exp\left(\tilde{j}k_z\left(z-z_0\right)\right)\exp\left(-k_0^2/\sigma^2\right)\right] \\ H_l^{CTW} &= \exp\left(\tilde{j}k_x x\right)\exp\left(\tilde{j}k_y y\right)\xi^{-1}\left[\exp\left(\tilde{j}k_z\left(z-z_0\right)\right)Y_{TE}\exp\left(-k_0^2/\sigma^2\right)\right] \\ Y_{TE} &= k_z/\eta_0 k_0 \end{aligned} \tag{1}$$

where k_x, k_y represent transverse wave-numbers, which are assumed to be constant numbers (independent of frequency). k_z is normal wave-number, $k_0 = 2\pi f/c$, and $\tilde{j} = \sqrt{-1}$. η_0 is the impedance of free space. The term $\exp\left(-k_0^2/\sigma^2\right)$ corresponds to a Gaussian pulse used to limit the bandwidth of incident wave. ξ^{-1} represents the inverse Fourier transform. If k_x, k_y are constant numbers, that means k_l is constant, so we can conclude that in the CTW wave different frequencies correspond different incident angles.

The x- and y- field components of the CTW wave can be calculated as,

$$\begin{aligned} E_x^{CTW} &= -\frac{k_y}{k_l}E_t^{CTW}, \quad E_y^{CTW} = \frac{k_x}{k_l}E_t^{CTW} \\ H_x^{CTW} &= \frac{k_x}{k_l}H_l^{CTW}, \quad H_y^{CTW} = \frac{k_y}{k_l}H_l^{CTW} \end{aligned}. \tag{2}$$

They can be added to the computational domain by using total-field/scattered-field method [1].

B. Formulations of the NWCS-SFDTD method

In the NWCS-SFDTD method, the field updating for one time step is performed using two

procedures. The relations between the field components of the novel weakly conditionally stable SFDTD scheme can be represented as,

$$([I]+[A])U^{n+\frac{1}{2}}=([I]+[B])U^{n} \tag{3}$$

$$([I]+[C])U^{n+1}=([I]+[D])U^{n+\frac{1}{2}}, \tag{4}$$

where $U^n=[E_x^n\ E_y^n\ E_z^n\ H_x^n\ H_y^n\ H_z^n]$ and $[I]$ denotes the unit matrix,

$$[A]=\begin{bmatrix}0 & \Delta t/2\varepsilon\square D_1\\ \Delta t/2\mu\square D_2^T & 0\end{bmatrix},[B]=\begin{bmatrix}0 & -\Delta t/2\varepsilon\square D_2\\ -\Delta t/2\mu\square D_1^T & 0\end{bmatrix} \tag{5}$$

$$[C]=\begin{bmatrix}0 & -\Delta t/2\varepsilon\square D_1^T\\ -\Delta t/2\mu\square D_2 & 0\end{bmatrix},[D]=\begin{bmatrix}0 & \Delta t/2\varepsilon\square D_2^T\\ \Delta t/2\mu\square D_1 & 0\end{bmatrix}, \tag{6}$$

$$[D_1]=\begin{bmatrix}0 & 0 & 0\\ 0 & 0 & D_x\\ 0 & D_y & 0\end{bmatrix},[D_2]=\begin{bmatrix}0 & 0 & 0\\ -2D_z & 0 & D_x\\ D_y & 0 & 0\end{bmatrix}, \tag{7}$$

where ε,μ represent the permittivity and permeability, Δt is the time step size. D_1^T, D_2^T represent the transpose of D_1, D_2, respectively. D_x, D_y, D_z are the first-order central difference operators along the x-, y- and z- axes.

Incorporating the optimization parameters α, β and γ [16, 17], and by inserting equations (5)-(7) into equations (3) and (4), we have,

$$E_x^{n+1/2}=E_x^n \tag{8a}$$

$$E_y^{n+1/2}=E_y^n+\frac{\gamma\Delta t}{\varepsilon\partial z}\partial H_x^n-\frac{\alpha\Delta t}{2\varepsilon\partial x}\partial\left(H_z^{n+1/2}+H_z^n\right), \tag{8b}$$

$$E_z^{n+1/2}=E_z^n-\frac{\beta\Delta t}{2\varepsilon\partial y}\partial\left(H_x^{n+1/2}+H_x^n\right), \tag{8c}$$

$$H_x^{n+1/2}=H_x^n+\frac{\gamma\Delta t}{\mu\partial z}\partial E_y^{n+1/2}-\frac{\beta\Delta t}{2\mu\partial y}\partial\left(E_z^{n+1/2}+E_z^n\right), \tag{8d}$$

$$H_y^{n+1/2}=H_y^n, \tag{8e}$$

$$H_z^{n+1/2}=H_z^n-\frac{\alpha\Delta t}{2\mu\partial x}\partial\left(E_y^{n+1/2}+E_y^n\right), \tag{8f}$$

for the first-half time-step. And

$$E_x^{n+1}=E_x^{n+1/2}-\frac{\gamma\Delta t}{\varepsilon\partial z}\partial H_y^{n+1/2}+\frac{\beta\Delta t}{2\varepsilon\partial y}\partial\left(H_z^{n+1}+H_z^{n+1/2}\right) \tag{9a}$$

$$E_y^{n+1}=E_y^{n+1/2}, \tag{9b}$$

$$E_z^{n+1}=E_z^{n+1/2}+\frac{\alpha\Delta t}{2\varepsilon\partial x}\partial\left(H_y^{n+1}+H_y^{n+1/2}\right), \tag{9c}$$

$$H_x^{n+1}=H_x^{n+1/2}, \tag{9d}$$

$$H_y^{n+1}=H_y^{n+1/2}-\frac{\gamma\Delta t}{\mu\partial z}\partial E_x^{n+1}+\frac{\alpha\Delta t}{2\mu\partial x}\partial\left(E_z^{n+1}+E_z^{n+1/2}\right), \tag{9e}$$

$$H_z^{n+1}=H_z^{n+1/2}+\frac{\beta\Delta t}{2\mu\partial y}\partial\left(E_x^{n+1}+E_x^{n+1/2}\right), \tag{9f}$$

for the second-half time-step. The control parameters α, β, and γ used in the above formulations contribute to a reduction of the numerical dispersion error.

It can be seen from these equations that only equations (8b)-(8d), (8f), (9a), (9c), (9e), and (9f) need to be solved. However, none of them can be updated directly, because they all include the unknown components on both sides of the equations. In the first-half time-step, updating of $E_y^{n+1/2}$ component needs the unknown $H_z^{n+1/2}$ components at the same time, so the $E_y^{n+1/2}$ component has to be updated implicitly. Substituting equation (8f) into equation (8b) and by appropriate rearrangement we can obtain the equation for $E_y^{n+1/2}$,

$$\begin{aligned}&E_y^{n+1/2}\big|_{i,j+1/2,k}-\frac{\alpha^2\Delta t^2}{4\varepsilon\mu\Delta x^2}\left(\begin{matrix}E_y^{n+1/2}\big|_{i+1,j+1/2,k}-\\ 2E_y^{n+1/2}\big|_{i,j+1/2,k}+E_y^{n+1/2}\big|_{i-1,j+1/2,k}\end{matrix}\right)\\ &=E_y^n\big|_{i,j+1/2,k}+\frac{\gamma\Delta t}{\varepsilon\Delta z}\left(H_x^n\big|_{i,j+1/2,k+1/2}-H_x^n\big|_{i,j+1/2,k-1/2}\right)\\ &-\frac{\alpha\Delta t}{\varepsilon\Delta x}\left(H_z^n\big|_{i+1/2,j+1/2,k}-H_z^n\big|_{i-1/2,j+1/2,k}\right)\\ &+\frac{\alpha^2\Delta t^2}{4\varepsilon\mu\Delta x^2}\left(E_y^n\big|_{i+1,j+1/2,k}-2E_y^n\big|_{i,j+1/2,k}+E_y^n\big|_{i-1,j+1/2,k}\right).\end{aligned} \tag{10}$$

Similarly, in the first-half time-step, updating of the $E_z^{n+1/2}$ component in equation (8c) needs the $H_x^{n+1/2}$ components at the same time. Substituting equation (8d) into equation (8c) we can obtain the equation for $E_z^{n+1/2}$,

$$\begin{aligned}&E_z^{n+1/2}\big|_{i,j,k+1/2}-\frac{\beta^2\Delta t^2}{4\varepsilon\mu\Delta y^2}\left(\begin{matrix}E_z^{n+1/2}\big|_{i,j+1,k+1/2}-\\ 2E_z^{n+1/2}\big|_{i,j,k+1/2}+E_z^{n+1/2}\big|_{i,j-1,k+1/2}\end{matrix}\right)\\ &=E_z^n\big|_{i,j,k+1/2}-\frac{\beta\Delta t}{\varepsilon\Delta y}\left(H_x^n\big|_{i,j+1/2,k+1/2}-H_x^n\big|_{i,j-1/2,k+1/2}\right)\\ &-\frac{\beta\gamma\Delta t^2}{2\varepsilon\mu\Delta y\Delta z}\left(\begin{matrix}E_y^{n+1/2}\big|_{i,j+1/2,k+1}-E_y^{n+1/2}\big|_{i,j+1/2,k}\\ -E_y^{n+1/2}\big|_{i,j-1/2,k+1}+E_y^{n+1/2}\big|_{i,j-1/2,k}\end{matrix}\right)\\ &+\frac{\beta^2\Delta t^2}{4\varepsilon\mu\Delta y^2}\left(E_z^n\big|_{i,j+1,k+1/2}-2E_z^n\big|_{i,j,k+1/2}+E_z^n\big|_{i,j-1,k+1/2}\right).\end{aligned} \tag{11}$$

After $E_y^{n+1/2}$ and $E_z^{n+1/2}$ are obtained, $H_x^{n+1/2}$ and $H_z^{n+1/2}$ can be explicitly updated by using

equations (8f) and (8d). The components $E_x^{n+1/2}$ and $H_y^{n+1/2}$ in the first-half time-step need not be solved. In the second-half time-step, updating of the E_x^{n+1} component needs the unknown H_z^{n+1} components at the same time. Substituting equation (9f) into equation (9a) we can obtain the equation for E_x^{n+1},

$$E_x^{n+1}\Big|_{i+1/2,j,k} - \frac{\beta^2\Delta t^2}{4\varepsilon\mu\Delta y^2}\left(\begin{array}{l} E_x^{n+1}\big|_{i+1/2,j+1,k} - \\ 2E_x^{n+1}\big|_{i+1/2,j,k} + E_x^{n+1}\big|_{i+1/2,j-1,k}\end{array}\right)$$
$$= E_x^{n+1/2}\Big|_{i+1/2,j,k} - \frac{\gamma\Delta t}{\varepsilon\Delta z}\left(H_y^{n+1/2}\Big|_{i+1/2,j,k+1/2} - H_y^{n+1/2}\Big|_{i+1/2,j,k-1/2}\right)$$
$$+\frac{\beta\Delta t}{\varepsilon\Delta y}\left(H_z^{n+1/2}\Big|_{i+1/2,j+1/2,k} - H_z^{n+1/2}\Big|_{i+1/2,j-1/2,k}\right)$$
$$+\frac{\beta^2\Delta t^2}{4\varepsilon\mu\Delta y^2}\left(\begin{array}{l} E_x^{n+1/2}\big|_{i+1/2,j+1,k} - \\ 2E_x^{n+1/2}\big|_{i+1/2,j,k} + E_x^{n+1/2}\big|_{i+1/2,j-1,k}\end{array}\right) . \quad (12)$$

In the same way by substituting equation (9e) into equation (9c) we can obtain the equation for E_z^{n+1},

$$E_z^{n+1}\Big|_{i,j,k+1/2} - \frac{\alpha^2\Delta t^2}{4\varepsilon\mu\Delta x^2}\left(\begin{array}{l} E_z^{n+1}\big|_{i+1,j,k+1/2} \\ -2E_z^{n+1}\big|_{i,j,k+1/2} + E_z^{n+1}\big|_{i-1,j,k+1/2}\end{array}\right)$$
$$= E_z^{n+1/2}\Big|_{i,j,k+1/2} + \frac{\alpha\Delta t}{\varepsilon\Delta x}\left(H_y^{n+1/2}\Big|_{i+1/2,j,k+1/2} - H_y^{n+1/2}\Big|_{i-1/2,j,k+1/2}\right)$$
$$-\frac{\alpha\gamma\Delta t^2}{2\varepsilon\mu\Delta x\Delta z}\left(\begin{array}{l} E_x^{n+1}\big|_{i+1/2,j,k+1} - E_x^{n+1}\big|_{i+1/2,j,k} \\ -E_x^{n+1}\big|_{i-1/2,j,k+1} + E_x^{n+1}\big|_{i-1/2,j,k}\end{array}\right)$$
$$+\frac{\alpha^2\Delta t^2}{4\varepsilon\mu\Delta x^2}\left(\begin{array}{l} E_z^{n+1/2}\big|_{i+1,j,k+1/2} \\ -2E_z^{n+1/2}\big|_{i,j,k+1/2} + E_z^{n+1/2}\big|_{i-1,j,k+1/2}\end{array}\right) . \quad (13)$$

After E_x^{n+1} and E_z^{n+1} are obtained, the components H_y^{n+1} and H_z^{n+1} can be updated straightforwardly by using equations (9e) and (9f). In the second-half time-step the components E_y^{n+1} and H_x^{n+1} need not be solved.

To solve equation (10), the periodic boundary condition needs to be combined. Because k_x, k_y are independent of frequency, there are no time delay in the $x-y$ plane, so in the first-half time-step the PBC for the CTW wave can be implemented in the same way as the PBC for normal incidence [1],

$$E_y^{n+1/2}\left(N_{x4}, j+\frac{1}{2}, k\right) = E_y^{n+1/2}\left(N_{x1}, j+\frac{1}{2}, k\right)e^{\tilde{j}k_xP_x} \quad (14)$$

$$E_z^{n+1/2}\left(i, N_{y4}, k+\frac{1}{2}\right) = E_z^{n+1/2}\left(i, N_{y1}, k+\frac{1}{2}\right)e^{\tilde{j}k_yP_y} , \quad (15)$$

$$E_z^{n+1/2}\left(N_{x4}, j, k+\frac{1}{2}\right) = E_z^{n+1/2}\left(N_{x1}, j, k+\frac{1}{2}\right)e^{\tilde{j}k_xP_x} , \quad (16)$$

$$H_x^{n+1/2}\left(i, N_{y1}-1, k+\frac{1}{2}\right) = H_x^{n+1/2}\left(i, N_{y4}-1, k+\frac{1}{2}\right)e^{-\tilde{j}k_yP_y} \quad (17)$$

$$H_z^{n+1/2}\left(N_{x1}-1, j, k+\frac{1}{2}\right) = H_z^{n+1/2}\left(N_{x4}-1, j, k+\frac{1}{2}\right)e^{-\tilde{j}k_xP_x} \quad (18)$$

$$H_z^{n+1/2}\left(i, N_{y1}-1, k+\frac{1}{2}\right) = H_z^{n+1/2}\left(i, N_{y4}-1, k+\frac{1}{2}\right)e^{-\tilde{j}k_yP_y} \quad (19)$$

where, N_{x1}, N_{x4}, N_{y1}, N_{y4} represent the nodes of electric fields on the unit cell boundary. $P_x = N_{x4}\Delta x$, $P_y = N_{y4}\Delta y$ are the dimensions of the unit cell in the x- and y- direction, respectively. In the second-half time-step the PBC for the CTW wave can be implemented similarly.

By substituting equations (14)-(19) into equation (10) we can get,

$$[\mathrm{M}]\,\vec{E}_y = \vec{d} \quad (20)$$

where $\vec{d}$ represents the right-hand vector of equation (10) and $\vec{E}_y$ is unknown in general. [M] is obtained from equation (10) for each column of E_y, so equation (10) can be written as,

$$\begin{bmatrix} n & m & & & \rho \\ m & n & m & & \\ & \cdots & \cdots & \cdots & \\ & & m & n & m \\ \tau & & & m & n \end{bmatrix}\begin{bmatrix} E_y^{n+1/2}\big|_{N_{x1},j+1/2,k} \\ E_y^{n+1/2}\big|_{N_{x1}+1,j+1/2,k} \\ \vdots \\ E_y^{n+1/2}\big|_{N_{x4}-1,j+1/2,k} \end{bmatrix} = \begin{bmatrix} d(N_{x1}) \\ d(N_{x1}+1) \\ \\ \vdots \\ d(N_{x4}-1) \end{bmatrix} \quad (21)$$

$$m = -\frac{\Delta t^2\alpha^2}{4\varepsilon\mu\Delta x^2}, n = 1+\frac{\Delta t^2\alpha^2}{2\varepsilon\mu\Delta x^2} , \quad (22)$$

where $\rho = m\cdot e^{-\tilde{j}k_xP_x}$, $\tau = m\cdot e^{\tilde{j}k_xP_x}$.

The coefficient matrix [M] is not a tridiagonal matrix, so it can't be solved with the efficient forward-elimination and backward-substitution method directly. By using the Sherman Morrison formula, two auxiliary linear problems are defined [18],

$$[N]\,\vec{E}_{y1} = \vec{d} \quad (23)$$

$$[N]\,\vec{E}_{y2} = \vec{v}_1 , \quad (24)$$

$$[N] = [M] - \vec{v}_1\vec{v}_2{}^T , \quad (25)$$

$$\vec{v}_1 = \begin{bmatrix} \rho^{1/2} & 0 & \cdots & 0 & \tau^{1/2} \end{bmatrix}^T , \quad (26)$$

$$\vec{v}_2 = \begin{bmatrix} \tau^{1/2} & 0 & \cdots & 0 & \rho^{1/2} \end{bmatrix} . \quad (27)$$

So the solution of equation (21) is obtained via,

$$\vec{E}_y = \vec{E}_{y1} + \varsigma \vec{E}_{y2} \quad (28)$$

$$\varsigma = -\frac{\vec{v}_2^{\,T} \vec{E}_{y1}}{1 + \vec{v}_2^{\,T} \vec{E}_{y2}} . \quad (29)$$

By observation, one can find that matrix [M] in equation (20) is related to matrix [N]. Because [N] is a tridiagonal matrix, the auxiliary linear problems can be solved efficiently by using forward-elimination and backward-substitution method. Equations (11), (12), and (13) can be solved in the same way.

From the equations derived above, it can be seen that at each time step, the proposed method requires solution of four implicit updates and four explicit updates, while it needs to solve six implicit updates and six explicit updates in the ADI-SFDTD scheme. So we can find, the implementation of the NWCS-SFDTD method is simpler than the ADI-SFDTD method.

In the NWCS-SFDTD method the maximum time-step size is only determined by one spatial increment as it is in [14]. This is especially useful when the simulated structure has a fine-scale dimension in one or two directions. A small spatial increment can be used in the direction with fine scale and a larger spatial increment can be used in the direction with coarse scale. If we perform the implicit-difference scheme in the direction with a larger spatial increment, the time-step size is thus determined by the larger spatial increments. For example, the size of the structure in the z-direction is larger than those in the x- and y-directions. By setting $\Delta z = 10\Delta y = 10\Delta x$, the maximum time-step size meeting the stability condition of the NWCS-SFDTD algorithm can be determined as $\Delta t = \Delta z / c$, while the maximum time-step size for the conventional SFDTD method is $\Delta t = \dfrac{1}{c\sqrt{\Delta x^{-2} + \Delta y^{-2} + \Delta z^{-2}}} = \dfrac{\Delta z}{c\sqrt{201}}$. As a result, computational resources can be saved considerably.

III. NUMERICAL RESULTS

In this section a numerical example is presented to demonstrate the proposed NWCS-SFDTD method. Simulation results are carried out using the NWCS-SFDTD method, the conventional SFDTD method and the ADI-SFDTD method for comparison.

In the example, it is applied to calculate the reflection coefficient of EBG structure, the analyzed model is shown in Fig. 1. The structure is a periodic array of metallic squares with thin slots embedded in a dielectric slab. The dielectric slab has relative permittivity $\varepsilon_r = 4.0$. The physical dimensions of the geometry are $w = 5\text{mm}$, $d = 2.5\text{mm}$, $h = 25\text{mm}$. The sizes of the thin slots are 0.5mm. The space increments are $\Delta x = \Delta y = \Delta z/5 = 0.5$ mm. The computational domain is truncated by 16-layer PML in the z direction. So it contains 20×20×102 cells. The CTW wave is introduced into the computational domain, with the transverse wave-number k_x ranges from 0 m^{-1} to 200 m^{-1}. To satisfy the stability condition of the FDTD algorithm, the time-step size for the conventional SFDTD is $\Delta t \le 1.16$ ps, and the time-step size for the NWCS-SFDTD algorithm is only determined by increment Δz, that is $\Delta t \le 8.33$ ps. So in the simulation, the time-step size for the SFDTD method is kept constant $\Delta t = 1.16$ ps, while in the ADI-SFDTD and the NWCS-SFDTD method two time-step sizes are chosen, namely, 1.16 ps and 8.33 ps.

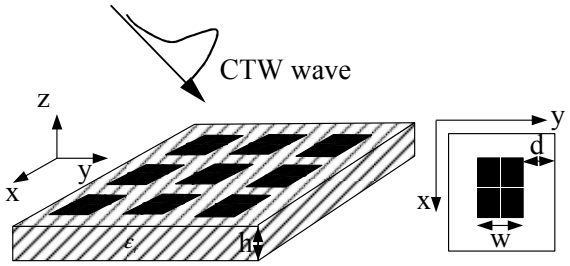

Fig. 1. The geometry of the numerical example.

Figure 2 shows the reflection coefficient of the EBG structure with the time-step size 1.16 ps for the conventional SFDTD, the NWCS-SFDTD, and the ADI-SFDTD method, respectively. It can be seen from these figures that both the proposed NWCS-SFDTD method and the ADI-SFDTD method agree well with the conventional SFDTD method, which means when the time-step size is small both the NWCS-SFDTD method and the ADI-SFDTD method have high accuracy.

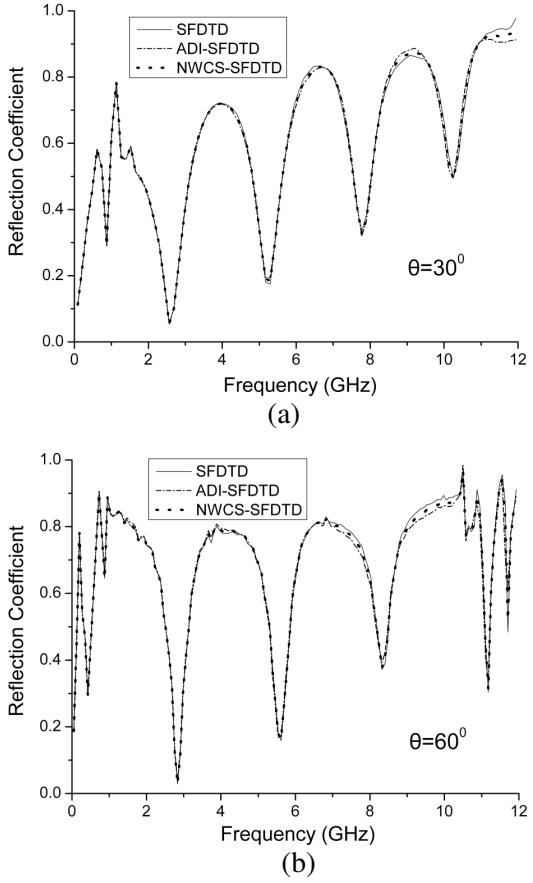

Fig. 2. Reflection coefficients for the conventional SFDTD (Δt = 1.16 ps), the NWCS-SFDTD (Δt = 1.16 ps), and the ADI-SFDTD (Δt = 1.16 ps) method for $\theta = 30^{o}$ and $\theta = 60^{o}$.

When the time-step size increases to 8.33 ps, the results are shown in Fig. 3. From Fig. 3 we can see when the time-step size increases both the ADI-SFDTD method and the proposed method have a deviation from the conventional SFDTD method. It is also shown that the discrepancy is larger at high frequencies than low frequencies. However, the deviation of the NWCS-SFDTD method is smaller than the ADI-SFDTD method. It is apparent that the proposed method has higher accuracy than the ADI-SFDTD method.

To reduce the numerical dispersion error, we employ the improved NWCS-SFDTD method with dispersion control parameters [19],

$$\alpha = \frac{\Delta x \tan\left(\frac{1}{2}ck\Delta t\right)}{c\Delta t \sin\left(\frac{1}{2}k\Delta x\right)},\quad \gamma = \frac{\Delta z \tan\left(\frac{1}{2}ck\Delta t\right)}{c\Delta t \sin\left(\frac{1}{2}k\Delta z\right)},\quad \beta = 1. \quad (30)$$

So when the time-step size is 8.33 ps, $\alpha = \gamma = 1.0246, \beta = 1$ are obtained. It can be seen from Fig. 4 that the results with dispersion control parameters reach a good agreement with the conventional SFDTD method.

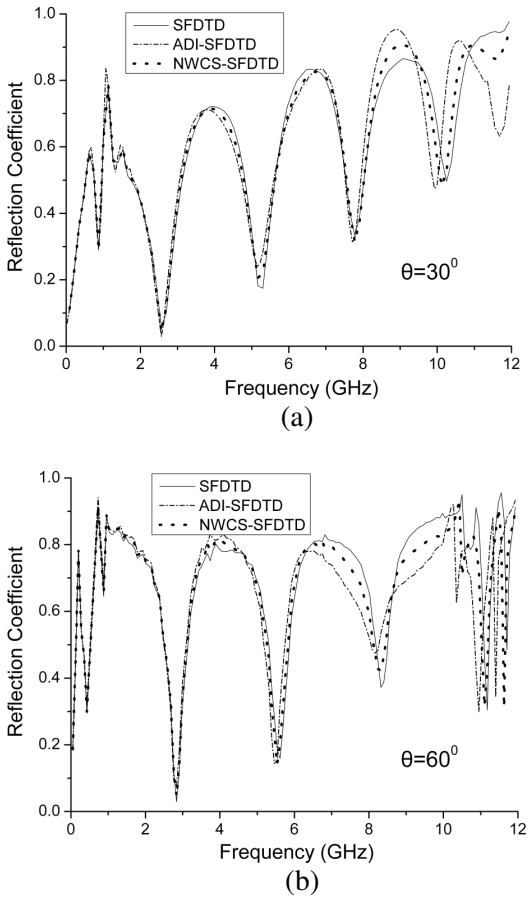

Fig. 3. Reflection coefficients for the conventional SFDTD (Δt = 1.16 ps), the NWCS-SFDTD (Δt = 8.33 ps) and the ADI-SFDTD (Δt = 8.33 ps) method for $\theta = 30^{o}$ and $\theta = 60^{o}$.

Finally, we mention the computational efficiency of the proposed NWCS-SFDTD method. On a Core2 2.4-GHz machine, it took the conventional SFDTD method 67446.6 seconds and the NWCS-SFDTD method (with the time-step size 8.33 ps) 17207.4 seconds to run the same simulation, which is 25737.3 seconds in the ADI-SFDTD method. So compared with the ADI-SFDTD method, the proposed method has higher efficiency. The CPU running time for this method is about 2/3 of the ADI-SFDTD method.

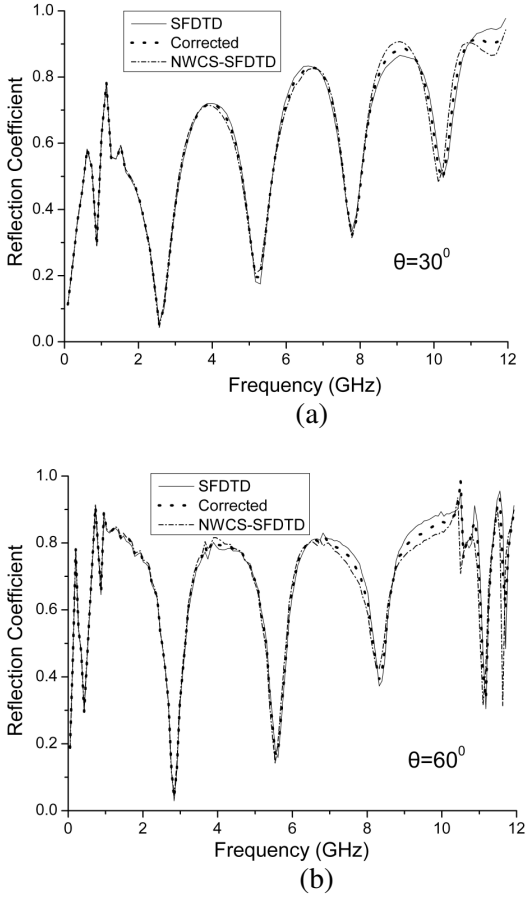

Fig. 4. Reflection coefficients calculated by the NWCS-SFDTD method (Δt = 8.33 ps) and the improved method with dispersion control parameters for $\theta = 30^{o}$ and $\theta = 60^{o}$.

IV. CONCLUSION

In this paper, we present a novel weakly conditionally stable SFDTD method to solve periodic structures at oblique incidence. Numerical results indicate that the proposed method is accurate and efficient. The CPU time for the proposed method can be reduced to about 2/3 of the ADI-SFDTD method. For the same time-step size, the proposed method not only has higher efficiency than the ADI-SFDTD method, but also higher accuracy.

ACKNOWLEDGMENT

This work was supported by Chinese National Science Foundation under Grant No. 60971063.

REFERENCES

[1] A. Taflove and S. Hagness, *Computational Electrodynamics: The Finite-Difference Time-Domain Method*, 2nd ed. Boston, MA: Artech House, 2000.

[2] B. Henin, A. Elsherbeni, F. Yang, and V. Demir, "FDTD formulation for the scattering from metamaterial under obliquely incident plane," *26th Annual Review of Progress in Applied Computational Electromagnetics (ACES)*, pp. 474-478, 2010.

[3] J. Wang, T. Zhao, J. Song, and T. Kamgaing, "Modeling of multilayered media for oblique incidence using effective medium theory," *28th Annual Review of Progress in Applied Computational Electromagnetics (ACES)*, pp. 812-817, 2012.

[4] T. Maruyama, Y. Oda, J. Shen, N. Tran, and H. Kayama, "The design of reflectarray using dual resonant characteristics of mushroom like structure," *28th Annual Review of Progress in Applied Computational Electromagnetics (ACES)*, pp. 780-785, 2012.

[5] T. Ikiz and M. K. Zateroglu, "Diffraction of obliquely incident plane waves by an impedance wedge with surface impedcances being equal to the intrinsic impedance of the medium," *Applied Computational Electromagnetics Society (ACES) Journal*, vol. 26, no. 3, pp. 199-205, 2011.

[6] P. Harms, R. Mittra, and K. Wai, "Implementation of the periodic boundary condition in the finite-difference time-domain algorithm for FSS structures," *IEEE Trans. Antennas Propagat.*, vol. 42, pp. 1317-1324, 1994.

[7] Y. Mao and B. Chen, "Parallel implementation of the split-field FDTD method for the analysis of periodic structure," *IEEE the 8th International Symposium on Antennas Propagation and EM Theory Proceeding*.

[8] A. Aminian and R.-S. Yahya, "Spectral FDTD: a novel technique for the analysis of oblique incident plane wave on periodic structures," *IEEE Trans. Antennas Propagat.*, vol. 54, pp. 1818-1825, 2006.

[9] Y.-F. Mao, B. Chen, H.-L. Chen, and Q. Wu, "Unconditionally stable SFDTD algorithm for solving oblique incident wave on periodic structures," *IEEE Microw. Wireless Compon. Lett.*, vol. 19, pp. 257-259, 2009.

[10] Y. Wakabayashi, J. Shibayama, J. Yamauchi, and H. Nakano, "A locally one-dimensional finite difference time domain method for the analysis of a periodic structure at oblique incidence," *Radio Science*, vol. 46, pp. 1-9, 2011.

[11] I. Ahmed and Z. Chen, "Error reduced ADI-FDTD methods," *IEEE Antennas and Wireless Propagat. Lett.*, vol. 4, pp. 323-325, 2005.

[12] J. Chen and A. Zhang, "A subgridding scheme based on the FDTD method and HIE-FDTD method," *The Applied Computational Electromagnetic Society (ACES) Journal*, vol. 26, no. 1, Jan. 2011.
[13] Y. Mao, B. Chen, et al., "WCS-FDTD algorithm for periodic structures," *IEEE Antennas and Wireless Propagat. Lett*., vol. 10, pp. 1236-1238, 2011.
[14] J. Chen and J. Wang, "A novel WCS-FDTD method with weakly conditional stability," *IEEE Trans. Electromagn. Compat.*, vol. 49, no. 2, pp. 419-426, May 2007.
[15] J. Chen and J. Wang, "A novel body-of –revolution finite-difference time-domain method with weakly conditional stability," *IEEE Microw. Wireless Compon. Lett.*, vol. 18, no. 6, pp. 377-379, June 2008.
[16] A.-P. Zhao, "Two special notes on the implementation of the unconditionally stable ADI-FDTD method," *Microwave and Optical Tech. Lett.*, vol. 33, no. 4, pp. 273-277, 2002.
[17] H. Zheng and K. Leung, "An efficient method to reduce the numerical dispersion in the ADI-FDTD," *IEEE Trans. Microw. Theory Tech.*, vol. 53, no. 7, pp. 2295-2301, July 2005.
[18] J.-W. Thomas, *Numerical Partial Differential Equations: Finite Difference Methods*, Berlin, Germany: Springer Verlag, 1995.
[19] M. Wang, Z. Wang, and J. Chen, "A parameter optimized ADI-FDTD method," *IEEE Antennas Wireless Propag. Lett.*, vol. 2, pp. 118-121, May 2003.

Yun-Fei Mao was born in Zhejiang province, China, in 1984. He received the B. S. degrees, the M.S. degree and the Ph.D. degree in Electric Systems from Nanjing Engineering Institute, Nanjing, China, in 2006, 2009, and 2013 respectively. He is currently working in China Satellite Maritime Tracking and Control Department, Yuan Wang, Jiangyin 214400, China. His research interests include computational electromagnetic and electro-magnetic tracking.

Bin Chen was born in Jiangsu, China, in 1957. He received the B.S. and M.S. degrees in Electrical Engineering from Beijing Institute of Technology, Beijing, China, in 1982 and 1987, respectively, and the Ph.D. degree in Electrical Engineering from Nanjing University of Science and Technology, Nanjing, China, in 1997. Currently, he is a Professor at National Key laboratory on Electromagnetic Environment and electro-optical Engineering, PLA University of Science and Technology. His research includes computational electromagnetics, EMC and EMP.

Xiao-Xu Yin was born in Hubei province, China, in 1978. He received the B.S. degrees in Wuhan university, Wuhan, China, in 1999. He is currently working in China Satellite Maritime Tracking and Control Department, Yuan Wang, Jiangyin 214400, China. His research interests include electromagnetics and electromagnetic tracking.

Jian Chen was born in Jiangsu province, China, in 1976. He received He received the B.S. North Western Industry University, Xi'an, China, in 1999. He is currently working in China Satellite Maritime Tracking.

Efficient Analysis of Multilayer Microstrip Problems by Modified Fast Directional Multilevel Algorithm

Hua Chen [1, 2]

[1]Faculty of Science, Kunming University of Science and Technology, Kunming, 650500, China
93056460@qq.com

[2] Key Laboratory of Unconventional Metallurgy, Ministry of Education, Kunming University of Science and Technology, Kunming 650093, China

Abstract ─ Fast directional multilevel algorithm (FDMA) combined with quad-tree structure is presented for analyzing multilayer microstrip problems. This method is successfully applied to analyze scattering in free space and it is extended to solve multilayer mircrostrip problems in this paper. The quad-tree structure is employed for the layer containing the microstrip patch, and then the defined of far field for every observed group is modified. There is only Kernel evaluation in low rank representation so that the surface-wave is extracted for the far-field Green's functions expansion when the dielectric substrate is thick or relative permittivity is large. The memory requirement and the CPU time per iteration of the multilayer microstrip structure is presented, which show the accuracy and efficiency of this method.

Index Terms - Modified fast directional multilevel algorithm, multilayer microstrip structures, S-parameters, and transmission coefficient.

I. INTRODUCTION

The method of moments (MoM) [1, 2] is preferred in the analysis of microstrip structures, such as mircrostrip antennas, microwave integrated circuits, and microstrip interconnects. The first kind is the so-called spectral domain MoM [3], which is time-consuming evaluation of doubly infinite integrals for integrands are highly oscillatory and decay slowly. The second kind is the spatial domain MoM, which is proposed by Michalski and Hsu in [4] for scattering by microstrip patch antennas in a multilayered medium. However, for large-scaled complex microstrip structures, it is impractical to solve resultant matrix equation because it has a memory requirement of O (N^2) and computational complexity is proportional to O (N^3). Many fast algorithms are developed to simulate large-scale microstrip problems, including frequency domain method [5-14] and spectral domain method [15-17]. The frequency domain method is more popular than spectral domain method because of escaping of Sommerfeld integral.

The frequency domain method includes the adaptive integral method (AIM) [5], the fast multipole algorithm (FMA) [6-8] and the multilevel matrix decomposition algorithm (MLMDA) [9], etc. These methods are successfully employed to analyze microstrip problems in conjunction with the discrete complex image method (DCIM) [10-11]. To be noticed, though the FMA is successfully applied to the microstrip problems, the procession is always difficult because of its dependence on the Green's function. At the beginning, FMA is tried to combine with DCIM to solve the static and two-dimensional problems [6]. Unfortunately, it will be lack of accuracy when the frequency is high. Though, FMA is employed in [7] for full wave analysis, the implementation is very complicated because the surface-wave poles are extracted in DCIM. The FMA also has been applied to thin layer structures as the thin stratified medium fast multipole algorithm [12], which is adaptive to thin-stratified media.

The fast directional multilevel algorithm is originally applied in the analysis of scattering problem of free space [13]. The method is Kernel independent and the Green's function is expanded by low rank representation, which is demonstrated efficiently in [13-14]. In this paper, the method is successfully applied to deal with planar microstrip structures in multilayered medium. There is only Kernel evaluation in low rank representation so that it is easily implemented in full wave analysis.

Submitted On: Nov. 29, 2012
Accepted On: Jan. 27, 2014

A quad-tree structure other than oct-tree structure is used for multilayered medium. However, the quad-tree structure is used for the layer, which contains the metallic patch. As a result, the definition of far field in our method has made some modifications. The DCIM is employed to efficiently evaluate the Sommerfeld integral and the surface wave contribution is considered for the far field of the Green's functions.

The interactions between the nearby groups are accounted for directly. For far apart groups, the interaction between the groups is accelerated by FDMA. The definition of high frequency regime and low frequency regime is the same as in the free space [13-14], except that the high frequency regime or low frequency regime in the neighboring layer must be considered now. Numerical results are presented to demonstrate the efficiency of this method.

II. FORMULATION

In this paper, the analysis is based on the mixed potential integral equation (MPIE) [14]. The microstrips are divided into triangular elements and the current is expanded using planar Rao-Wilton-Glisson (RWG) basis functions [2]. Consider a multilayered medium shown in Fig. 1. The dielectric constant of the substrates are ε_{r1}, ε_{r2}, ε_{r3}, etc, corresponding to the thickness d_1, d_2, d_3, etc. The boundary condition associated with the tangential electric field on a perfectly conducting surface, we obtain,

$$\hat{n}\times\mathbf{E}^s(\mathbf{r}) = -\hat{n}\times\left[\mathbf{E}^i(\mathbf{r})+\mathbf{E}^r(\mathbf{r})\right], \quad on \;\; S \tag{1}$$

where $\mathbf{E}^s$ refers to the scattered field excited by the current on the conducting surface of the antenna S. $\mathbf{E}^i$ denotes the incident electric field. The MPIE can be written as,

$$j\omega\mu_0\hat{n}\times\left[\mathbf{A}(\mathbf{r})+\frac{1}{k_0^2}\nabla\Phi(\mathbf{r})\right] = \hat{n}\times\left[\mathbf{E}^i(\mathbf{r})+\mathbf{E}^r(\mathbf{r})\right] \tag{2}$$

where

$$\mathbf{A}(\mathbf{r}) = \iint_S G_a(\mathbf{r},\mathbf{r}')\cdot\mathbf{J}(\mathbf{r}')dS', \tag{3}$$

$$\Phi(\mathbf{r}) = \iint_S G_q(\mathbf{r},\mathbf{r}')\nabla\cdot\mathbf{J}(\mathbf{r}')dS' . \tag{4}$$

The symbol G_a denotes Green's functions for the magnetic vector potential while G_q for the electric scalar potential. Both G_a and G_q can be obtained by an inverse Hankel transform of their spectral domain Sommerfeld integral [17],

$$G_{a,q} = \int_{-\infty}^{+\infty}\tilde{G}_{a,q}H_0^{(2)}(k_\rho\rho)k_\rho dk_\rho . \tag{5}$$

Both G_a and G_q are formed by three parts respectively,

$$G_a = G_{a0} + G_{a,ci} + G_{a,sw} \tag{6}$$

$$G_q = G_{q0} + G_{q,ci} + G_{q,sw} . \tag{7}$$

G_{a0} and G_{q0} represent the contribution from the quasi-dynamic images, which dominate in the near-field region,

$$G_{a0} = \frac{\mu_0}{4\pi}\left(\frac{e^{-jk_0r_0}}{r_0}-\frac{e^{-jk_0r_0'}}{r_0'}\right) \tag{8}$$

$$G_{q0} = \frac{1}{4\pi\varepsilon_0}\left(\frac{e^{-jk_0r_0}}{r_0}+K\frac{e^{-jk_0r_0''}}{r_0''}+\sum_{n=1}^{\infty}K^{n-1}(K^2-1)\frac{e^{-jk_0r_n'}}{r_n'}\right), \tag{9}$$

where $K=(1-\varepsilon_r)/(1+\varepsilon_r)$. $G_{a,ci}$ and $G_{q,ci}$ represent the contribution from the complex images, which dominates in the intermediate region. They can be obtained by applying DCIM and using Sommerfeld identity,

$$G_{a,ci} = \frac{\mu_0}{4\pi}\sum_{i=1}^{N}a_i\frac{e^{-jk_0r_i}}{r_i} \tag{10}$$

$$G_{q,ci} = \frac{1}{4\pi\varepsilon_0}\sum_{i=1}^{N}a_i'\frac{e^{-jk_0r_i'}}{r_i'} . \tag{11}$$

The third part stands for the contribution from the surface waves, which dominates in the far-field region,

$$G_{a,sw} = \frac{\mu_0}{4\pi}(-2\pi j)\,\mathrm{Res}_1 H_0^{(2)}(k_{\rho p}\rho)k_{\rho p} \tag{12}$$

$$G_{q,sw} = \frac{1}{4\pi\varepsilon_0}(-2\pi j)\,\mathrm{Res}_2 H_0^{(2)}(k_{\rho p}\rho)k_{\rho p} . \tag{13}$$

In the above equations, $r_n=\sqrt{\rho^2+(2nh)^2}$, h is the thickness of substrate. $r_i'=\sqrt{\rho^2-b_i^2}$ and $r_i''=\sqrt{\rho^2-b_i'^2}$, where a_i , a_i' , b_i and b_i' are complex coefficients obtained by Prony's method. Galerkin's method is applied, which results in a matrix equation,

$$\mathbf{ZI} = \mathbf{V} . \tag{14}$$

Using the fast directional multilevel algorithm, the matrix-vector product $\mathbf{ZI}$ can be written as,

$$\mathbf{ZI} = \mathbf{Z}_N\mathbf{I} + \mathbf{Z}_F\mathbf{I}$$

Here $\mathbf{Z}_N$ is the near part of $\mathbf{Z}$ and is computed directly. $\mathbf{Z}_F$ is the far part of $\mathbf{Z}$ and the computation of $\mathbf{Z}_F$ is accelerated by FDMA. Those elements in $\mathbf{Z}_F$ are not explicitly computed and stored.

III. FAST DIRECTIONAL MULTILEVEL ALGORITHM

The FDMA is originally developed in [14] for solving N-body or N-point problems. Then the

algorithm is applied for electromagnetic scattering problem via combined field integral equation in [13]. After that, we leverage Calderlon identity for preconditioning FDMA to improve the convergence of EFIE [18-19]. Now, the FDMA is extended to solve multilayer microstrip problems.

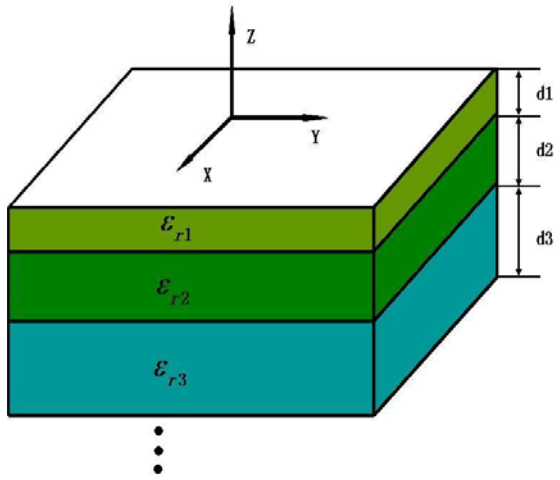

Fig. 1. The geometry of multilayered medium.

A. The construction of low rank representations

As in [13, 14, 17, 18], we need to construct low rank representations for Green's function. The most process of implementation for this part is the same except that the Green's function used here is described in equations (6) and (7). Quad-tree structure is employed here, which will be discussed in part B, therefore the random sampling is based on a square box,

$$G_a(\boldsymbol{r}_i,\boldsymbol{r}_j) \approx \sum_{p,q} G_a(\boldsymbol{r}_i,\boldsymbol{r}_p) d_{pq} G_a(\boldsymbol{r}_q,\boldsymbol{r}_j). \quad (15)$$

We also need to construct the low rank representation for electric scalar potential G_q. Fortunately, the process is the same as above. It can be seen that the process of the construction in layered medium is almost the same as in free space described in [13]. Differently, We need to repeat the above process twice for G_a and G_q respectively, corresponding to store two sets of locations $\{\boldsymbol{r}_p\}$, $\{\boldsymbol{r}_q\}$ and the matrix **D** for every layer. The detailed implementation of FDMA using MPIE formulation can refer to [13, 14, 17, 18].

B. The quad-tree structure for layered medium

The oct-tree structure is usually used for three dimension structures with layered medium. Therefore, the oct-tree is originally adopted for the multilayer microstrip problem, but it is not memory efficient because of the three dimension sampling in part A. In this paper, quad-tree structure other than oct-tree is applied for multilayered medium and we make some modification when quad-tree structure is adopted. Take two-layered medium for example, and assume that metallic patch is contained in two-layered medium.

We first enclose all the patches of the first layer in a small square box, then the box is subdivided into small boxes until the smallest box at the lowest level. The boxes are organized into a quad-tree structure with the smallest boxes at the bottom of the inverted tree, and the largest box at the root of the inverted tree. The same operation is done for the second layer. We can get the final quad-tree structure for two layers shown in Fig. 2 (a) - (b). Figure 2 (a) stands for the grouping method in the low frequency regime, and the group size is smaller than one wavelength. Figure 2 (b) stands for the group size, is larger than one wavelength in the high frequency regime.

Assuming that the blue box Y in the first level is the observed box, and the corresponding box of Y in the second layer is also in blue color. All the boxes of two layers in red color are defined as the near field area of box Y while the boxes in yellow color are defined as the far field area. In other words, the boxes in yellow color of the two layers are all the far field interaction group of observed box Y. It is because that the thickness of the substrate is always thin, therefore, we can define the far field boxes of Y are all the yellow boxes in both layers.

IV. NUMERICAL RESULTS

In this section, a number of numerical examples are presented to demonstrate the efficiency of the FDMA for solving linear systems arising from the discretization of MPIE for analyzing microstrip structures. In the implementation of the FDMA, the restarted version of GMRES algorithm [20] is used as the iterative method. All experiments are performed Core-2 8400 with 3 GHz CPU and 4 GB RAM in double precision. The iteration process is terminated when the normalized backward error is reduced by 10^{-3} for all examples.

The first example concerns the *S*-parameters from a four-section low-pass filter [21]. The geometry is depicted in Fig. 3 (a), where ε_r= 10.8 and the substrate thickness is d = 0.0254 *mm*. The width of the patch are L_1=10.12 *mm*, L_2=6.12 *mm*, L_3=2.8 *mm*, L_4=1.3 *mm*, L_5=9.8 *mm*, L_6=3.5 *mm*, with W_s=1 *mm*, W=W_c= 0.3 *mm*, W_5 = 0.2 *mm*, W_6 = 4 *mm*, W_f = 0.57 *mm*, G = 0.2 *mm*, L_c = 1.78 *mm*, and L_f = 15 *mm*. The unit voltage source is applied

and the S-parameters of this low-pass filter are shown in Fig. 3 (b). One level FDMA is used here and the finest group size is no larger than 0.05 λ at the smallest frequency. The results from FEKO [22] are also given in Fig. 3 (b) for comparison. Our results are in well agreement with the results from FEKO.

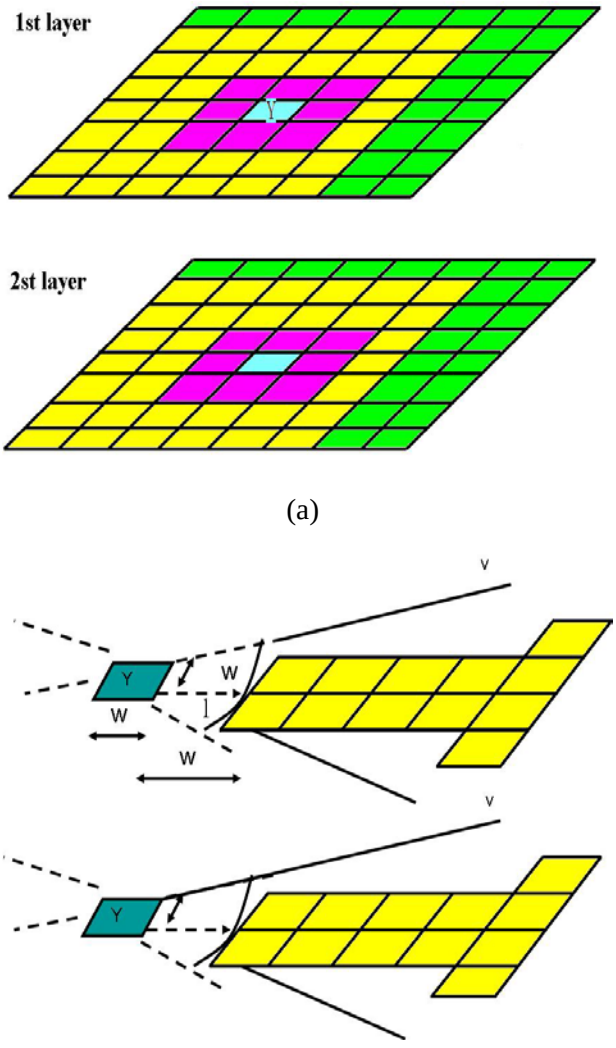

Fig. 2. (a) The grouping method for two layer-media in the low frequency regime and (b) the grouping method for two layer-media in the high frequency regime.

It can be observed that the results of the S-parameter are in well agreement below 4 GHz and 8 GHz to 10 GHz. Though, the agreement with the FEKO between 4 GHz to 8 GHz is not good, it can be satisfied with the engineering requirement because the S-parameters are all below 40 dB. It can be concluded that the FDMA is stable even at low frequency regime.

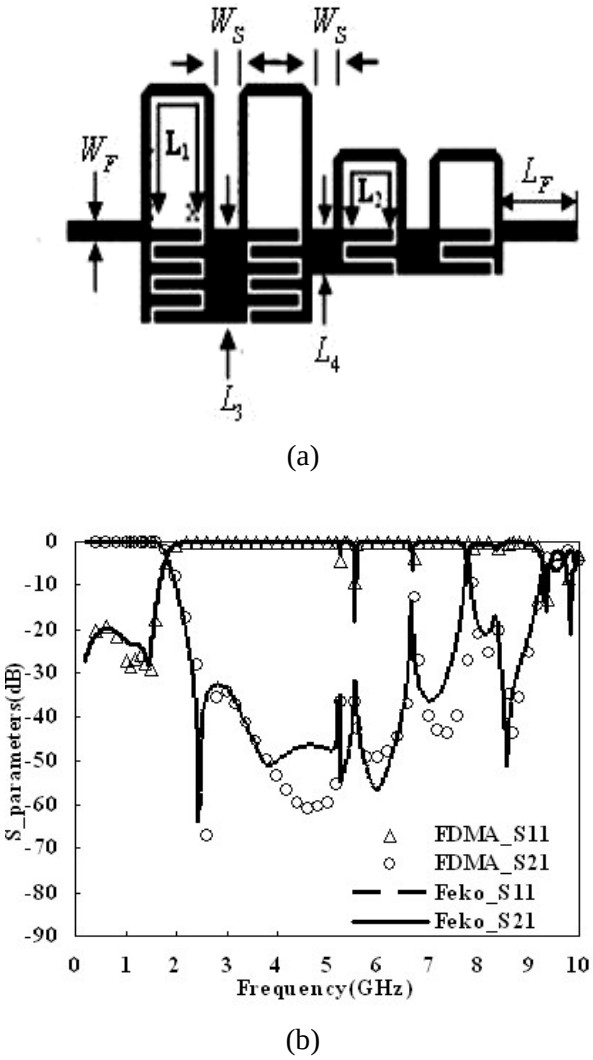

Fig. 3. (a) The configuration of four-section low-pass filter and (b) S-parameters of the four-section low-pass filter.

The following example is a quasi-periodic structure, which is analyzed as two layers microstrip structures with relative permittivity ε_r = 3.38. FDTD or FEM is often used for the simulation of periodic structure. Some new methods also come forth to deal with such special problem [23-24]. Though, different from common microstrip structure, the process of FDMA for periodic structure is the same as microstrip structure.

The proposed quasi-periodic structure with seven periods is shown in Fig. 4 (a)-(c). In our simulation, the unit voltage source is applied, with f_0 = 3GHz. We applied quad-tree in the first level for mircostrip line and in the second level for metal patch. We use three levels FDMA, and the results of *S*-parameters in Figs. 5 and 6 agree well with the results simulated by Ansoft designer.

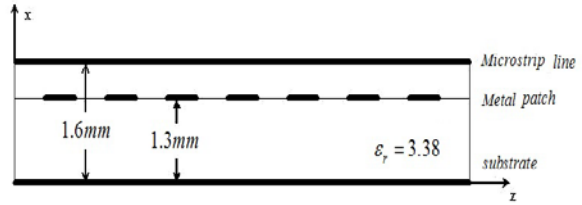

(a)

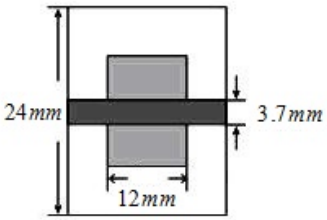

(b)

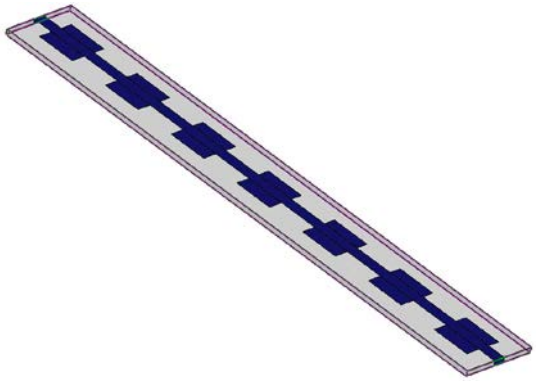

(c)

Fig. 4. (a) The configuration of a microstrip EBG structure, (b) proposed microstrip EBG structure, and (c) top view of a cell of the proposed microstrip EBG structure.

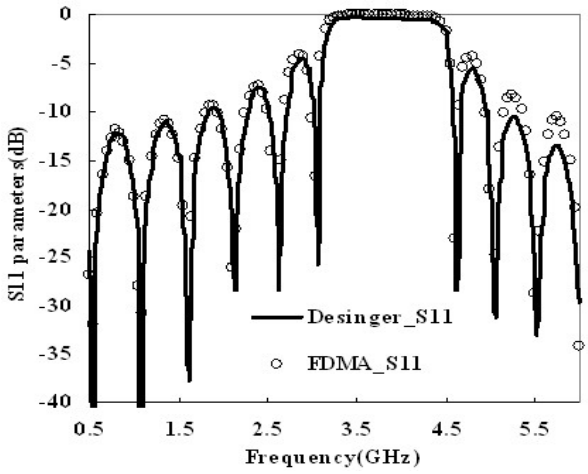

Fig. 5. S11 parameter of the EBG structure.

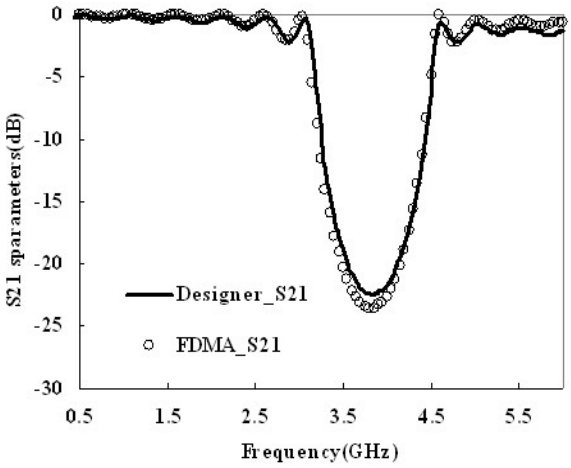

Fig. 6. S21 parameter of the EBG structure.

The next structure is a finite planar frequency selective surface (FSS). The transmission coefficient is defined as,

$$T = \left| -E^{ia} + E^{s} \right|^2 \Big/ \left| E^{ia} \right|^2 \qquad (16)$$

where E^{ia} denotes the quantities relative to the incident field and E^{s} is the far field at the transmission direction or the reflection direction. Our theoretic foundation is that the reflection coefficient of the metallic plate is 1 while its transmission coefficient is 0. Since the metallic plate is special form FSS. It implies that we can calculate E^{ia} using the far field of the metallic plate. It is obvious to obtain that $E^{ia} = -E^{s}_{metallic\ plate}$ at the transmission direction. $E^{s}_{metallic\ plate}$ denotes the far field of the metallic plate under the same incident plane wave. Then the transmission coefficient of general finite FSS can be calculated using,

$$T = \left| -E^{s}_{metallic\ plate} + E^{s} \right|^2 \Big/ \left| E^{s}_{metallic\ plate} \right|^2 . \qquad (17)$$

The transmission of the octagonal loop FSS embedded in a three-layered medium is investigated. The FSS array consists of 20×20 octagonal loop elements with number of unknowns 25600 as shown in Fig. 7. The dielectric constant of the substrates are ε_{r1} = 3.0, ε_{r2} = 1.0006, and ε_{r3} = 3.0 and the corresponding thickness of the substrates are 0.18 *mm*, 10.0 *mm*, and 0.18 *mm*, respectively. The outer radius of the element is 3.5 *mm* and the inner radius is 3 *mm*. The dimensions of the unit are T_x = 8 *mm*, T_y = 8 *mm*. The incident wave is TE polarization wave with $\theta^i = 30^\circ, \phi^i = 0^\circ$ and the skew angle is 60º. The patch of octagonal loop FSS is in the third layer, as a result, we just employed the quad-tree

in the third level. The three-level FDMA is used here. As shown in Fig. 8, the transmission coefficients of the 20×20 octagonal loop FSS arrays are plotted. It can be observed that the transmission coefficient of the finite FSS simulated by our method has a good agreement with the characteristic of the infinite FSS simulated by Ansoft designer.

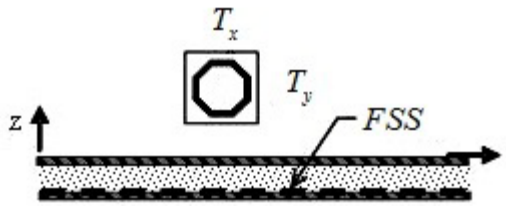

Fig. 7. The configuration of the octagonal loop FSS.

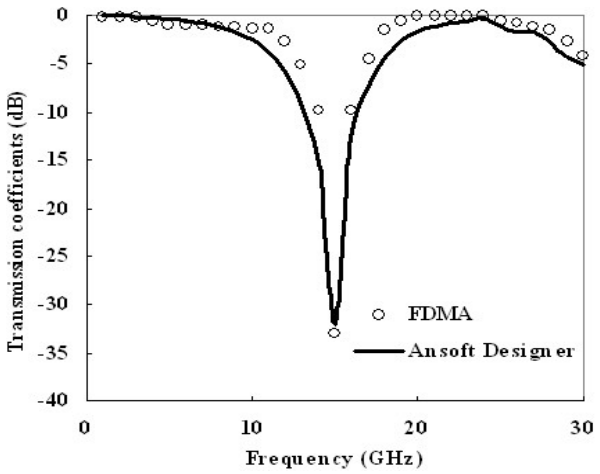

Fig. 8. The transmission loss curves versus frequency by the octagonal loop FSS arrays.

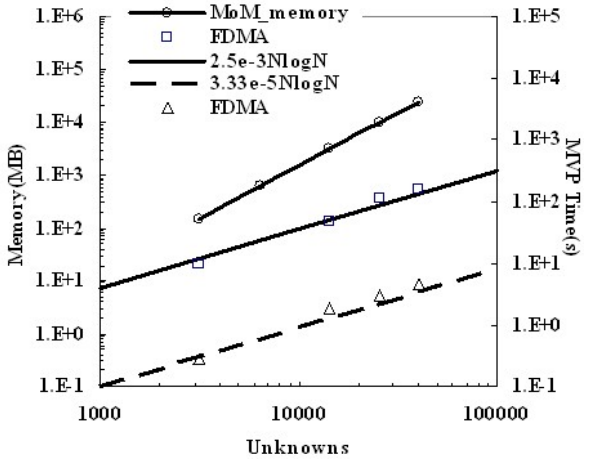

Fig. 9. The Complexity of FDMA for memory requirement and MVP time per iteration.

In this part, a series FSS array which consists of 8×8, 15×15, 20×20, and 25×25 octagonal loop elements are considered. The dielectric constant and the configuration of the octagonal loop FSS are the same as above. Assuming the incident angles of plan wave are $\theta^i = 30^o$, $\phi^i = 0^o$ at 15 GHz. The matrix vector product (MVP) time per iteration and the memory requirement versus the number of unknowns are plotted in Fig. 9. It is can be observed that the CPU time per iteration and the memory requirement are all scaled as O (N Log N).

VI. CONCLUSION

In this paper, the fast directional multilevel algorithm is first applied for analyzing multilayer microstrip problems. The EBG structure and the finite FSS arrays are considered as multilayer microstrip structure, while the corresponding S-parameters and transmission coefficient are computed. The new method is easily implemented because it is Kernel independent. With the aid of DCIM, the MPIE is discretized in the spatial domain. The efficiency of this method is demonstrated by numerical results.

ACKNOWLEDGMENT

The author would like to thank Dr. Jiang Zhaoneng for providing useful discussions and Prof. R. S. Chen for his useful instruction. Thank the support of the International S&T Cooperation Program of China (No.2012DFA70570), the Yunnan Provincial International Cooperative Program (No. 2011IA004), Yunnan Provincial Foundation Program (No. 2013FZ016), the National Technology Research and Development Program of China (No. 2013AA064003), National Science Foundation of China (No. 51304097).

REFERENCES

[1] R. F. Harrington, *Field Computation by Moment Methods*, Malabar, Fla.: R. E. Krieger, 1968.

[2] S. M. Rao, D. R. Wilton, and A. W. Glisson, "Electromagnetic scattering by surfaces of arbitrary shape," *IEEE Trans. Antennas Propag.*, vol. 30, no. 3, pp. 409-418, 1982.

[3] E. H. Newman and D. Forrai, "Scattering from a microstrip patch," *IEEE Trans. Antennas Propagat.*, vol. 35, pp. 245-251, March 1987.

[4] K. A. Michalski and C. G. Hsu, "RCS computation of coax-loaded microstrip patch antennas of arbitrary shape," *Electromag.*, vol. 14, Jan. ~ Mar., pp. 33-62,1994.

[5] F. Ling, C. F. Wang, and J. M. Jin, "An efficient algorithm for analyzing large-scale microstrip

structures using adaptive integral method combined with discrete complex image method," in *IEEE APS Int. Symp. Dig*., vol. 3, pp. 1778-1781, 1998.

[6] L. Gurel and M. I. Aksun, "Electromagnetic scattering solution of conducting strips in layered media using the fast multipole method," *IEEE Microwave Guided Wave Lett.*, vol. 6, pp. 277-279, Aug. 1996.

[7] P. A. Macdonald and T. Itoh, "Fast simulation of microstrip structures using the fast multipole method," *Int. J. Numer. Modeling: Electron. Networks, Devices, Fields*, vol. 9, pp. 345-357, 1996.

[8] F. Ling, J. M. Song, and J. M. Jin, "Multilevel fast multipole algorithm for analysis of large-scale microstrip structures," *IEEE Microwave Guided Wave Lett.*, vol. 9, pp. 508-510, Dec. 1999.

[9] J. Parron, J. M. Rius, and J. R. Mosig, "Application of the multilevel matrix decomposition algorithm to the frequency analysis of large microstrip antenna arrays," *IEEE Trans. Magn*., vol. 38, no. 2, pp. 721-724, Mar. 2002.

[10] D. G. Fang, J. J. Yang, and G. Y. Delisle, "Discrete image theory for horizontal electric dipoles in a multilayered medium," *Proc. IEEE, Pt. H*, vol. 135, pp. 297-303, Oct. 1988.

[11] Y. L. Chow, J. J. Yang, D. G. Fang, and G. E. Howard, "A closed-form spatial Green's function for the thick microstrip substrate," *IEEE Trans. Microwave Theory Tech.*, vol. 39, pp. 588-592, Mar. 1991.

[12] J. S. Zhao, W. C. Chew, C. C. Lu, E. Michielssen, and J. M. Song, "Thin-stratified medium fast-multipole algorithm for solving microstrip structures," *IEEE Trans. Microwave Theory Tech*., vol. 46, pp. 395-403, Apr. 1998

[13] H. Chen, K. W. Leung, and E. N. Yung, "Fast directional multilevel algorithms for analyzing wave scattering," *IEEE Trans. Antennas Propag.*, vol. 59, no. 7, July, pp. 962-974, 2011.

[14] B. Engquist and L. Ying, "Fast directional multilevel algorithms for oscillatory kernels," *SIAM Journal on Scientific Computing*, vol. 29, no. 4, pp. 1710-1737, 2007.

[15] T. Vaupel, "A fast spectral domain solver for the characterization of large microwave structures in multilayered environments," *Applied Computational Electromagnetics Society* (ACES) *Journal*, vol. 24, no. 5, pp. 493-503, October 2009.

[16] K. A. Michalski and J. R. Mosig. "Multilayered media Green's functions in integral equation formulations," *IEEE Transaction on Antennas and Propag*., vol. 3, pp. 508-519, 1997.

[17] K. Michalski and D. Zheng "Electromagnetie scattering and radiation by surfaces of arbitrary surfaces of arbitrary shape in layered media, Part I: Theory," *IEEE Trans. Antennas Propag*., vol. 38, no. 3, pp. 335-344, Aug. 1990.

[18] H. Chen, J. Zhu, R. S. Chen, and Z. H. Fan, "Fast direction multilevel algorithm combined with Calderon multiplicative preconditioner for stable electromagnetic scattering analysis," *Microwave Opt. Technol. Lett.*, vol. 52, no. 9, pp. 1963-1969, 2010.

[19] H. Chen, J. Zhu, R. S. Chen, and Z. H. Fan, "Calderon multiplicative preconditioner for acceleration of fast direction multilevel algorithm for scattering problem," *Proceedings ICMMT*, Chengdu, P. R. China, 8-11 May, 2010.

[20] Y. Saad, *Iterative Methods for Sparse Linear System*, PWS Publishing Company, 1996.

[21] W. H. Tu and K. Chang, "Compact microstrip low-pass filter with sharp rejection," *IEEE Trans. Microw. Wireless Compon. Lett.*, vol. 15, no. 6, pp. 404-407, June 2006.

[22] U. Jakobus, M. Schoeman, J. Tonder, D. Ludick, and W. Burger, "Selection of new features in the electromagnetic solution kernel of FEKO suite 6.0," *27th Annual Review of Progress in Applied Computational Electromagnetics (ACES)*, pp. 308-313, Williamsburg, Virginia, March 2011.

[23] F. Hu, J. Song, and T. Kamgaing, "IE analysis of scattering from multilayered doubly periodic array of 3-D PEC objects using equivalence principle and connection scheme," *27th Annual Review of Progress in Applied Computational Electromagnetics (ACES)*, pp. 482-487, Williamsburg, Virginia, March 2011.

[24] E. A. Hajlaoui, H. Trabelsi, A. Gharsallah, and H. Baudrand, "Analysis of photonic band gap using multilayer contribution of wave concept iterative process MLC-WCIP," *Applied Computational Electromagnetics Society (ACES) Journal*, vol. 24, no. 3, pp. 352-357, June 2009.

Hua Chen was born in Anhui Province, China. She received her Ph.D. degree in Nanjing University of Science and Technology (NJUST), She is currently working in Kunming University of Science and Technology(KMUST), at Kunming, China. Her current research interests include computational electromagnetics, antennas and electromagnetic scattering and propagation, electromagnetic modeling of microwave integrated circuits.

Convex Optimization Based Sidelobe Suppression for Adaptive Beamforming with Subarray Partition

S. Xiaofeng, X. Jia, Z. Ying, and K. Ling

Department of Electrical Engineering
University of Electronic Science and Technology of China, Chengdu, 611731, China

Abstract ─ This paper proposes a convex optimization based method to suppress sidelobe in adaptive beamforming at subarray level. Usually phase shift rather than amplitude tapering is implemented at element level to maximize signal to noise ratio. Nevertheless, sidelobe control can be realized at subarray level. The proposed approach is realized by adding a constraint minimizing the difference between weights at subarray level and element-level Chebyshev synthesis into the optimal conditions. Compared with penalty function method, simulations show that for a uniform linear array, the proposed method can suppress sidelobe level considerably, especially the lobes close to mainlobe. Furthermore, it is able to produce better shaped main lobe, which is extremely close to the referenced pattern.

Index Terms - Adaptive beamforming, convex optimization, sidelobe control, and subarray level.

I. INTRODUCTION

Adaptive beamforming is a significant realm in phase array radar. To reduce the complexity of hardware and alleviate computational load, subarray partition is usually considered [1, 2]. In addition, low sidelobe is often required to guarantee the performance against non-stationary cluster or reverberation [3, 4]. Many pattern synthesizing methods were developed to generate low sidelobe [5-7]. However, element tapering reduces the global gain of antennas, which results in signal-to-noise (SNR) loss. Thus, forming adaptive pattern with low sidelobes digitally at subarray level is a feasible solution.

One of the most used algorithms is minimized variance distort response (MVDR). Its apparent disadvantage is high sidelobes when sample matrix is used instead of the true covariance matrix [4]. Much relevant work has been done in recent years to deal with sidelobe controlling. Carlson proposed the diagonal sample matrix inversion (LSMI) [8] to solve the problem by adding an appropriate number to the covariance matrix. It was proved to be simple and effective, but there is no close solution for the optimal number. Penalty function method has to select a loading value k^2 to determine the adaptive weights. As the value of k^2 increases, the property of sidelobe suppression improves but interference cancelling degrades [3]. Second order cone (SOC) [9] is the method using optimization to control sidelobe. Although the method in [9] can get desired low sidelobe exactly, sidelobe region and sampling density should be defined beforehand. A small number of samplings may result in unexpected high sidelobe jittering, while a large number of samplings will lead to intensive computation. Furthermore, inappropriate sidelobe region definition may cause high sidelobe close to the main lobe in [9]. Sparse constraint is utilized to suppress the sidelobe level in [10]. However, it may fail to null mainlobe interference when its mainlobe region is set relative broad to enhance robustness of the beamformer against steering vector error. More recently, iterative algorithms based on evolutionary has been exploited in pattern synthesis [11, 12]. Despite their advantages, they have the drawback of complicated feeding network and high computational burden [13].

This paper proposes a new alternative convex optimization based approach to suppress sidelobe in adaptive beamforming at subarray level. It saves

Submitted On: April 26, 2013
Accepted On: Jan. 26, 2014

the trouble of definition of threshold, sidelobe region, and sampling density. We construct the formula by imposing interferences cancelling on optimization conditions while setting object to minimize the difference between element level equivalent weights and Chebyshev tapering. Simulation results indicate that the convex optimization based approach can suppress sidelobe effectively, which simultaneously tune out inferences from sidelobe or mainlobe. The validity and feasibility of the proposed algorithm are verified with Matlab simulation.

II. SIGNAL MODEL

A uniform linear array (ULA) with *N* isotropic elements is considered in this paper. Interval between elements is half of the carrier wavelength, i.e., $d = \lambda/2$. The array is divided into *L* non-overlapped subarrays. When *K* far field narrow band signals from θ_1, θ_2,..... θ_K are imposed on the array, the received data at element level $\vec{x}_{ele}$ is [14],

$$\vec{x}_{ele}(m) = A\vec{s}(m) + N(m) \tag{1}$$

where $\vec{s}(m) = [s_1(m),...,s_K(m)]^T$, represents the *K* incident signals at the m^{th} snapshot. $(.)^T$ denotes the transposition operator. $N(m) = [n_1(m), n_2(m),..., n_N(m)]^T$ is the Gaussian sensor noise with zero mean and variance σ_n^2. *A* is an array manifold vector and $A = [\vec{a}(\theta_1), \vec{a}(\theta_2),..., \vec{a}(\theta_K)]$. $\vec{a}(\theta_i)$ is the steering vector and $\vec{a}(\theta_i) = [e^{j\varphi_1}\ e^{j\varphi_2}\ ...\ e^{j\varphi_N}]^T$. φ_n is the phase difference of the n^{th} sensor relative to the origin from θ_i. Thus φ_n is defined as,

$$\varphi_n = \frac{2\pi \sin\theta_i}{\lambda} \cdot x_n \tag{2}$$

where x_n is the coordinate of n^{th} sensor. It is assumed that the array is symmetric to the origin and *N* is oven. Thus,

$$x_n = \left(n - \frac{N+1}{2}\right)d\ ,\ n = 1, 2, ..., N\ .$$

The element to subarray transformation matrix is given by [2],

$$T_d = D_{\vec{w}} \cdot D_{\theta_d} \cdot T\ , \tag{3}$$

where θ_d is the direction of the desired signal. $\vec{w}$ is an $N\times1$ vector, denoting element amplitude tapering. *T* is an $N\times L$ matrix, containing zeros and ones, which are determined by the division of subarrays. Both $D_{\theta d}$ and $D_{\vec{w}}$ are diagonal matrices, i.e., $D_{\theta_d} = diag\{a_1(\theta_d), a_2(\theta_d),..., a_N(\theta_d)\}$, $D_{\vec{w}} = diag\{w_1, w_2,..., w_N\}$. When no amplitude tapering is imposed at element level, i.e., $w_i = 1$, $D_{\vec{w}} = I$, where *I* represents identity matrix.

We denote the weights vector at subarray level by $\vec{w}_{sub}$. Then the pattern with subarray partition is given by,

$$f(\theta) = \left(T_d \cdot \vec{w}_{sub}\right)^H \cdot \vec{a}(\theta) \tag{4}$$

where $(\cdot)^H$ is the Hermitian transposition operator.

The received data at subarray level, $\vec{x}_{sub}$, as shown in Fig. 1, can be obtained by [2],

$$\vec{x}_{sub} = T_d^H \cdot \vec{x}_{ele}\ . \tag{5}$$

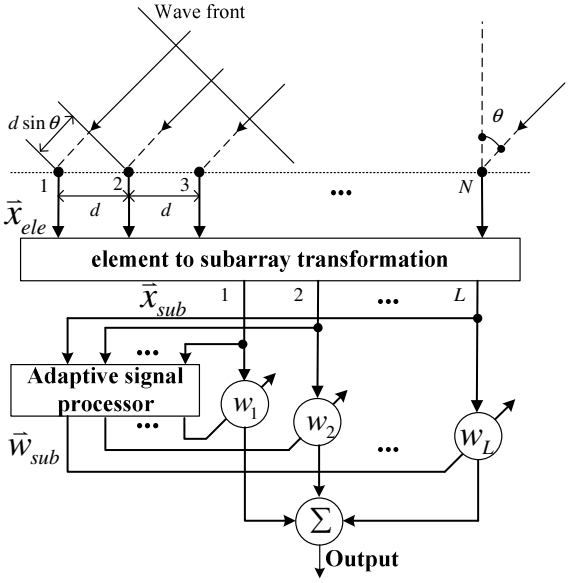

Fig. 1. A functional block diagram of an adaptive ULA with subarray partition.

The covariance matrix is defined as,

$$\begin{aligned} R_{sub} &= E\left\{\vec{x}_{sub} \cdot \vec{x}_{sub}^{\ H}\right\} \\ &= E\left\{T_d^{\ H} \cdot (\vec{x}_{ele} \cdot \vec{x}_{ele}^{\ H}) T_d\right\} \\ &= T_d^{\ H} E\left\{\vec{x}_{ele} \cdot \vec{x}_{ele}^{\ H}\right\} T_d \\ &= T_d^{\ H} R_{ele} T_d \end{aligned}\ . \tag{6}$$

In practice, it is difficult to get the theoretical value of R_{ele}, generally its approximate estimation is used instead [15],

$$\hat{R}_{ele} = \frac{1}{N_{sap}} \sum_{m=1}^{N_{sap}} \vec{x}_{ele}(m) \cdot \vec{x}_{ele}{}^{H}(m), \qquad (7)$$

where N_{sap} is the sampling rate, and $N_{sap} = 2N$ in this paper [16].

III. CONVEX OPTIMIZATION BASED ADAPTIVE BEAMFORMING WITH SIDELOBE CONTROL

A subarray level adaptive beamformer is achieved by grouping the array elements into subarrays on which conventional beamforming is performed and applying an adaptive beamforming algorithm to the subarray outputs as shown in Fig. 1. Signals in each subarray channel are multiplied by a complex weight. The number of adaptive coefficients is therefore the number of subarrays L instead of the total number of elements N, which reduces the computational load manifestly in $\vec{w}_{sub}$ calculation.

In many practical applications, to get higher SNR, antenna is preferred to be used without attenuation. This may invalidate sidelobe suppression contributed by element amplitude tapering. Nevertheless, we may try to minimize the difference between $\vec{w}_{ref}$ and $T \cdot \vec{w}_{sub}$ with constraint of interference nulling. Here, $\vec{w}_{ref}$ is the optimal element tapering for quiescent low sidelobe pattern synthesis. $T \cdot \vec{w}_{sub}$ can be regarded as the equivalent element amplitude tapering with subarray partition.

Chebyshev tapering is often desirable in linear array since it gives smallest possible beamwidth for a given low, uniform sidelobe level [13, 17]. Therefore, we set $\vec{w}_{cheby}$ as reference element tapering. To form adaptive beam with sidelobe restriction at subarray level, the following optimization problem is proposed,

$$\begin{aligned} &\min \ \left\| T \cdot \vec{w}_{sub} - \vec{w}_{cheby} \right\|^2 \\ &s.t.: \ \left(T \cdot \vec{w}_{sub} \right)^H \vec{a}\left(\theta_k \right) = 0 \\ &\qquad k = 1, 2, ..., K < L \end{aligned} \qquad (8)$$

where $\| \bullet \|$ denotesthe Euclid norm. θ_k represents the direction of the k^{th} interference. $\vec{w}_{sub}$ is the optimization variables. Interferences are assumed incoherent with each other. However, in general, we have no prior information of interferences, i.e., θ_k is unknown. Nevertheless, in the situation of strong interferences and small signal, the optimal weight vector tends to be orthogonal to the interference subspace [15]. Thus we can modify equation (8) as,

$$\begin{aligned} &\min \ \left\| T \cdot \vec{w}_{sub} - \vec{w}_{ref} \right\|^2 \\ &s.t. \quad \vec{w}_{sub}^H \cdot J = 0 \end{aligned} \qquad (9)$$

where J denotes the interference subspace (ISS) at subarray level, which can be obtained from $\hat{R}_{sub}$. Rank the eigenvalues of $\hat{R}_{sub}$ in descending order as $\lambda_1 \geq \cdots \geq \lambda_K > \lambda_{K+1} \geq \cdots \geq \lambda_L$. Eigenvectors, $\vec{u}_1, \vec{u}_2, \cdots, \vec{u}_K$, corresponding to the first K large eigenvalues, span the ISS. To determine the dimension of ISS, we use the Akaike information criterion (AIC) [18],

$$\begin{aligned} &AIC(k) = -2\ln \left[\frac{\prod_{i=k+1}^{L} \lambda_i^{\frac{1}{L-k}}}{\frac{1}{L-k} \sum_{i=k+1}^{L} \lambda_i} \right]^{(L-k)N_{sap} + 2k(2L-k)} \\ &\hat{K} = \min\left\{ AIC(k), k = 0, 1, ..., L-1 \right\} \end{aligned} \qquad (10)$$

where L is the number of eigenvalues. $\hat{K}$ is the estimation of the dimension of ISS. The standard form of convex optimization problems is given in [19],

$$\begin{aligned} &\min \quad f_0(x) \\ &s.t. \quad f_i(x) \leq 0, \ i = 1, ..., m \\ &\qquad a_i^T x = b_i, \quad i = 1, ..., p \end{aligned} \qquad (11)$$

where $f_0, ..., f_m$ are convex functions. When the objective functions as well as the inequality constraint functions are convex, and the equality constraint functions $h_i(x) = a_i^T x - b_i$ are affine, equation (11) is a convex problem [19]. Extending the objective function in equation (9) yields,

$$\begin{aligned} &\left\| T \cdot \vec{w}_{sub} - \vec{w}_{ref} \right\|^2 \\ &= \vec{w}_{sub}^H T^H T \vec{w}_{sub} - 2\,\mathrm{Re}\left[\vec{w}_{ref}^H T \vec{w}_{sub} \right] + \vec{w}_{ref}^H \vec{w}_{ref} \end{aligned} \qquad (12)$$

It is obvious the objective function is quadratic. In addition, equality constraint in equation (9) is apparently affine. Thus equation (9) belongs to convex optimization. Several public solvers are available to solve convex optimization such as CVX, SeDuMi, YALMIP, etc. YALMIP is used in our simulation, since the toolbox makes the development of optimization problems in general and avoid simmediate use of other solvers error-prone, even when parameterized matrices and variables are complex [20].

To facilitate the use of YALMIP toolbox, we modify the problem expression slightly. A new scalar non-negative variable t is introduced. It is obviously that $\vec{w}_{sub} = \arg\min_{\vec{w}_{sub}} \left\| T \cdot \vec{w}_{sub} - \vec{w}_{cheby} \right\|^2$ is equivalent to the following expression,

$$\min_{\vec{w}_{sub}} t \quad s.t. \ \left\| T \cdot \vec{w}_{sub} - \vec{w}_{ref} \right\|^2 \le t \ . \tag{13}$$

Therefore equation (9) can be converted into the following form [9],

$$\begin{aligned} &\min t \\ &s.t.: \vec{w}_{sub}^H J = 0 \\ &\begin{bmatrix} I_{N\times N} & T \cdot \vec{w}_{sub} - \vec{w}_{ref} \\ \left(T \cdot \vec{w}_{sub} - \vec{w}_{ref} \right)^H & t \end{bmatrix} \ge 0 \end{aligned} \tag{14}$$

when t reaches its minimum, we get the optimal $\vec{w}_{sub}$. When the YALMIP toolbox is installed in Matlab properly, optimization can be realized with following commands. It is assumed that the reader is familiar with Matlab.

```
  t = sdpvar(1);
  % real part of wsub
wsub_r=sdpvar(subN,1,'full');
  % imaginary part of wsub
wsub_i=sdpvar(subN,1,'full');
wsub = wsub_r+j.*wsub_i;
  % equality constraint
cond=set((wsub)'*J==0);
  M = [eye(eleN),(T*wsub-w_ref);…
      (T*wsub-w_ref)',t];
 %combine equality constraint and
   inequality constraint
  cond = cond+set(M>= 0);
obj = t;
solvesdp(cond,obj);
```

The number of iterations grows with problem size as $O(\sqrt{N})$ [21]. In our simulations, the algorithm converged after 8~10 iterations.

IV. SIMULATION RESULTS

For all simulations in this paper, a uniform linear array (ULA) consisting of 96 elements with $\lambda/2$ spacing is used. ULA is utilized because of its merit of simplest geometry and excellent directivity [22]. In our simulations, the array is divided into 16 symmetrical subarrays as [8, 7, 6, 7, 5, 6, 5, 4, 4, 5, 6, 5, 7, 6, 7, 8], so that grating lobes are suppressed. An element-level Chebyshev tapering with -40 dB sidelobe magnitude is set as referenced weights for the proposed method. We compare our method with penalty function [17], where subarray-level Chebyshev tapering with the same sidelobe level is chosen. Its scalar weighting factor k = 20. We assume that there is no look direction gain constraint. Thus the formula for penalty function we chose is given as equation (14) in [17],

$$\vec{w}_{pen} = k^2 \left(R_{sub} + k^2 I \right)^{-1} \vec{w}_{cheb} \tag{15}$$

where I is a 16 order identity matrix. $\vec{w}_{cheb}$ is a 16×1 vector. Signal of interest is neglected since it is usually possible to form the interference covariance matrix with signal absent in radar applications [23]. Interference to noise ratio (INR) is 30 dB.

A. Performance of beam pattern control

In this section, θ_d = 5°. We compare penalty function method with the proposed algorithm in two scenarios: Two sidelobe interferences from [11°, –9°] and one mainlobe interference from 6.5°. In the first example, two sidelobe interferences in direction of 11° and –9° are imposed. Patterns are plotted in Fig. 2. Both adaptive patterns are able to achieve high interference inhibition gain, lower than -70 dB. However, it is observed that the proposed method performs outweighs penalty function in maintaining low sidelobe, especially lobes close to mainlobe. The first sidelobe level can be as low as -41dB. Additionally, the proposed method produces a better shaped mainlobe, of which the width is the same as reference pattern.

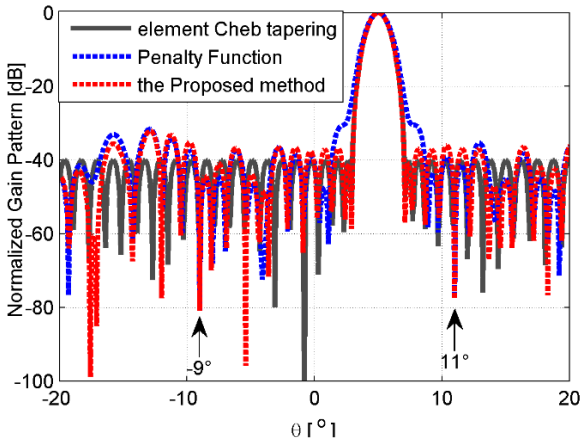

Fig. 2. Normalized pattern with two sidelobe interferences from 11° and −9°.

Figure 3 illustrates adaptive patterns in presence of a mainlobe interference from 6.5°, 1.5° away from the desired signal. Both the two algorithms can prohibit interference effectively. However, the proposed method dose better in suppressing sidelobes near the mainlobe.

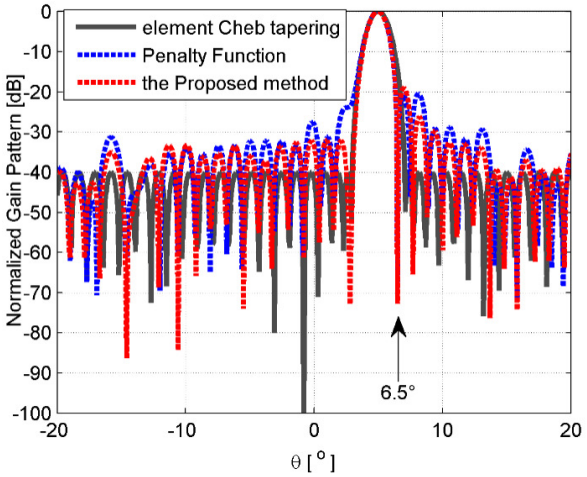

Fig. 3. Normalized pattern with one mainlobe interference from 6.5°.

B. SINR comparison

Figure 4 depicts the output SINR versus scanning angle θ. Interference comes from −3°. The SINR is calculated via [10],

$$SINR(\theta)_{ouput} = \frac{\sigma_s^2 \vec{w}^H \vec{a}(\theta) \vec{a}^H(\theta) \vec{w}}{\vec{w}^H R_{sub} \vec{w}} \quad (16)$$

where $\vec{w}$ denotes adaptive weights at subarray level. $\vec{a}(\theta)$ is subarray-level steering vector. σ_s^2 is the power of desired signal and $\sigma_s^2 = 1$ in this simulation. According to linearly constrained minimum variance (LCMV) criterion, the optimum adaptive weights at subarray level we use to calculate optimal SINR are given as follows [24, 25],

$$\vec{w}_{opt} = \mu R_{sub}^{-1} \vec{a}(\theta_d)_{sub} \quad (17)$$

where μ is a positive constant and does not affect the calculation of SINR.

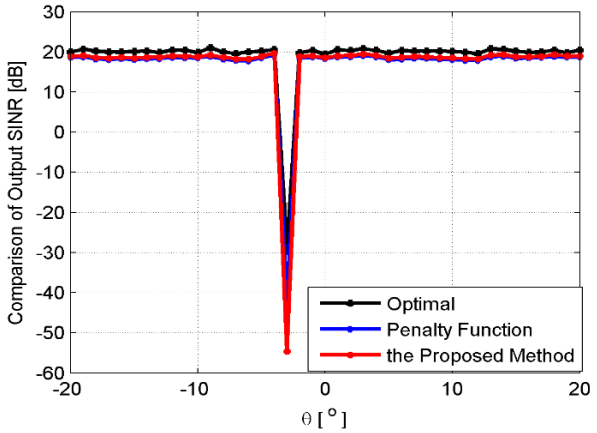

Fig. 4. SINR comparison of the three methods.

It can be seen from Table 1 that the proposed method has higher SINR compared with penalty function while performing better in sidelobe controlling. Both adaptive subarray tapering suffer a small SINR loss. This is the price paid to get much lower sidelobe.

Table 1: SINR comparison [dB].

Methods	SINR	SINR Loss
Optimal	20.25	--
Penalty Function	18.53	-1.72
Proposed method	18.88	-1.37

V. DISCUSSIONS AND CONCLUSION

A. Discussions

Compared with quiescent Chebyshev tapering pattern, the other two adaptive patterns have evident sidelobe jitter. This is caused mainly by subarray number and size. More subarrays allow optimized weights closer to reference tapering. Equally division will lead to grating lobe. How to choose a suitable subarray partition is complicated

and usually needs compromise. Further study is under gone. Meanwhile, the proposed method suffers a small SINR loss, which is the cost of proposed method. Thus, a tradeoff should be considered in practical situations.

B. Conclusion

In this paper, a convex optimization based method is proposed to form adaptive sum beam with sidelobe control at subarray level. Compared with penalty function method, the proposed method has the merits of considerably reducing sidelobe adjacent to mainlobe, and producing better shaped mainlobe. Moreover, our optimization problem is formulated without parameters predetermining. The aforementioned merits of the proposed method have been verified by computer simulations.

ACKNOWLEDGEMENT

The author wishes to acknowledge the financial support of the National Science Foundation of China through Grant no. 61101094 and no. 61201275.

REFERENCES

[1] U. Nickel, "Subarray configurations for digital beamforming with low sidelobes and adaptive interference suppression," *Proc. IEEE International Radar Conference*, Alexandria, USA, pp. 714- 719, May 1995.

[2] P. Lombardo and D. Pastina, "Pattern control for adaptive antenna processing with overlapped sub-arrays," *IEEE Radar*, 2003.

[3] G. Herbert, "A new projection based algorithm for low sidelobe pattern synthesis in adaptive arrays," *Radar 97*, no. 449, pp. 14-16, Oct. 1997.

[4] J. Wang, R. Krlin, and X. Lu, "Sidelobe control using optimization methods in adaptive beamforming," *Adaptive Antenna Arrays: Trend and Applications*, Springer, July 2004.

[5] C. Dolph, "A current distribution for broadside array which optimizes the relationship between beamwidth and sidelobe level," *Proc. IRE*, vol. 34, pp. 335-345, June 1946.

[6] T. Taylor, "Design of line source antennas for narrow beamwidth and low sidelobes," *IEEE Trans. on Antennas and Propagation*, vol. 3, pp. 16-28, Jan. 1955.

[7] R. Elliot, "Design of line source antennas for narrow beamwidth and asymmetric low sidelobes," *IEEE Trans. on Antennas and Propagation*, vol. 23, pp. 100-107, 1975.

[8] B. Carlson, "Covariance matrix estimation errors and diagonal loading in adaptive arrays," *IEEE Trans. on Aerospace and Electronic Systems*, vol. 24, no. 4, pp. 397-401, 1988.

[9] J. Liu, et al, "Adaptive beamforming with sidelobe control using second-order cone programming," *Pro. of IEEE Sensor Array and Multichannel Signal Processing Workshop*, Rosslyn, VA, pp. 461-464, 2002.

[10] Y. Zhang, H. Zhao, J. Lie, B. Ng, and Q. Wan, "Robust beamforming technique with sidelobe suppression using sparse constraint on beampattern," *Applied Computational Electromagnetics Society (ACES) Journal*, vol. 25, no. 11, pp. 947-955, Nov. 2010.

[11] Y. Chen, S. Yang, and Z. Nie, "The application of a modified differential evolution strategy to some array pattern synthesis problems," *IEEE Trans. Antennas Propag*., vol. 56, no. 7, pp. 1919-1927, July 2008.

[12] P. Rocca, R. Haupt, and A. Massa. "Interference suppression in uniform linear arrays through a dynamic thinning strategy," *IEEE Trans. on Antennas and Propagat.*, vol. 59, no. 12, Dec. 2011.

[13] M. Bataineh. "On Chebyshev array design using particle swarm optimization," *Journal of Electromagnetic Analysis and Applications*, pp. 213-219, March 2011.

[14] W. Li, Y. Li, L. Guo, and W. Yu, "An effective technique for enhancing anti-interference performance of adaptive virtual antenna array," *Applied Computational Electromagnetics Society (ACES) Journal*, vol. 26, no. 3, pp. 234-240, March 2011.

[15] U. Nickel, "Principle of adaptive array processing," *Advanced Radar Systems, Signal and Data Processing*, pp. 5-1–5-20, 2006.

[16] I. Reed, D. Mallett, and L. Brennan, "Rapid convergence for a digital adaptive array radar," *IEEE Trans*. AEs-10: pp. 853-863, 1974.

[17] D. Hughes and J. McWihirter, "Penalty function method for sidelobe control in least squares adaptive beamforming," *Advanced Signal Processing Algorithms*, vol. 2563, July 1995.

[18] M. Wax and T. Kailath, "Detection of signals by information theoretic criteria," *IEEE Trans, ASSP*, pp. 387-392, 1985.

[19] B. Stephen and V. Lieven, *Convex Optimization*, Cambridge University Press, New York, 2009.

[20] J. Löfberg, "YALMP: a toolbox for modeling and optimization in MATLAB," *Proceedings of the CACSD Conference*, Taipei, Taiwan, 2004.

[21] V. Lieven and B. Stephen, "Semi definite Programming," *SIAM Review* 38, pp. 49-95, March 1996.

[22] R. Shubair, S. Jimaa, and A. Omar, "Robust adaptive beamforming using least mean mixed norm algorithm," *Applied Computational Electromagnetics Society (ACES) Journal*, vol. 23, no. 3, pp. 262-269, Sep. 2008.
[23] L. Rees, J. Mallett, and L. Brennan, "Rapid convergence rate in adaptive arrays," *IEEE Trans. AES*, vol. 10, no. 6, pp. 853-863, 1974.
[24] K. Buckley, "Spatial/Spectral filtering with linearly constrained minimum variance beamformers," *IEEE Trans, on ASSP*, vol. 35, no. 3, pp. 249-266, 1987,
[25] H. Hu and H. Zhang, "Study on ADBF for difference beam at subarray level with sidelobe level," *IEEE International Symposium on Microwave, Antenna, Propagation, and EMC Technologies for Wireless Communications*, pp. 714-717, 2007.

Optimum Design of Conformal Array Antenna with a Shaped Radiation Pattern and Wideband Feeding Network

M. H. Rahmani and A. Pirhadi

Department of Electrical Engineering
Shahid Beheshti University G.C (SBU), Tehran, Iran
mohammadhassan.rahmani.1@ens.etsmtl.ca, a_pirhadi@sbu.ac.ir

***Abstract*—** In the present work, a circular conformal array with wideband printed dipole antennas and wideband feeding network has been designed to obtain a fully constrained cosecant squared radiation pattern using particle swarm optimization (PSO) algorithm and mutual coupling compensation. Using the circular conformal design leads to a decrease of around 33% of the length of the array antenna compared with that of the vertical linear array. Moreover, a better performance of the coverage region and side lobe fall after this area obtains by using this configuration.

Index Terms - Conformal array antenna, mutual coupling, particle swarm optimization, shaped beam, and wideband feeding network.

I. INTRODUCTION

Conformal antennas were first introduced in avionics to be integrated with the curve shape of the aircrafts in order to overcome aerodynamic limitations. Nowadays, in order to decrease the physical size of the array antenna or fit it with different shapes, conformal arrays are widely used in various vehicles, high speed trains, satellites, and military surveillance radars. The implementation of some radiation patterns is more accessible using the conformal arrays and they can overcome both physical and radiation patterns restrictions. Different microstrip conformal arrays have been introduced in the literature [1-3]. Shaped beam array antennas are of a great interest in the wireless community. The key aspect in the design of this type of array antennas is to set the elements excitations including phase and amplitude and the position of array elements to obtain a desired radiation pattern. To this end different analytical and numerical methods have been proposed until now [4]. However, in recent years, with the emergence of evolutionary optimization methods like genetic algorithms, differential evolution, and particle swarm optimization lots of researches have been carried out for the design of array antennas [5-7]. The design and synthesis of an array antenna for a desired radiation pattern is often affected by the mutual coupling effect between its elements. In fact, this effect will cause in a difference between the theoretical synthesis and the practical implementation [8]. In order to consider the far field mutual coupling of the elements in the synthesis process, the complex active radiation pattern of each element in the presence of the other elements must be used [9-11]. The particle swarm optimization (PSO) is a well-known evolutionary search method that has been used in different electromagnetic applications including array antennas throughout the last decade. In contrast with other stochastic algorithms, the PSO is proven to be easier to implement, adjust, and realize. Moreover, with a good choice of the initial values, the PSO can be guided in order to reach a more applicable result with a better timing efficiency [12-16].

In this paper, a new method of synthesis and design of the conformal array antenna has been proposed. Because of the variation of elements orientation and mutual coupling effect, the radiated fields of elements are different from each other and it must be considered in the array factor equation, which is used by the PSO. Independent from the shape of the conformal array, this method can be developed for the design of various shapes of the conformal array in which only the active complex patterns of each elements vary in the array factor. This method is fast, easy to implement, and avoids complicated calculations. The conformal array, which is synthesized and designed in this research is a circular array for surveillance

Submitted On: Feb. 14, 2013
Accepted On: Jan. 27, 2014

radars applications.

The feeding network has an important role in the array antenna design because the resulting radiation pattern and bandwidth of the whole system is highly dependent on it. Various methods have been used to design and implement the feeding network [1]. However, for a shaped radiation pattern, the feeding network design includes more challenges as it includes various phase shifters and power dividers. The usage of Wilkinson power dividers and delay line phase shifters has the advantage of delivering the exact decimal powers and phase shifts. However, they suffer from isolation issues and highly dependency with the frequency [29]. In this paper, we use a novel approach to design a feeding network that can deliver non-symmetric accurate powers and phase shifts with Wilkinson power dividers and wideband delay line phase shifters in the whole desired frequency band. The structure of this article is as follows: section II consists of an introduction to the development of the PSO for current project. In section III, the element that is used in the array and the conformal array configuration are presented and detailed. Section IV presents the simulation results with an investigation in mutual coupling compensation using complex active element patterns and the PSO. The fifth section is dedicated to the design of the wideband feeding network, which provides a stable phase shift and power splitting over the whole bandwidth.

II. USING THE PSO TO SYNTHESIZE OF CONFORMAL ARRAY ANTENNA

Generally, the parameters to control the radiation pattern of an array antenna are the amplitude and phase of excitation current of array elements [1]. The far-field array factor for a linear phased array of isotropic elements with inter-element distance of d and the wave number of $k = 2\pi d/\lambda$, which is placed on the z-axis, is $AF(\theta) = \sum_{n=1}^{N} A_n e^{jkn\cos\theta + j\varphi_n}$, where λ is the free space wavelength, n is the element number. A_n and φ_n are the amplitude and phase excitation of the n^{th} element, respectively. The goal is to define these amplitudes and phases using the PSO algorithm. Because of the mutual coupling effect and the changing the elements' direction in the conformal array, the active pattern of each element is different from the other elements. For this matter we have to consider the amplitude and phase of the pattern of each element in the presence of other elements, which is named, $E_n(\theta, \varphi)$ where θ and φ are the angular coordinates of a point in far field. In the following simulations θ changes from 0^o to 180^o while φ is 0^o and -180^o. The radiation pattern equation [7-8] is,

$$F(\theta, \varphi) = \sum_{n=1}^{N} A_n e^{j\varphi_n} E_n(\theta, \varphi). \qquad (1)$$

A_n and φ_n represent the amplitude phase of the n^{th} element excitation, respectively. In the above formulation the information related to the positioning of the elements is stored in $E_n(\theta, \varphi)$.

In 1995, Eberhart and Kenedy introduced the particle swarm optimization algorithm, which was an imitation of swarms of fish, bees, and birds when exploring the space to find the maximum amount of food. The importance of this algorithm is due to its fast and precise convergence, simple calculation steps, and easy implementation, which are the result of the Newtonian law of motion, which is the foundation of this algorithm [17-18]. The PSO is used to optimize continuous and discrete functions and is widely used in electromagnetic. It has been implemented in different applications like pattern synthesis of array antennas, reflector antennas optimization, corrugated horns optimization, patch antennas design, frequency selective surfaces, and microwave absorbers [19-22]. Tedious works in the field of array antenna synthesis using the PSO have been carried out until now [11-15, 19-24]. In the following section the PSO is developed for conformal array optimization.

A. Development of the PSO

In the original PSO, particles (amplitude and phase of the elements) are generated randomly and they can displace freely within the imposed boundary values of the solution space [17]. Although this will reduce the probability of immature convergence and increases the preciseness of the method, it usually leads to non-realistic amplitudes and phases and sometimes makes the implementation of the feeding network impossible. If the relative amplitude of two adjacent elements is too much, the fabrication of the related power splitter will be practically impossible as it will need too thick arms. Moreover, in the point of view of phases, high inter-element phase difference will make the construction of the wideband phase shifters more difficult.

The original PSO algorithm is developed to control massive changes of inter-elements amplitudes and phases of the excitations. To this end, the domain of input random variables is divided between elements to control the relative amplitudes and phase differences between adjacent elements. This means that X_1 is no longer a matrix of a completely random numbers between X_{max} and X_{min}, but it is guided in such a way that each number is allowed to be chosen randomly in restricted domain, which is defined as follows,

$$s = \frac{x_{\max} - x_{\min}}{n} \tag{2}$$

$$a(\mu_n) = X_{\min} + (\mu_n - 1)s \ , \tag{3}$$

$$X = \{a(\mu_n) + (a(\mu_n + 1) - a(\mu_n))\gamma\}. \tag{4}$$

In the above formulation $\mu_n=\{1,2,...,N\}$ according to the n^{th} element of the array, and γ is a random number between [0, 1]. X_{max} and X_{min} are, respectively the maximum and the minimum of acceptable values for amplitudes and phases. Then, the position of the particles through the algorithm is updated using equations (5) and (6),

$$V_{k+1}^i = w_k V_k^i + r_1 c_1 (Pb^i - X_k) + r_2 c_2 (Gb - X_k) \tag{5}$$

$$X_{k+1}^i = X_k^i + V_{k+1}^i, \tag{6}$$

where V_k^i is the velocity of the i^{th} particle in the k^{th} iteration, X_k^i is the position of the i^{th} particle in the k^{th} iteration. w_k is the weighting coefficient of the k^{th} iteration, r_1 and r_2 are random matrices, and $c_1=c_2=2$ are called the acceleration coefficients. Pb^i is the best position of the particle i^{th} during its exploration and Gb is the global best of the whole group. The weighting coefficient, w, is set to change linearly with equation (7),

$$w_k = w_{\max} - \frac{(w_{\max} - w_{\min}) * (k-1)}{k_{\max}}, \tag{7}$$

where k is the iteration number with the maximum of $k_{max}=150$, $w_{min}=0.2$ is the minimum of the weighting factor, and $w_{max}=0.9$ is its maximum. As a result of applying such procedure for obtaining the initial values, the relative amplitude and inter-element phase difference is controlled and massive changes, which lead to the complexity of the feeding network are avoided. In order to increase the efficiency of the algorithm the desired pattern is divided to different parts and the error for each part is calculated with different weights. As shown in Fig. 1, the desired pattern is a cosecant squared pattern, which is divided into 4 regions with different weights.

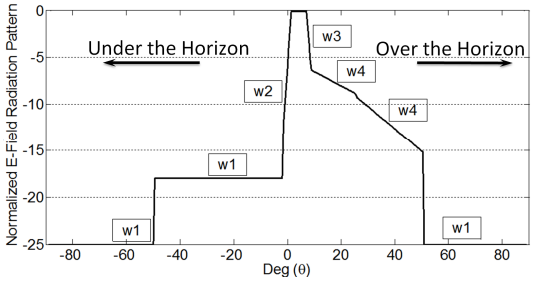

Fig. 1. Desired pattern with different weighting parts.

The error for this desired pattern is calculated as presented in equation (8),

$$\begin{aligned} Error = {} & w1\sum_{-90}^{a1}\left|F_d - F_N\right| + w2\sum_{a1+1}^{a1-1}\left|F_d - F_N\right| + \\ & w3\sum_{a}^{b}\left|F_d - F_N\right| + w4\sum_{b+1}^{b1}\left|F_d - F_N\right| + \\ & w4\sum_{b1+1}^{90}\left|F_d - F_N\right| \end{aligned} \tag{8}$$

where F_d is the desired pattern and F_N is the normalized calculated array factor, which is given in each iteration using the amplitudes and phases delivered by the algorithm. w1, w2, w3, and w4 are the weights. In the above illustration, the region between 0^o and 50^o is called the coverage region of the radiation pattern, and consequently, 50^o to 60^o is the quick fall region and 60^o to $90^o$is the side lobe region. Aside from the physical length of the array antenna, another advantage of using the conformal shape of the array is that it can deliver a better performance in the coverage and quick fall regions, which will be shown in next sections. This shape has been used in military surveillance radars and includes various imposed constraints such as different side lobe levels and horizon angles.

III. ANTENNA ARRAY CONFIGURATION

A. Wideband microstrip dipole antenna

The designed array consists of 8 elements of wideband microstrip dipole array (MDA) with balun working at the centre frequency of 1.1 GHz. It has been generally proved that MDA needs a balanced feed that could be a λ/4 coaxial balun. For a printed dipole this could be replaced by an integrated balun, which delivers broadband performance [25] and has been used in antenna array applications [26]. To achieve a better impedance matching with 50 Ω with wideband performance, instead of using a

quarter wavelength transformers, the feed point of the integrated balun is adjusted as described in [27]. The schematic of the single element reflection coefficient of the MDA is shown in Fig. 2 (a). Also the normalized E-field radiation amplitude and phase of this antenna are depicted in Fig. 2 (b) and (c).

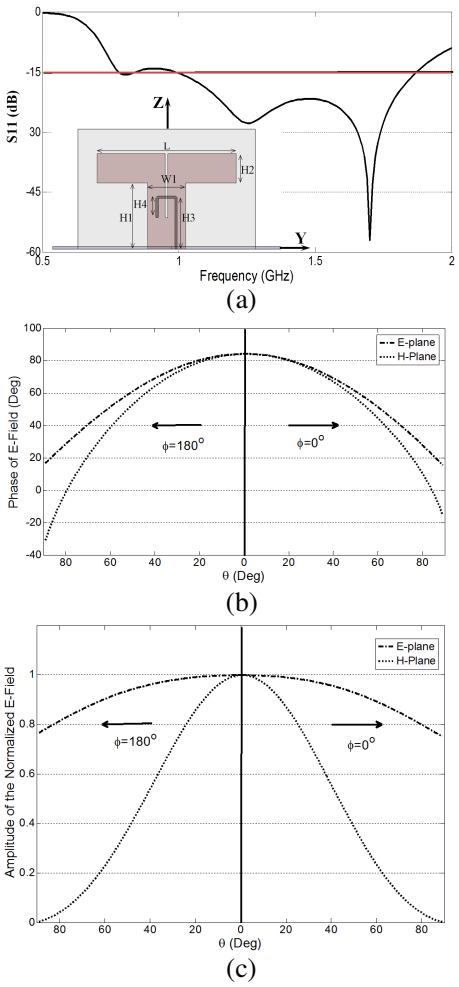

Fig. 2. Single printed dipole antenna with H1 = 52 mm, H2 = 23 mm, H3 = 40 mm, H4 = 15.3 mm, 1 = 30 mm, L1 = 110 mm: (a) reflection coefficient, (b) phase of radiated E-fields, and (c) amplitude of radiated E-fields.

B. Conformal array configuration

In this section, three different array configurations are presented, simulated, and synthesised to derive the desired radiation pattern. The first configuration is a linear array of 8 MDA elements. The schematic view of the array is shown in Fig. 3 (a). As it is seen it has a height of 1200 mm. In order to decrease the height and obtain a low profile configuration, another configuration (Fig. 3 (b)), which consists of a diagonal array with an angle of 45° related to the horizontal plane is presented. The height of this configuration is 860 mm, which is 28.3 % smaller than the vertical configuration. However, to obtain a smaller array the third array structure, which is a circular conformal array is presented that has a height of 800 mm, thus providing a physical size of around 33 % smaller than the first linear structure. For this array the MDA elements are implemented on the outer surface of a sphere with the radius of 800 mm. Figure 3 (c) depicts the circular array antenna. The inter-element distance for these three arrays is 0.8 λ at the centre frequency of 1.1 GHz.

The antennas are printed on an Ro4003 substrate with a relative dielectric constant of ε_r = 3.38 and a thickness of 32 mil. Moreover, a ground plane is designed in the array structure in order to increase the array directivity. The simulation and analysis has been performed by Ansoft HFSS [30] software based on the finite element method.

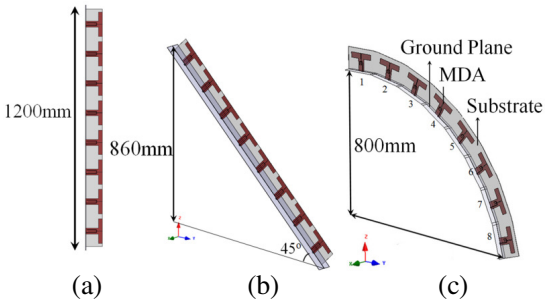

Fig. 3. Array configurations, (a) the linear array, (b) the diagonal array, and (c) the circular conformal array.

IV. OPTIMIZATION AND SIMULATION PROCEDURE

A. Array synthesis with an investigation of the array structure

As mentioned in the previous section, due to the presence of mutual coupling between the array elements, the radiation patterns of the array elements are different from each other. Therefore, we have to use the complex active radiation fields to calculate the radiation pattern of the array. The active radiation patterns of some elements of the conformal circular array are shown in the Fig. 4 (a) and (b) as terms of amplitude and phase. It is clearly observed that the far-field pattern of each element is different from that of others.

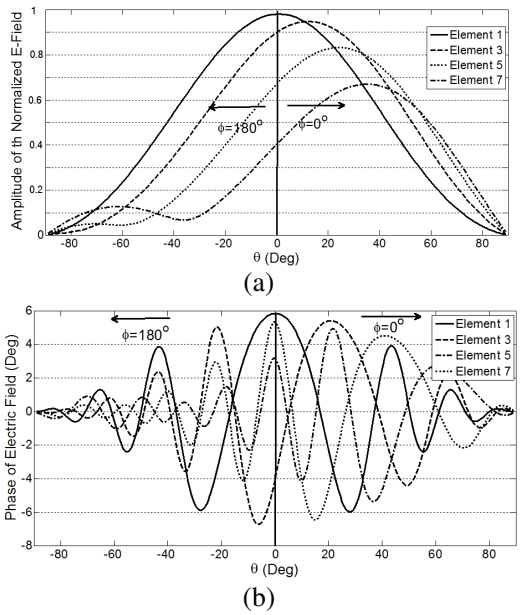

Fig. 4. (a) The normalized E-fields of elements 1, 3, 5, and 7 in the array and (b) the phase of E-field of elements 1, 3, 5, and 7 in the array.

B. Simulation and optimization results

First, using the three mentioned array structures in Fig. 3, we have performed the PSO in Matlab to synthesize a cosecant squared radiation pattern with a coverage region of 50°. Figure 5 (a) represents the convergence rate of the applied developed PSO and Fig. 5 (b) depicts the resulted radiations patterns.

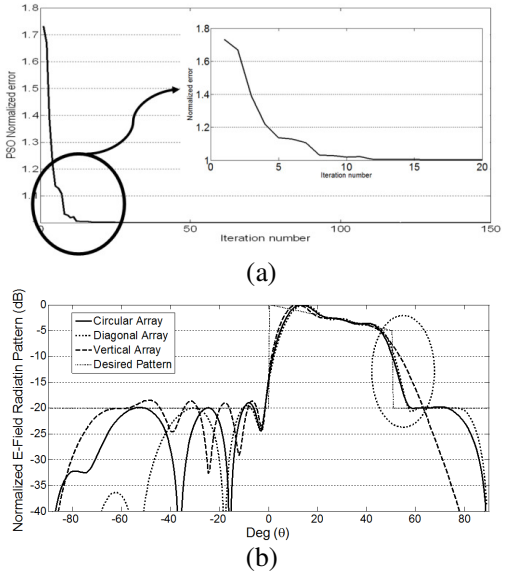

Fig. 5. (a) Convergence diagram of the PSO and (b) optimized E-field radiation pattern of three array antennas for coverage area of 50°.

The algorithm converges in less than 50 iterations. As it is seen in Fig. 5 (b), all these three arrays can produce the desired coverage, however, the circular and the diagonal arrays have a better performance right after 50°. In other situation, for wider coverage region, the desired radiation pattern has been changed in such a way to produce a coverage region of 60°. We have performed the PSO method to synthesize and compare the resulting radiation patterns of these three arrays. The result has been shown in Fig. 6.

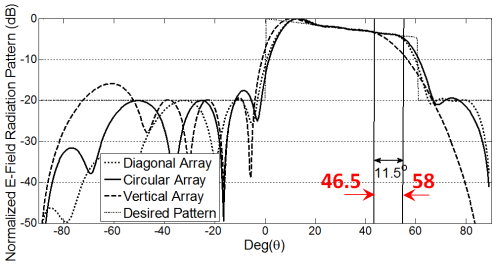

Fig. 6. Optimization resulted E-field radiation pattern of three arrays for coverage area of 60°.

As it is observed in Fig. 6, the diagonal and the circular array can produce the wider coverage region with respect to linear array. As a result, we conclude that the circular conformal array is more advantageous than the diagonal and the linear array because:

1- It has a smaller physical height than the diagonal and the linear array.

2- It has a better side lobe level fall than the linear array.

3- Its resulted coverage region is wider than the linear array.

C. Simulation of the final synthesized array

As was mentioned, the conformal circular array can produce the wider coverage region and better side lobe level fall with smaller physical height. Hence, this structure has been used in the following section to synthesize the desired radiation pattern of Fig. 1. In order to show that the mutual coupling effects on the radiation pattern have been fully considered and compensated, the resulted amplitudes and phases from the PSO process have been used as the element excitations of the simulated array in the Ansoft HFSS software. The resulted E-field radiation patterns from the PSO and the simulation have been compared in Fig. 7. As it is seen, these two radiation patterns have good agreement because the mutual coupling is fully

considered in the optimization process. The derived amplitudes and phases are shown in Fig. 8. It is seen that, by using the developed PSO method, the relative amplitude between the adjacent elements are between 0.5 and 1. Moreover, the phase differences between the adjacent elements are between 0^o and 150^o. These ease the complexity of making the feeding network.

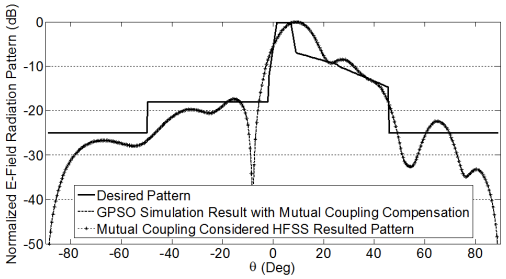

Fig. 7. Radiation pattern of normalized E-field of 8 elements MDA with far field mutual coupling compensation.

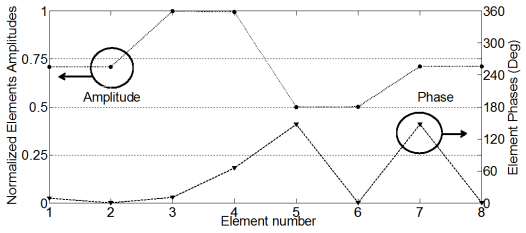

Fig. 8. Amplitudes and phases excitation of the array.

V. DESIGN OF THE FEEDING STRUCTURE

After determining the optimum amplitudes and phases of the array elements, to obtain the desired radiation pattern, it is necessary to design a suitable feeding network. In this case, as a result of using the developed PSO, the inter-element phase shift is linear and limited so that the phase shifters are easier to design. Moreover, the inter element relative amplitudes are limited and easily possible to implement.

The feeding network consists of some non-symmetrical and symmetrical power dividers. The optimum tapering of amplitudes of the array elements is obtained by adjusting the ratio of power dividers. As mentioned before, embedded active element patterns combined with the PSO are used to compensate the far-field mutual coupling. However, the inter-port coupling is an important issue that affects greatly the performance of the designed array. To minimize this effect, the Wilkinson power dividers that provide two isolated ports are used to isolate the output ports and minimize the inter-port coupling [28]. In addition, to obtain the optimum phase distribution in the operating frequency, the delay line phase shifters are used to adjust the phases of the elements. The most challenge in the design of the feeding network is the narrowband behaviour of the delay line phase shifters. For this application, the desired band width is about 30% in the centre frequency of 1.1 GHz and it requires designing the wideband phase shifters.

A. Designing the feed network at the centre frequency

The schematic view of the feeding network before phase shift correction is shown in Fig. 9.

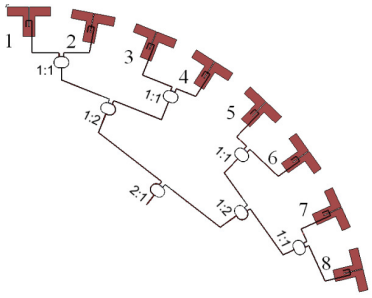

Fig. 9. Schematic view of the feeding network before phase shift correction.

In Fig. 9 the values of the power dividers are described based on the splitting ratio of each arm. For example, 1:2 means that the right arm takes twice the power than the left arm. Each power divider has its own power splitting ratio based on the optimization results.

To design the feed network, at first, each equal and non-equal Wilkinson power divider is separately designed according to the desired power splitting ratio and desired phase shift at the centre frequency. The dimensions of the Wilkinson power dividers that have been used in this feeding network have been shown in Fig. 10. Then the whole feed network is made by uniting these separate power dividers. At this step, the feeding network delivers the proper power to each element with the desired phase shift at the centre frequency. The simulation of the power dividers, phase shifters, and the whole feeding network has been done in HFSS software. The output powers of this feeding network over the desired frequency band are shown in Fig. 11.

Power Divider	W1	W2	D
1 :1	0.8mm	0.8mm	27mm
2 :1	1.8mm	0.4mm	27mm
1 :2	0.4mm	1.8mm	27mm

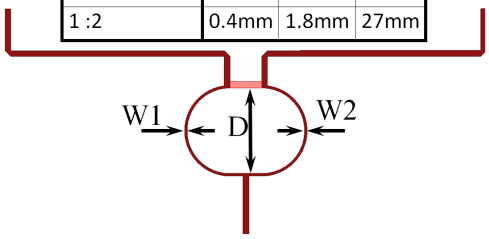

Fig. 10.Wilkinson power divider dimensions.

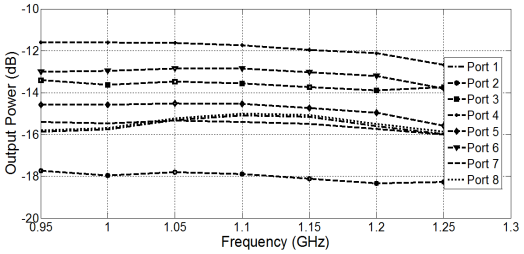

Fig. 11. Resulted output power of each port.

The results show that the output power produced by each port is nearly stable over the whole frequency band and does not need correction. Figure 12 shows the resulted phase shift of each port.

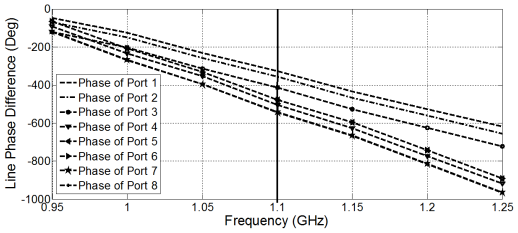

Fig. 12. Resulted output phase shift of each port.

As it is seen in Fig. 12, due to the different lengths of paths, the phase difference between the ports are not stable over the whole frequency band and the slope of the phase shifts is different for each output port. This will result in the degradation of the resulted pattern thus making the need for phase shift correction indispensable.

B. Output phase difference correction within the desired bandwidth

To correct the resulted phase differences in such a way that they become stable over the whole frequency band the following steps should be performed. First, we have to find the port with the maximum slope and consider it as reference. Here the reference port is port No. 8 as it has the longest length. Then, by increasing the length of the microstrip lines in other routes and also using wideband phase shifters we have to increase the phase slope of other ports to reach the reference slope. All this procedure should be executed in such a way that the phase shift does not change at the center frequency. The wideband phase shifter consists of a wilds phase shifter, which is fully described in [29]. It consists of two open and short circuited λ/8 stubs or one λ/4 circuited open stub. By changing the ratio of W1/W2 it is possible to obtain different phase shifts with increasing the slope of the phase shift of the line. Figure 12 shows the phase shift slope correction of the above phase shifters. Table 1 summarizes the wideband phase shifters that are used in this paper along with their dimensions.

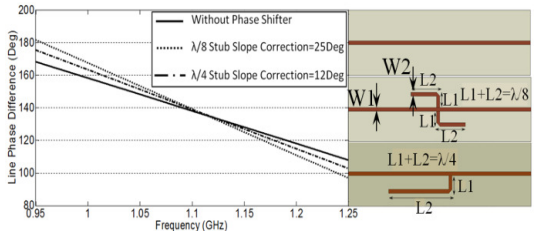

Fig. 13. Wilds phase shifters and their phase difference corrections.

Table 1: Wideband wilds phase shifters used in this project with their dimensions.

	W1/W2	Resulted Phase Shift
Double Stub	18	54°
Double Stub	3	25°
Double Stub	0.36	150°
Single Stub	1	33°

C. Final wideband feeding network

By executing the previously described phase shift correction procedure, a wideband feeding network with stable phase shift and power split ratio is achieved. The schematic view of the final feeding network is shown in Fig. 13. Figure 15 shows the resulted output phase shifts after the phase correction procedure over the whole frequency band.

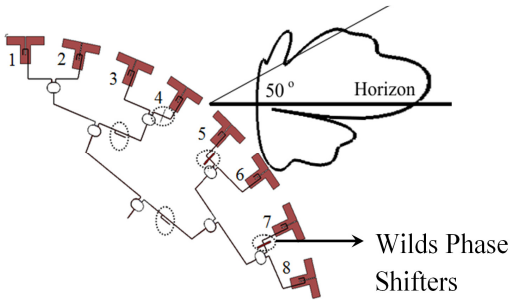

Fig. 14. Final feeding network and array antenna structure after phase shift correction.

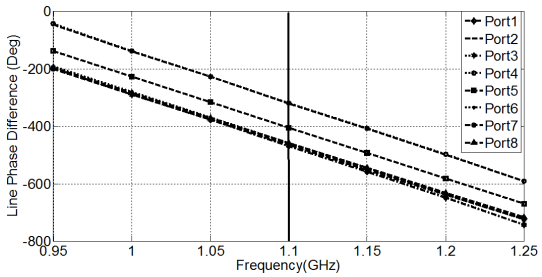

Fig. 15. Output phase shift of each port after correction.

As seen in this figure, after the phase shift correction procedure, the slope of the output phase shift for all ports is finally equal, and consequently, the phase difference between ports is stable within the whole frequency band. Figure 16 shows the output power of the final feeding network.

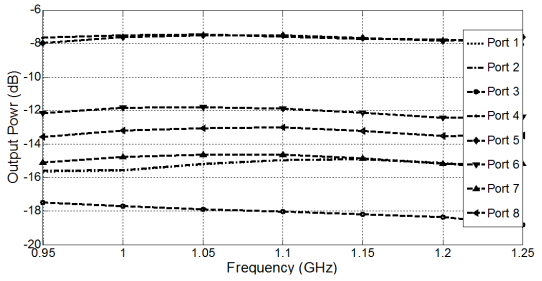

Fig. 16. Output power of each port after correction.

The resulted output power is almost stable in desired bandwidth and no correction is needed for this case. To finalize the design of the MDA array, the designed array and the wideband feeding network are united and simulated all together. The final results are shown in Fig. 17. In this figure, the resulted radiation pattern of the optimization algorithm, which had been performed in the center frequency has been compared with the feeding network output results at 0.95 GHz, 1.1 GHz, and 1.25 GHz. It is well depicted that the resulted patterns by the feeding network have good agreement with that of the optimization results of the center and the end of the desired frequency band.

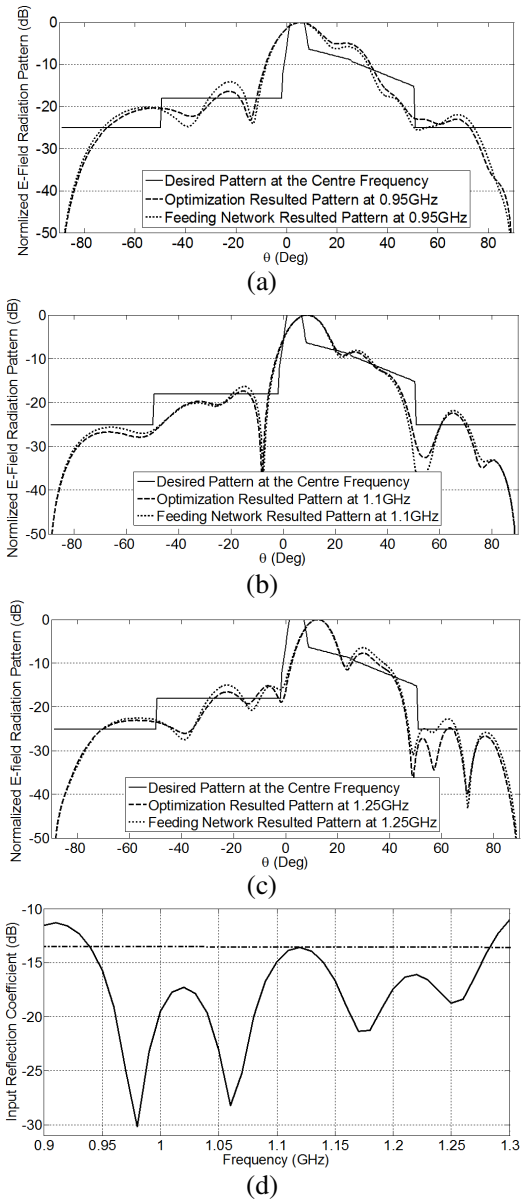

Fig. 17. Final E-field radiation pattern (a) f = 0.95 GHz, (b) f = 1.1 GHz, (c) f =1.25 GHz, and (d) the input reflection coefficient of the array antenna.

VI. CONCLUSION

In this article, a circular conformal array has been designed, analyzed and simulated to obtain

a fully constrained cosecant squared pattern using a modified PSO algorithm. The designed array consists of an 8 elements printed dipole with the inter-element distance of d = 0.8 λ working at the central frequency of 1.1 GHz and placed on the outer surface of a sphere with the radius of 800 mm. The comparison between a vertical linear array, diagonal linear array and the circular conformal array with the same inter-element distance depicted that the height of the former array is 33% less than that of the vertical linear array and near 7% less than that of the diagonal array, thus producing a lower profile array antenna. Moreover, the performance of these three arrays on the coverage area and side lobe fall after this area has been investigated and it has been observed that the circular and the diagonal arrays have a quicker fall right after the coverage area and can produce a wider coverage region. The PSO algorithm, along with the method of the active element patterns has been used to synthesize the array with the consideration of the far field mutual coupling. Finally, a wideband and isolated feeding network, which is able to produce desired excitations for a consistent cosecant squared pattern over the desired frequency band has been designed using equal and non-equal Wilkinson power splitters and wideband phase shifters.

REFERENCES

[1] L. Josefsson and P. Persson, *Conformal Array Antenna Theory and Design*, USA: John Wiley and Sons, 2006.

[2] A. Zaghloul, M. Parsa, and S. Kumar, "Investigation of a microstrip antenna array conformal to a paraboloidal surface," *23rd Annual Review of Progress in Applied Computational Electromagnetics (ACES)*, pp. 1608-1615, Italy, March 2007.

[3] K. Xiao, Y. Li, F. Zhao, S. Chai, and J. Mao, "Analysis of microstrip antennas using the volume surface integral equation formulation and the pre-corrected fast Fourier transform method," *Applied Computational Electromagnetics Society (ACES) Journal*, vol. 26, no. 11, pp. 922-929, Nov. 2011.

[4] D. Kurup, M. Himdi, and A. Rydberg, "Synthesis of uniform amplitude unequally spaced antenna arrays using the deferential algorithm," *IEEE Trans. Antennas Propagat.*, vol. 51, pp. 2210-2217, 2003.

[5] D. Gies and Y. Rahmat-Samii, "Particle swarm optimization for reconfigurable phase differentiated array design," *Microwave and Optical Technology Letters*, vol. 38, no. 3, 2003.

[6] D. W. Boeringer and D. H. Werner, "Particle swarm optimization versus genetic algorithms for phased array synthesis," *IEEE Trans. Antennas Propagat.*, vol. 52, no. 3, 2004.

[7] I. Gupta and A. Ksienski, "Effect of mutual coupling on the performance of adaptive arrays," *IEEE Trans. Antennas and Propagat.*, vol. 31, no. 5, pp. 785-791, 1983.

[8] D. Kelley and W. Stutzman, "Array antenna pattern modelling method that includes mutual coupling effects," *IEEE Trans. Antennas Propagat.*, vol. 41, pp. 1625-1632, 1993.

[9] P. Darwood, P. Fletcher, and G. Hilton. "Mutual coupling compensation in small planar array antennas," *IEE Proc. Microw. Antennas Propagat.*, vol. 145, pp. 1-6. 1998.

[10] P. Fletcher and M. Dean, "Derivation of orthogonal beams and their application to beamforming in small phased arrays," *IEE Proc. Microw. Antennas Propagat.*, vol. 143, pp. 304-308, 1996.

[11] S. Zhang, S.-X. Gong, Y. Guan, and S. Zhang, "A novel IGA- PSO hybrid algorithm for the synthesis of sparse arrays," *Progress in Electromagnetics Research*, vol. 89, pp. 121-134. 2009.

[12] Z. Hang, S.-X. Gong, and S. Zhang, "A modified PSO for low sidelobe concentric ring arrays synthesis with multiple constraints," *Journal of Electromagnetic Waves and Applications*, vol. 23, no. 11, pp. 1535-1544, 2009.

[13] J. Pérez and J. Basterrechea, "Hybrid particle swarm-based algorithms and their application to linear array synthesis," *Progress in Electromagnetics Research*, vol. 90, pp. 63-74, 2009.

[14] Z. Zaharis, S. Goudos, and T. Yioultsis, "Application of boolean PSO with adaptive velocity mutation to the design of optimal linear antenna arrays excited by uniform amplitude current distribution," *Journal of Electromagnetic Waves and Applications*, vol. 25, no. 10, pp. 1422-1436, 2011.

[15] M. Rahmani and A. Pirhadi, "Shaped beam microstrip dipole antenna synthesis using guided particle swarm optimization," *ACES Conference*, 2012.

[16] S. Walker and D. Chatterjee, "Study of exact and high-frequency code solvers for applications to a conformal dipole array," *Applied Computational Electromagnetics Society (ACES) Journal*, vol. 24, no. 6, pp. 550-558, Dec. 2009.

[17] J. Kennedy and R. Eberhart, "Particle swarm optimization," *Proc. IEEE Int. Conf. Neural Networks*, vol. 4, pp. 1942-1948, 1995.

[18] R. Eberhart and Y. Shi, "Particle swarm optimization, developments, applications, and

resources," *Proc. Cong. Evol. Comput.*, vol. 1, pp. 81-86, 2001.

[19] J. Robinson and Y. Rahmat-Samii, "Particle swarm optimization in electromagnetics," *IEEE Trans. Antennas Propagat.*, vol. 52, no. 2, pp. 397-407, Feb. 2004.

[20] D. Gies and Y. Rahmat-Samii, "Particle swarm optimization (PSO) for reflector antenna shaping," *IEEE Antennas Propagat. Soc. Int. Symp. Dig.*, vol. 3, pp. 2289-2293, June 2004.

[21] W. Liu, "Design of multiband CPW-fed monopole antenna using a particle swarm optimization approach," *IEEE Trans. Antennas Propagat.*, vol. 53, no. 10, pp. 3273-3279, Oct. 2005.

[22] S. Genovesi, R. Mittra, A. Monorchio, and G. Manara, "Particle swarm optimization for the design of frequency selective surfaces," *IEEE Antennas Wireless Propagat. Lett.*, vol. 1, no. 5, pp. 277-279, Dec. 2006.

[23] W. Li and X. Shi, "An improved particle swarm optimization algorithm for pattern synthesis of phased arrays," *Progress in Electromagnetics Research*, PIER vol. 82, pp. 319-332, 2008.

[24] S. Goudos, V. Moysiadou, T. Samaras, K. Siakavara, and J. Sahalos, "Application of a comprehensive learning particle swarm optimizer to unequally spaced linear array synthesis with sidelobe level suppression and null control," *IEEE Antennas and Wirel. Propag. Lett.*, vol. 9, 2010.

[25] B. Edward and D.Rees, "A broadband printed dipole with integrated balun," *Microw. J.*, pp. 339-344, May 1987.

[26] J.-P. Bayard, "Analysis of infinite arrays of microstrip-fed dipoles printed on protruding dielectric substrates and covered with a dielectric radome," *IEEE Trans. Antennas Propagat.*, vol. 42, pp. 82-89, Jan. 1994.

[27] R. LinLi, T. Wu, B. Pan, K. Lim, J. Laskar, and M. Tentzeris, "Equivalent circuit analysis of a broadband printed dipole with adjusted integrated balun and an array for base station applications," *IEEE Trans. Antennas Propagat*, vol. 57, no. 7, July 2009.

[28] E. Wilkinson, "An N-way hybrid power divider," *IRE Trans. on MTT*, vol. 116, Jan. 1960.

[29] R. Wilds, "Try λ/8 stubs for fast fixed phase shifts," *Microwaves and RF*, vol. 18, pp. 67-68, 1979.

[30] http://www.ansys.com/Products/Simulation+Technology/Electromagnetics/Signal+Integrity/ANSYS+HFSS

Mohammad Hassan Rahmani received his B.Sc. and M.Sc. degrees in Electrical Engineering 2008 and 2011 from Azad University, Tehran, Iran andShahid Beheshti University (SBU), Tehran, Iran, respectively. His major research interests are the development and design of wideband phased array antennas for wireless communications, evolutionary algorithms, and shaped beam antennas synthesis. He is currently pursuing his Ph.D. studies at École de Technologie Supérieure in Montreal, Canada.

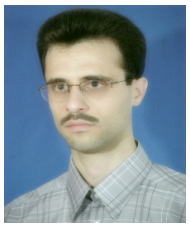

Abbas Pirhadi received B.Sc. degree in Electrical Engineering from the Isfahan University of Technology, Isfahan, Iran 2000, and M.Sc. and Ph.D. degree in Communication Engineering from Tarbiat Modares University (TMU), Tehran, Iran in 2002 and 2007, respectively. From 2002 to 2006, he joined the antenna and propagation group of the Iran Telecommunication Research Center (ITRC) as a researcher. Also, in 2008 he joined the Shahid Beheshti University (SBU) where he is the Assistant Professor at the faculty of Electrical and Computer engineering. His research interests include microwave antennas, theoretical and computational electromagnetic with applications to antenna theory and design.

A Tri-Band Antenna for Wireless Applications using Slot-Type SRR

D.-L. Jin, T.-T. Bu, J.-S. Hong, J.-F. Wang, and H. Xiong

School of Physical Electronics
University of Electronic Science and Technology, Chengdu, 610054, China
jindalinyu@163.com, butingting1990@gmail.com, cemlab@uestc.edu.cn, 773882005@qq.com,
xiong1226han@126.com

Abstract ─ A tri-band microstrip-fed slot antenna for WLAN/WiMAX applications is proposed and investigated. Three operating bands are obtained by inserting split ring resonator (SRR) slots for band-rejected design. An electromagnetic (EM) model of this antenna is simulated by Ansoft HFSS. The principle of operation and parametric of the proposed antenna are also provided. The measured -10 dB bandwidth for return loss is from 2.39 GHz – 2.48 GHz, 3 GHz – 3.7 GHz, and 5 GHz – 7 GHz, covering the WLAN (2.4/5.2/5.8) and WiMAX (3.5/5.5) bands. The proposed antenna achieves a stably omni-directional radiation pattern and acceptable gain at all three operating frequency bands.

Index Terms – Slot antennas, SRR, tri-band antennas, and WiMAX/WLAN applications.

I. INTRODUCTION

With the rapid development of the wireless communication, the multiband antennas have great interest for the application to communication systems. A printed monopole antenna is very attractive and suitable for the multiband WLAN/WiMAX applications owing to their simple structures, low profile, good impedance matching, low cost, and omni-directional radiation patterns [1-17]. Numerous monopole designs have been investigated for wireless systems. Multiband monopole antenna can be realized by employing a parasitic or shorted element to the monopole antenna [1-4], appropriately etching slots in radiating elements [8-10], using various radiating elements of different shapes [11-13] and various feeding structure[15-17].

However, the first method will increase the manufacturing cost and difficulty in fabricating. Most of the reported multiband antennas combine the last three method have either large antenna sizes or complex structures. In [18], a triple-band unidirectional coplanar antenna with high gain and good impedance matching is proposed for WLAN/WiMAX applications, but the size is 100×60 mm^2. A CPW-fed mirrored-L monopole antenna has distinct triple-band, but the geometry of the antenna is complicated and the size (77×53 mm^2) is relatively large [19].

In this paper, a novel triple band planar monopole antenna with complementary split ring resonators (SRR) is proposed. The antenna is simple in structure and reduced the size compared to the conventional printed monopole antenna. By embedding different shaped SRR slots into a rectangular patch [20] for band-rejected design, a triple-band antenna with compact size, low profile, good radiation performance, and without conductor-backed plane is obtained. From the measured results, the impedance bandwidth for -10 dB return loss at 2.44 GHz, 3.5 GHz, 5.5 GHz operating bands can be respectively up to 0.09 GHz, 0.7 GHz, and 2 GHz. The proposed antenna is suitable for multiband wireless communication systems such as the wireless local-area network (WLAN) 2.4/5.2/5.8 and the world interoperability for microwave access (WiMAX) 3.5/5.5 operations owing to its omni-directional radiation patterns and good impedance characteristics.

II. ANTENNA DESIGN

Figure 1 shows the geometry of the proposed multiband antenna. The antenna is printed on 1.2 mm thick FR4 substrate of relative permittivity 4.4

Submitted On: Dec. 26, 2012
Accepted On: Feb. 2, 2014

with overall dimensions of 26×32 mm^2. The radiation element of the triple band antenna simply composed of a rectangular monopole with SRR slots and 50 Ω microstrip feeding line is printed on the top side of substrate. The width (W_1) and length (L_1) of the microstrip feed line is designed as 2.2 mm to achieve the 50 Ω characteristic impedance. Figure 2 illustrated the photograph of the fabricated antenna. For detailed design, all parameters of the proposed antenna are simulated and optimized using the Ansoft HFSS in finite-element moment based full-wave solver.

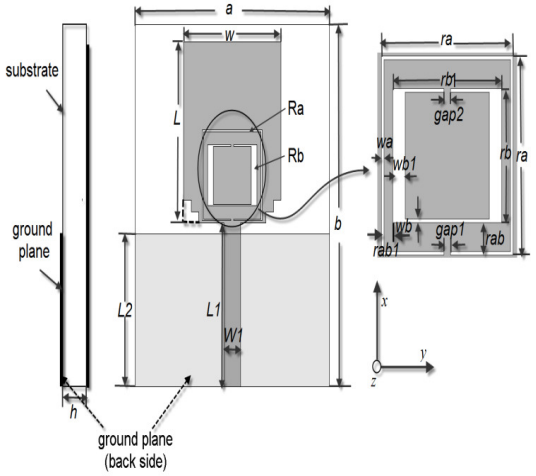

Fig. 1. Geometry of the proposed antenna.

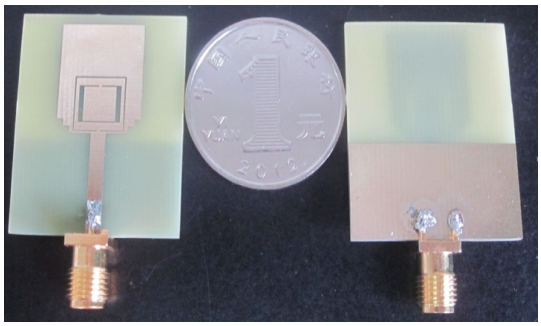

Fig. 2. Photograph of the proposed triple band antenna.

The dimensions of the designed antenna after optimization are: a = 26 mm, b = 32 mm, W = 13 mm, L = 16 mm, W_1 = 2.2 mm, L_1 = 14.5 mm, L_2 = 13.5 mm, ra = 8 mm, rb = 5.4 mm, $rb1$ = 6.6 mm, rab = 1.1 mm, $rab1$ = 0.5 mm, $gap1$ = $gap2$ = 0.4 mm, wa = wb = 0.2 mm, $wb1$ = 0.8 mm. As shown in Fig. 3, the initial antenna has a wide bandwidth from 3.1 GHz – 7 GHz, and the performance beyond 7 GHz is out of our interest for WLAN/WiMAX applications. It also can be seen from the figure that the inner split ring (*Rb*) is for notched the 3.8 GHz – 4.9 GHz and the lower band at 2.44 GHz is attributed to the outer split ring (*Ra*). Then the final triple band antenna for wireless applications is obtained by combined the inner and outer split ring. The detail performance of the SRR will be given as the following.

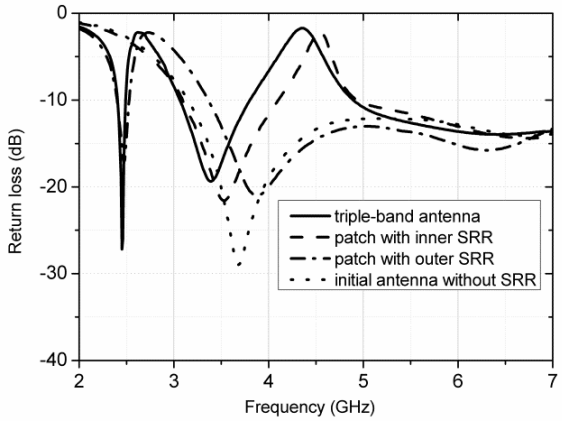

Fig. 3. Simulated return losses for the different structures.

A. The inner split ring inserting

The initial wideband antenna has a bandwidth from 3.1 GHz to 7 GHz as shown in Fig. 3. From Fig. 4 (a), it can be seen that the initial wideband monopole antenna consists of a regular rectangle patch and ground plane, while the staircase pattern is used to broadband, because the electromagnetic coupling between the rectangular patch and the ground plane is affected by the two staircase pattern notches [21-23]. In order to reduce the EMI, band-notched function covering the 3.8 GHz – 4.9 GHz is desired. The band-notched (3.8 GHz – 4.9 GHz) antenna is illustrated in Fig. 4 (c). As shown in Fig. 5, *wb1* is an important parameter to broad the notched band. The notched band is extended to 4.9 GHz, while *wb1* change from 0.2 mm to 0.8 mm. The inner split ring (*Rb*) is designed to get the notched band. The simulated current distribution of the wideband antenna at the notched frequency 4.4 GHz is shown in Fig. 6. Note that the currents are manly distributed around the SRR filter structure. The length of SRR slots is determined by,

$$Ls = \frac{\lambda_g}{2} = \frac{\lambda_0}{2\sqrt{\varepsilon_e}} = \frac{c}{2\sqrt{\varepsilon_e} f_0} \quad (1)$$

where f_0 is the band-notch frequency (4.4 GHz), $\varepsilon_e = (\varepsilon_r + 1)/2$, is the effective dielectric constant, and c is the speed of light in free space. The inner SRR leads to the desired notch frequency at 4.4 GHz (3.8 GHz – 4.9 GHz), and the length Ls = 21.6 mm is about half of the guided wavelength (λg/2) calculated at 4.4 GHz.

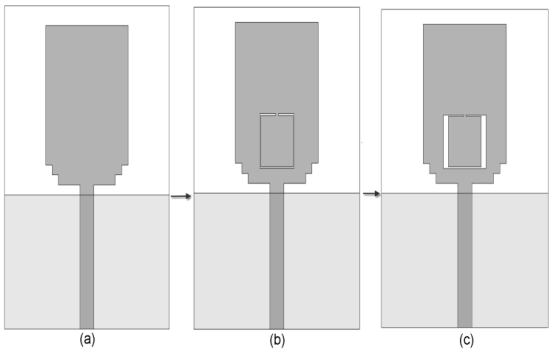

Fig. 4. (a) Initial monopole antenna, (b) band-notched antenna with inner split ring inserting (*wb1* = 0.2 mm), and (c) band-notched antenna with inner split ring inserting (*wb1* = 0.8 mm).

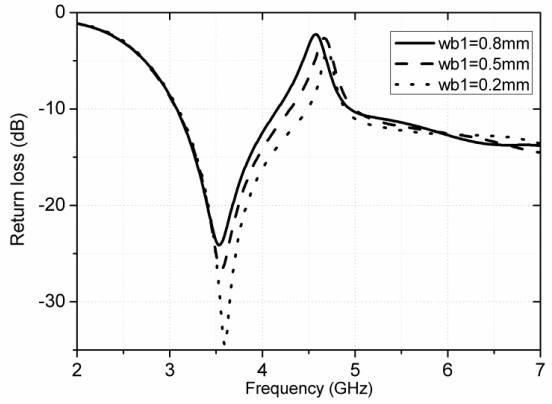

Fig. 5. Simulated return loss for different *wb1*.

Parameters *rb1* and *gap2* are varied with a range of values also as part of the optimization process. As shown in Fig. 7, the notched band shifts to higher frequency as *rb1* and *gap2* increase. As *rb1* and *gap2* gradually increased to 6.6 mm and 0.4 mm, a good impedance match is achieved and the notched antenna can be suitable for reduce EMI with the higher band (3.8 GHz – 4.9 GHz), and the wideband antenna is adjusted to dual band antenna.

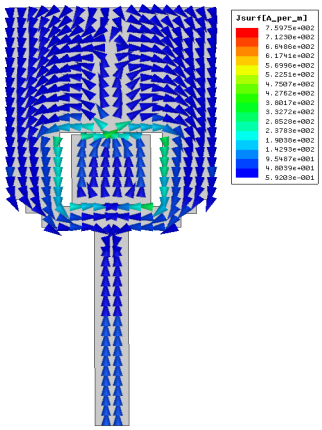

Fig. 6. The surface current distribution at this rejection frequency (4.4 GHz).

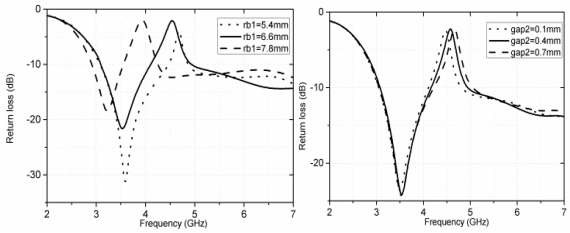

(a) (b)

Fig. 7. Simulation results for different parameters, (a) S_{11} for parameter *rb1* and (b) S_{11} for parameter *gap2*.

B. The outer split ring inserting

After getting the higher band-notched (3.8 GHz – 4.9 GHz) antenna, the outer split ring (*Ra*) embedded into the antenna is analyzed. The lower WLAN band (at 2.44 GHz) is obtained after embedding the *Ra*, while the band (2.5 GHz – 3.05 GHz) is notched. The length of *Ra* slot is determined by *Lsb* = 32 mm (about half of the guided wavelength (λ_g/2) calculated at 2.68 GHz).

Figure 8 illustrated the effects of the parameters *ra* and *wa*. From the figure, it is observed that the notched band shifts to lower frequency as *ra* increases, while the impedance matching of the antenna is improved as *wa* reduce. The current distribution at 2.68 GHz (notched frequency) and 2.44 GHz (resonant frequency) is given in Fig. 9, it can be seen that the current manly distributed around the *Ra* at the notched frequency 2.68 GHz.

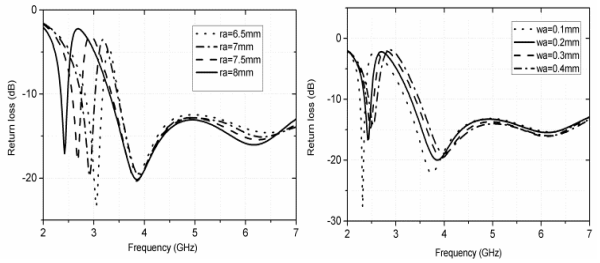

(a) (b)

Fig. 8. Simulation results for different parameters, (a) S_{11} for parameter *ra* and (b) S_{11} for parameter *wa*.

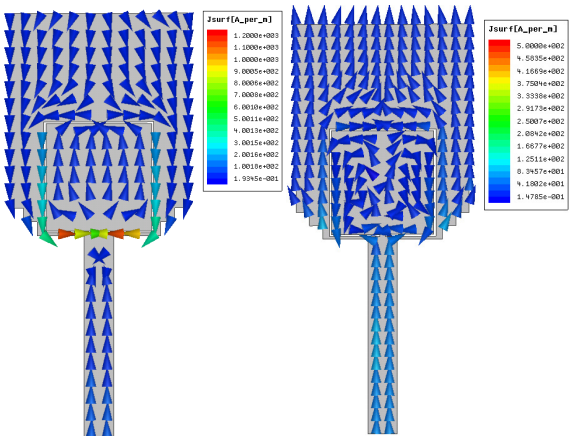

(a) (b)

Fig. 9. Simulated surface current distribution at 2.68 GHz, and 2.44 GHz; (a) 2.68 GHz and (b) 2.44 GHz.

III. RESULTS AND DISCUSSION

A triple band antenna prototype is fabricated on low cost FR4 ($\varepsilon_r = 4.4$, $\tan\delta = 0.02$) substrate. We use Rohde and Schwarz ZVB 20 vector network analyzer to measure return-loss of the proposed antenna. The antenna with Rohde and Schwarz ZVB 20 vector network analyzer is shown in Fig. 10. The simulated and measured return-loss (S_{11}) characteristics of the proposed antenna obtained using HFSS 13.0 and the Rohde and Schwarz ZVB 20 vector network analyzer is shown in Fig. 11. From the measured results, three relative impedance bandwidths with -10 dB return loss are about 3.7 % (2.39 GHz – 2.48 GHz), 20.8% (3 GHz – 3.7 GHz), and 30% (5 GHz – 7 GHz), respectively, which show good agreement with the simulated results. The differences between the simulation and measurements could be due to the SMA connector and the manufacturing limits.

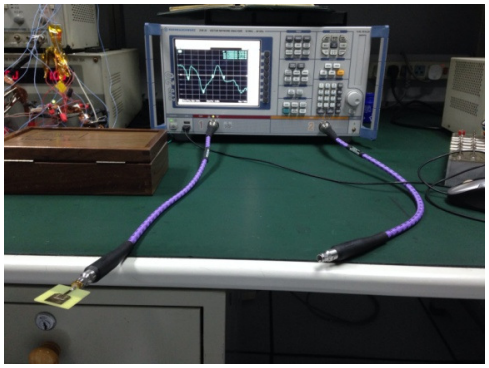

Fig. 10. Photograph of proposed triple band antenna with Rohde and Schwarz ZVB 20 vector network analyzer.

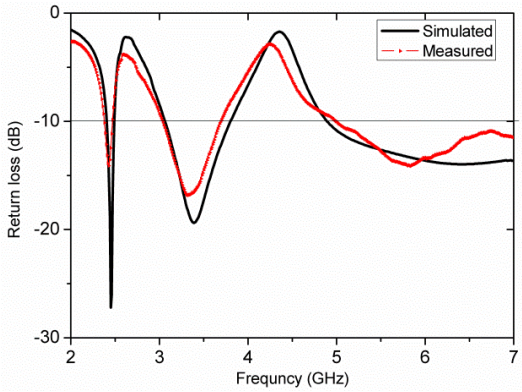

Fig. 11. Simulated and measured S_{11} for proposed triple band antenna.

The radiation patterns of the proposed antenna were measured in an anechoic chamber at UESTC with SATIMO antenna measurement system as shown in Fig. 12. The measured far-field radiation patterns of the proposed triple band antenna in the E-plane (*xz*-plane) and H-plane (*yz*-plane) at 2.44 GHz, 3.5 GHz, and 5.5 GHz are plotted in Fig. 13. It can be seen that the antenna behaves quite similarly to the typical printed monopoles. The H-plane patterns are almost omni-directional, while the E-plane patterns exhibit dipole-like behaviors at these frequencies. The measured peak gain from 2 GHz to 7 GHz is plotted in Fig. 14. As expected, the antenna gain exhibits two significant decreases at 2.7 GHz and 4.6 GHz, thus clearly indicating the effect of notched bands.

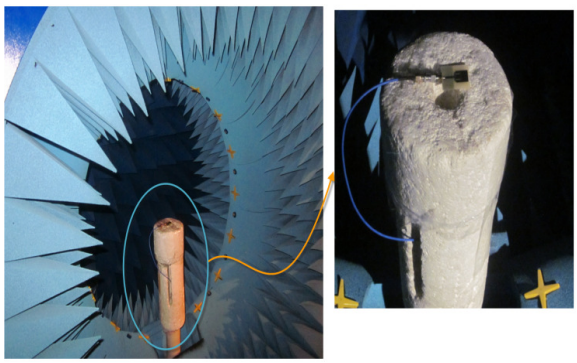

Fig. 12. Photograph of proposed triple band antenna in an anechoic chamber.

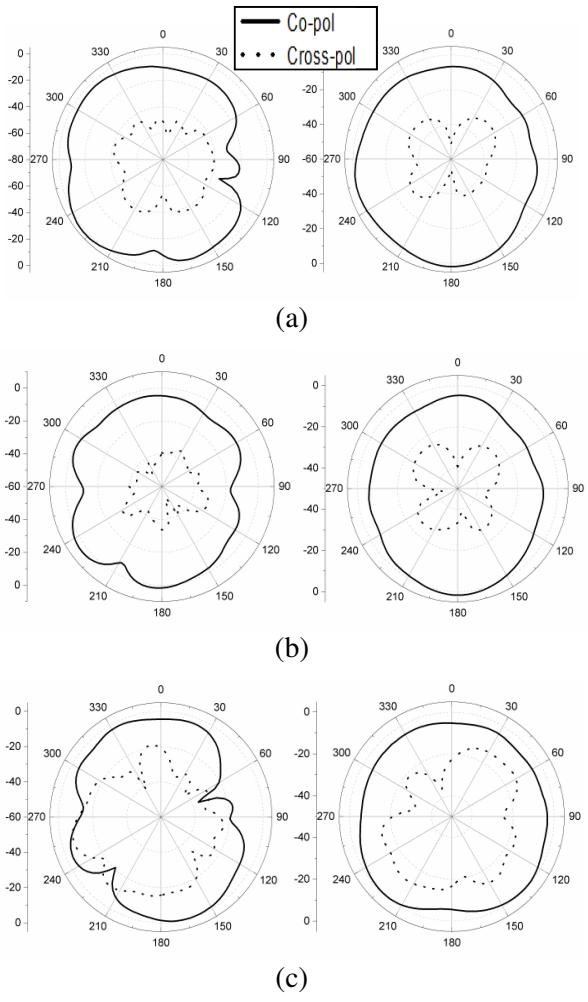

Fig. 13. Measured radiation patterns of the proposed antenna; (a) 2.44 GHz, (b) 3.5 GHz, and (c) 5.5 GHz.

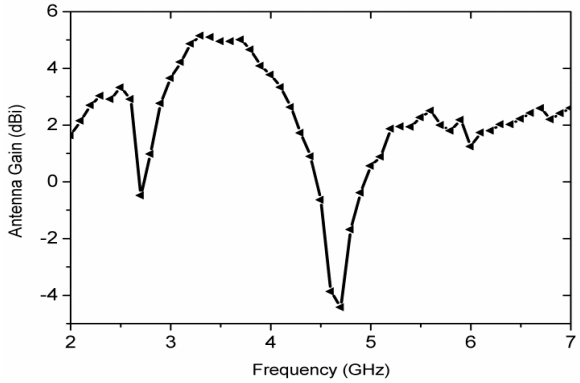

Fig. 14. Measured peak gain of the proposed antenna.

IV. CONCLUSION

A compact triple band antenna in simple structure for WLAN/WiMAX is proposed. This antenna consists of a regular microstrip-fed rectangle printed monopole antenna and a rectangle ground plane without slots. By embedding complementary split ring in the radiation element for band-rejected design, which does not increase the dimensions of the initial antenna, the triple band antenna is obtained. The measured results show that the impedance bandwidths range from 2.39 GHz – 2.48 GHz, 3 GHz – 3.7 GHz, and 5 GHz – 7 GHz, good performance for the WLAN (2.4/5.2/5.8) and WiMAX (3.5/5.5) bands. In addition, the proposed antenna has good radiation patterns and gains in the three operating bands. So this simple structure antenna is excellent candidate for wireless communications.

ACKNOWLEDGMENT

This work was supported by the National Natural Science Foundation of China (No.61172115 and No.60872029), the High-Tech Research and Development Program of China (No.2008AA01Z206), the Aeronautics Foundation of China (No.20100180003), and the Fundamental Research Funds for the Central Universities (No.ZYGX2009J037).

REFERENCES

[1] Y.-C. Chen, et al., "A compact triple-band planar monopole antenna for WLAN and WiMAX applications," *Antenna Technology (IWAT), International Workshop*, pp. 311-314, 2013.

[2] J. Y. Jan and L. C. Tseng, "Small planar monopole antenna with a shorted parasitic inverted-L wire for wireless communications in the 2.4-, 5.2-, and 5.8-GHz bands," *IEEE Trans. Antennas Propag.*, vol. 52, pp. 1903-1905, 2004.

[3] C. Y. Pan, C. H. Huang, and T. S. Horng, "Printed crisscross monopole antenna with a square con ductor-backed parasitic plane for dual-band WLAN applications," *Microw. Opt. Technol. Lett.*, vol. 46, pp. 541-543, 2005.

[4] A. A. Ibrahim, A. E. Safwat, and H. El-Hennawy, "Triple-band microstrip-fed monopole antenna loaded with CRLH unit cell," *IEEE Antennas Wirel. Propag. Lett.*, vol. 10, pp. 1547-1550, 2011.

[5] D. L. Jin, J. S. Hong, and H. Xiong, "Dual wideband antenna for WLAN/WiMAX and satellite system applications based on a metamaterial transmission line," *Chin. Phys. Lett.*, vol. 29, no. 10, pp. 104101-104101-3, Oct. 2012.

[6] K. L. Sheeja, P. K. Sahu, S. K. Behera, and N. Dakhli, "Compact tri-band metamaterial antenna for wireless applications," *Applied Computational Electromagnetics Society (ACES) Journal*, vol. 27, pp. 947-955, 2009.

[7] A. Almutairi, N. A. Aljuhaishi, and S. F. Mahmoud, "New compact and broadband patch antenna configurations for wireless applications," *Applied Computational Electromagnetics Society (ACES) Journal*, vol. 24, pp. 437-445, 2009.

[8] X. Li, Y. F. Wang, X. W. Shi, W. Hu, and L. Chen, "Compact triple-band antenna with rectangular ring for WLAN and WiMAX applications," *Microw. Opt. Technol. Lett.*, vol. 54, pp. 286-289, 2012.

[9] D. D. Krishna, M. Gopikrishna, and C. K. Aanandan, "A CPW-fed triple band monopole antenna for WiMAX/WLAN applications," *Microwave Conference, EuMC 38th European*, pp. 897-900, 2008.

[10] M. C. Tang, S. Xiao, T. Deng, D. Wang, J. Guan, B. Wang, and G. D. Ge, "Compact UWB antenna with multiple band-notches for WiMAX and WLAN," *IEEE Trans. Antennas Propag.*, vol. 59, pp. 1372-1376, 2011.

[11] Y. L. Kuo and K. L. Wong, "Printed double-T monopole antenna for 2.4/5.2 GHz dual-band WLAN operations," *IEEE Trans. Antennas Propag.*, vol. 51, no. 9, pp. 2187-2192, 2003.

[12] K. G. Thomas and M. Sreenivasan, "Compact triple band antenna for WLAN/WiMAX applications," *Electron. Lett.*, vol. 45, pp. 811-812, 2009.

[13] L. Bing, J. S. Hong, and B. Z. Wang, "A novel circular disc monopole antenna for dual-band WLAN applications," *Applied Computational Electromagnetics Society(ACES) Journal*, vol. 27, pp. 41-448, 2012.

[14] P. Wang, G. J. Wen, and Y. J. Huang, "Compact CPW-fed planar monopole antenna with triple-band operation for WLAN/WiMAX applications," *Applied Computational Electromagnetics Society (ACES) Journal*, vol. 27, pp. 691-696, 2012.

[15] C. N. Chiu and H. R. Chen, "A compact and wideband balance-fed triangular-monopole antenna for DCS/PCS/UMTS/WLAN/WiMAX applications," *Microw. Opt. Technol. Lett.*, vol. 50, pp. 971-974, 2008.

[16] J. H. Lu and H. M. Chin, "Planar compact U-shaped patch antenna with high-gain operation for Wi-Fi/WiMAX application," *Applied Computational Electromagnetics Society (ACES) Journal*, vol. 26, pp. 82-86, 2011.

[17] J. Y. Sze, C. I. G. Hsu, and J. J. Jiao, "CPW-fed circular slot antenna with slit back-patch for 2.4/5 GHz dual-band operation," *Electron. Lett.*, vol. 42, pp. 563-564, 2006.

[18] R. L. Li, T. Wu, and M. M. Tentzeris, "A triple-band unidirectional coplanar antenna for 2.4/3.5/5-GHz WLAN/WiMax applications," *IEEE International Symposium on Antennas & Propagation & USNC/URSI National Radio Science Meeting*, USA, June, 2009.

[19] S. Chaimool and K. L. Chung, "CPW-fed mirrored-L monopole antenna with distinct triple bands for WiFi and WiMAX applications," *Electron. Lett.*, vol. 45, pp. 928-U17, 2009.

[20] W. J. Lui, C. H. Cheng, and H. B. Zhu, "Improved frequency notched ultrawideband slot antenna using square ring resonator," *IEEE Trans. Antennas Propag.*, vol. 55, pp. 2445-2450, 2007.

[21] J. H. Jung, W. Choi, and J. Choi, "A small wideband microstrip-fed monopole antenna," *IEEE Microw. Component Lett.*, vol. 15, 10, pp. 703-705, 2005.

[22] S. W. Su, K. L. Wong, and C. L. Tang, "Ultra-wideband square planar monopole antenna for ieee 802.16a operation in the 2-11-GHz band," *Microw. Opt. Technol. Lett.*, vol. 42, pp. 463-466, 2004.

[23] W. Jiang and W. Che, "A novel UWB antenna with dual notched bands for WiMAX and WLAN applications," *IEEE Antennas Wirel. Propag. Lett.*, vol. 11, pp. 293-296, 2012.

Da-lin Jin was born in Sichuan, China. She received her B.S. degree in Electronics Information Science and Technology from Chengdu University of Information Technology in 2010. She is a graduate student major in Radio Physics in the University of Electronic Science and Technology of China now.

Her research interests include left-handed metamaterials technology and the applications of antenna with metamaterials.

Ting-ting Bu was born in Guizhou, China. She received her B.S. degree in University of Electronic Science and Technology of China in 2008. She is a master in Electronics and Communications Engineering of the University of Electronic Science and Technology of China now. Her research interests is antenna technology.

Jing-song Hong received the B.Sc. degree in electromagnetics from Lanzhou University, China, in 1991, and the M.Sc. and Ph. D. degrees in electrical engineering from the University of Electronic Science and Technology of China (UESTC), in 2000 and 2005, respectively. He is now a professor with UESTC. From 1991 to 1993, he was a Circuit Designer with the Jingjiang Radar Factory, Chengdu, China. From 1993 to 1997, he was a Testing Engineer with SAE Magnetics (HK) Ltd, Guangdong, China. From 1999 to 2002, he was a Research Assistant with the City University of Hong Kong. His research interest includes the use of numerical techniques in electromagnetics and the use of microwave methods for materials characterization and processing.

Full Band MIMO Monopole Antenna for LTE Systems

P. Zibadoost [1], J. Nourinia [1], C. Ghobadi [1], S. Mohammadi [1], A. Mousazadeh [2], and B. Mohammadi [3]

[1] Department of Electrical Engineering, Urmia University, Urmia, 57153, Iran
payam.zibadoost@yahoo.com, j.nourinia@urmia.ac.ir, ch.ghobadi@urmia.ac.ir,sma364@yahoo.com

[2] Department of Engineering, Science and Research branch,
Islamic Azad University, Tehran, 14778-93855, Iran,
asgar.musazadeh@yahoo.com

[3] Young Researchers and Elites club, Sanandaj Branch,
Islamic Azad University, Sanandaj, Iran
b.mohammadi@urmia.ac.ir

***Abstract*—** A novel printed planar monopole antenna for LTE multi-input and multi-output (MIMO) application is proposed. By adding six ellipticals on top of the antenna, we enhance the lower frequency bandwidth. The idea for this is gotten from [1, 2]. These papers designed by using log periodic technique with the number of rectangle and flare elements . Also, by cutting E-shaped slots in the ground plane, additional resonance is excited, and hence much wider impedance bandwidth can be produced. The proposed antenna provides all of the LTE bands between 0.65 GHz to 4 GHz. In order to provide low mutual coupling and envelope correlation, two of the antennas are combined with orthogonal polarizations. The mutual coupling and envelope correlation coefficient (ECC) of the antenna are lower than -21 dB and 0.002 across the operation bands, and total active reflection coefficient (TARC) is less than 0.35. The designed antenna has small size area of 55 × 94 mm^2, which has a small size with respect to recently reported antennas.

Index Terms - Long term evolution (LTE), multi-input and multi-output (MIMO), monopole antenna, and mutual coupling.

I. INTRODUCTION

Nowadays, there is an increased interest in research on multi-input and multi-output (MIMO) systems in the wireless communication. This technology is probably the most established to truly reach the promised transfer data rates of 4G communication [3]. To be more precise, the fourth mobile-phone generation is set to be the long term evolution (LTE) and is scheduled to operate in different bands from 400 MHz to 4 GHz [4]. This antenna has the ability to increase the capacity of channel using the spatial properties of multipath. It is necessary to have a number of uncorrelated antennas at each end of the communication link. So it seems to be very essential to design adequate antenna due to use in MIMO systems. As revealed in many literatures [5-12], both of non-printed MIMO antennas such as planar-inverted F antennas (PIFAs) and printed MIMO antennas are proposed. However, among the antennas which are used for MIMO application, printed antennas are more appropriate due to their low cost, easy fabrication, and their capability of easily being integrated to small terminal devices.

A number of planar monopoles to improve the impedance bandwidth have been investigated [13-15]. Moreover, in [15] fractal monopole antenna using the Sierpinski carpet geometry is described that caused to wideband, broadband, and multiband antenna. In this paper a novel multiband

Submitted On: April 8, 2013
Accepted On: Feb. 2, 2014

printed planar monopole antenna for LTE MIMO application is presented. First by adding six ellipticals on top of the antenna, the bandwidth in lower frequency is improved. In the proposed structure, by cutting a pair of E-shaped slots in the ground plane, additional resonance is provided. As a result, the designed antenna covers all of the LTE bands. Two elements of such antennas are used for MIMO applications. The size of the proposed antenna is smaller than the antennas reported recently [5, 6]. The proposed structure obtains low mutual coupling and envelope correlation due to the orthogonal polarization. Also, good return loss and radiation pattern characteristics are obtained in the frequency band of interest. Simulated and measured results are presented to validate the usefulness of the proposed antenna structure for LTE systems.

II. ANTENNA DESIGN

The base structure of the proposed MIMO antenna is shown in Fig. 1, which is printed on an FR4 substrate with relative permittivity 4.4 and thickness of 1.6 mm. The monopole is rectangular with width 2 mm and length 54 mm. The antenna is fed by a microstrip line with width 2 mm to match 50 Ω SMA connector for signal transmission. The antenna has two layers, the top layer and the bottom layer. On the top layer there is monopole antenna with 6 elliptical elements. On the bottom layer there are grounds with E-shape slots. The geometrical parameters of ellipticals described in Fig. 2 and Table 1. The two identical antenna elements have the same structures and dimensions. The two antenna elements are spaced with a gap "Gap1".

Figure 1 shows that this kind of monopole antenna covers a little frequency band. However, only the monopole antenna cannot cover more LTE bands. Then 6 ellipticals and E-shaped slots are added. As illustrated in Fig. 2, 6 ellipticals are used to control the impedance bandwidth and return loss level by modifying the capacitance between the patch and ground plane in a lower frequency bandwidth. To further enhance the matching, we use a pair of E-shaped slots in the antenna's ground plane. These slots create an additional path for the surface current, which produce an additional resonance, and as a result, increase the bandwidth. The optimal dimensions of the designed antenna are specified in Fig. 3 and Table 1.

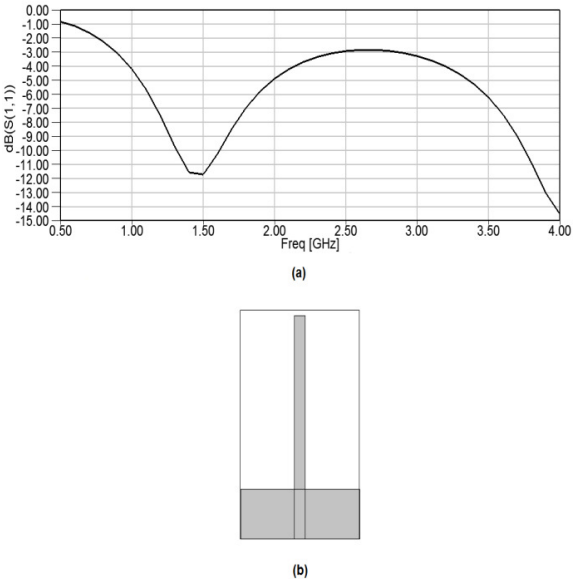

Fig. 1. (a) S(1,1) and (b) the base structure of the antenna.

In addition to the traditional antenna parameters, such as radiation pattern, and reflection coefficients, new parameters and aspects have to be included in the design for MIMO systems. MIMO coupling between antenna elements is a key factor to achieve high antenna performance in the MIMO antenna configuration. For a low mutual coupling, antennas must be far away from each other, but the space for the internal antenna is not enough to obtain low correlation and mutual coupling. In this paper we present a structure for the MIMO antenna elements in which the identical two antenna elements are orthogonally placed. As a result, the two antenna elements have orthogonal polarization, which can reduce the mutual coupling between the two antennas. Figure 4 shows the simulated 3D radiation patterns of the two antenna elements. It can be seen that the two antenna elements have orthogonal polarizations.

III. RESULTS AND DISCUSSION

In this section, the MIMO monopole antenna with various design parameters was constructed, and the experimental results are presented and discussed. The parameters of this proposed

antenna are studied by changing one parameter at a time and fixing the others. The simulated results are obtained using the Ansoft simulation software High Frequency Structure Simulator (HFSS) and measured in an anechoic chamber. For understanding well the operation of the proposed MIMO antenna, first we studied a single monopole antenna, because the MIMO structure consists of two identical antenna with orthogonal polarizations. Then we studied the MIMO antenna characteristics.

Tabel 1: The geometrical parameters of the elliptics (cw = clockwise and ccw = counter clock wise).

	Major Radius	Ratio	Center of elliptic	Degree of rotation to x-axis
Ellip-1	**14**	**0.6**	**(20.86,32.43)**	**15(ccw)**
Ellip-2	**14**	**0.6**	**(9.14,32.43)**	**15(cw)**
Ellip-3	**10**	**0.8**	**(8.55,43.62)**	**15(ccw)**
Ellip-4	**10**	**0.8**	**(21.45,43.62)**	**15(cw)**
Ellip-5	**8**	**0.1**	**(26.64,20.52)**	**15(ccw)**
Ellip-6	**8**	**0.1**	**(3.36,20.52)**	**15(cw)**

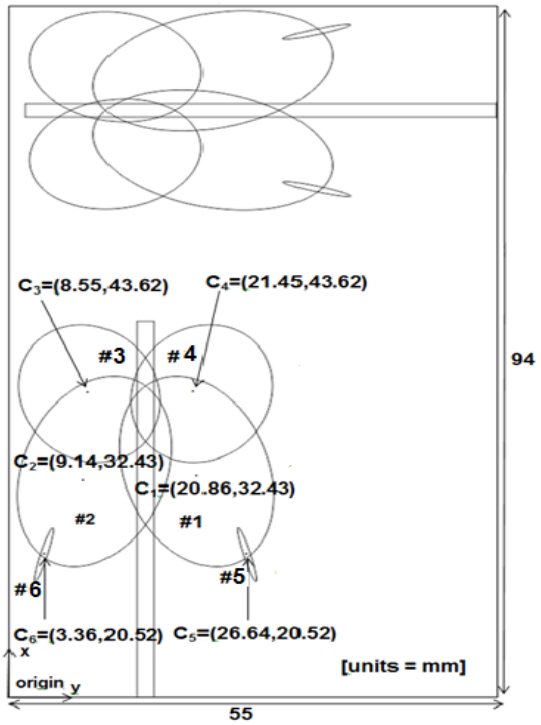

Fig. 2. The top view of the proposed antenna.

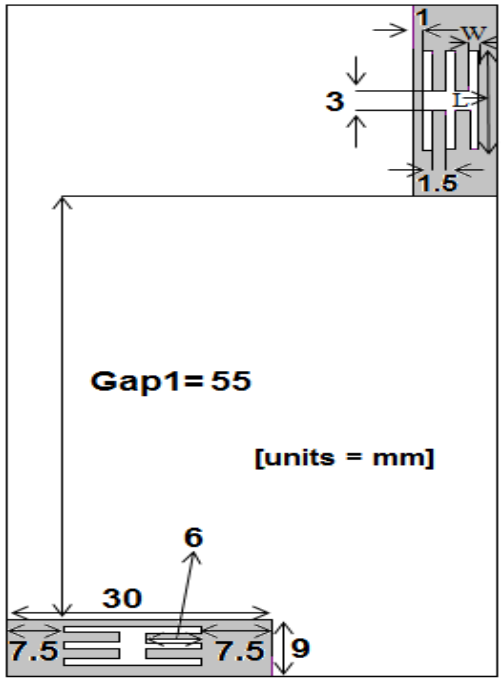

Fig. 3. The bottom view of the proposed antenna.

To design a novel antenna, and also in order to increase the frequency bandwidth, simple monopole is loaded with 6 ellipticals as displayed in Fig. 2. These ellipticals play important role inimpedance matching of this antenna because they can control the electromagnetic coupling effects between the patch and the ground plane and improve the band width. Figure 5 shows the structure of various antennas used for performance simulation studies. Return loss characteristics for simple monopole [Fig. 5 (a)], simple monopole with 2, 4, and 6 ellipticals [Fig. 5 (b)- (c)- (d)], and with two E-shaped slots in the ground plane [Fig. 5 (e)] are compared in Fig. 6. As shown in Fig. 6, in order to generate a new resonance (3.4 GHz), we use a pair of E-shaped slots in the center of the ground plane.

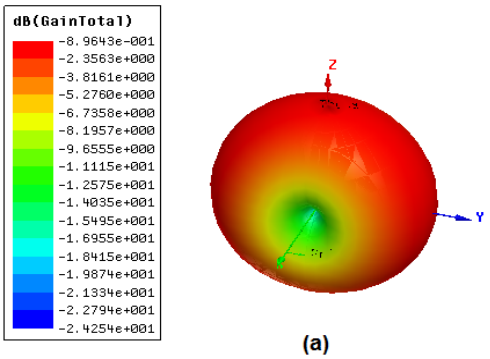

(a)

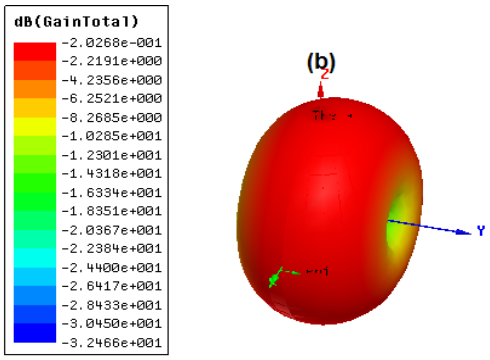

Fig. 4. 3D radiation patterns of two antenna elements.

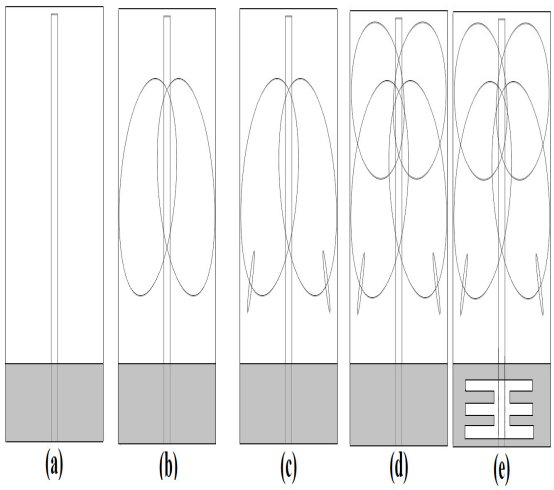

Fig. 5. (a) Basic structure, (b) with 2 elliptics, (c) with 4 elliptics, (d) with 6 elliptics, and (e) with 6 elliptics and E-shaped slots.

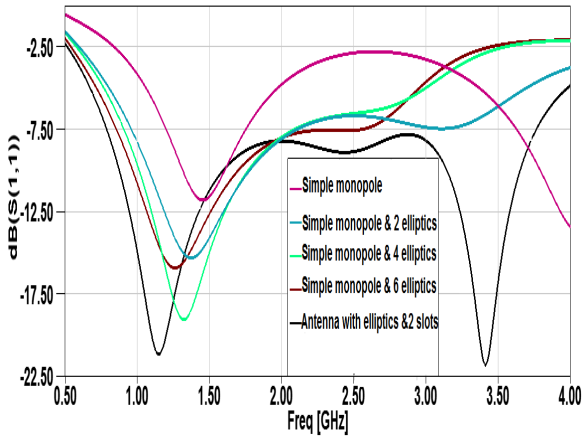

Fig. 6. Simulated return loss for basic structure without and with elliptics and E-shaped slots.

To understand the effects of these slots, the simulated current distribution on the radiating patch and ground plane is presented in Fig. 7 (a). It can be observed from Fig. 7 (a) that the current is concentrated on the edges of the interior and exterior of the E-shaped slots at 3.4 GHz. Therefore, the antenna impedance changes at this frequency due to the resonant properties of the E-shaped slots. Figure 7 (b) shows the effects of L and W on impedance matching and second resonance. After comparison the best case is selected.

A prototype of the proposed MIMO antenna as shown in Fig. 8 was constructed and tested. Figure 9 shows the simulated and measured return loss. The measured -6 dB S(1,1) and S(2,2) are not equal because the structure is not symmetrical. The mutual coupling between the two ports is less than -21 dB across the common bandwidth, as shown in Fig. 9 (c). As shown in Fig. 9, there exists a discrepancy between measured data and simulated results. This could be due to the effect of the SMA port. In order to confirm the accurate return loss characteristics for the designed antenna, it is recommended that the manufacturing and measurement process be performed carefully.

Figures 10 and 11 show the radiation patterns of antennas 1 and 2, respectively. Antenna 1 has an omnidirectional vertically polarized pattern in the x-z plane and antenna 2 generates horizontally polarized in the y-z plane. As shown in Figs. 10 and 11 the omnidirectional properties, particularly at low frequencies are not good. This is mostly due to the small ground plane effects and the change of excited surface current distributions on the system ground plane at low frequencies. The omni-directional patterns can enhance and increase the channel capacity [9]. In general, when two linearly polarized antenna are orthogonally located to each other, they can provide polarization diversity by reducing the mutual coupling between them. Therefore, these orthogonal radiation patterns and high isolation (> 21 dB) give the lower ECC (< 0.002), which is less than a recommended value [9] of 0.5, as shown in Fig. 12. The ECC is obtained by using the far field radiation patterns [10]. However, this process requires complex and advanced calculation. Assuming that an antenna operates in a uniform multipath environment, the correlation coefficient can be calculated by S-parameters [16],

$$ECC = \frac{|S_{11}^{*}S_{12} + S_{21}^{*}S_{22}|^2}{(1-|S_{11}|^2-|S_{21}|^2)(1-|S_{22}|^2-|S_{12}|^2)} \quad (1)$$

Array's total active reflection coefficient (TARC) for a two port antenna as described in [17], can be showed in Fig. 12. Thus the proposed antenna is more attractive for MIMO application. The isolation between two polarizations will increase by increasing the dimension of spacing Gap1. Figure 13 shows the effect of Gap1.

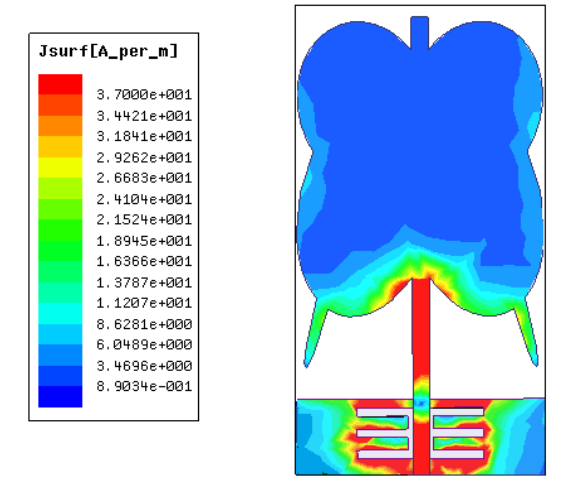

(a)

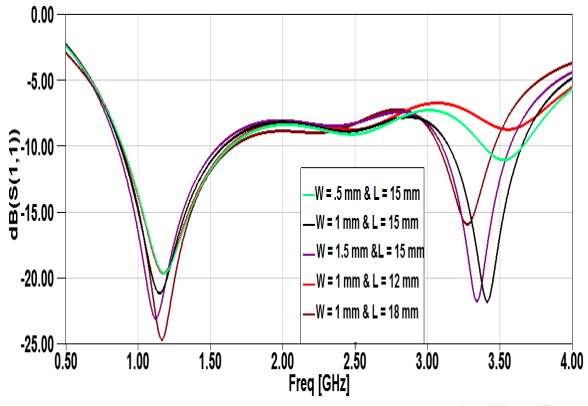

(b)

Fig. 7. (a) Simulated current distribution on the radiating patch and ground plane at 3.4 GHz and (b) simulated return loss characteristics of the antenna with different values of L and W.

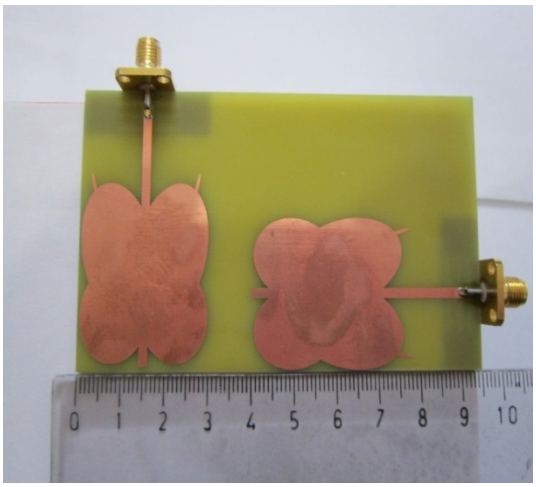

Fig. 8. Photograph of the constructed antenna.

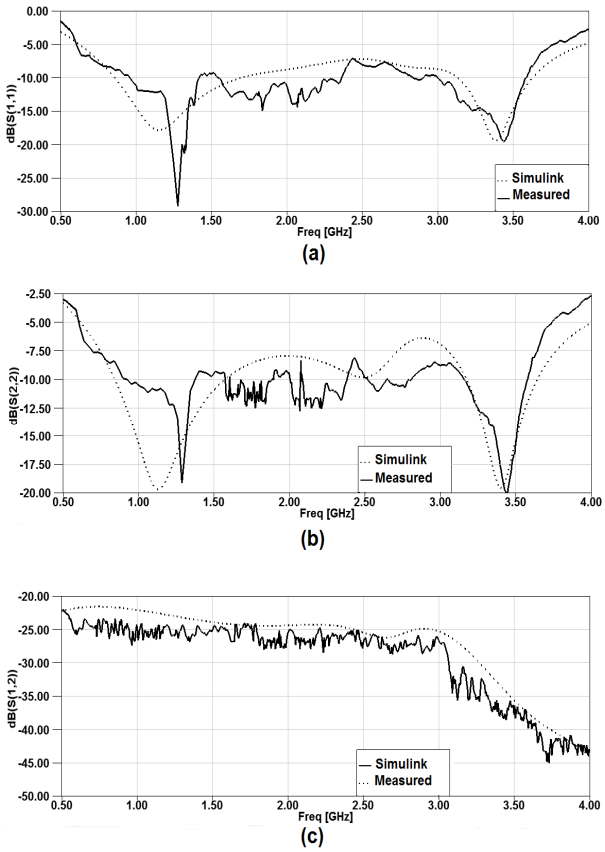

Fig. 9. Simulated and measured (a) S(1,1), (b) S(2,2), and (c) S(1,2) (when S(1,1) of one port is measured, the other port ended with 50 Ω load).

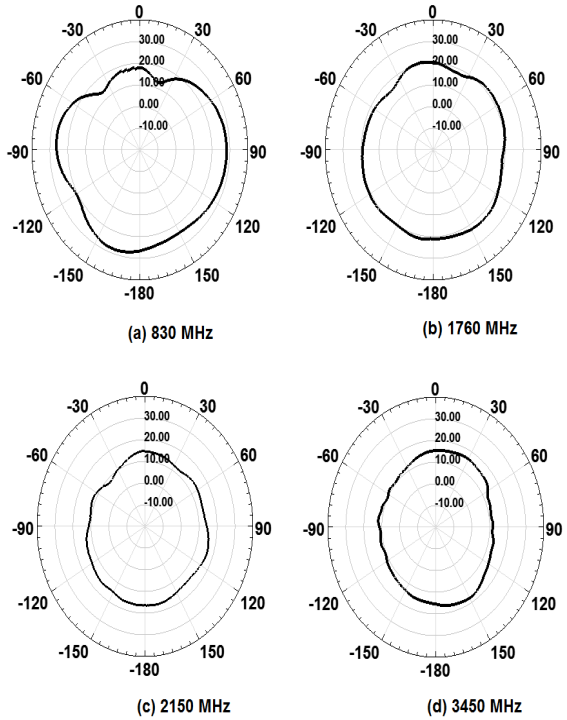

Fig. 10. Measured radiation patterns of antenna 1 in the x-z plane [unit : dB].

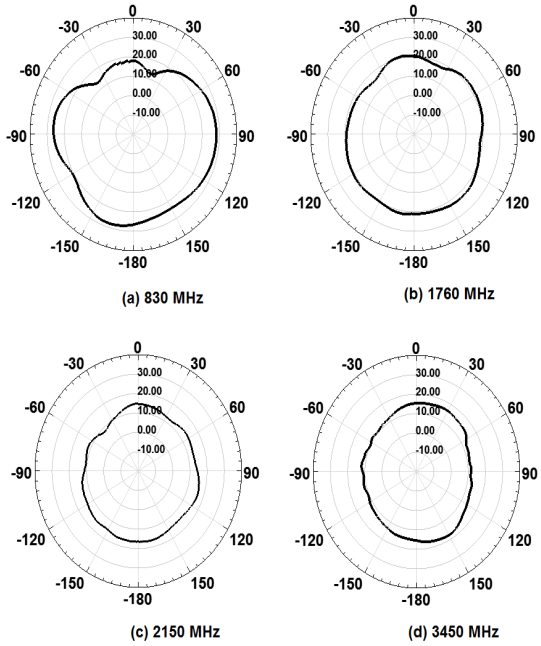

Fig. 11. Measured radiation patterns of antenna 2 in the y-z plane [unit : dB].

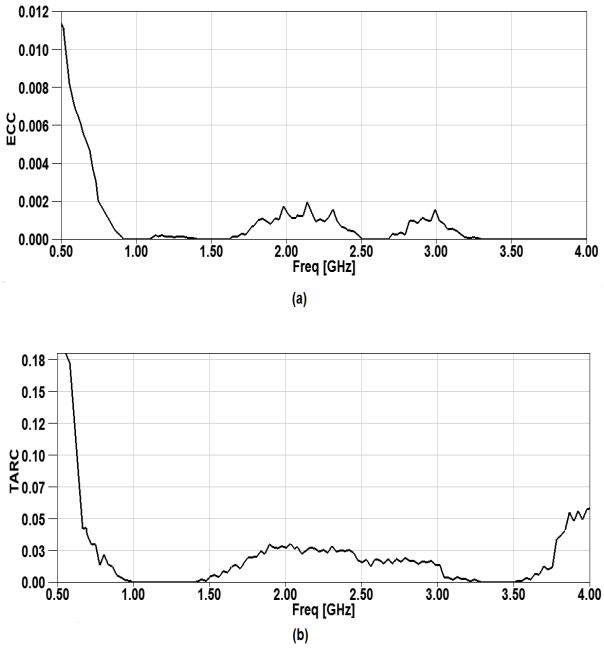

Fig. 12. (a) ECC and (b) TARC.

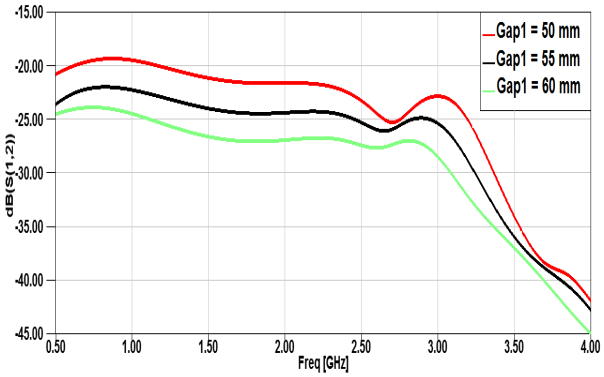

Fig. 13. Simulated S(1,2) with different value of Gap1.

IV. CONCLUSION

In this paper a novel planar monopole antenna for LTE MIMO system has been proposed and implemented. Simulated and measured results showed that the antenna can cover all of the LTE frequency bands. By adding 6 ellipticals, the lower frequency bandwidth is improved and by cutting two E-shaped slots in the ground plane, additional resonance are excited and hence wider impedance bandwidth can be produced. Good return loss and radiation pattern characteristics are obtained in the frequency band of interest. The antenna has high isolation (> 21). Moreover, low ECC and TARC is

achieved by a pattern diversity. The designed antenna has a small size. Simulated and measured results show that the proposed antenna will provide better propagation channel and enhance the capacity of MIMO antenna for LTE applications.

REFERENCES

[1] E. Vila-Navarro, J. M. Blanes, J. A. Carrasco, C. Reig, and E. A. Navarro, "A new bi-faced log periodic printed antenna," *Microwave and Optical Technology Letters*, vol. 48, no. 2, pp. 402-405, Feb. 2006.

[2] M. A. Karim, M. A. Rahim, and T. Masri, "Fractal Koch dipole antenna for uhf band application," *Microwave and Optical Technology Letters*, vol. 51, no. 11, pp. 2612 - 2614, Nov. 2009.

[3] Y. Yu, G. Kim, W. Seong, and J. Choi,"A MIMO antenna with a two stage ground for USB dongle," *Microwave and Optical Technology Letters*, vol. 53, no. 2, pp. 418-422, Feb. 2011.

[4] R. Bhatti, S. Yi, and S. Park, "Compact antenna array with port decoupling for LTE-Standardized Mobile Phones," *IEEE Antennas and Wireless Propagation Letters*, vol. 8, pp. 1430-1433, 2009.

[5] Y. Yao, X. Wang, and J. Yu, "Multiband planar monopole antenna for LTE MIMO systems," *International Journal of Antennas and Propagation*, Article ID 890705, 6 pages, 2012.

[6] S. H. Lee, C. Y. Yang, and W. G. Yang, "High isolation MIMO antenna design by using ground slits for mobile handset," *Proc. PIERS*, August, 2012.

[7] A. R. Mallahzadeh, S. F. Seyyedrezaei, N. Ghahvehchian, S. Nezhad, and S. Mallahzadeh, "Tri-band printed monopole antenna for WLAN and WiMAX MIMO systems," *in Proceedings of the 5th European Conference on Antennas and Propagation (EUCAP)*, pp. 548-551, April 2011.

[8] H. T. Chattha, Y. Huang, X. Zhu, and Y. Lu, "Dual-feed PIFA diversity antenna for wireless applications," *Electronics Letters*, vol. 46, no. 3, pp. 189-190, 2010.

[9] Q. Luo, J. R. Pereira, and H. M. Salgado, "Reconfigurable dualband C-shaped monopole antenna array with high isolation," *Electronics Letters*, vol. 46, no. 13, pp. 888-889, 2010.

[10] Y. Li, Z. Zhang, W. Chen, Z. Feng, and M. F. Iskander, "A dual polarization slot antenna using a compact CPW feeding structure," *IEEE Antennas and Wireless Propagation Letters*, vol. 9, pp. 191-194, 2010.

[11] S. M. Nezhad and H. R. Hassani, "A novel triband E-shaped printed monopole antenna for MIMO application," *IEEE Antennas and Wireless Propagation Letters*, vol. 9, pp. 576-579, 2010.

[12] J. Zhu, M. A. Antoniades, and G. V. Eleftheriades, "A compact tri-band monopole antenna with single-cell metamaterial loading," *IEEE Trans. Antennas Propag.*, vol. 58, no. 4, pp. 1031-1038, 2010.

[13] N. Ojaroudi, M. Ojaroudi, and Sh. Amiri, "Enhanced bandwidth of small square monopole antenna by using inverted U-shaped slot and conductor-backed plane," *Applied Computational Electromagnetics Society (ACES) Journal*, vol. 27, no. 8, pp. 685-690, August 2012.

[14] S. Zainud-Deen, R. Al-Essa, S. Ibrahem, "Overlapped printed monopole antennas for ultra wideband applications," *26th Annual Review of Progress in Applied Computational Electromagnetics (ACES),* pp. 607-611, Tampere, Finland, April 2010.

[15] M. Naghshvarian-Jahromi and, N. Komjani-Barchloui, "Analysis of the behavior of Sierpinski carpet monopole antenna," *Applied Computational Electromagnetics Society (ACES) Journal*, vol. 24, no. 1, pp. 32-36, February 2009.

[16] S. Blanch, J. Romeu, and I. Corbella, "Exact representation of antenna system diversity performance from input parameter description," *Electron. Lett.*, vol. 39, pp. 705-707, May 2003.

[17] R. G. Vaughan and J. B. Andersen, "Antenna diversity in mobile communication," *IEEE Transactions on Vehicular Technology.*, vol. 36, no. 4, pp. 149-172, 1987.

Payam Zibadoost was born, in Khoy, Iran in 1985. He received his B.Sc. degree in Electrical Engineering (Telecommunication) from Urmia University Urmia, Iran, in 2009 and now he is a M.Sc. student of Electrical Engineering (Telecommunication) in this university. His primary research interests are in MIMO antenna design, and microwave components.

Javad Nourinia received his B.Sc. in Electrical and Electronic Engineering from Shiraz University and M.Sc. degree in Electrical and Telecommunication Engineering from Iran University of Science and Technology, and Ph.D. degree in Electrical and Telecommunication from University of Science and Technology, Tehran Iran in 2000. From 2000 he was an

Assistant Professor and now he is a Professor in the Department of Electrical Engineering of Urmia University, Urmia, Iran. His primary research interests are in antenna design, numerical methods in electromagnetic, microwave circuits.

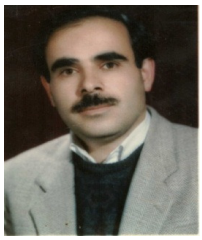

Changiz Ghobadi was born in June, 1960 in Iran. He received his B.Sc. in Electrical Engineering-Electronics and M.Sc. degrees in Electrical Engineering-Telecommunication from Isfahan University of Technology, Isfahan, Iran and Ph.D. degree in Electrical-Telecommunication from University of Bath, Bath, UK in 1998. From 1998 he was an Assistant Professor and now he is a Professor in the Department of Electrical Engineering of Urmia University, Urmia, Iran. His primary research interests are in antenna design, radar and adaptive filters.

Saeid Mohammadi was born in Urmia, Iran 1984. He received his B.Sc. and M.Sc. degrees in Electrical Engineering (Telecommunication) from Urmia University Urmia, Iran in 2008 and 2010, respectively. His primary research interests are in antenna design, numerical methods in electromagnetic, microwave components.

Asghar Mousazadeh was born in Naghadeh, Iran in 1985. He received his B.Sc. degree in Electrical Engineering (Telecommunication) from Urmia University, Urmia, Iran, in 2010 and M.Sc. degree in Electrical Engineering (Telecommunication) from Islamic Azad University, Science and Research Branch, Tehran, Iran, in 2012. His primary research interests are in antenna design, and microwave components.

Bahman Mohammadi was born in Divandareh, Iran 1989. He received the B.Sc. degree in Electrical Engineering from Tabriz University, Tabriz, Iran, in 2011, where he is currently working toward the M.Sc. degree in Electrical Engineering from Urmia University, Urmia, Iran. His research interests include electromagnetic computationand wideband passive microwave devices (couplers, filters, phase shifters, etc.).

Triangular-Arranged Planar Multiple-Antenna for UWB-MIMO Applications

X.-S. Yang, S.-G. Qiu, and J.-L. Li

School of Physical Electronics
University of Electronic Science and Technology of China, 610054, Chengdu, China
xsyang@uestc.edu.cn

Abstract ─ A triangular-arranged (TA) planar multiple-antenna is proposed. It consists of three ultra-wideband (UWB) planar monopole antenna elements, with the centers and the ports of the elements arranged at the vertexes of two regular triangles, thus the polarization of each element is 120° different. The performance of the TA multiple-antenna is investigated by simulation and measurement, and the measured results agree with the simulated ones in reasonable precision. Within the ultra-wide bandwidth of 3.4 GHz – 12 GHz, the return loss at each port is better than 10 dB, and the isolation between any two ports is higher than 20 dB. Furthermore, good omni-directional radiation pattern is obtained over the interesting frequency band. A linear-arranged (LA) three-element multiple-antenna is compared with the proposed TA antenna. Comparison between the TA antenna and the LA antenna validates the advantages of the proposed one, which consequently is suitable for UWB-MIMO applications.

Index Terms – Antennas, isolation, multiple-input multiple-output (MIMO), and ultra-wideband (UWB).

I. INTRODUCTION

Due to the large bandwidth, ultra-wideband (UWB) possesses a lot of advantages, such as enabling high data rates transmission, providing high reliability for the wireless communications. It has become a hot topic in wireless communication fields over the past decade. Moreover, the advantages of UWB can be further improved by combining multiple-antenna techniques. Multiple-input multiple-output (MIMO) systems, which have multiple-antenna units at both transmitter and receiver sides, can take advantage of the multipath components sufficiently to enhance the performance of wireless systems. Consequently, UWB combined with MIMO technique (UWB-MIMO) is a feasible method to achieve extremely high data rates and high robustness for wireless communication systems [1]. Besides, UWB-MIMO is suitable for obtaining high-precision localization and radar imaging.

As a key component of UWB system, UWB antenna has attracted a lot of research interests in both the academic and industrial fields [2-3]. For some applications, directional antennas, which radiate energy in a fixed direction, are requisite. However, the antennas with omni-directional radiation characteristics are usually more attractive. This is due to the particular requirements of UWB, especially the limits on equivalent isotropically radiated power (EIRP) imposed by many spectrum regulators, as well as the need of some applications, such as ranging and radar, which have signals arrive from any unpredictable direction. As a result, ultra-wide pattern bandwidth becomes an important design requirement for UWB antennas, i.e., the radiation pattern remains approximately omni-directional over the ultra-wide bandwidth. However, many existing UWB antennas have ultra-wide impedance bandwidth, but not pattern bandwidth.

For an UWB-MIMO system, not only the characteristics of the antenna elements, but also the mutual coupling between elements, will affect the performance of the system. The mutual coupling, which exists between any closed antenna elements, will deteriorate the pattern characteristic

Submitted On: Oct. 30, 2012
Accepted On: Jan. 27, 2014

and is a very important factor when designing an UWB-MIMO antenna system. In order to improve the isolation between UWB antenna elements, some researches have been performed. For example, closed radiators are arranged orthogonally, thus the neighboring elements are orthogonally polarized [4], which will decrease the mutual coupling remarkable. Besides, elements with different dielectrics or with different radiation characteristics are put together to form a multiple-antenna, which also decrease the mutual coupling between elements [2, 5]. In some cases, structures with high isolation characteristics are placed between antenna elements, which are also helpful for the reduction of mutual coupling [6, 7]. Since the UWB-MIMO system is in the start stage, a lot of effort is needed to improve the performance of the antenna system.

In [3], a series of planar monopole antennas using genetic algorithm (GA), with the goal to achieve omni-directional pattern and uniform gain over the ultra-wide frequency band have been designed. In this paper, one of the optimized planar monopole antennas, i.e., antenna E in [3], is used to form a planar multiple-antenna. Antenna E in [3] has very good impedance matching performance and omni-directional radiation pattern over 2.6 GHz – 10.6 GHz bandwidth. Since the multiple-antenna structure has important influences on the performance of MIMO systems, such as fading correlation (and thus capacity) of a communication system, as well as ability to resolve directions of multipath components. Linear-arranged (LA) antenna are the simplest structure, we show that they have significant drawbacks, in particular related to mutual coupling between the antenna elements. We thus propose a triangular-arranged (TA) multiple-antenna, and analyze its performance.

The rest of the paper is organized as follows: in section II, the multiple-antenna structure is depicted. Section III describes the simulated and measured results of the TA antenna and the LA antenna. Section IV gives the conclusion.

II. ANTENNA STRUCTURE

The element of the proposed triangular-arranged (TA) multiple-antenna is an optimized planar monopole antenna with rounded-corner-rectangular ground plane, which is antenna E in [3]. The structure of the TA multiple-antenna is shown in Fig. 1. Three identical elements are printed on a hexagon substrate, with a thickness of 0.76 mm and dielectric permittivity of 2.94. The patches and microstrip feed lines are printed on the top side and the grounds are on the bottom side. The centers of the patches and the feed ports of the elements are arranged at the vertices of two regular triangles, thus the polarization of each element is 120° different. The distance between any two patch centers *d* is set to 40 mm, which is the free space half wavelength at 3.75 GHz. A prototype is fabricated and three SMA connectors are used to feed the antenna, as shown in Fig. 1 (b).

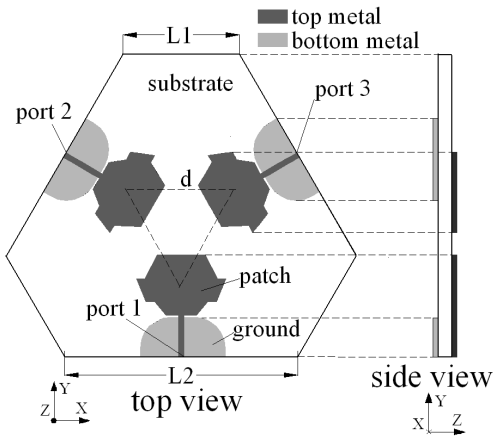

(a)

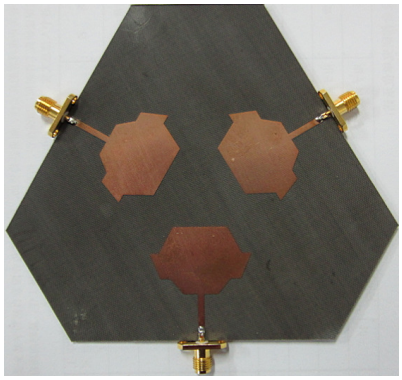

(b)

Fig. 1. The proposed triangular- arranged (TA) planar antenna; (a) schematic diagram, left: top view, right: side view; L_1=47 mm, L_2=76.9 mm, d=40 mm and (b) the fabricated antenna.

A linear-arranged (LA) planar multiple-antenna is designed and fabricated to compare with the TA antenna. The elements and the

substrate of the LA antenna are the same as that of the TA antenna. As shown in Fig. 2, three identical elements are aligned on a rectangular substrate. The distance between the adjacent elements centers is also 40 mm, the same as that of the TA antenna.

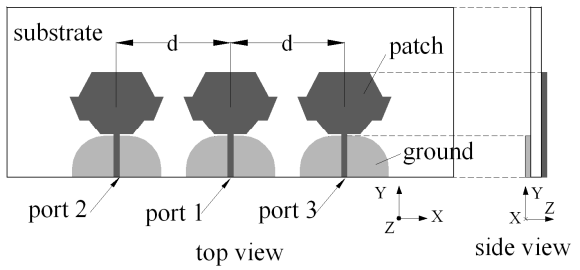

Fig. 2. Geometry of the linear-arranged (LA) antenna, d=40 mm; left: top view, right: side view.

III. SIMULATED AND MEASURED RESULTS

The characteristics of the two antennas are investigated by both simulation and measurement. The simulation is performed with the Ansoft's HFSS. The measurement of S-parameters is carried out by means of a vector network analyzer, Agilent 8363B, and that of the radiation pattern is implemented by a SATIMO near field antenna testing system.

The simulated and measured S-parameters of the two antennas are shown in Fig. 3. As shown in Fig. 3 (a), the $|S_{11}|$s of both TA and LA antennas are nearly below -10 dB within the bandwidth of 2.6 GHz – 12 GHz, which indicates good impedance matching performances. The $|S_{21}|$s of both TA and LA antennas are given in Fig. 3 (b). Within the bandwidth of 3.4 GHz – 12 GHz, the measured and simulated isolations of the TA antenna are higher than 20 dB, while those of the LA antenna are only higher than 14 dB. Obviously, the isolation of TA is better than that of LA, especially at the higher frequency. This characteristic is very appropriate for the UWB-MIMO communication system, which requires lower correlation between different antenna elements. The simulated and measured results agree with each other in reasonable precision.

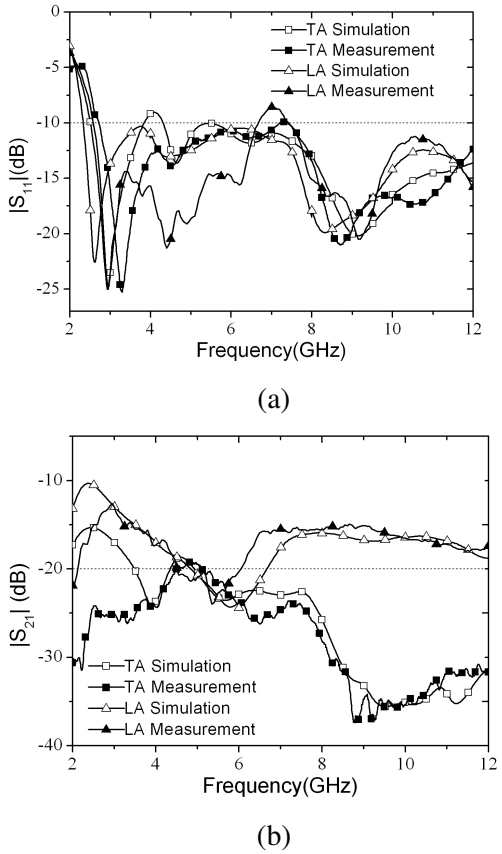

Fig. 3. Simulated and measured S-parameters of the TA and LA antennas, (a) $|S_{11}|$ and (b) $|S_{21}|$.

Figure 4 shows the simulated and measured radiation patterns of both TA and LA antennas at frequencies of 3.0 GHz, 5.5 GHz, and 9.5 GHz. The pattern is normalized with respect to the peak value of each case. In the simulation and measurement of radiation pattern, only one port (e.g., port 1) is excited while the other two ports are terminated with 50 Ω impedance loads. It can be seen that, in the H-plane, over the interesting bandwidth, the TA antenna has better omni-directional patterns than the LA antenna, even at higher frequency, which is very helpful for UWB applications. Simulated and measured results agree with each other in reasonable precision.

Besides, the simulated antenna gain is plotted, as shown in Fig. 5. It can be seen that the peak gain over the frequency band of 3 GHz – 10 GHz is stable, and the maximum fluctuation is about 3 dB.

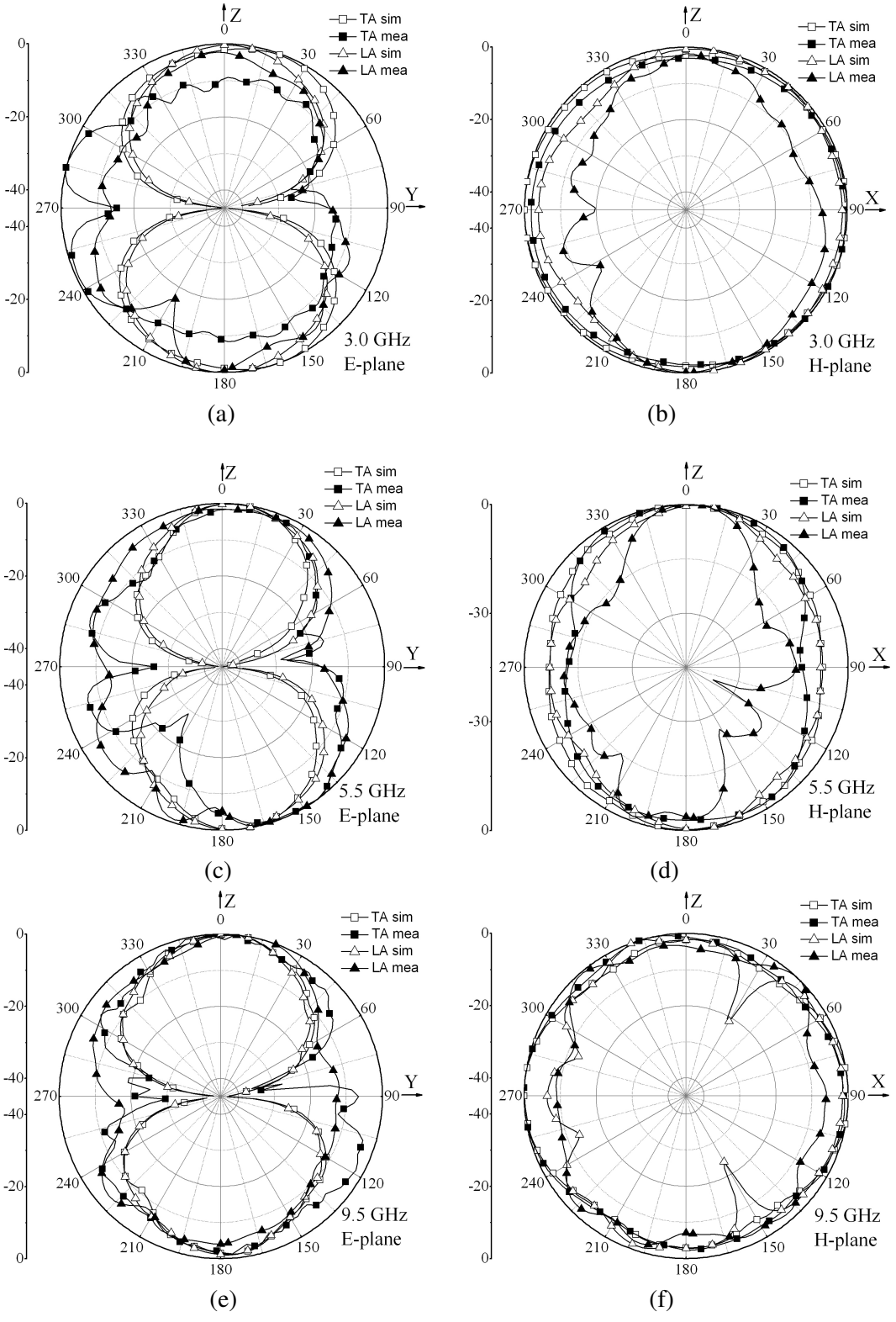

Fig. 4. Simulated and measured radiation patterns of the TA- and LA-arranged antennas at different frequencies, (a) 3.0 GHz, H-plane, (b) 3.0 GHz, E-plane, (c) 5.5 GHz, H-plane, (d) 5.5 GHz, E-plane, (e) 9.5 GHz, H-plane, and (f) 9.5 GHz, E-plane.

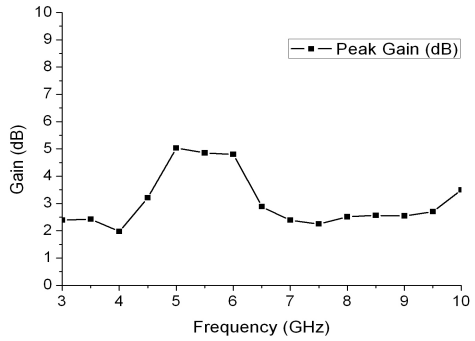

Fig. 5. Simulated peak gain of the TA-arranged antenna with one element active.

IV. CONCLUSION

A novel triangular-arranged (TA) three-element planar UWB multiple-antenna has been proposed for UWB-MIMO applications. The antenna has very good impedance and radiation characteristics over 3.4 GHz – 10.6 GHz frequency band. Compared to a linear-arranged (LA) planar multiple-antenna, the TA antenna has lower mutual coupling between different ports, especially at higher frequency, which results in better omni-directional pattern for each element. It is the excellent performance and the special arrangement of the elements, that makes the good performance of the propose TA antenna.

It is true that the TA antenna is a little larger than the LA antenna, which is an obvious weak point for the application in portable devices. However, it can be used in fixed UWB-MIMO wireless devices, and it provides a feasible choice for three-element multiple-antenna. For the portable UWB-MIMO devices, more compact structure must be adopted.

ACKNOWLEDGMENT

This work was supported by the Natural Science Foundation of China (61271027, 61331007).

REFERENCES

[1] T. Kaiser, Z. Feng, and E. Dimitrov, "An overview of ultra-wide-band systems with MIMO," *Proceedings of the IEEE*, vol. 97, no. 2, pp. 285-314, 2009.

[2] J. A. Park, H. K. Yoon, Y. J. Yoon, and C. H. Lee, "A compact polarization diversity antenna for UWB systems," *Asia-Pacific Microwave Conference*, pp. 1-4, 2008.

[3] X.-S. Yang, K. T. Ng, S. H. Yeung, and K. F. Man, "Jumping genes multi objective optimization scheme for planar monopole ultra wideband antenna," *IEEE Trans. Antennas Propagat.*, vol. 56, no. 12, pp. 3659-3666, 2008.

[4] G. Adamiuk, S. Beer, W. Wiesbeck, and T. Zwick, "Dual-orthogonal polarized antenna for UWB-IR technology," *IEEE Antennas and Wireless Propagat. Lett.*, vol. 8, pp. 981-984, 2009.

[5] A. I. Najam, Y. Duroc, and S. Tedjini, "Design and characterization of an antenna system for UWB-MIMO communications systems," *Proceedings of the Fourth European Conf. on Antennas and Propagat.* , pp. 1-5, 2010.

[6] S. Zhang, Z. Ying, J. Xiong, and S. He, "Ultrawideband MIMO/diversity antenna with a tree-like structure to enhance wideband isolation," *IEEE Antennas and Wireless Propagat. Lett.*, vol. 8, pp. 1279-1283, 2009.

[7] T. S. P. See and Z.-N. Chen, "An ultrawideband diversity antenna," *IEEE Trans. Antennas Propagat.*, vol. 57, no. 6, pp. 1597-1605, 2009.

Xue-Song Yang received the Ph.D. degree in Radio Physics from UESTC, Chengdu, China. She joined the UESTC in 2002, where she is currently an associate professor. She has been a research fellow at the City University of Hong Kong, a Visiting Scholar at the University of Southern California. Her current research interests include antennas and wireless channel modeling.

Shi-Gui Qiu received the M.Sc. degree in Radio Physics from UESTC, China, in 2012. He is currently an engineer at the Kuang-Chi Institute of Advanced Technology. His current research interests include antennas design and wireless communication.

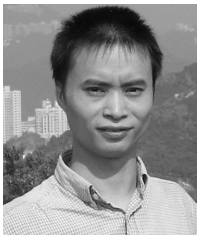

Jia-Lin Li received the Ph.D. degree in electronic engineering from the City University of Hong Kong, Hong Kong, in 2009. Since Sept. 2009, he has been with the School of Physical Electronics, UESTC, where he is currently a Professor. His research interests include the high performance active/passive microwave/millimeter-wave antennas, circuits and systems realized on PCB, multilayer PCB, LTCC, etc.

UWB Monopole Antenna with Compact Polygon-Shaped Patch for Portable Devices

T. Sedghi [1], V. Rafii [2], and M. Moosazadeh [1]

[1] Department of Electrical Engineering, Urmia Branch, Islamic Azad University, Urmia, Iran

[2] Young Researchers and Elite Club, Urmia Branch, Islamic Azad University, Urmia, Iran
sedghi.tohid@gmail.com, vhdrafiei@gmail.com

Abstract ─ In this paper, a small ultra wideband (UWB) antenna with co-planar waveguide (CPW) feed, consisting of a polygon-shaped design on the patch and a ground plane truncated with two mirror rectangular–shaped notches is designed for ultra wideband (UWB) applications. In this proposed antenna, through increasing the number of cuts inside the initial patch, a proper control on the upper frequency of the band can be achieved. The overall dimension of the antenna is 19×19 ×1 mm^3 and fed by 50 Ω coplanar waveguide. The proposed antenna is developed and its VSWR is compared with the simulated result. The proposed antenna operates in the adopted bandwidth (3.1 GHz-10.6 GHz) with VSWR < 2, and covers it very well from 3 GHz to 14.9 GHz, which provides fractional bandwidths of more than 132%. The effect of the ground plane notch on the optimization of the VSWR is discussed in detail.

Index Terms - CPW-fed, small monopole antenna, truncated ground plane, and ultra wideband (UWB) antenna.

I. INTRODUCTION

The requirement for high data rates wireless communication becomes more and more vital and various solutions have been recommended. With the rapid development of these wireless systems, the design of the UWB antennas has been given lots of concentration, since they are the key elements to radiate and receive the signals [1]. There have been great progresses in the design of ultra wideband antennas and devices in recent years. Several impedance variation techniques are applied to previous works such as [2-4], wide rectangular slots and circular slots with hexagonal forms [2]. One of the major challenges in the design of ultra wideband antennas is how to achieve small size antennas with low weight and desired radiation pattern characteristics and electrical properties in the band of interest [3]. The numerous number of slots causes to more bandwidth and the optimum feed structure gives the good impedance matching [4]. Recently, some coplanar waveguide (CPW)-fed printed monopole antenna have been reported [5-11].

In this letter the polygon-shaped form on the patch has been used for increasing impedance bandwidth and better impedance matching. By using this design and the numerous numbers of cuts inside the patch the impedance matching is increased. Proposed antenna is designed with a mirror of rectangular-shaped slots on the ground plane, so impedance matching is desirable due to both these slots. The antenna has outstanding properties such as small size, desirable VSWR level, simple structure, and good omni-directional radiation pattern.

II. MONOPOLE ANTENNA DESIGN

The geometry of the CPW-fed antenna is shown in Fig. 1. The antenna is constructed with a substrate made of FR4, with the thickness of 1 mm and the relative dielectric constant ε_r = 4.4. The CPW feed-line has a center width W_c =2.4 mm and a g_c = 0.3 mm for 50 Ω impedance. A polygon-shaped patch with the radius of R is connected to the rectangular – shaped patch with width of W_p. For the impedance matching, the

Submitted On: Dec. 27, 2012
Accepted On: Jan. 3, 2014

distance between the patch and the CPW- ground plane is indicated with a Gap = L_c - L. For increasing the upper frequency band, a pair of mirror rectangular-shaped notches is located on the ground plane. In most of the reported antennas so far, the slots on the patch are designed horizontally and vertically in the form of different geometric shapes. In this proposed antenna, for increasing the path of surface current, we use some cuts on the patch, which results in both the production of additional resonance and an increase in the bandwidth. The simulated results are obtained using the Ansoft simulation software high-frequency structure simulator (HFSS). The optimal parameters of the constructed antenna are as follows: W_{sub} = 19 mm, L_{sub} = 19 mm, R = 8 mm, NC = 10, W_p = 4 mm, L_c = 2.8 mm, g_c = 0.3 mm, W_c = 2.4 mm, L = 1 mm, and Gap = 0.4 mm.

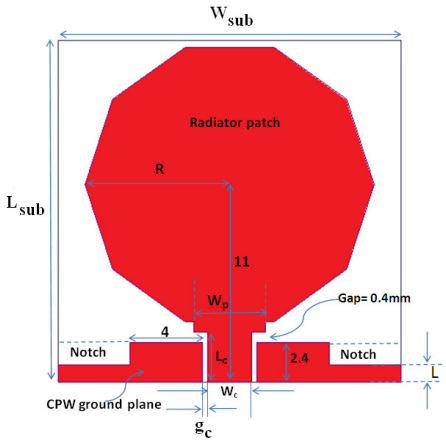

Fig. 1. Configuration of the proposed antenna with a pair of rectangular-shape notches on the ground plane and a polygon-shaped design on the patch.

III. SIMULATION AND MEASUREMENT RESULTS

After introducing the proposed antenna, we investigate the difference value of L, W_p, L_c, and NC parameters. With fixed value of R, we investigate the effective NC (number of cut) parameter. Figure 2 indicates the simulated VSWR characteristics with the difference values for NC. This figure clearly shows that sensitivity of upper frequency band in Fig. 2 is more. In other words, with increasing of NC, upper frequency band increases widely. In this simulation, the optimized value of 10 for the NC (number of cut) has been selected. Figure 3 indicates the simulated VSWR characteristics with the difference values for L. It can be observed that by decreasing the length of the L notch, the upper frequency is increased. The CPW ground plane plays an important role in the proposed antenna impedance matching. Figure 4 shows the simulated VSWR curves with difference values for W_p, while R is fixed in 8 mm. With doing several experiments, Wp is fixed in 4 mm. Figure 5 indicates distribution of currents at 10 GHz for polygon-shaped form. This figure shows that by inserting numbers of cuts around patch, currents are regularly concentrated around this polygon form. The printed monopole antenna, whose physical prototype is shown in Fig. 6, was tested in the antenna measurement laboratory at Iran Telecommunication Research Center (ITRC). The simulated and measured VSWR of the proposed antenna is plotted in Fig. 7. The figure clearly shows that the constructed antenna very well covers the intended VSWR of < -10 dB for 3.1 GHz - 10.6 GHz from 3 GHz to 14.9 GHz. Also, it is obvious that a little difference occurred between the two curves results in the position of resonance about 9 GHz, which is caused by SMA port effects in laboratory.

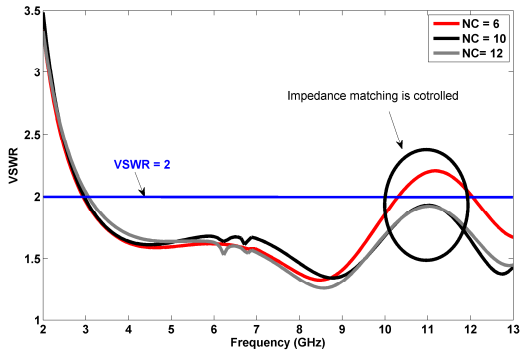

Fig. 2. Simulated VSWR characteristics for various values of NC.

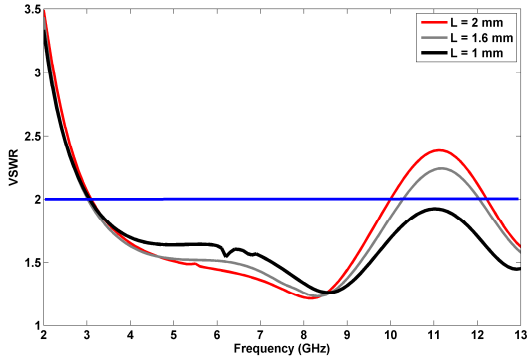

Fig. 3. Simulated VSWR characteristics of the proposed antenna with various values of L.

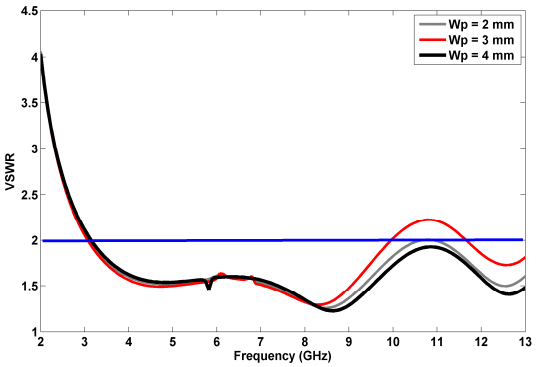

Fig. 4. Simulated VSWR characteristics of the proposed antenna with various values of Wp (L in 1 mm and NC in 10 is fixed).

Figure 8 shows the measured antenna gain from 3 GHz to 11 GHz for the proposed antenna. From this figure, we can find that, in different frequencies, the whole tendency of the antenna gains enhance with the frequency increases from 3 GHz to 11 GHz. Figure 9 shows the measured radiation pattern in frequencies 3.5 GHz, 5.5 GHz, 7.5 GHz, and 9.5 GHz, in H-plane (xz-plane), and E-plane (yz-plane). From Fig. 9 it can be realized that the proposed antenna acts similarly as a printed monopole antennas in the middle and lower frequency bands. Also, the figure is approximately indicative of omni-directional radiation pattern in the xz-plane.

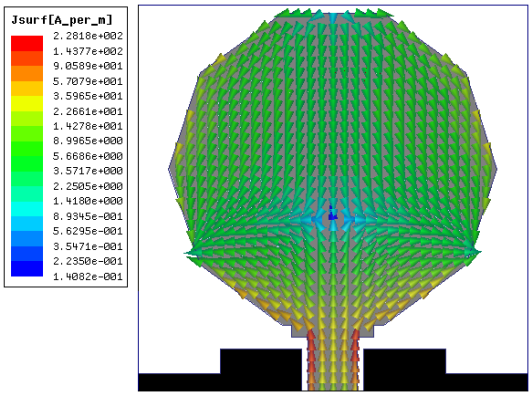

Fig. 5. Simulated current distributions on the patch with polygon-shaped form at 10 GHz.

IV. CONCLUSION

In this study, a small CPW-fed antenna with a polygon-shaped design with the numbers of cuts around the patch is proposed for ultra wideband (UWB) applications. This antenna has been designed with equal cuts on the circular patch and generating a polygon-shaped form and also a pair of mirror rectangular-shaped notches in the CPW ground plane. By inserting the numbers of cuts around the patch, we can achieve a proper control on the upper frequencies of the band. The antenna exhibits a simple structure and good VSWR level. Proposed antenna is suitable for ultra wideband systems with proper dimensions and aforementioned characteristics.

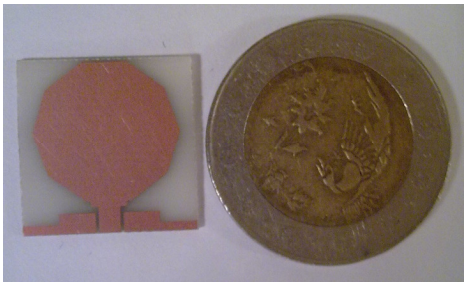

Fig. 6. Photograph of the proposed antenna.

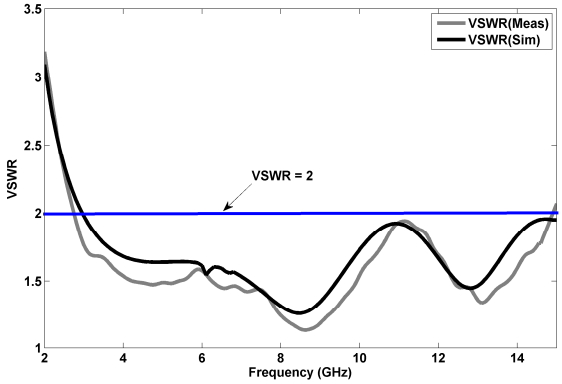

Fig. 7. Comparison between measured and simulated VSWR for the proposed antenna.

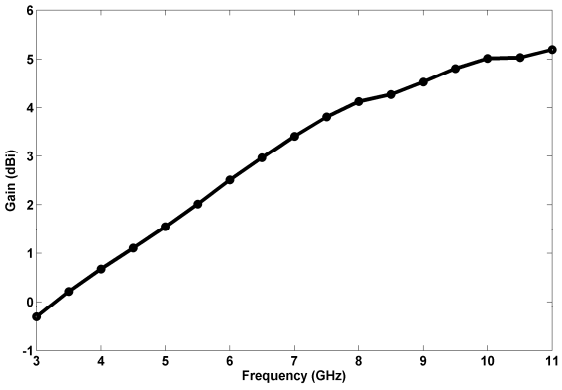

Fig. 8. Measured antenna gain of the proposed antenna.

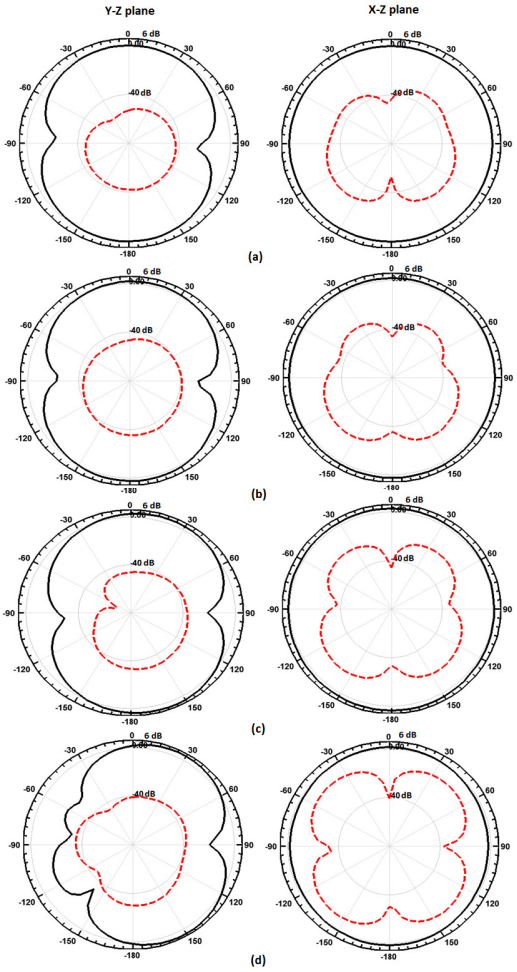

Fig. 9. Measured radiation pattern of the proposed antenna, (a) 3.5 GHz, (b) 5.5 GHz, (c) 7.5 GHz, and (d) 9.5 GHz. The solid line and red dash line are co-polar and cross-polar, respectively.

REFERENCES

[1] H. Schantz, *The Art and Science of UWB Antennas*, Artech House, Norwood, MA, 2005.

[2] FCC 1st Report and Order on Ultra-Wideband Technology, 2002.

[3] FCC 1st Report and Order on Ultra-Wideband Technology FCC, Washington, Dec. 2001.

[4] W. Weng, "Optimal design of an ultra-wideband antenna with the irregular shape on radiator using particle swarm optimization," *Applied Computational Electromagnetics Society (ACES) Journal*, vol. 27, no. 5, pp. 427-434, May 2012.

[5] N. Ojaroudi, M. Ojaroudi, and Sh. Amiri, "Enhanced bandwidth of small square monopole antenna by using inverted U-shaped slot and conductor-backed plane," *Applied Computational Electromagnetics Society (ACES) Journal*, vol. 27, no. 8, pp. 685-690, August 2012.

[6] M. Majidzadeh and C. Ghobadi, "Compact microstrip-fed monopole antenna with modified slot ground plane for UWB applications," *Applied Computational Electromagnetics Society (ACES) Journal*, vol. 27, no. 10, pp. 801-807, Oct. 2012.

[7] R. Azim, M. Islam, and N. Misran, "Design of a planar UWB antenna with new band enhancement technique," *Applied Computational Electromagnetics Society(ACES) Journal*, vol. 26, no. 10, pp. 856-862, Oct. 2011.

[8] J. Liang, L. Guo, C. Chiau, X. Chen, and C. Parini, "Study of CPW-fed circular disc monopole antenna for ultra wideband applications," in *Proc. IEE Microw. Antennas Propag.*, pp. 520-526, 2005.

[9] C. Lee, T. Yo, C. Luo, C. Tu, and Y. Juang, "Broadband disk monopole antenna with a circular CPW-feeding line," in *Proc. IEEE AP-S Int. Symp.*, Honoluu, HI, pp. 773-776, 2007.

[10] W. Tong and Z. Hu, "A CWP fed circular monopole antenna for ultra wideband wireless communications," in *Proc. IEEE AP-S Int. Symp.* vol. 3, pp. 528-531, 2005.

[11] N. Chen and Y. Liang, "Coplanar-waveguide fed circular disc monopole antenna with improved radiation characteristics," in *2nd Proc. Eur. Conf. Antennas Propag.*, Edinburgh, U.K. pp. 1-6, 2007.

Tohid Sedghi received the B.S degree in Electronic Engineering from IAU, Urmia Branch, Urmia, Iran, in 2007. He graduated from M.Sc. in Electrical Engineering at University of Urmia, Iran in 2009. Now he is working toward Ph.D. He is the author or coauthor of several refereed journal articles and conference papers. His research interests include, antenna miniaturization, optimization, method, monopole antennas, slot antennas, hybrid antennas, circular polarization antennas, diversity antennas, mobile phone and wireless local-area net work antennas, and antenna applications.

Vahid Rafii was born in Urmia, Iran, in 1986. He received the B.Sc. degree in Communication Engineering from the Urmia Azad University, in 2008 and M.Sc. degree in Communication Engineering from Urmia University, Urmia, Iran, in 2013. His research interests include antenna array, array feed networks, and their antenna applications.

Mahdi Moosazadeh received the B.Sc. degree in Electronic Engineering from IAU, Urmia Branch, Urmia, Iran, in 2005. He graduated from M.Sc. in Electrical Engineering at IAU, science research branch, Tehran, Iran in 2008. Now he is working toward Ph.D. His research interests include, monopole antennas, slot antennas, circular polarization antennas, diversity antennas, mobile phone and metamaterials.

Microstrip-Fed Small Slot Antenna with Dual Band-Notched Function for UWB Wireless Communications

N. Ojaroudi [1], M. Ojaroudi [2], and N. Ghadimi[2]

[1] Department of Electrical Engineering
Germi Branch, Islamic Azad University, Germi, Iran

[2] Young Researchers Club
Ardabil Branch, Islamic Azad University, Ardabil, Iran
m.ojaroudi@iauardabil.ac.ir

Abstract ─ A simple and compact microstrip-fed ultra wideband (UWB) slot antenna with dual band-notch characteristic for UWB applications has been presented. In order to increase the impedance bandwidth of the square slot antenna, we insert a T-shaped slot in the ground plane that with this structure UWB frequency range can be achieved. Additionally, by using a pair of L-shaped slits at the square radiating stub, a dual band-notch performance has been obtained. The measured results reveal that the presented dual band-notch slot antenna offers a wide bandwidth with two notched bands, covering all the 5.2 GHz / 5.8 GHz WLAN, 3.5 GHz / 5.5 GHz WiMAX and 4 GHz C bands. The designed antenna has a small size of 20×20 mm^2. Good return loss and radiation pattern characteristics are obtained in the frequency bands of interest.

Index Terms ─ L-shaped slit, microstrip-fed slot antenna, T-shaped slot, and ultra-wideband communication systems.

I. INTRODUCTION

In UWB communication systems, one of key issues is the design of a compact antenna while providing wideband characteristic over the whole operating band. Consequently, a number of planar slots with different geometries have been experimentally characterized [1, 2]. Moreover, other strategies to improve the impedance bandwidth have been investigated [3-6]. The frequency range for UWB systems between 3.1 GHz to 10.6 GHz will cause interference to the existing wireless communication systems, such as, the wireless local area network (WLAN) for IEEE 802.11a operating in 5.15 GHz – 5.35 GHz and 5.725 GHz – 5.825 GHz bands, WiMAX (3.3 GHz – 3.6 GHz), and C-band (3.7 GHz – 4.2 GHz), so the UWB antenna with a single and dual band-stop performance is required [7-10].

A simple method for designing a novel and compact microstrip-fed slot antenna dual band-notch characteristics for UWB applications has been presented. In the proposed structure, by inserting a T-shaped slot in the ground plane, we can gave an UWB frequency range and by using a pair of L-shaped slits on the square radiating stub, dual band-notch characteristic is obtained. Simulated and measured results are presented to validate the usefulness of the proposed antenna structure for UWB applications.

II. ANTENNA DESIGN

The presented small square slot antenna fed by a 50-Ω microstrip line is shown in Fig. 1, which is printed on an FR4 substrate of thickness 0.8 mm, permittivity 4.4, and loss tangent 0.018. The basic slot antenna structure consists of a square radiating stub, a feed line, and a ground plane. The proposed antenna is connected to a 50-Ω SMA connector for signal transmission.

Regarding defected ground structures (DGS), the creating slots in the ground plane provide an additional current path. Moreover, this structure changes the inductance and capacitance of the input impedance, which in turn leads to change the bandwidth. The DGS applied to a microstrip line

Submitted On: Oct. 2, 2012
Accepted On: Jan. 27, 2014

causes a resonant character of the structure transmission with a resonant frequency controllable by changing the shape and size of the slot [8]. Therefore, by cutting a T-shaped slot at the ground plane and carefully adjusting its parameters, much enhanced impedance bandwidth may be achieved. In this structure, The L-shaped slits perturb the resonant response and also acts as a half wave resonant structure [6]. At the notch frequency, the current concentrated on the edges of the interior and exterior of the L-shaped slit. As a result, the desired high attenuation near the notch frequency can be produced.

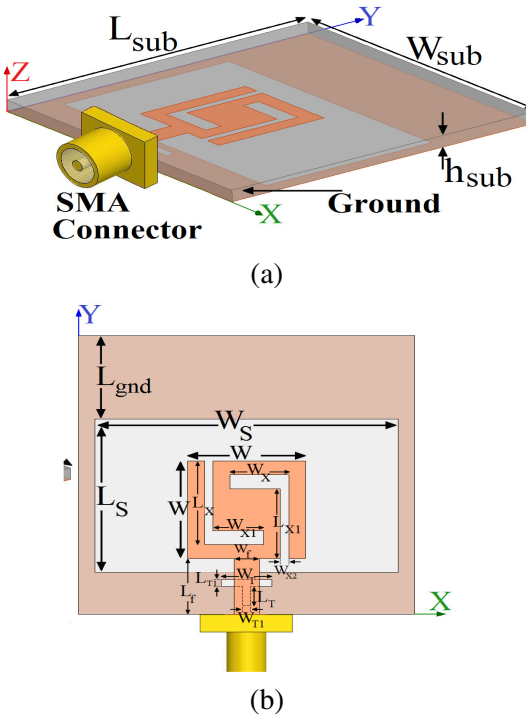

Fig. 1. Geometry of the proposed microstrip slot antenna, (a) side view and (b) top view.

The optimal dimensions of the designed antenna are as follows: W_{sub} = 20 mm, L_{sub} = 20 mm, W_S = 18 mm, L_S = 11 mm, h_{sub} = 0.8 mm, W_f = 1.5 mm, L_f = 4 mm, W = 7 mm, W_T = 3.5 mm, L_T = 1.5 mm, W_{T1} = 0.5 mm, L_{T1} = 1.5 mm, W_X = 4 mm, L_X = 6 mm, W_{X1} = 3.5 mm, L_{X1} = 5.5 mm, W_{X2} = 0.5 mm, and L_{gnd} = 6 mm.

III. RESULTS AND DISCOSSIONS

The proposed microstrip-fed slot antenna with various design parameters were constructed, and the numerical and experimental results of the input impedance and radiation characteristics are presented and discussed. The Ansoft simulation software high-frequency structure simulator (HFSS) [11] is used to optimize the design and agreement between the simulation and measurement is obtained. Figure 2 shows the structure of the various antennas used for dual notch performance simulation studies.

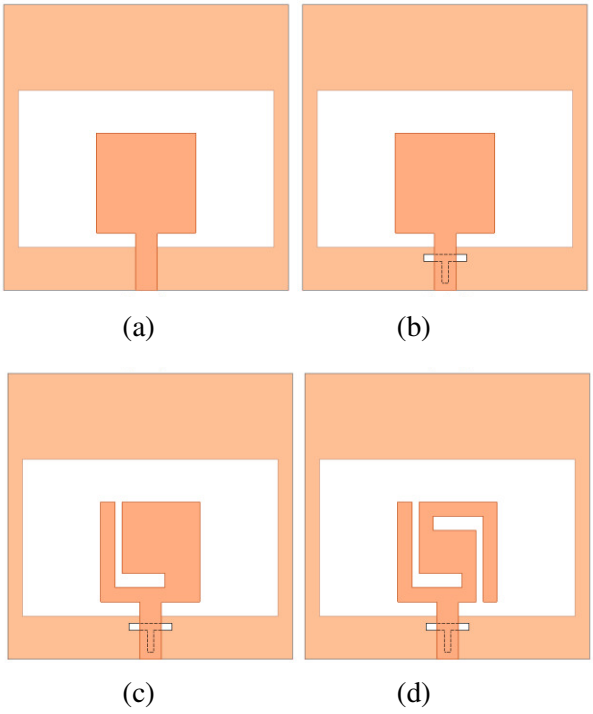

Fig. 2. (a) The ordinary square slot antenna, (b) antenna with a T-shaped slot in the ground plane, (c) antenna with a T-shaped slot in the ground plane and an L-shaped slit in the radiating stub, and (d) the proposed slot antenna.

VSWR characteristics for the ordinary square slot antenna (Fig. 2 (a)), with a T-shaped slot in the ground plane (Fig. 2 (b)), with a T-shaped slot in the ground plane and an L-shaped slit at the radiating stub (Fig. 2 (c)), and the proposed slot antenna (Fig. 2 (d)) are compared in Fig 3. As shown in Fig. 3, it is observed that the upper frequency bandwidth is affected by using the T-shaped slot. As shown in Fig. 3, the first notch frequency bandwidth is sensitive to the single L-shaped slit on the radiating stub, and also by inserting a pair of L-shaped slits at the radiating stub a dual band–notch function is achieved that

covering all the 5.2 GHz / 5.8 GHz WLAN, 3.5 GHz / 5.5 GHz WiMAX and 4 GHz C bands [12-15].

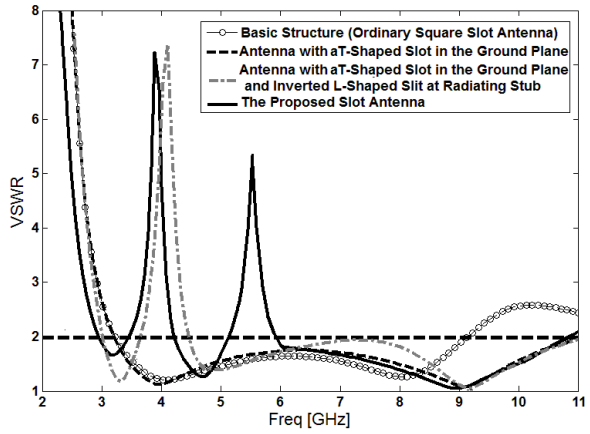

Fig. 3. Simulated VSWR characteristics for the various square slot antenna structures shown in Fig. 2.

To understand the phenomenon behind this dual band-notch UWB performance, on the radiating stub at the notch frequencies of 3.9 GHz and 5.5 GHz is presented in Fig. 4 (a), and 4 (b) respectively. It can be observed in Fig. 4 (a) and 4 (b) that the current concentrated on the edges of the interior and exterior of the L-shaped slits at 3.9 GHz and 5.5 GHz. Therefore, the antenna impedance changes at these frequencies due to the band notch properties.

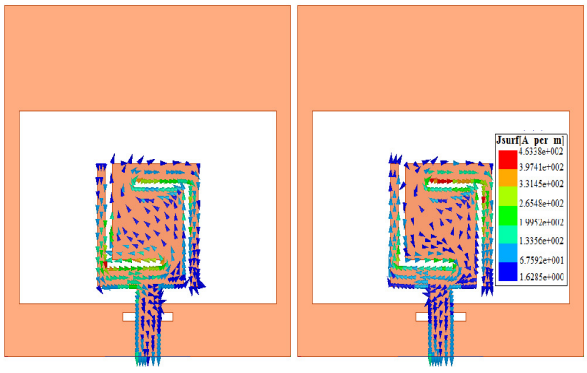

(a) (b)

Fig. 4. Simulated surface current distributions for the proposed antenna on the radiating stub (a) at the first notch frequency (3.9 GHz) and (b) at the second notch frequency (5.5 GHz).

The simulated input signal and impulse response for the proposed antenna is shown in Fig. 5. A first-order Rayleigh pulse is used as the source signal to drive the transmitter [16]. One of the characteristics of UWB signals is pulse distortion, which is inherently determined by their huge bandwidth. Good impedance matching over the operating frequency band is desired to minimize reflection loss and to avoid pulse distortion [17]. Therefore, the signal distortions shown in Fig. 5 are mainly due to the bandwidth mismatch between the source pulse and the antenna. As a result, some frequency components of the pulse cannot be transmitted effectively by the monopole, leading to the distortions of the received signal.

The proposed antenna with optimal design was built and tested in the antenna measurement laboratory at Microwave Technology Company (MWT). The measured and simulated VSWR characteristics of the proposed antenna are shown in Fig. 6. The fabricated antenna has the frequency band of 3.08 GHz to over 10.83 GHz with two rejection bands around 3.37 GHz – 4.3 and 5.1 GHz – 6.05 GHz. As shown in Fig. 6, there exists a discrepancy between measured data and the simulated results. This discrepancy between measured and simulated results is mostly due to a number of parameters such as the fabricated antenna dimensions as well as the thickness and dielectric constant of the substrate on which the antenna is fabricated, the wide range of simulation frequencies and also the effect of SMA soldering.

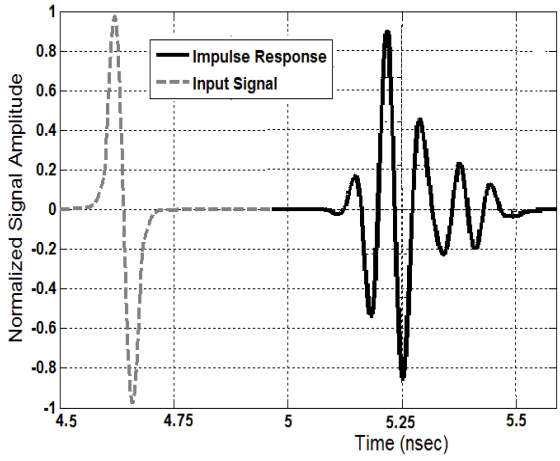

Fig. 5. Simulated time-domain analysis (input signal and impulse response).

In a physical network analyzer measurement, the feeding mechanism of the proposed antenna is composed of a SMA connector and a microstrip line (the microstrip feed line is excited by an SMA connector) whereas the simulated results are obtained using the Ansoft simulation software high-frequency structure simulator (HFSS), that in HFSS by default, the antenna exited by wave port that it is renormalized to a 50-Ohm full port impedance, therefore this discrepancy between measured data and the simulated results could be due to the effect of the SMA port [6]. In order to confirm the accurate VSWR characteristics for the designed antenna, it is recommended that the manufacturing and measurement process need to be performed carefully, besides, SMA soldering accuracy and FR4 substrate quality needs to be taken into consideration. In conclusion, as the slot is a short radiator, the SMA connector can modify its impedance matching.

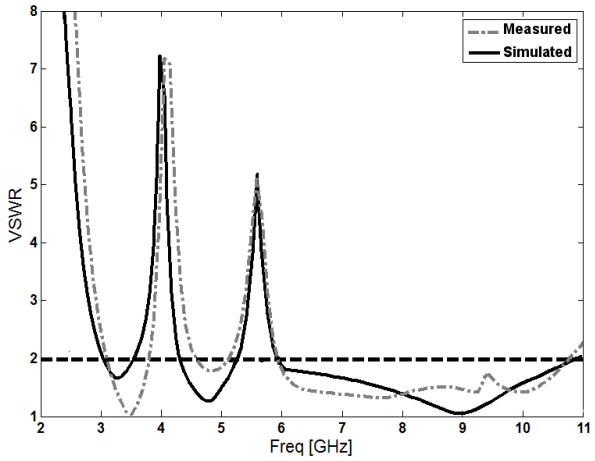

Fig. 6. Measured and simulated VSWR for the proposed slot antenna.

Figure 7 shows the measured radiation patterns including the co-polarization and cross-polarization in the H-plane (x-z plane) and E-plane (y-z plane). The main purpose of the radiation patterns is to demonstrate that the antenna actually radiates over a wide frequency band. It can be seen that the radiation patterns in x-z plane are nearly omnidirectional for the two frequencies [18-21]. Figure 8 shows the effects of the L-shaped slits at the square radiating stub, on the maximum gain in comparison to the same antenna without them.

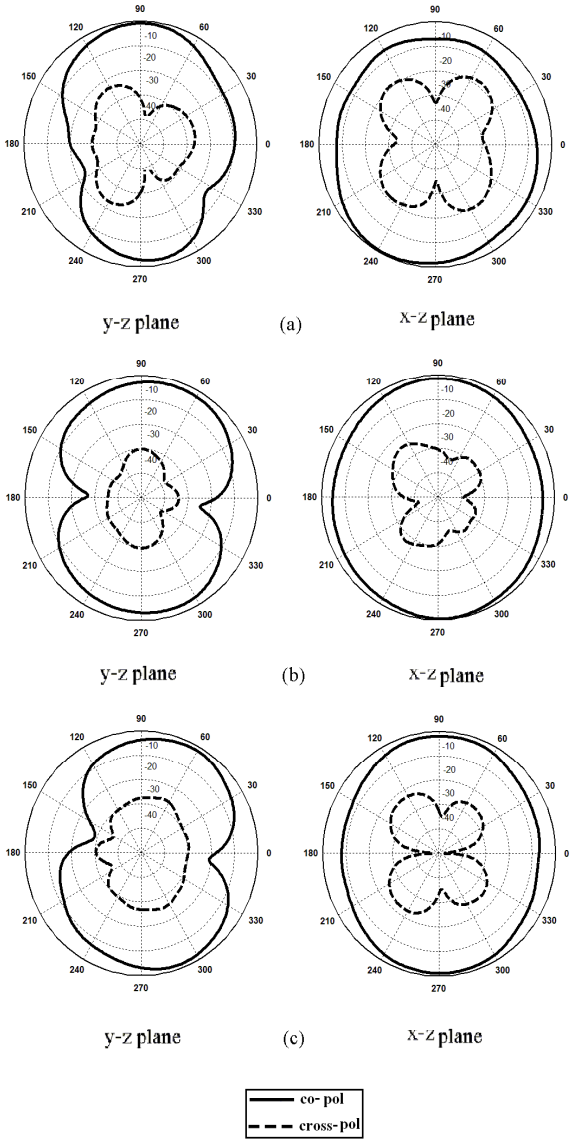

Fig. 7. Measured radiation patterns of the proposed antenna (a) 4.7 GHz, (b) 7.5 GHz, and (c) 10 GHz.

As shown in Fig. 8, the basic structure (ordinary slot antenna with) has a gain that is low at 2 GHz and increases with frequency [8]. It is found that the gain of the basic structure is decreased with the use of the L-shaped slits at the square radiating stub. It can be observed in Fig. 8 that by using the L-shaped slits at the square radiating stub, two sharp decrease of maximum gain in the notched frequencies band at 3.9 GHz and 5.5 GHz are shown. For other frequencies outside the notched frequencies band, the antenna gain with the filter is similar to those without it.

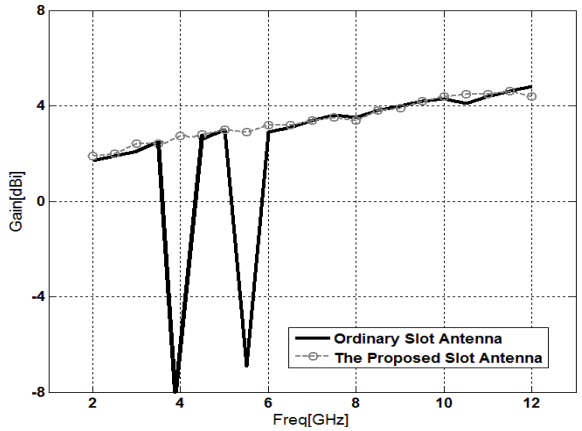

Fig. 8. Maximum gain comparisons for the ordinary slot antenna (simulated) and the proposed antenna (measured) in the z-axis direction (x-z plane).

IV. CONCLUSION

In this paper, we propose a novel design of ultra wide band slot antenna with dual band-notch function. The presented slot antenna can operate from 3.08 GHz to 10.83 GHz with two rejection bands around 3.37 GHz – 4.3 GHz and 5.1 GHz – 6.05 GHz. By cutting a T-shaped in the ground plane we can give UWB frequency range, and also by inserting a pair of L-shaped slits at radiating stub, dual frequency band-notch function can be achieved. The designed antenna has a small size. Good antenna radiation behavior within the UWB frequency range have also been obtained.

ACKNOWLEDGMENT

The authors are thankful to Microwave Technology (MWT) Company staff for their beneficial and professional help (www.microwave-technology.com).

REFERENCES

[1] M. Ojaroudi and A. Faramarzi, "Multi-resonance small square slot antenna for ultra-wideband applications," *Microwave and Optical Tech. Letters*, vol. 53, no. 9, Sep. 2011.

[2] M. Partovi, N. Ojaroudi, and M. Ojaroudi, "Small slot antenna with enhanced bandwidth and band-notched performance for UWB applications," *Applied Computational Electromagnetics Society (ACES) Journal*, vol. 27, no. 9, pp. 772-778, Sep. 2012.

[3] B. Siahkal-Mahalle, M. Ojaroudi, and N. Ojaroudi, "Enhanced bandwidth small square monopole antenna with band-notched functions for UWB wireless communications," *Applied Computational Electromagnetics Society (ACES) Journal*, vol. 27, no. 9, pp. 759-765, Sep. 2012.

[4] M. Ojaroudi, N. Ojaroudi, and Y. Ebazadeh, "Dual band-notch small square monopole antenna with enhanced bandwidth characterestics for UWB applications," *Applied Computational Electromagnetics Society (ACES) Journal*, vol. 27, no. 5, pp. 420-426, May 2012.

[5] A. Valizade, Ch. Ghobadi, J. Nourinia, N. Ojaroudi, and M. Ojaroudi, "Band-notch slot antenna with enhanced bandwidth by using Ω shaped strips protruded inside rectangular slots for UWB applications," *Applied Computational Electromagnetics Society (ACES) Journal*, vol. 27, no. 10, pp. 816-822, Oct. 2012.

[6] G. Zhang, J. Hong, B. Wang, and G. Song, "Switched band-notched UWB/WLAN monopole antenna," *Applied Computational Electromagnetics Society (ACES) Journal*, vol. 27, no. 3, pp. 256-260, March 2012.

[7] R. Rouhi, Ch. Ghobadi, J. Nourinia, and M. Ojaroudi, "Ultra-wideband small square monopole antenna with band notched function," *Microwave and Optical Tech. Letters*, vol. 52, no. 8, August 2010.

[8] S. Yzadanifard, R. Sadeghzadeh, and M. Ojaroudi, "Ultra-wideband small square monopole antenna with variable frequency band-notch function," *Progress In Electromagnetics Research C*, vol. 15, pp. 133-144, 2010.

[9] X. Ma, W. Shao, and G. He, "A novel dual narrow band-notched CPW-fed UWB slot antenna with parasitic strips," *Applied Computational Electromagnetics Society (ACES) Journal*, vol. 27, no. 7, pp. 581-586, July 2012.

[10] Z. Zhou, L. Li, and J. Hong, "A novel compact monopole antenna with triple high quality rejected bands for UWB applications," *Applied Computational Electromagnetics Society (ACES) Journal*, vol. 27, no. 8, pp. 654-659, August 2012.

[11] Ansoft High Frequency Structure Simulation (HFSS), Ver. 13, Ansoft Corporation, 2010.

[12] N. Ojaroudi and M. Ojaroudi, "Dual band-notched monopole antenna with multi-resonance characteristic for UWB wireless communications," *Progress in Electromagnetics Research*, vol. 40, pp.188-199, 2013.

[13] N. Ojaroudi, S. Amiri, and F. Geran, "A novel design of reconfigurable monopole antenna for UWB applications," *Applied Computational Electromagnetics Society (ACES) Journal*, vol. 28, no. 6, pp. 633-639, July 2013.

[14] N. Ojaroudi and M. Ojaroudi, "An UWB slot antenna with band-stop notch," *IET Microw. Antennas Propag.*, vol. 10, pp. 831-835, 2013.
[15] M. Ojaroudi and N. Ojaroudi, "Low profile slot antenna with dual band-notched function for UWB systems," *Microw. Opt. Technol. Lett.*, vol. 55, pp. 951-954, 2013.
[16] N. Ojaroudi and M. Ojaroudi, "Novel design of dual band-notched monopole antenna with bandwidth enhancement for UWB applications," *IEEE Antennas Wireless Propag. Lett.*, vol. 12, pp. 698-701, 2013.
[17] N. Ojaroudi, "Compact UWB monopole antenna with enhanced bandwidth using rotated L-shaped slots and parasitic structures," *Microw. Opt. Technol. Lett.*, vol. 56, pp.175-178, 2014.
[18] N. Ojaroudi and M. Ojaroudi, "An UWB slot antenna with band-stop notch," *IET Microw. Antennas Propag.*, vol. 10. pp. 831-835, 2013.
[19] N. Ojaroudi and M. Ojaroudi, "Novel design of dual band-notched monopole antenna with bandwidth enhancement for UWB applications," *IEEE Antennas Wireless Propag. Lett.*, vol. 12, pp. 698-701, 2013.
[20] N. Ojaroudi and M. Ojaroudi, "Application of the protruded strip structures to design an ultra-wideband slot antenna with variable frequency band-stop function," *Microw. Opt. Technol. Lett.*, vol. 55, pp. 1312-1316, 2013.
[21] N. Ojaroudi, M. Ojaroudi, and Sh. Amiri, "Compact UWB microstrip antenna with satellite down-link frequency rejection in X-band communications by etching an E-shaped step-impedance resonator slot," *Microw. Opt. Technol. Lett.*, vol. 55, pp. 922-926, 2013.

Nasser Ojaroudi was born on 1986 in Germi, Iran. He received his B.Sc. degree in Electrical Engineering from Azad University, Ardabil Branch. From 2011, he is working toward the M.Sc. degree in Telecommunication Engineering at Shahid Rajaee Teacher Training University. Since March 2008, he has been a Research Fellow in the Microwave Technology Company (MWT), Tehran, Iran. His research interests include microstrip antennas for radar systems, ultra-wideband (UWB) and small antennas for wireless communications, microwave passive devices and circuits, and microwave/millimeter systems.

Mohammad Ojaroudi was born on 1984 in Germi, Iran. He received his B.Sc. degree in Power Electrical Engineering from Azad University, Ardabil Branch and M.Sc. degree in Telecommunication Engineering from Urmia University. From 2010, he is working toward the Ph.D. degree at Shahid Beheshti University. Also from July 2013 he has been working, as a research visitor in University of Tennessee, Knoxville, USA. From 2007 until now, he is a Teaching Assistant with the Department of Electrical Engineering, Islamic Azad University, Ardabil Branch, Iran. Since March 2009, he has been the Chief Executive Officer (CEO) in the Microwave Technology Company (MWT), Tehran, Iran. From 2012, Dr. Ojaroudi is a member of the IEEE Transaction on Antennas and Propagation (APS) reviewer group and the Applied Computational Electromagnetic Society. His research interests include analysis and design of microstrip antennas, design and modeling of microwave structures, radar systems, and electromagnetic theory. He is author and coauthor of more than 150 journal and international conferences papers. His papers have more than 600 citations with 13 h-index.

Noradin Ghadimi was born in Ardabil-Iran in 1985, and received the B.Sc. degree in Electrical Engineering from the Islamic Azad University, Ardabil Branch, Ardabil, Iran, in 2009 and the M.Sc. degree in Electrical Engineering from the Islamic Azad University Ahar Branch, Ahar, Iran , in 2011. His research interests include Power System Protection, modeling and analysis of Distributed Generations, renewable energy and communications systems.

Compact Dual-Wideband Bandpass Filter Using a Novel Multiple-Mode Resonator

Jin Xu

College of Electronic Information
Northwestern Polytechnical University, Xi'an, 710072, P.R. China
xujin2njust@126.com

Abstract — This paper presents a novel dual-wideband bandpass filter (BPF) structure, which consists of a two-end shorted stepped-impedance resonator with two pairs of non-identical stepped-impedance open stubs (SIOSs) and a uniform-impedance open stub (UIOS) symmetrically loaded on its high impedance section. The designed BPF has a directly coupled configuration, which can also introduce transmission zero (TZ) for filter design. The loaded SIOSs and UIOS not only excite multiple resonant modes but also introduce multiple TZs. After carefully arranging these resonant modes and TZs, the TZs can divide multiple resonant modes into multiple useful groups, which can be utilized to exploit two wideband passbands. The TZs between two passbands can improve passband selectivity and the band-to-band isolation. As an example, a dual-wideband BPF centered at 1.57 / 5.59 GHz with -3 dB fractional bandwidth of 53% by 16% is designed and fabricated. The fabricated filter has a compact size of $0.16\lambda_g \times 0.106\lambda_g$. The measured results also exhibit a low insertion loss, good return loss and wide stopband.

Index Terms **-** Bandpass filter (BPF), dual-band, multiple- mode resonator (MMR), and stepped-impedance resonator (SIR).

I. INTRODUCTION

With the development of modern multi-service technology, dual-wideband bandpass filter (BPF) with compact size is great in demand for a single RF module to handle dual high data-rate communication modes. So far, various dual-band BPFs have been reported. However, most of these reported dual-band BPFs exhibit narrow passband [1-5]. One of the few literatures report the dual-wideband performance [6-9]. In [6], a dual-wideband BPF using frequency mapping and stepped-impedance resonators (SIRs) is reported, with the drawback of a complex design procedure and large circuit size. In [7], a dual-wideband BPF is developed by using the short-circuited SIRs, but it lacks passband selectivity. Two opposite hook-shaped resonators in [8] and four comb-loaded resonators in [9] are used to design the dual-wideband BPF. These two filters exhibit a high passband selectivity and compact size, but using multiple resonators. Recently, an attractive method using a single multiple-mode resonator (MMR) has been applied to develop compact dual-/multiple-band BPFs. Actually, MMR is widely used in the design of wideband filter [10-12]. Then, it is found that the multiple resonant modes of MMR can be arranged to be several mode groups in some structures, which can be applied to realize dual-/multiple-passband. In the author's previous work [13], two dual-mode, dual-wideband BPFs with sharp selectivity have been designed by using a quadruple-mode resonator. However, the etched ground plane configuration is involved, which increases the installation complexity.

The motivation of this paper is to design a novel microstrip dual-wideband BPF with single layer configuration, compact size, simple topology and quick design procedure. By properly arranging multiple resonant modes and multiple transmission zeros (TZs) of proposed structure, a dual-wideband BPF centered at 1.57 GHz / 5.59 GHz with -3 dB fractional bandwidth (FBW) of 53% by 16% are designed and fabricated. Detailed design of the filter as well as its simulated and measured results is presented and discussed.

Submitted On: May 12, 2013
Accepted On: Feb. 2, 2014

II. THEORETICAL ANALYSIS OF PROPOSED DUAL-BAND STRUCTURE

The configuration of the proposed dual-wideband BPF structure is shown in Fig. 1. Figure 2 (a) gives a transmission line model of the proposed structure. The proposed structure consists of a two-end shorted stepped-impedance resonator (SIR) with a pair of stepped-impedance open stubs (named SIOS1) loaded at the impedance junctions of the shorted SIR, the other pair of stepped-impedance open stubs (named SIOS2) symmetrically loaded on its Z_2-impedance section and a uniform impedance open stub (named UIOS) loaded at the center of Z_2-impedance section. The I/O ports are directly connected to the proposed structure. Due to its symmetrical configuration, Fig. 2 (b) and (c) give its even-/odd-mode equivalent circuits, respectively. The TPs can be derived under the transverse resonant condition that two oppositely oriented input impedances at the same position are zero. According to such theorem, the transmission poles (TPs) under the even-/odd-mode excitation satisfy,

$$\mathrm{Im}(Z_l + Z_{r,e}) = 0 \tag{1a}$$

$$\mathrm{Im}(Z_l + Z_{r,o}) = 0, \tag{1b}$$

where,

$$Z_l = Z_2[(jZ_{in\_SIOS1}Z_1\tan\theta_1 + jZ_2\tan(\theta_2/2 - \theta_{a1})(Z_{in\_SIOS1} + jZ_1\tan\theta_1)] / [Z_2(Z_{in\_SIOS1} + jZ_1\tan\theta_1) - Z_{in\_SIOS1}Z_1\tan\theta_1\tan(\theta_2/2 - \theta_{a1})] \tag{2a}$$

$$Z_{r,e} = Z_{in\_SIOS2}Z_2(2Z_{in\_UIOS} + jZ_2\tan\theta_{a1}) / [Z_{in\_SIOS2}(Z_2 + j2Z_{in\_UIOS}\tan\theta_{a1}) + Z_2(2Z_{in\_UIOS} + jZ_2\tan\theta_{a1})], \tag{2b}$$

$$Z_{r,o} = \frac{jZ_{in\_SIOS2}Z_2\tan\theta_{a1}}{Z_{in\_SIOS2} + jZ_2\tan\theta_{a1}}, \tag{2c}$$

$$Z_{in\_SIOS1} = jZ_{s11}\frac{Z_{s11}\tan\theta_{s11} - Z_{s12}\cot\theta_{s12}}{Z_{s11} + Z_{s12}\tan\theta_{s11}\cot\theta_{s12}}, \tag{2d}$$

$$Z_{in\_SIOS2} = jZ_{s21}\frac{Z_{s21}\tan\theta_{s21} - Z_{s22}\cot\theta_{s22}}{Z_{s21} + Z_{s22}\tan\theta_{s21}\cot\theta_{s22}}, \tag{2e}$$

$$Z_{in\_UIOS} = -jZ_u\cot\theta_u, \tag{2f}$$

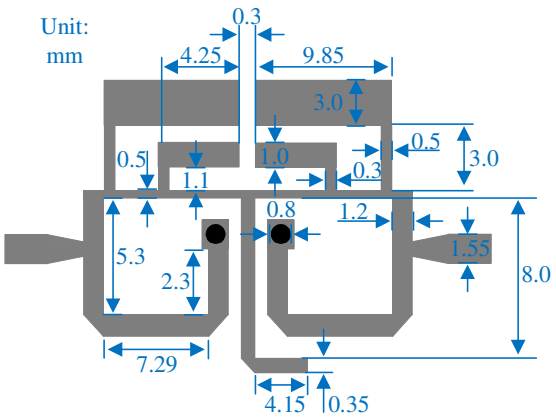

Fig. 1. Physical configuration of proposed dual-wideband BPF.

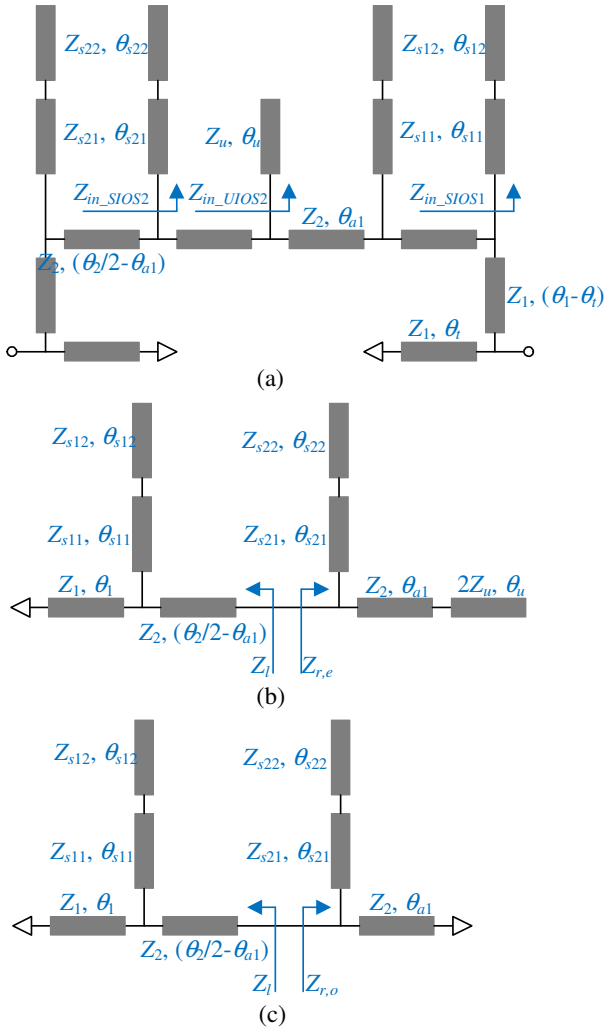

Fig. 2. (a) Transmission line model of proposed dual-wideband BPF, (b) even-mode equivalent circuit, and (c) odd-mode equivalent circuit.

If the input impedances of the SIOS1, SIOS2, and UIOS equal to zero, respectively, this is equivalent to introducing virtual grounds at the connected points. The signal from the input port will be shorted to ground and cannot transfer to the output port. Thus, the SIOS1, SIOS2, and UIOS will produce three series of TZs (f_{zs1}, f_{zs2}, and f_{zu}) for the proposed dual-wideband BPF structure. According to equations (2d), (2e), and (2f), these three series of TZs can be determined by,

$$Z_{s11}\tan\theta_{s11} - Z_{s12}\cot\theta_{s12} \quad (3a)$$

$$Z_{s21}\tan\theta_{s21} - Z_{s22}\cot\theta_{s22}, \quad (3b)$$

$$\cot\theta_u = 0. \quad (3c)$$

Equation (3c) can be rewritten as,

$$f_{zu} = \frac{n\pi f_0}{2\theta_u}, \quad n = 1, 3, 5\cdots \quad (4)$$

where f_0 represents the design frequency. Thus, f_{zu} can be separately controlled by θ_u. When θ_t equals to half-wavelength at f_{zt}, the input impedance looking into the tapped point will be also zero for directly coupled configuration, owing to the impedance invariance characteristic of half-wavelength line. Therefore, the feeding lines directly connected to the resonator not only act as I/O ports but also can produce a series of TZs. Such TZs due to the directly coupled configuration can be determined by,

$$f_{zt} = \frac{n\pi f_0}{\theta_t}, \quad n = 1, 2, 3\cdots \quad (5)$$

f_{zt} cannot be tunable freely, and the location of the tapped point θ_t is mainly determined by the required design condition. Subsequently, equations (1), (3a), (3b), (4), and (5) allow one to determine the frequency locations of all the even-/odd-mode TPs and TZs.

As an example, the central frequencies (CFs) of two passbands are specified at 1.575/5.5 GHz. There are various designing parameters that can be tuned to achieve such goal. The electrical length of shorted SIR ($2\theta_1+\theta_2$) is mainly decided by the specified f_0. In this design, ($2\theta_1+\theta_2$) = 150° at f_0 = 1.575 GHz is tuned to make the first mode group locate at around f_0. $\theta_1 = \theta_2$ is preset for the design simplicity. Z_1 is mainly determined by the required resonator susceptance and Z_1 = 58 Ω is preselected. SIOS1, SIOS2, UIOS, and the directly coupled configuration will generate four series of TZs. In the practical design, there are only four TZs (1^{st} f_{zs1}, 1^{st} f_{zs2}, 1^{st} f_{zu}, and 1^{st} f_{zt}) within the interested frequency range. It is found that the 1^{st} f_{zs1} and 1^{st} f_{zu} should be placed between two passbands. Since $\theta_{s12} = \theta_2/2$ is set for the following layout convenience, the frequency locations of the 1^{st} f_{zs1} are then tuned by $t_{s1} = \theta_{s11}/(2\theta_1+\theta_2)$ and $r_{s1} = Z_{s12}/Z_{s11}$. In this filter design, t_{s1} = 0.1 and $t_u = \theta_u/(2\theta_1+\theta_2)$ = 0.25 is pre-selected to make the 1^{st} f_{zs1} close to the lower side of the first passband and the 1^{st} f_{zu} close to the upper side of the second passband. The SIOS2 can be freely sliding on Z_2-impedance section. In this design, $\theta_{a1} = \theta_2/4$ is pre-selected for the design simplicity. Since $\theta_{s22} = \theta_{a1}$ is set for the following layout convenience, the frequency locations of the 1^{st} f_{zs2} are then tuned by $t_{s2} = \theta_{s21}/(2\theta_1+\theta_2)$ and $r_{s2} = Z_{s22}/Z_{s21}$. It is also found that the 1^{st} f_{zs2} should be placed between two passbands. Thus, t_{s2} = 0.02 is pre-selected. Due to the required external quality factor, the tapped position θ_t will be not very long, so that the 1^{st} f_{zt} together with 1^{st} f_{zs2} located beyond two passbands can extend the stopband. Under the remaining designing parameters at f_0 = 1.575 GHz selected as $r_{12} = Z_2/Z_1$ = 1.5, $r_u = Z_u/Z_1$ = 2, $r_{s11} = Z_{s11}/Z_1$ = 1.5, $r_{s12} = Z_{s12}/Z_{s11}$ = 0.35, $r_{s21} = Z_{s21}/Z_1$ = 2, $r_{s22} = Z_{s22}/Z_{s21}$ = 0.6, and t = 0.86, Fig. 3 gives a typically weak coupling frequency response of proposed structure. The 1^{st} f_{zs1} and the 1^{st} f_{zu} divide the first seven resonant modes into two groups, i.e., f_{pe1} and f_{po1} in the first mode group and f_{pe3}, f_{po2}, f_{pe4} and f_{po3} in the second passbands, which can be used to develop dual-band BPF. The TP f_{pe2} can be tuned to close to the 1^{st} f_{zs1}, so as to avoid forming the spurious passband.

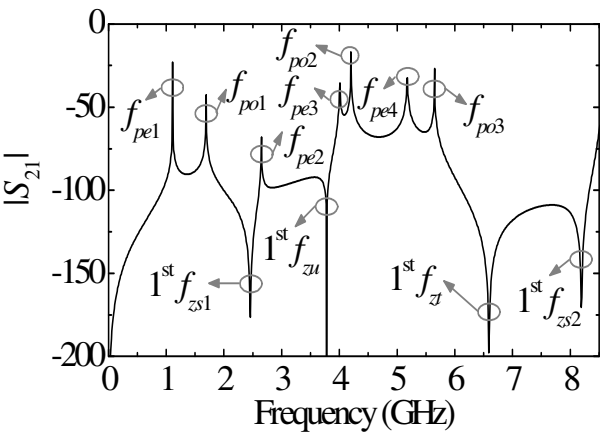

Fig. 3. Typically weak coupling frequency response of the proposed structure.

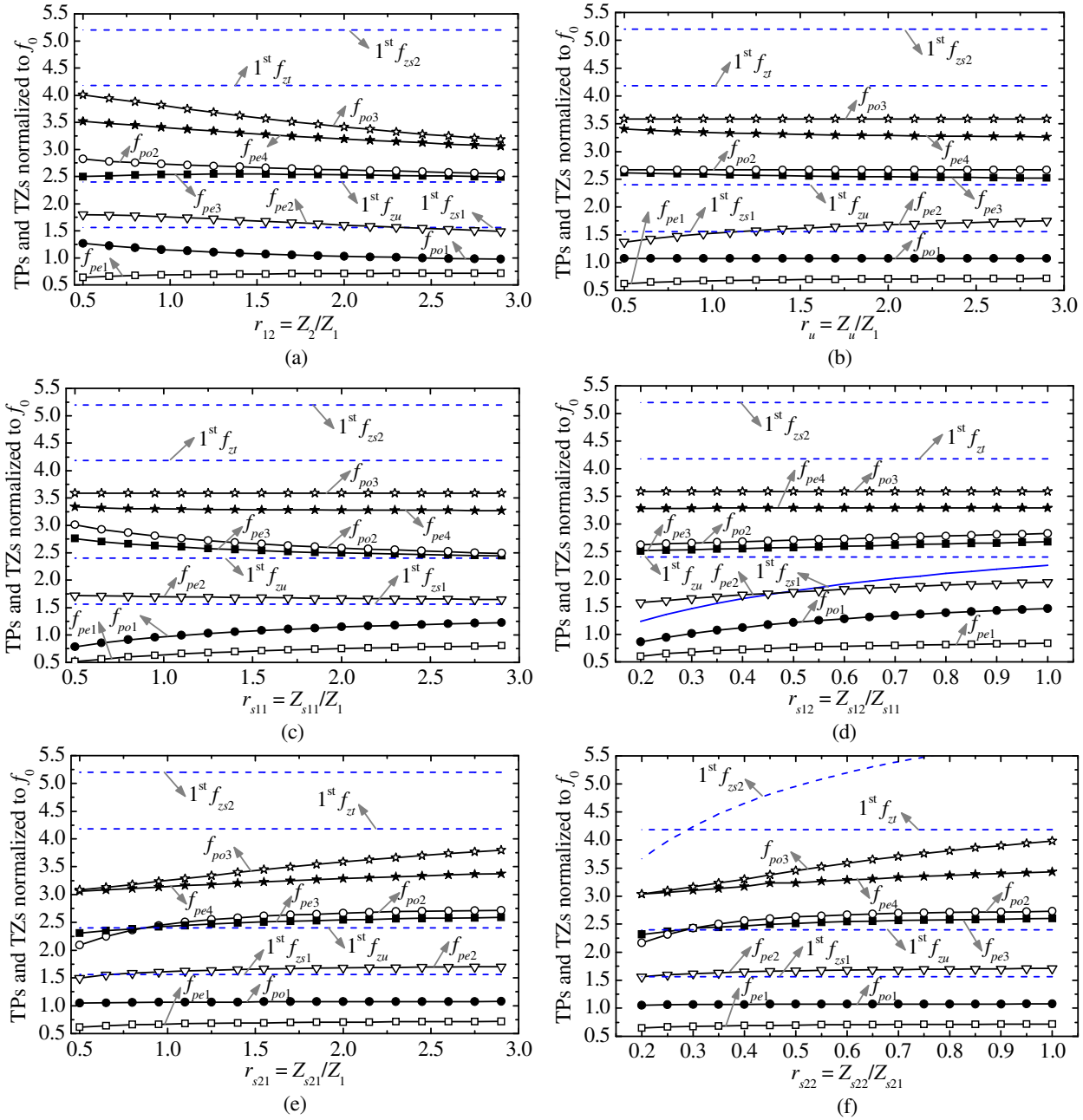

Fig. 4. Variation of TPs and TZs versus varied (a) r, (b) r_u, (c) r_{s11}, (d) r_{s12}, (e) r_{s21}, and (f) r_{s22}. When one designing parameter varies, the others keep in constant.

Based on the above discussion, the frequency locations of the resonant modes in each passband should be carefully tuned by r_{12}, r_u, r_{s11}, r_{s12}, r_{s21}, and r_{s22}, so as to achieve a good in-band performance of two passbands. Figure 4 gives the variation of all TPs and TZs versus varied r, r_{12}, r_u, r_{s11}, r_{s12}, r_{s21}, and r_{s22}. It can be seen in Fig. 4 (a) that as r increases, f_{po1} and f_{po3} move towards lower frequency while f_{pe1} and f_{pe3} do not shift dramatically. Since the above four TPs will mainly determine the bandwidths (BWs) and CFs of the two passbands, r should be firstly determined to acquire a roughly desired value of BWs and CFs of two passbands. To some extent, the BWs and CFs of the first passband can then be separately tuned by r_{s11} and r_{s12} as shown in Fig. 4 (c) and (d), while

the BWs and CFs of the second passband can be separately tuned by r_{s21} and r_{s22} as shown in Fig. 4 (e) and (f). It can be seen in Fig. 4 (d) that r_{s12} can be also used to tune the 1st f_{zs1} and f_{pe2} for achieving the goal of the free spurious-frequency isolation band. Thus, there is a tradeoff between such two purposes, when using r_{s12}. After the above five parameters are tuned to make the 1st f_{zs1} very close to f_{pe2}, r_u can be finally used to tune f_{pe2} for achieving the goal of the free spurious-frequency isolation band. Although the variation of r_u will affect the even-mode TPs, it can be seen in Fig. 4 (b) that all even-mode TPs except f_{pe2} do not change dramatically as it varies.

III. DUAL-WIDEBAND BPF DESIGN, SIMULATION, AND MEASURED RESULTS

Actually, it will be hard to directly find the final designing parameters, which can satisfy the desired in-band performance of two passbands and free spurious frequency isolation band simultaneously. So that the above initial designing parameters for dual-band BPF need to be optimized, which can be done with the help of ADS software. The designing parameters for dual-wideband BPF at f_0 = 1.575 GHz are optimized as Z_1 = 58 Ω, r_{12} = 1.6, $(2\theta_1 + \theta_2) = 144^o$, t_{12} = 0.31, r_u = 1.89, t_u = 0.23, r_{s11} = 1.6, r_{s12} = 0.34, t_{s1} = 0.07, r_{s21} = 2.22, r_{s22} = 0.59, t_{s2} = 0.022, and t_{s22} = 0.46. Under such designing parameters, two passbands of the filter are centered at 1.575 GHz / 5.435 GHz with -3dB fractional bandwidth of 57.8% by 20.7%, respectively. The filter is designed on ARlon DiClad 880 substrate (ε_{re} = 2.2, h = 0.508 mm). The whole structure is optimized by using the full-wave EM simulator HFSS and the optimized physical dimensions are labeled in Fig. 1. Figure 5 plots the external quality factor of two passbands against d_t. The external quality factor of the first passband (Q_{e1}) and the external quality factor of the second passband (Q_{e2}) are extracted by the following equation,

$$Q_{ex1,2} = \frac{f_{c1,2}}{\Delta_{1,2}} = \frac{f_{c1,2}}{\Delta_{(\pm\pi/2)1,2}} \tag{6}$$

where $\Delta_{1,2}$ and $\Delta f_{(\pm\pi/2)1,2}$ represents -3dB bandwidths and the frequency bandwidth of S_{11} phase curve changing $\pm\pi/2$ with respect to $f_{c1,2}$, respectively. As d_t increases, Q_{e1} slightly decreases while Q_{e2} apparently increases. The ascent rate of Q_{e2} is greater than the descent rate of Q_{e1}. In this paper, d_t = 15.765 is selected for two passbands. The overall circuit size is 22.38 mm × 14.85 mm, corresponding to $0.16\lambda_g \times 0.106\lambda_g$, where λ_g represents the guided wavelength of a 50 Ω microstrip line at 1.57 GHz. The photograph of the fabricated filter is shown in Fig. 6.

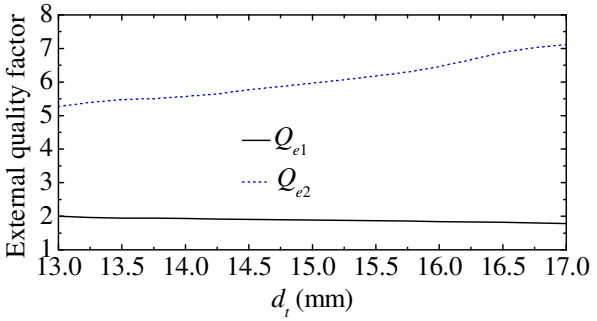

Fig. 5. External quality factor against d_t.

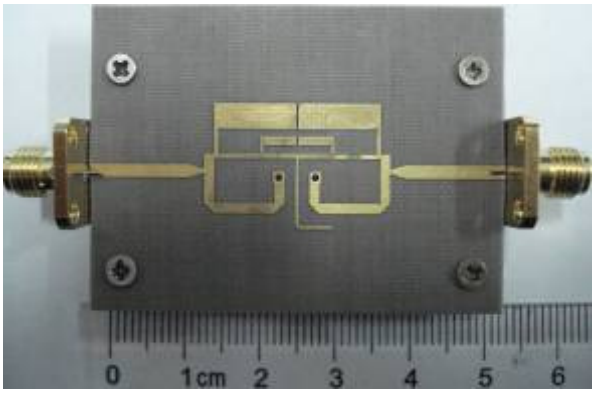

Fig. 6. Photograph of the fabricated dual-wideband BPF.

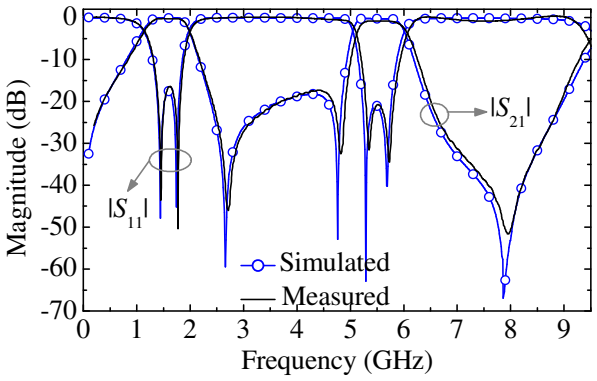

Fig. 7. Simulated and measured results of the fabricated dual-wideband BPF.

Table 1: Performance comparison with reported works.

	IL at CF(dB)/ -3 dB FBW	Roll of rate (dB/GHz)	Isolation (dB)	Circuit area (λ_g^2)
[6]	0.5/47.6%, 2/48.4%	33/200/80/100	> 40	3.33×1.08
[7]	0.8/54%, 0.8/20%	15/18/18/10	> 25	0.3×0.3
[8]	0.55/19.5%, 1.31/15.1%	99/75/87/56	> 13	0.065×0.147
[9]	1.1/32%, 2.5/13%	112/41/71/81	> 30	0.464×0.06
[13]	0.1/57.1%, 0.8/20.8%	63/45/71/50	> 30	0.40×0.05
This work	0.3/53%, 0.8/16%	22/39/74/35	> 17	0.16×0.106

The simulated and measured results of fabricated dual-band BPF are plotted in Fig. 7. Good agreement can be observed between the simulation and measurement results. There are some discrepancies, which are attributed to the fabrication error as well as the SMA connectors. The measured central frequencies (CFs) and -3 dB FBW of two passbands are 1.57 GHz / 5.59 GHz and 53% by 16%, respectively. The measured insertion losses (ILs) at two CFs are 0.3 dB / 0.8 dB while the return losses are better than 17 dB / 20 dB. There are only two TPs that can be observed in the second passband. This is because that f_{pe3} close to f_{po2} will merge into one poles, which is the same to f_{pe4} and f_{po3}. The band-to-band isolation is better than 17 dB from 2.3 GHz to 4.9 GHz. The fabricated filter also has -20 dB rejection level stopband from 6.5 GHz to 8.95 GHz. There is only one TZ within the stopband that can be observed in Fig. 7. This is because that the 1st f_{zt} will be very close to the 1st f_{zs2} after optimization. These two TZs merge into one TZ finally.

The comparison between the performances of some reported dual-wideband BPFs and the proposed one is summarized in Table 1. After comparison, it can be known that the proposed dual-wideband BPF in this paper has the merits of lower insertion losses, more compact size, and simpler physical topology.

IV. CONCLUSION

A dual-wideband BPF centered at 1.57 GHz / 5.59 GHz with -3 dB FBW of 53% by 16 % and compact size of $0.16\lambda_g \times 0.106\lambda_g$ are presented in this paper. Measured results also show its merits of low insertion loss, good return loss, sharp passband selectivity, and good band-to-band isolation. The proposed filter has simple topology and design procedure. All these merits make it attractive in modern dual high data-rate communication system.

REFERENCES

[1] M. Hayati, A. Khajavi, and H. Abdi, "A Miniaturized microstrip dual-band bandpass filter using folded UIR for multimode WLANs," *Applied Computational Electromagnetics Society (ACES) Journal*, vol. 28, no. 1, pp. 35-40, January 2013.

[2] S. Sun, "A dual-band bandpass filter using a single dual-mode ring resonator," *IEEE Microw. Wireless Compon. Lett.*, vol. 21, no. 6 pp. 298-300, 2011.

[3] Y. Sung, "Dual-mode dual-band filter with band notch structures," *IEEE Microw. Wireless Compon. Lett.*, vol. 20, no. 2, pp. 73-75, 2011.

[4] J. Xu, C. Miao, and W. Wu, "A compact and high isolation dual-mode dual-band bandpass filter with tunable transmission zeros," *J. of Electromag. Waves and Appl.*, vol. 26, no. 17-18, pp. 2390-2397, 2012.

[5] X. Li and J. Zeng, "A novel dual-band microstrip bandpass filter design and harmonic suppression," *Applied Computational Electromagnetics Society (ACES) Journal*, vol. 28, no. 4, pp. 348-352, April 2013.

[6] A.-S. Liu, T.-Y. Huang, and R.-B. Wu, "A dual-wideband filter design using frequency mapping and stepped-impedance resonators," *IEEE Trans. Microw. Theory Tech.*, vol. 56, no. 12, pp. 2921-2929, 2008.

[7] K.-S. Chin and J.-H. Yeh, "Dual-wideband bandpass filter using short-circuited stepped-impedance resonators," *IEEE Microw. Wireless Compon. Lett.*, vol. 19, no. 3 pp. 155-157, 2009.

[8] Z. Zhang, Y.-C. Jiao, X.-M. Wang, and S.-F. Cao, "Design of a compact dual-band bandpass filter using opposite hook-shaped resonator," *IEEE Microw. Wireless Compon. Lett.*, vol. 21, no. 7 pp. 359-361, 2011.

[9] C.-W. Tang and Y. Hsu, "Design of wide-single-/dual-passband filters with comb-loaded resonators," *IET Microw. Antennas Progap.*, vol. 6, no. 1 pp. 10-16, 2012.

[10] C. Liu, T. Jiang, Y. Li, and J. Zhang, "A novel UWB filter with WLAN and RFID stop-band rejection characteristics using tri-stage radial loaded stub resonators," *Applied Computational Electromagnetics Society (ACES) Journal*, vol. 27, no. 9, pp. 749-758, Sep. 2012.

[11] S. Gao, S. Xiao, and J.-L. Li, "Compact ultra-wideband (UWB) bandpass filter with dual notched bands," *Applied Computational Electromagnetics Society (ACES) Journal*, vol. 27, no. 10, pp. 795-800, Oct. 2012.

[12] Y. Li, H. Yang, Y. Wang, and S. Xiao, "Ultra-wideband bandpass filter based on parallel-coupled microstrip lines and defected ground structure," *Applied Computational Electromagnetics Society (ACES) Journal*, vol. 28, no. 1, pp. 21-26, Jan. 2013.

[13] J. Xu, W. Wu, and C. Miao, "Compact and sharp skirts microstrip dual-mode dual-band bandpass filter using a single quadruple-mode resonator (QMR)," *IEEE Trans. Microw. Theory Tech.*, vol. 61, no. 3, pp. 1104-1113, 2013.

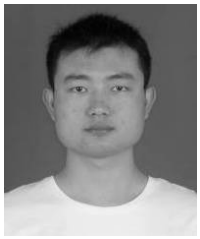

Jin Xu was born in AnHui, China, in 1987. He received the B.Eng. degree in Information Countermeasure Technology and Ph.D. degree in Information and Communication Engineering from Nanjing University of Science and Technology (NUST), Nanjing, China, in 2009 and 2013, respectively. He is currently an Associate Professor with the College of Electronic Information, Northwestern Polytechnical University, Xi'an, China. His research interests include UWB technology, MCM technology, microwave passive/active components, microwave and millimeter-wave MMICs developed on SiGe, phased array radar and wireless communication system.

From February 2011 to September 2011, he was an attached Ph.D. student in Institute of Microelectronics, Singapore. From October 2011 to September 2012, he joined MicroArray Technologies Corporation Limited, Chengdu, P.R. China, where he was an IC R&D Engineer. Since 2011, he has served as a reviewer for some journals including IEEE Microwave Wireless Component Letters, International Journal of Electronics, PIER and JEMWA.

A Novel Compact Low-Pass Filter using Defected Ground Structure for Sharp Transition Band

A. Mohammadi and M. N. Azarmanesh

Microelectronic Research Laboratory, Urmia University, Urmia 57159, Iran
Khallegh60@gmail.com, m.azarmanesh@urmia.ac.ir

Abstract ─This paper presents a simple technique to design a low-pass filter using defected ground structure (DGS) having a remarkable sharp response in transition band and rejection better than -20 dB up to 20 GHz. The fabricated filter has a 3 dB cutoff frequency at 3.4 GHz and it is as small as 22 mm × 12 mm. The insertion loss in the pass-band is less than 0.6 dB from DC to 3.1 GHz. The design of the filter is simple and it gives desired frequency response. Measured results show good agreement with simulated ones.

Index Terms ─ Bandpass, band-reject, defected ground structure (DGS), maximally flat prototype, and roll-off rate.

I. INTRODUCTION

Low-pass filters play an important role in RF circuits and systems, which rejects the higher harmonics and spurious responses of circuits. Conventional implementation of a low-pass filter (LPF) involves the use of open stubs or stepped-impedance microstrip lines. These structures have gradual cutoff response that only by increasing the number of sections, filter rejection characteristic can be improved. This improving method increases the passband insertion loss and filter physical size.

Defected ground structures (DGS) have been reported to improve the performance of traditional microstrip-based low-pass filters (LPF) [1-4] i.e., rejection properties of LPF have been improved. A DGS structure offers series connected quasi-lumped inductive element to a microstrip line. Its implementation reduces the length of LPF. The performances of low-pass filter, i.e., sharpness factor (the ratio of pole frequency to cutoff frequency), suppression of harmonics in the stop-band and low insertion loss in the passband; are significantly affected by the type of DGS slots.

The initial investigations on DGS have been carried out around simple geometrical shapes include square, circle, and triangle [1]. The simple geometrical shape DGS slots are modeled as a series-connected lossless inductor and capacitor (LC) parallel resonator [1]. Typical properties of LPFs can be obtained by using periodic defected ground structure (DGS) [2]. In periodic structures usually LPF is designed with conventional methods like Chebyshev [3] or Bessel [4] prototype. After that the equivalent LC circuit of DGS slots is used to realize the reactive elements of designed LPF [3]. In this method we need some diagrams, which show the equivalent inductance or capacitance versus the relative area of DGS [3].

In periodic DGS method we need to increase the number of sections for having a sharp response [5]. For example, to design a flat (low ripple) LPF with Chebyshev prototype, for a sharpness factor better than 1.1 and 20 dB attenuation in pole frequency we need a filter with order of nine or more [6]. As mentioned earlier by increasing the number of sections (to have a sharp response) the passband insertion loss and filter physical size is increased.

In this paper a new method to design a filterusing DGS slots is presented. In the proposed method we designed the top layer conventionally and after that by adding some DGS units to the bottom layer, we obtain desired filter responses. DGS units lead to some attenuation pole frequencies. By adjusting the dimensions of DGS units the pole frequencies can be controlled, consequently filter characteristics like sharpness factor and stop-band rejection can be adjusted.

Submitted On: Dec. 18, 2012
Accepted On: Jan. 27, 2014

II. INTRODUCING TWO DGS UNITS

It has always been a challenge for a defected ground structure (DGS) to obtain simultaneously a low resonant frequency and a small circuit area. Some papers have related the resonant frequency to the size of DGS (area which DGS is surrounded) [7]. But there are some results that show we can have lower resonant frequency with lower size [8]. In the following subsections two usual DGS are going to be introduced. The first one has a sharp attenuation pole in frequency response, which can be used to make transition band of LPF as sharp as possible. The second one has a wide attenuation pole, which can be used to extend band-stop.

A. First DGS unit resonator

Figure 1 (a) shows the schematic of DGS unit resonator. This DGS has two parallel stubs, which are bent. This resonator is excited by a 50 Ω microstrip line. This kind of DGS usually used for band-stop filter [8]. Band-stop filter can be designed by cascading several band-stop resonators. After that we should adjust the coupling amongst different resonators. If two or more of this DGS unit are used with a sufficient distance among them, the attenuation in pole frequency will be increased [8]. This DGS unit can be modeled by LC circuit shown in Fig. 1 (b). The parameters of this LC circuit model are obtained from frequency response.

The value of Lp and Cp are found from the following equations [1],

$$C_p = \frac{5f_c}{\pi[{f_p}^2 - {f_c}^2]} \quad pF \tag{1}$$

$$L_p = \frac{25}{C_p(\pi f_p)^2} \quad nH \ . \tag{2}$$

The symbol $f_p$is the pole frequency and $f_c$is the 3-dB cutoff frequency. The dimensions of Fig. 1 are as follows: L = 5.4 mm, L1 = 2.6 mm, L2 = 3.6 mm, L3 = 1.7 mm, L4 = 2.5 mm, L5 = 1.2 mm, L6 = 0.4 mm, G = 0.2mm and the width of microstrip line is 1.6 mm. The resonant frequency is affected by any changes in the dimensions of DGS. This unit has been designed on a substrate with dielectric constant 2.2 and thickness of 0.635 mm. The simulation results of this structure, which has been done by HFSS [9] are shown in Fig. 2.

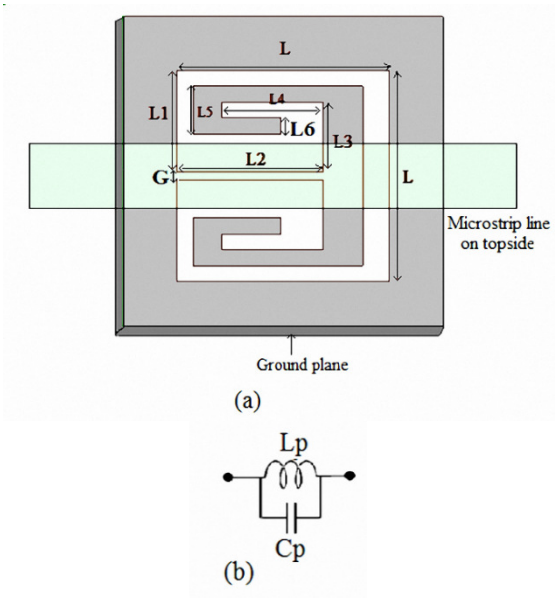

Fig. 1 (a) Schematic of the first DGS unit and (b) equivalent circuit.

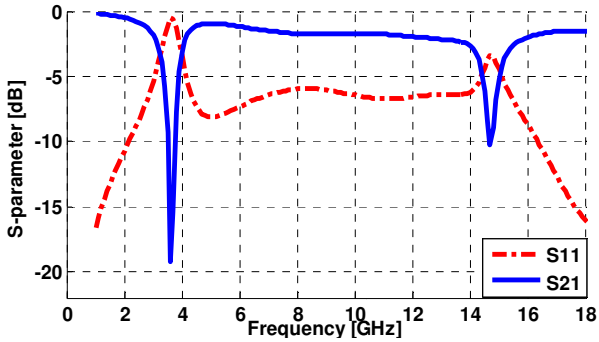

Fig. 2. Simulated S-parameters for DGS unit shown in Fig. 1.

As illustrated in Fig. 2 there are two attenuation poles in the frequency response of this DGS. One of them is in 3.6 GHz and the other one in 14.7 GHz. Totally if all dimensions become larger with the same scale (the area of slot becomes larger), the resonant frequency will decrease. This is because of an increase in the inductive reactance of the slot [3]. Simulation for different area has been done on a 50 Ω microstrip line. The first attenuation pole frequency versus different area of DGS is plotted in Fig. 3. The second pole is located beyond 7 GHz and does not affect our design procedure.

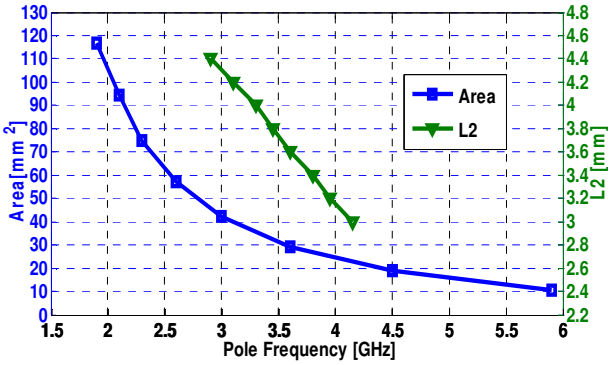

Fig. 3. First pole frequency versus DGS area (left axis) and L2 (right axis).

As Fig. 3 shows, by changing the area of DGS we would have a desired pole in a wide range of frequency from 1.8 GHz to 6 GHz. Moreover, by altering other dimensions of DGS unit, the attenuation pole frequency will change as well. In Fig. 3 we can also see increasing the length L2 causes a noticeable decrease in the attenuation pole frequency. Another parameter, which has a significant effect on pole frequency is the width G. Figure 4 shows that when G increases, the attenuation pole frequency increases as well. This is due to an increase in the capacitance property of the slot [10], [11].

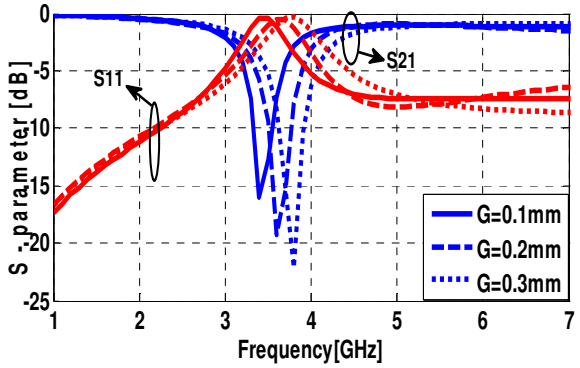

Fig. 4. Simulated S-parameter for G variation.

These results illustrate there are three or more degrees of freedom to design DGS slot and the selectivity is high enough to get the desired attenuation pole frequency.

B. Second DGS unit resonator

All DGS slots can be grouped in two categories: (i) simple DGS slot and (ii) complex DGS slot. In the first category there are simple geometrical shapes; such as square, triangle, circle and etc. In the second group the slot-heads of DGS have more complex geometrical shapes; such as H-shape, open-square [12], spiral [12], and inter-digital [12].

In this paper H-type DGS has been selected to produce the second pole of the LPF. The shape of H-type DGS is shown in Fig. 5. By adjusting values of a, b, c, L1, and W a desired resonant pole frequency could be obtained. The simulated S-parameters of this DGS as a function of L1 is shown in Fig. 6.

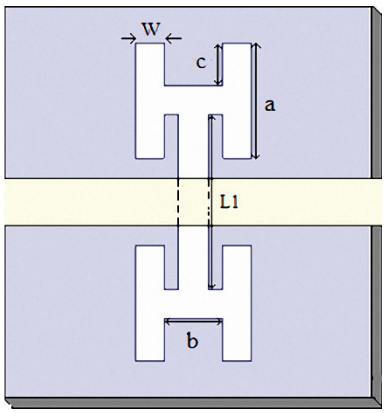

Fig. 5. Schematic of H-type DGS.

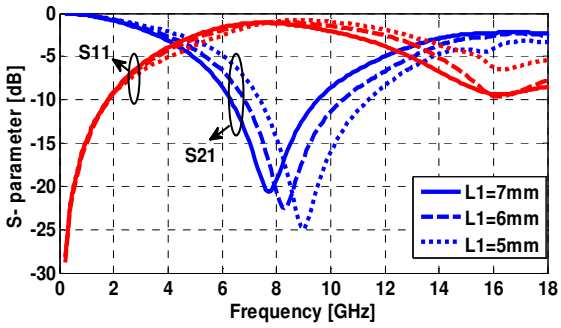

Fig. 6. Simulated S-parameter of H-type DGS for L1 variation.

Other dimensions of H-type DGS are as follows: a = 4 mm, b = 2 mm, c = 1.5 mm, and W = 1 mm. It is evident from Fig. 6 that as L1 decreases the attenuation pole frequency increases. Furthermore, we can see that the second DGS have a wide rejection around pole frequency, approximately from 5 GHz to 13 GHz, and it leads to a better stop-band rejection in LPF.

III. DESIGN LOW-PASS FILTER

A. Maximally flat low-pass filter

In the proposed design method, the desired band-rejection and sharpness of the LPF has been obtained by the use of DGS; therefore, it is better to use a prototype for top side, which gives a flat response through pass-band and maximally flat low-pass filter prototype with low order is the best choice. Since by increasing the order of filter, the size, the passband insertion loss, and nonlinearity of phase response will increase [6], we should choose low orders.

A LPF with cut-off frequency of 4.5 GHz, using conventional method, without ripple factor in the pass band (maximally flat response) has been designed [6]. The prototype has the following normalized components: g_1 = 0.6180, g_2 = 1.6180, g_3 = 2, g_4 = 1.6180, g_5 =0.6180. Three series inductances and two shunt capacitances of the prototype are computed by,

$$l_i = \frac{g_i Z_0}{\omega_c} \tag{3}$$

$$c_j = \frac{g_j}{\omega_c Z_0}, \tag{4}$$

where Z_0 = 50 Ω, ω_c= $2\pi f_c$, i=1, 3, 5 and j=2,4. The LC circuit and its equivalent distributed elements is shown in Fig. 7.

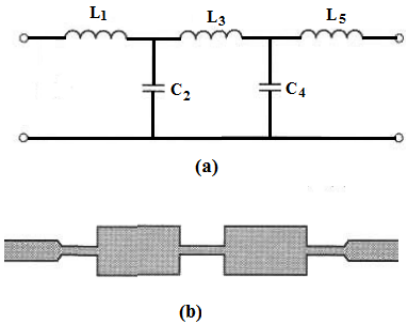

Fig. 7. (a) LC circuit and (b) equivalent distributed circuit.

The schematic of the designed LPF is shown in Fig. 8. To find the dimensions of the distributed element we can use following formulas,

$$\text{(inductor)} \qquad Bl \approx \frac{LR_0}{Z_h} \tag{5}$$

$$\text{(capacitor)} \qquad Bl \approx \frac{CZ_l}{R_0}, \tag{6}$$

where Bl is the electrical length of capacitor and inductor, R_0 is the filter impedance, Z_h and Z_l are the highest and lowest characteristic impedance that can be practically fabricated, L and C are normalized components (g_i).

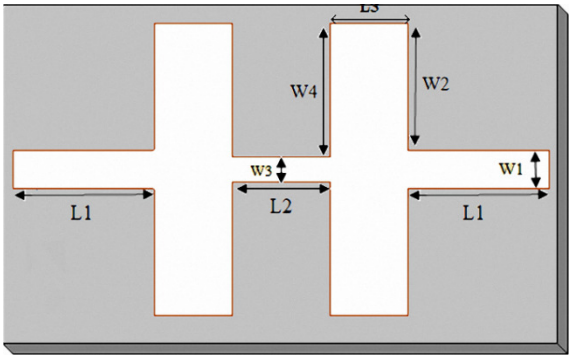

Fig. 8. Schematic of primary LPF.

After computing Bl, the length of distributed elements (l) can be calculated. The width of distributed elements, which refers to Z_h and Z_l can be calculated by following formulas [13]. For narrow strips (i.e., when $Z_0 > (44\text{-}\varepsilon_r)$ Ω),

$$\frac{w}{h} = \left(\frac{exp\, H}{8} - \frac{1}{4\exp H}\right)^{-1} \tag{7}$$

$$\text{H}=\frac{Z_0\sqrt{2(\varepsilon_r+1)}}{119.9} + \frac{1}{2}\left(\frac{\varepsilon_r-1}{\varepsilon_r+1}\right)\left(ln\frac{\pi}{2} - \frac{1}{\varepsilon_r} ln\frac{4}{\pi}\right). \tag{8}$$

And for wide strips (i.e., when $Z_0 < (44\text{-}2\varepsilon_r)$ Ω),

$$\frac{w}{h} = \frac{2}{\pi}\left[\left(d_{\varepsilon_r} - 1\right) - \ln\left(2d_{\varepsilon_r} - 1\right)\right] + \frac{(\varepsilon_r-1)}{\pi\varepsilon_r}\left[lnd_{\varepsilon_r-1} + 0.293 - \frac{0.517}{\varepsilon_r}\right] \tag{9}$$

$$d_{\varepsilon_r} = \frac{59.95\pi^2}{Z_0\sqrt{\varepsilon_r}}, \tag{10}$$

where h is the thickness of substrate and ε_r is the relative permittivity. Filter implementation from LC circuit to distributed elements is mentioned completely in [6]. In Table 1 the calculated dimensions of distributed elements are shown.

The LPF has been designed on the substrate having ε_r= 2.2 and thickness h = 0.635mm. The frequency response of the designed LPF is shown in Fig. 9. As it can be seen the roll-off rate is low and there is a small insertion loss in pass-band. Also after frequency of 14 GHz the rejection property is going to decrease. In the next part we will see that high roll-off rate, low insertion loss in pass-band and wide stop-band (up to 20 GHz)

could be obtained simultaneously by using proper DGS in correct position.

Table 1: Calculated dimensions of distributed elements.

section	Z_i=Z_l,Z_h(Ω)	$Bl_i(deg)$	W_i (mm)	L_i(mm)
1	57	30	1.6	5.8
2	12	21	12	3.2
3	110	52	1	4
4	12	21	12	3.2
5	57	30	1.6	5.8

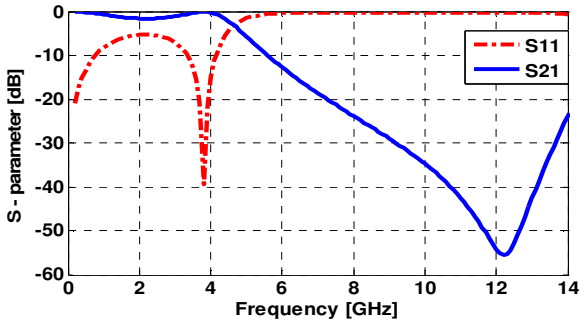

Fig. 9. Frequency response of primary LPF.

B. Adding DGS to primary designed LPF

In this part we want to show by adding DGS units to primary LPF the desired characteristics would be obtained. To design a LPF having a cutoff in 3.4 GHz and a 20 dB rejection band up to 20 GHz the following structure in Fig. 10 is proposed. As it can be seen from Fig. 10 three DGS units (in white color) have been used. Two of them are the same, which are located in a symmetry form. Some parts of DGS units, which are located behind the top layer components are shown with dashed line. The dimensions of the top layer components are like previous section.

The frequency response of the designed LPF is plotted in Fig. 11. It is evident from Fig. 11 that the sharpness of the transition band is really good. The first pole is designed to be located in 3.7 GHz. It has a rejection better than 45 dB. This pole leads to a 3 dB cutoff frequency in 3.4 GHz. By adjusting this pole frequency, which refers to the first DGS unit, the cutoff frequency can be controlled. As shown in Fig. 6, H-type DGS has a wide-band rejection response. By adjusting the pole of H-type DGS, a desired and wide rejection band will be obtained, consequently spurious frequency will be omitted.

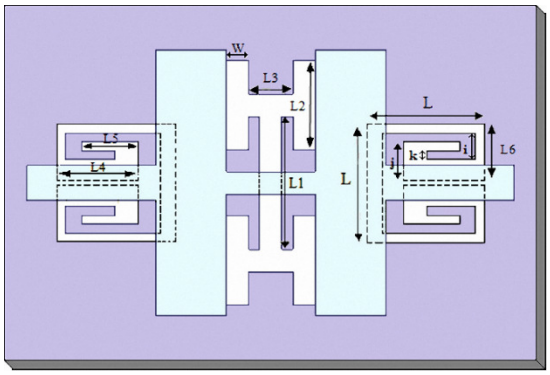

Fig. 10. Schematic of designed LPF.

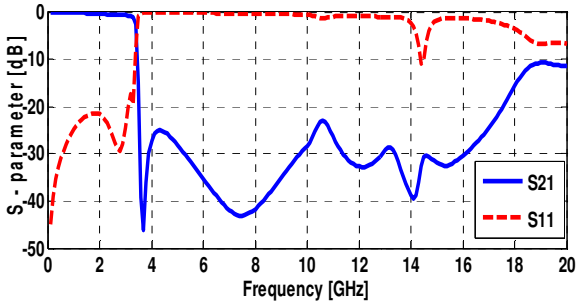

Fig. 11. Simulated frequency response of designed LPF.

IV. FABRICATION AND MEASURMENT

Figure 12 shows the photograph of the fabricated filter. Top view of LPF is in Fig. 12 (a), the dimensions of top view are those, which were designed in section III, part A. The dimensions of DGS unitsin bottom view according to Fig. 10 are as follows: L = 5.3 mm, L1 = 6 mm, a = 4 mm, b = 2 mm, c = 1.5 mm, d = 3.6 mm, e = 2.55 mm, f = 2.5 mm, W = 1 mm, i = 1.2 mm, j = 1.7 mm, k = 0.4 mm.

The proposed LPF has been fabricated on Rogers 5880 substrate having relative permittivity of 2.2 and thickness of 0.635 mm. The measurements have been done by using vector network analyzer Agilent E8363C. Figure 13 shows the comparison between the EM simulation, which is done by HFSS [9] and the measured S-parameters of the designed LPF. Good agreement between them is observed. After frequency of 18 GHz there is a spurious stop-band in simulated results while this spurious stop-band in fabricated LPF is completely suppressed, which is evident in measured results.

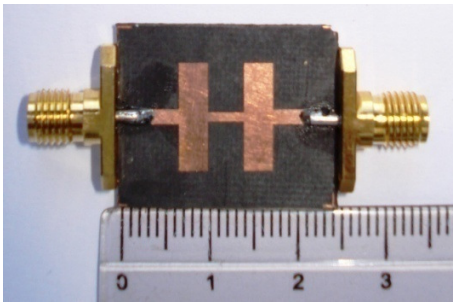

(a)

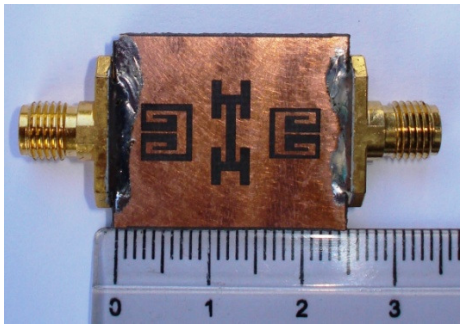

(b)

Fig. 12. Photograph of the fabricated LPF, (a) top view and (b) bottom view.

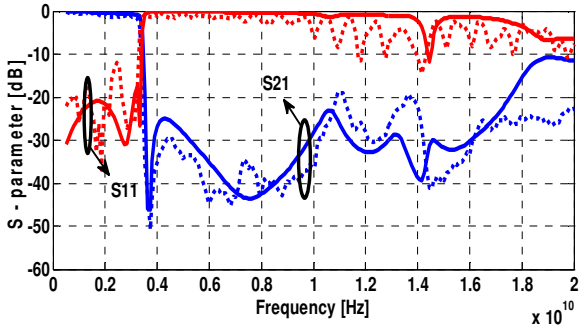

Fig. 13. Simulation (continuous line) and measured (dashed line) results.

V. CONCLUSION

A simple technique has been proposed to design a compact LPF. In this method both advantages of conventional filter design prototype and DGS suppression property are used simultaneously. Finally, a LPF with a really good sharpness and rejection level better than 20 dB up to 18 GHz has been designed and fabricated.The effective size of LPF is 22 mm × 12 mm. Measured results show good agreement with simulated ones.

ACKNOWLEDGMENT

Authors would like to thank the Iran Telecommunication Research center (ITRC) for their technical support.

REFERENCES

[1] A. Rahman, A. Verma, A. Boutejdar, and A. Omar, "Control of bandstop response of Hi-Lo microstrip lowpass filter using slot in ground plane," *IEEE Trans. Microw. Theory Tech.*, vol. 52, pp. 1008-1013, 2004.

[2] J. Lim, C. Kim, D. Ahn, Y. Jeong, and S. Nam, "Design of low-pass filters using defected ground structure," *IEEE Trans. Microw. Theory Tech.*, vol. 53, pp. 2539-2545, 2005.

[3] A. Kumar and A. Verma, "Design of compact seven poles low pass filter using defected ground structure," in *International Conference on Emerging Trends in Electronic and Photonic Devices & Systems*, Varanasi, 2009.

[4] A. Kumar and A. Verma, "Compact low pass bessel filter using microstrip DGS structure," in *Proceedings of Asia-Pacific Microwave Conference*, Yokohama City, 2010.

[5] S. Ting, K. Tam, and R. Martins, "Miniaturized microstrip lowpass filter with wide stopband using double equilateral U-shaped defected ground structure," *IEEE Microwave and Wireless Components Lett.*, vol. 16, no. 5, pp. 240-242, 2006.

[6] D. Pozar, *Microwave Engineering*, New York, John Wiley & Sons, Inc., pp. 392-398, 2005.

[7] A. Verma and A. Kumar, "Synthesis of microstrip lowpass filter using defected ground structures," *IET Microw. Antennas Propag.*, vol. 5, no. 12, pp. 1431-1439, 2011.

[8] S. Rehman, A. Sheta, and M. Alkanhal, "Compact bandstop filter using defected ground structure (DGS)," in *Electronics, Communications and Photonics Conference (SIECPC), Saudi International*, Riyadh, 2011.

[9] Ansoft HFSS V13.

[10] A. Safwat, S. Tretyakov, and A. Raisanen, "Defected ground and patch-loaded planar transmission lines," *IET Microwaves, Antennas & Propagation,* vol. 3, no. 2, pp. 195-204, 2009.

[11] M. Sharkawy, A. Boutejdar, F. Alhefnawi, and O. Luxor, "Improvement of compactness of lowpass/bandpass filter using a new electromagnetic coupled crescent defected ground structure resonators," *Applied Computational Electromagnetics Society (ACES) Journal*, vol. 25,

no. 7, pp. 570-577, 2010.

[12] A. Verma and A. Kumar, "Design of low-pass filters using some defected ground structures," *International Journal of Electronics and Communications (AEÜ)*, vol. 65, no. 10, pp. 864-872, 2011.

[13] T. Edwards and M. Steer, *Foundations of Interconnect and Microstrip Design*, John Wiley & Sons, Ltd., pp. 93, 2000.

Abdolkhalegh Mohamadi was born in Shiraz, Iran, in 1987. He received the B.S. degree in Electrical Engineering from Shiraz University, Iran, in 2009. He got his M.Sc. degree in Telecommunication Engineering from Urmia University, Iran, in 2012. He has participated in several research projects with Microelectronic Research Laboratory and Iranian companies. His research interests include adaptive filter, design and optimization of patch antenna and microstrip filter.

Mohammad Azarmanesh was born in Tabriz, Iran, in 1950. He received his B.S. degree in physics from Tabriz University, Iran, in 1973, his M.S degree inelectrical engineering from the University of Paris VI in 1976, his Ph.D degree in electrical engineering from Poly Technique De Toulouse, France. In 1979, he joined Applied Physics Department in Urmia University, where he worked effectively in founding ElectricalEngineering Department in 1983. In 1998, he worked with three other colleagues in developing Microelectronics Research Center in Urmia University. He is currently the head of Microelectronics Research Center. Dr. Azarmanesh is a member of Iranian Society of Electrical Engineers and a member of IEEE, Institute of Electronics, Information and Communication Engineers (IEICE) of Japan. He has published a book, Electromagnetic Field Theory (Urmia: Urmia University, 1996).

A Numerical Study on the Interaction Between Different Position of Cellular Headsets and a Human Head

R. Aminzadeh[1, 2], A. Abdolali[2], and H. Khaligh[3]

[1] School of Engineering and Science,
Sharif University of Technology-International Campus, Kish Island, 79417-76655, Iran
aminzadeh@kish.sharif.edu

[2] Bioelectromagnetics Research Group, Department of Electrical Engineering,
Iran University of Science and Technology, Tehran, 1684613114, Iran
abdolali@iust.ac.ir

[3] Department of Electrical and Computer Engineering,
University of Waterloo, Waterloo, N2L-3G1, Canada
h8hossei@uwaterloo.ca

Abstract ─ In this paper the interaction between a human head exposed to a bluetooth-based cellular headset in different positions is studied. The exposure to the electromagnetic fields is a concern when people use these devices. The interaction of human head and bluetooth mobile headsets has not been considered in related standards. In this research three installed positions for the headset and two scenarios for the user are defined. In the first scenario the user is in free space and in the second scenario the user is in a car. For both scenarios path loss, antenna gain, total isotropic sensitivity, and specific absorption rate values for three positions of the headset on the head are obtained. SEMCAD X software is used as an FDTD-based simulation platform for our numerical studies. The result of our study can help manufacturers to consider the compatibility of these devices with safety guidelines of electromagnetic exposure specified by relevant institutes. Designers of wireless devices can use results of this study to design new headsets that can be used in an appropriate position while the performance of the device is less affected by the human head and the environment.

Index Terms - Bluetooth, electromagnetic field, FDTD, headset, human head, and SEMCAD.

I. INTRODUCTION

Telecommunication technologies attract more users each day and spread all over the world. Cellular phones are a part of this technology that attract users from all different age groups. The continuous growth of high-end devices forces companies to ensure their new products to be compatible with safety guidelines specified by related standards like IEEE Standard-1528 [1] and International Electrotechnical Commission, IEC 62209-1 [2]. Bluetooth headsets are one of applications that communicate to the cellular phone via bluetooth protocol [3] at 2400 MHz-2450 MHz frequency range. The question is that: *Is user head exposure to bluetooth headsets safe*? To answer this question we aim to evaluate the interaction between a human head exposed to a bluetooth-based cellular headset. Several headset models are produced with different specifications. Each product has a different effect on the user head based on its antenna type, operation frequency, housing, case material, and installed position.

SAR measurement of a human head exposed to a bluetooth headset has not been considered in related standards [1, 2, 4-9]. This is while the interaction between human body and wireless devices has been an interesting subject of studies over the past sixteen years [10-15]. The effect of

Submitted On: Aug. 1, 2012
Accepted On: Jan. 27, 2014

human hand on antenna characteristics of cellular handsets such as total radiated power and far field behavior was studied in [10]. The effect of human body on implantable antennas was inspected in [11-13]. In [14] SAR computation and temperature distribution in human body has been investigated.

In [15] numerical analysis of the interaction between human head and cellular phones has been performed by modeling the phone as a metal box with an antenna inside or outside the box. In [16] authors have studied the effect of different case materials on induced SAR in a human head.

In this paper the finite-difference time-domain (FDTD) method is used because it is simpler and easier to implement, compared with the finite element method (FEM). Despite computational implementation, FDTD is used for easy comparison of our results with SAR measurement standards, which have been developed based on FDTD method (cf. [1, 2]). SEMCAD X software [17], an FDTD-based platform, is chosen due to its user friendly interface and capability of 3D-model analysis.

This paper is organized as follows: section II is a description of designed headset model; human head, car, and antenna models. Section III includes explanation of settings and configurations as well as grid generation. Section IV, presents the simulation results for path loss, antenna gain, total isotropic sensitivity, and specific absorption rate and a comparison of proposed scenarios and finally section V concludes the paper.

II. MODELING

A. Mobile headset

To study the interaction between mobile headsets and human head, a mobile headset model is designed based on real ones usually found at the market. To obtain more accurate results the effect of case material is also considered. In this paper acetal is considered as the case material for the mobile headset, it is used for the case material in mobile phone accessories [18]. Figure 1 shows the headset model. In the rest of the paper the term headset is used instead of mobile headset.

B. Human head

Because of the dependency of electrical properties of human head on frequency a dispersive model, SAM (specific anthropomorphic mannequin) phantom is used for a conservative estimate of SAR in compliance with international exposure standards. SAM is a simplified and homogeneous model of human head that contains SAM shell and liquid. SAM shell is a lossless plastic shell filled with a homogeneous liquid that has electrical properties of head tissue and has an ear spacer. Parameters of this phantom are different from the model introduced by IEEE standard committee (SCC34/SC2/WG1) [19]. The dielectric properties (relative permittivity and electrical conductivity) of SAM phantom [1] and acetal [18] at 2400 MHz – 2450 MHz are extracted and listed in Table 1. As SAM is a homogeneous model relative permittivity and conductivity values are considered. Headset is installed on the left ear at 30°, 52°, and 60°, which are three most common positions. SAM phantom with the headset at the angle of 30° is called model 1. Model 2 is referred to the position of headset at the angle of 52° and model 3 is the chosen name for headset, which is rotated by 60°. Two scenarios are considered for these three models; the first scenario is the situation where each model is simulated in free space. In the second scenario to study the effect of metal and dielectric parts, i.e., complex environments, each model is simulated while the user is in a car.

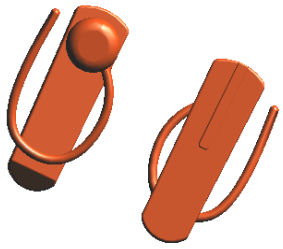

Fig. 1. Designed headset model.

Table 1: Dielectric properties of SAM phantom and acetal at 2400 MHz – 2450 MHz.

Material	$\delta(s/m)$	ε_r
SAM shell	0.0016	5
SAM liquid	1.8	39.2
acetal	0.002	2.8

Figure 2 shows SAM phantom and the headset installed at the angle of 60° (model 3); blue lines indicate the position of the headset in models 1 and 2.

C. Car model

A Ferrari, which is available in SEMCAD X software is chosen as the car model. Car seats, dashboard, glass, tires, and lights are assumed as dielectric parts. Other parts like body, chassis, wheels, door, hood, and brakes are considered as perfect electric conductor (PEC) parts. Figure 3 depicts the user inside the car model.

D. Antenna model

For bluetooth communications a planar inverted F-antenna (PIFA) is used in SEMCAD X. It operates at the range of 2400 MHz – 2450 MHz. A sinusoidal voltage source with a resistance of 50 ohm is used as the excitation source at the antenna feed point. This antenna has a coaxial feed point with the length of 1.8 mm and diameter of 0.2 mm. Figure 4 shows antenna configurations for the frequency range of 2400 MHz to 2450 MHz. Antenna parameters are also described in Table 2.

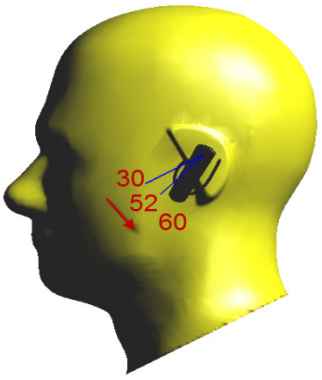

Fig. 2. SAM phantom and the installed headset at three positions.

Fig. 3. Car model and the user inside.

III. FDTD CONFIGURATION

A minimum spatial resolution of 2.0 × 2.0 × 2.0 mm^3 and a maximum spatial resolution of 5.0 × 5.0 × 5.0 mm^3 is set in the x, y, and z directions. The baseline resolution should be selected small enough to prevent ignoring certain baselines. It should also be noticed that selecting too small baseline resolution will results in smaller simulation time step and longer simulation time. As the wavelength is 124.91 mm so the minimum baseline resolution is set to 0.002 λ (0.24982 mm). The maximum step is usually set to approximately λ/10 as a rule-of-thumb [17]. But here to reduce dispersion errors produced automatically by using a non-uniform grid we choose the maximum step as λ/14 (0.07λ), which is equal to 8.7437 mm. The amount of generated FDTD-grid cells for model 1, 2, and 3 are 5.969 M cells (185×135×239) for the first scenario (free space) and 57.027 M cells (590×319×303) for the second scenario (car). In order to achieve a steady state condition, simulation time is set to 15 sinusoidal periods and total number of 2000 time steps with Δt = 3.33 *ps* is considered. To prevent over-refinement in neighboring cells the maximum ratio of the length of neighboring cells (grading ratio) is set as 1.2 and grading ratio relaxation of 10% is selected to increase the dynamics of the gridder. Refining factor is 10 for all solid regions. The absorbing boundary conditions (ABC) is set as uniaxial perfectly matched layer (U-PML) with 10 layers thickness where the minimum level of absorption at the outer boundary is greater than 99.9 %. A bounding box with a refinement in both upper and lower boundary of 0.06 for z-axis is also made for the antenna. The total simulation time was 14 minutes and 85 minutes for free space and the car, respectively (using a computer with core 2 quad CPU and 4 gigabytes of memory).

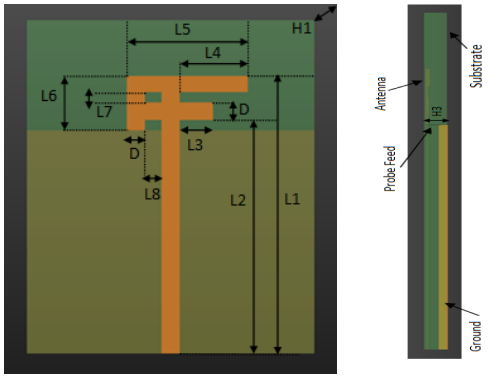

Fig. 4. Antenna configuration for the operation frequency of 2400 MHz – 2450 MHz.

Table 2: Antenna parameters.

Parameter	Length (mm)	Parameter	Length(mm)
L1	50	L5	21
L2	41.95	L6	10
L3	5.9	L7	1.95
L4	11.9	L8	3
D	3.05	H1	0.1

IV. RESULTS AND DISCUSSION

A. Path loss

We extract the simulation results for E-field and plot them in MATLAB™ software. The results are depicted in Figs. 5 and 6 for three models in both environments. The horizontal axis shows the distance that the E-field passes through the head from the left ear and the vertical axis shows the E-field strength in dB. These values are listed in Table 3. From the results it can be seen that the obtained path loss values for human head inside the car are lower than the free space due to the metal parts (frame) of the car that might serve as a shield and minimize the radiated energy, which results in an increase of E-field. As the headset angle increases, the path loss values for three models decreases in both scenarios. In other words by changing the position of the headset from 30° to 60°, the electric field drops to zero at a longer length. In model 2 the E-field has two lobes and is different from models 1 and 3. The reason is that at the angle of 52° the antenna is closer to the tissues that have high amount of water such as mouth and nose that attenuates the electric field for a short distance in the middle of the field path in the head because of their shape. The minimum path loss values (maximum E-field) are obtained for model 3 inside the car and free space. Computed maximum values of path loss are for model 1 in both scenarios.

B. Antenna gain

Simulated antenna gain for three models inside the car and free space were obtained and listed in Table 4. In free space by changing the headset position from model 1 to 3, gain value decreases. As the headset position changes from 30° to 60°, antenna radiation power decreases due to the reflection of some parts of radiated waves by the head. When the user is inside the car, antenna gain decreases more than free space because of radiated wave's reflection by metal parts in the car. Maximum gain value is obtained for model 1 (2.25 dBi) in free space and for model 2 (-5.42 dBi) inside the car. The antenna gain for models 1 and 2 are better than model 3 in free space. It can also be stated that the antenna gain is affected by the glass inside the car that absorbs more power than other dielectric parts as it is closer to the headset.

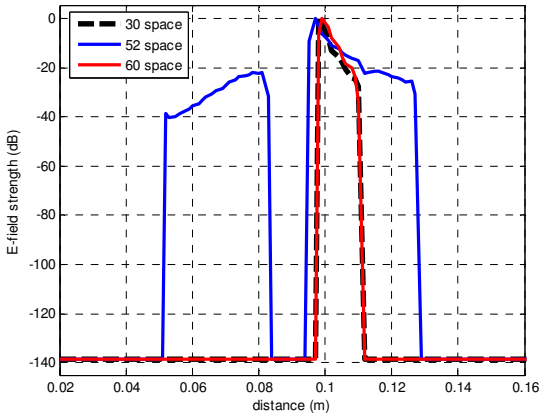

Fig. 5. Path loss simulations in free space; installation degrees are 30°, 52°, and 60°.

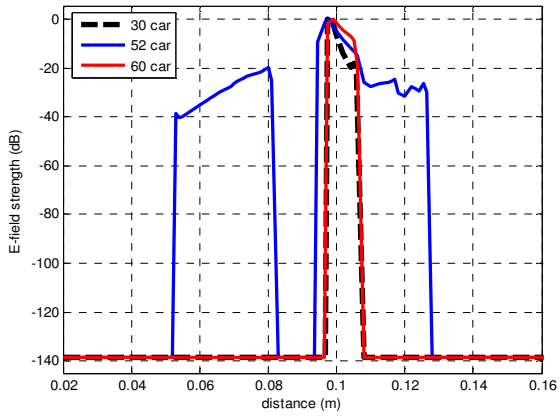

Fig. 6. Path loss simulations in car; installation degrees are 30°, 52°, and 60°.

Table 3: Simulated path loss values in dB.

Model	Model 1	Model 2	Model 3
Position	30°	52°	60°
Free Space	24.2	21.8	20.1
Car	20.8	19.3	9.6

Table 4: Simulated gain values in dBi.

Model	Model 1	Model 2	Model 3
Position	30°	52°	60°
Free Space	2.25	-2.40	-3.08
Car	-5.81	-5.42	-10.45

C. Total isotropic sensitivity

Total isotropic sensitivity (TIS) is a parameter used to determine the receiving performance and the efficiency of a wireless device. For a bluetooth-based headset TIS can be related to the maximum distance from the cellular phone at which the headset can operate well. Antenna gain, antenna mismatch, and noise can affect TIS. Table 5 describes simulated TIS values for three models inside the car and free space. As it can be seen in Table 5 the value of TIS in model 3 decreases compared with 1 and 2 while the user is in free space. When the headset position changes from model 1 to 3 in free space, the headset (antenna) interacts with more parts of the head and the impedance increases. In the car, the head impedance in model 2 is smaller than 1 and 3 and the best TIS value is obtained for model 2. On the other hand, for model 1 in the car the headset antenna is closer to the roof's foam and in model 3 the antenna is closer to the seats so a part of the transmitted energy is absorbed by these dielectrics in the car and results in fewer TIS.

D. SAR

In SAR computation by FDTD, the electric field components at the voxel edges are computed in the x, y, and z directions. SAR is defined as follows,

$$SAR = \frac{\sigma_E}{\rho}|E|^2, \quad (1)$$

where σ_E and ρ are the electric conductivity and mass density of the tissue, respectively, and $\boldsymbol{E}$ is the electric field. SEMCAD X software supports spatial peak SAR measurement defined by IEEE standard-1529 [9].

Antenna input power is set to 0.0025 W as the maximum radiation power for the second class bluetooth devices (headsets) in 2.4 GHz frequency range. Table 6 describes the results of SAR numerical measurements for three models in free space and inside the car. Based on the results the maximum value of SAR_{1g} is for model 1 in free space (0.1228 W/Kg) and is for model 2, inside the car (0.1153 W/Kg). The maximum value of SAR_{10g} in free space and inside the car belongs to model 2, 0.0458 W/Kg and 0.0486 W/Kg, respectively. It can be seen that SAR values inside the car are higher than SAR values in free space. As mentioned in section IV A, this is due to the metal frame of the car that might serve as a shield and minimize the radiated energy, which results in an increase of SAR. The results show that the SAR_{1g} and SAR_{10g} reach their minimum values for model 3 in free space and inside the car. As mentioned before, model 3 is closer to the seats and more energy is absorbed by the seats, so the SAR value decreases for model 3 compared with 1. All the results are lower than 0.123 W/Kg while due to IEEE C95.1-2005 standard the spatial peak SAR limit in USA is 1.6 W/Kg per 1g tissue and for Japan and European countries it is 2 W/Kg per 10 g tissue [20].

Table 5: Simulated TIS values in dBm.

Model	Model 1	Model 2	Model 3
Position	30°	52°	60°
Free Space	-56.32	-45.05	-38.26
Car	-30.90	-33.31	-26.71

Table 6: Averaged SAR_{1g} and SAR_{10g}values in human head for three models in free space and the car.

Free Space			
Model	**Model 1**	**Model 2**	**Model 3**
Position	**30°**	**52°**	**60°**
SAR_{1g} in head	0.1228	0.1075	0.0535
SAR_{10g} in head	0.0455	0.0458	0.0203
Car			
Position	**30°**	**52°**	**60°**
SAR_{1g} in head	0.0967	0.1153	0.0818
SAR_{10g} in head	0.0358	0.0486	0.0287

It is concluded that the safer model is model 3 that has the least SAR values both in free space and inside the car. Figures 7 and 8 show the slice field distribution of SAR 1g and 10g values for three models inside the car and free space, respectively. It can be seen that in model 1 the peak spatial SAR occurs at a higher region and closer to the ear compared with model 3.

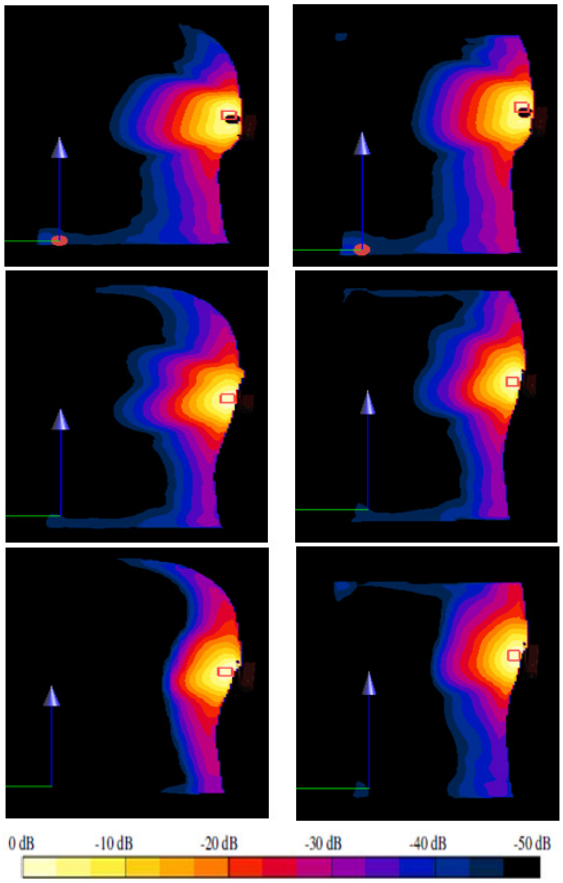

Fig. 7. Slice distribution of spatial peak SAR averaged over 1g for model 1, 2, and 3 (from top to bottom) in free space (left column) and inside the car (right column).

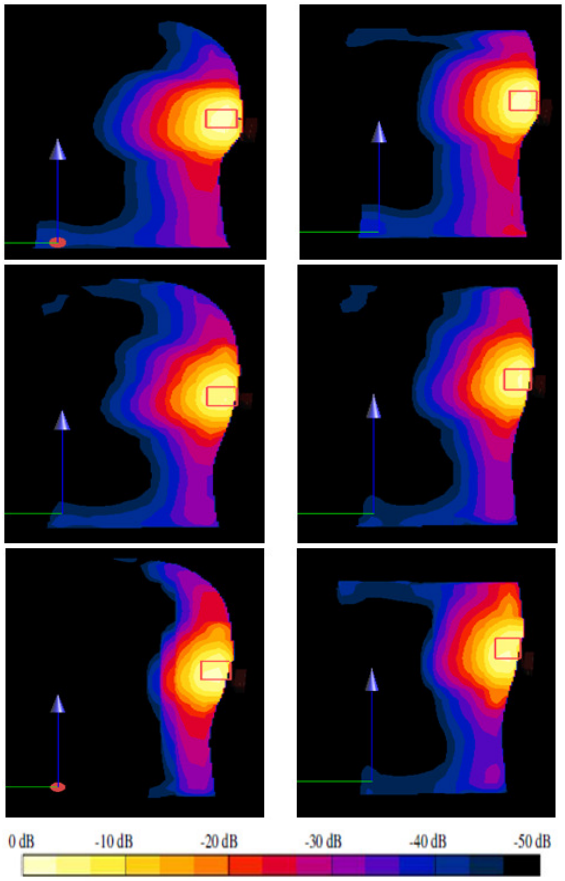

Fig. 8. Slice distribution of spatial peak SAR averaged over 10g for model 1, 2, and 3 (from top to bottom) in free space (left column) and inside the car (right column).

V. CONCLUSION

In this paper the interaction between a mobile headset and the human head was modeled and simulated. A mobile headset was designed and SAM phantom was used as a homogeneous head model. Three positions were defined for the mobile headset. A PIFA was used as a suitable antenna for bluetooth communications. Two scenarios where the user is in free space and inside the car were described. SEMCADX software was used as an FDTD-based simulation platform for our numerical studies. Finally, we discussed and obtained results for path loss, antenna gain, TIS, and SAR. Based on our results the best model in the proposed research was model 3, which had the minimum SAR values for both scenarios where the user was inside the car and in free space. Due to low radiation power of the antenna, a large part of the electric field was absorbed by dielectric parts or was reflected by metal parts in the car. This was while model 3 had the worst antenna gain in the car. The result of our study can help manufacturers to consider the compatibility of these devices with safety guidelines of electromagnetic exposure specified by relevant institutes. Designers of wireless devices can also use these results to design new headsets that can be used in an appropriate position while the performance of the device is less affected by the human head and the environment.

ACKNOWLEDGMENT

The authors would like to thank Schmid and Partner Engineering AG (SPEAG) for providing the license for SEMCADX software through *SEMCAD X for Science* agreement. In addition the

authors wish to thank Dr. K. Hajsadeghi from Sharif University of Technology for proof reading the paper and M. Ashiri and Marjan Joorabchi, M.Sc. students at Sharif University of Technology-International Campus, for their helpful comments on preparing the final draft of this paper.

REFERENCES

[1] IEEE Recommended Practice for Determining the Peak Spatial-Average Specific Absorption Rate (SAR) in the Human Head from Wireless Communications Devices: Measurement Techniques, IEEE Standard-1528, Dec. 2003.

[2] Standard, "Human exposure to radio frequency fields from hand-held and body-mounted wireless communication devices — Human models, instrumentation, and procedures — Part 1: Procedure to determine the specific absorption rate (SAR) for hand-held devices used in close proximity to the ear (frequency range of 300 MHz to 3 GHz)," IEC 62209-1, 2006.

[3] IEEE 802.15 Working Group for WPAN. Available online: http://www.ieee802.org/15/.

[4] Standard, "Product Standard to Demonstrate the Compliance of Mobile Phones with the Basic Restrictions Related to Human Exposure to Electromagnetic Fields (300 MHz – 3 GHz)," European Committee for Electrical Standardization (CENELEC), EN 50360, Brussels, 2001.

[5] Standard, "Basic Standard for the Measurement of Specific Absorption Rate Related to Exposure to Electromagnetic Fields from Mobile Phones (300 MHz – 3 GHz)," European Committee for Electrical Standardization (CENELEC), EN 50361, Brussels, 2001.

[6] Standard, "Specific Absorption Rate (SAR) Estimation for Cellular Phone," ARIB Standard-T56, 2002.

[7] Standard, "Evaluating Compliance with FCC Guidelines for Human Exposure to Radio Frequency Electromagnetic Fields," supplement C to OET Bulletin 65 (Edition 9701) FCC, 1997.

[8] Standard, "Electromagnetic Radiation - Human Exposure," ACA Radio Communications Standard, Schedules 1 and 2, 2003.

[9] Standard, "IEEE standard, Recommended Practice for Determining the Peak Spatial-Average Specific Absorption Rate (SAR) associated with the use of wireless handsets- computational techniques," IEEE-1529, draft standard.

[10] J. Krogerus, J. Toivanen, C. Icheln, and P. Vainikainen, "Effect of the human body on total radiated power and the 3-D radiation pattern of mobile handsets," *IEEE Trans. Instrum. Meas.*, vol. 56, no. 6, Dec. 2007.

[11] J. Gemio, J. Parron, and J. Soler, "Human body effects on implantable antennas for ISM bands applications: models comparison and propagation losses study," *Progress In Electromagnetics Research*, vol. 110, pp. 437-452, 2010.

[12] N. Vidal, S. Curto, J. M. Villegas, J. Sieiro, and F. M. Ramos, "Detuning study of implantable antennas inside the human body," *Progress In Electromagnetics Research*, vol. 124, pp. 265-283, 2012.

[13] H. Virtanen, J. Huttunen, A. Toropainen, and R. Lappalainen, "Interaction of mobile phones with superficial passive metallic implants," *Phys. Med. Biol.*, vol. 50, no. 26892700, 2005.

[14] T. Wessapan, S. Srisawatdhisukul, and P. Rattanadecho, "Specific absorption rate and temperature distributions in human head subjected to mobile phone radiation at different frequencies," *International Journal of Heat and Mass Transfer*, vol. 55, no. 347359, 2012.

[15] M. Okoniewski and M. Stuchly, "A study of the handset antenna and human body interaction," *IEEE Trans. Microw. Theory Tech.*, vol. 44, no. 10, pp. 1855-1864, 1996.

[16] R. Aminzadeh, M. Ashiri, and A. Abdolali, "SAR computation of a human head exposed to different mobile headsets using FDTD method," *In Proc. Progress In Electromagnetics Research Symposium*, KL, Malaysia, pp. 1131-1134, March 2012.

[17] SEMCAD X by SPEAG, "Reference Manual for the SEMCAD Simulation Platform for Electromagnetic Compatibility, Antenna Design and Dosimetry," Schmid & Partner Engineering AG (SPEAG), http://www.speag.com.

[18] Y. Cho, S. Hwang, O. Ishida, and S. Park, "Dual band internal antenna of PIFA type for mobile handsets and the effect of the handset case and battery," *In Proc. of IEEE Antennas. Propag. Int. Symposium*, vol. 1A, pp. 487-490, July 2005.

[19] B. Beard, W. Kainz, T. Onishi, et al., "Comparisons of computed mobile phone induced SAR in the SAM phantom to that in anatomically correct models of the human head," *IEEE Trans. Electromagn. Compat.*, vol. 48, no. 2, pp. 397-407, 2006.

[20] Standard, "IEEE Standard for Safety Levels with Respect to Human Exposure to Radio Frequency Electromagnetic Fields, 3kHz to 300 GHz, Amendment2: Specific Absorption Rate (SAR) Limits for the Pinna," IEEE Standard C95.1b, 2005.

Reza Aminzadeh was born in Iran in 1987. He received his B.Sc. degree in Electrical Engineering in 2010. He is currently working toward the M.Sc. degree in Electrical Engineering at Sharif University of Technology-International Campus. Currently he works as a research assistant at computational electromagnetics laboratory at Sharif University of Technology. Since 2010 he has been with the Bioelectromagnetics research group, at Iran University of Science and Technology (IUST) as a research assistant.

He has been Associate editor of PEAK magazine (National Scientific Student's Organization of Electrical Engineering) from 2011 to 2012. His main research areas are computational electromagnetics, wave propagation modeling in human body, bioelectromagnetics, microwave imaging and tomography. Since 2012 he has been a member of computational electromagnetic technical committee (TC9) of the IEEE EMC society and TC95-subcommittee 4 of international committee on electromagnetic safety (ICES). He served as technical program committee member of IEEE International Conference on Ultra-Wideband (ICUWB) in 2012 and 2013 and also IEEE international symposium on electromagnetic compatibility (EMC 2013).

Ali Abdolali was born in Tehran, Iran, on May3, 1974. He received B.S. degree from the University of Tehran, and M.S. degree from the University of Tarbiat Modares, Tehran, and the Ph.D.degree from Iran University of Science and Technology (IUST), Tehran, Iran, all in Electrical Engineering, in 1998, 2000, and 2010, respectively. In 2010, he joined the Department of Electrical Engineering, Iran University of Science and Technology, Tehran, Iran, where he is an assistant Professor of electromagnetic engineering. His research interests include electromagnetic wave scattering, Radar Cross Section (RCS), Radar Absorbing Materials (RAM), EM Waves controlling, cloaking, metamaterials, EM Waves in complex media (anisotropic, inhomogeneous, dispersive media, metamaterials), Frequency Selective Surfaces (FSS), Bio-electromagnetism (BEM). He has authored or coauthored over 40 papers in international journals and conferences.

Hadi Hosseinzadeh Khaligh received his B.Sc. in Materials Engineering at the University of Tehran, Iran. He is currently pursuing his M.Sc. in Nanotechnology in the Department of Electrical and Computer Engineering. His research is focused on the integration of metal nanowires into novel electronic devices.

Ultra Low RCS Measurement Using Doppler Frequency Shift

E. S. Kashani, Y. Norouzi, A. Tavakoli, and P. Dehkhoda

Department of Electrical Engineering, Amirkabir University of Technology, Tehran, Iran
alamkashani@aut.ac.ir, y.norouzi@aut.ac.ir, tavakoli@aut.ac.ir, pdehkhoda@ aut.ac.ir

Abstract **–** A new clutter removal method is proposed for ultra-low RCS measurement in anechoic chamber. In the proposed method, the target is moved along the line of sight of the radar in a sinusoidal manner. This movement generates some Doppler frequency shift. At the receiver, a filter matched to this Doppler shifter signal is implemented digitally. While the matched filter removes clutter signal largely it preserves the echo from the moving target. As it is shown through analytic estimation as well as simulations, the method can attenuate the clutter and noise level far beyond previously suggested methods. It also removes some of the difficulties in higher frequencies that exist in previous methods.

Index Terms **-** Clutter signal, Doppler effect, matched filter, and radar cross section (RCS) measurement.

I. INTRODUCTION

Radar cross section (RCS) is a crucial term in radar equation and the detection range of any radar system changes with the fourth root of the RCS of the target. This fact necessitates the true estimation of the RCS of the target before any radar system design.

While the RCS of simple shapes can be calculated analytically, for most complicated objects the analytical solutions cannot be obtained easily. In such cases, even computer simulation programs are not so helpful since these programs take a lot of time and memory to solve the RCS problem. Therefore, direct RCS measurement methods are the best practical ones to determine the true RCS of these targets. Basically in the methods the target is placed in an anechoic chamber and is illuminated using radar with known parameters (i.e., transmitted power, antenna gain, and system losses). The echo signal is received and processed and the power of this signal is measured. Then the radar equation is used to determine the RCS of the target that is denoted by σ in the following equation [1],

$$\sigma = \frac{P_r}{P_T} \times \frac{(4\pi)^3 R^4 L}{G^2 \lambda^2}. \quad (1)$$

Here P_r and P_T are the received and transmitted powers, respectively. R is the distance from radar phase center to target, L is the radar system loss, G is the radar antenna gain, and λ is the wavelength. While the basic method is capable to estimate the RCS of large objects, one is not sure about its accuracy for small targets. This is because any practical anechoic chamber has some (minor) wave reflection. The reflection is received by radar and is added to that of the object. For small objects, the additional signal may be comparable with target echo and will cause measurement error. Modern design of novel stealth vehicles with reduced radar signatures has made the conventional RCS measurement methods inefficient. Therefore, other methods should be developed to be able to measure much smaller RCS values. Some authors have proposed other methods in order to get better results in estimating the RCS of small objects.

Since the very beginning of radar appearance, estimation of the radar cross section (RCS) of targets has been of great concern to radar designers. Since a 1dB reduction of the RCS of the target yields roughly 6% reduction of radar detection range. While the RCS of simple objects can be calculated using well-defined electromagnetic methods such as method of moments (MOM) [2], or physical optics (PO) [3], it is not easy to find a simple solution for RCS of complex objects. Since then many people have developed different methods for RCS measurement or estimation.

Submitted On: Sept. 29, 2012
Accepted On: Jan. 27, 2014

One of the primary and basic methods of RCS measurements is to illuminate the target with nano-second pulses and measure the power of the reflected echo [4], this measurement should be done in an anechoic chamber. The necessary conditions for such an anechoic chamber have been presented in [5]. Although the nano-second pulse method is simple in theory, it needs a high power transmitter as well as a large anechoic chamber. The above deficiencies have led to find some simpler measurement methods such as linear FM (LFM) [6] or stepped frequency methods [7]. Also in [8], Polcrass has described the implementation of stepped frequency method with low PRF pulses to achieve the RCS estimation for big objects. Schöne and Riegger have described in [9] how a vector network analyzer can be used to measure the RCS of targets by using FMCW or stepped frequency stimulation. Kent in [10] has described some calibration targets to be used for RCS measurement device calibration. The accuracy of the RCS measurement methods is evaluated in [11]. A review of all basic RCS measurement methods can be found in [12].

Many RCS measurement researches concentrate on polarimetric RCS estimation [13]. In [14], Sarabandi and his team have developed a polarimetric RCS measurement by using single antenna. Muth in [15] and Welsh, Kent and Buterbugh in [16], have described a calibration method for such a task.

Large chambers are required for many ordinary RCS measurements but they are not accessible in many cases. To overcome this difficulty some authors have concentrated on RCS measurement techniques for small chambers [17, 18], and on near field to far field transformation [19]. In [20] Broquetas and Palau have produced a planar wave in a small chamber by using an offset parabolic reflector. Much of the recent research about RCS measurement has been concentrated on clutter and noise removal in order to achieve result that is more accurate. In [21] Hantscher and Diskus have developed a wide band noise reduction method for accurate RCS measurement. In [22] target moved along the line of sight and the change in the phase of reflected echo is used in an LMS estimation returned process to remove clutter contaminations from signal. In [23] Broquetas and Palau have suggested inverse synthetic aperture radar (ISAR) processing methods to remove the clutter signal during target RCS measurement. Finally, Burns and Subotic in [24] have proposed independent component analysis (ICA) for clutter removal from target echo signal.

In this paper, we propose a clutter reduction method based on Doppler frequency shift and matched filter concept. The combination of our method with previous ones can reduce the noise and clutter signal drastically, so enables the system to estimate the RCS of ultra-small objects.

The paper is organized as follows: In section II, basic low RCS measurement methods are presented and their difficulties are expressed from [7, 25, 26]. In section III, we present our new method and apply it to a concrete case. In section IV, the method is simulated in order to evaluate its performance under more realistic conditions. The final section gives the conclusion and some suggestions for more research.

II. BASIC CLUTTER REMOVAL METHODS

While different authors have presented different RCS measurement methods, not all methods are capable to measure the RCS of ultra- small object. In this section, we will study the methods applicable for ultra-small object. The most well-known low radar cross section measurements are as follows.

A. Time gating in step frequency method

In step frequency continuous wave measurement, RCS is measured at many different frequencies, and inverse Fourier transform (IFFT) is used to convert frequency samples to time (range). The time (range) profile helps us to eliminate signals not equidistance to the antenna as the target. This elimination is called time gating. As it is shown in [7], by using the time gating, all clutters that are not equidistant with target to the radar would be removed. But equidistant clutters cannot be removed.

B. Coherent background subtraction method

In CBS method, a background RCS measurement is made over the desired frequency band in the empty chamber, then the target is placed in the chamber and the measurement is repeated. If the scattering vector (phase and amplitude) of the first stage is subtracted from the scattering vector of the second one at each

measured frequency and aspect angle, the result is the right target's signal. As it is shown in [25] this method have several difficulties especially at higher microwave frequencies.

C. Direct path signal removal method

The principle of the method as it is shown in [26] is the same as the background subtraction method. One can see the structure of the method in Fig. 1.

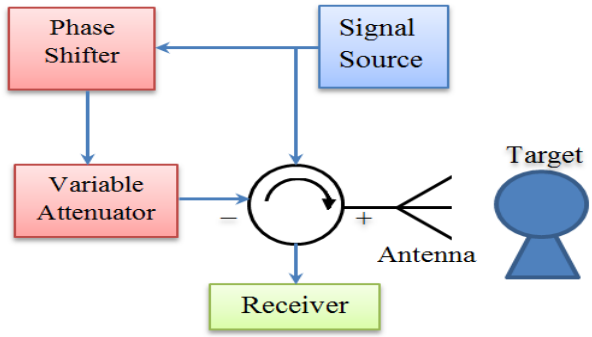

Fig. 1. System block diagram for direct path signal removal method.

In the method with no target in anechoic chamber, the attenuator and the phase shifter is adjusted so that at the output of the power combiner just noise can be detected. In the next step, target is placed in chamber and in this case, the signal received from the collector is the target's RCS. In this method, the same difficulty appears as in the background subtraction method. Therefore, in high frequencies, it cannot be applied. Also because of the restricted dynamic range of the phase shifter and attenuator, clutter cancellation cannot be done properly. Therefore, the method cannot achieve high dynamic ranges.

III. THE METHOD BASED ON DOPPLER FREQUENCY SHIFT

Figure 2 shows the structure of the proposed method. In the below design, the following methods are used simultaneously to reduce the existing clutter: direct path signal removal, time gating clutter removal, and Doppler frequency shift effect.

In the following, all previous methods are formulated and the level of clutter removal is determined.

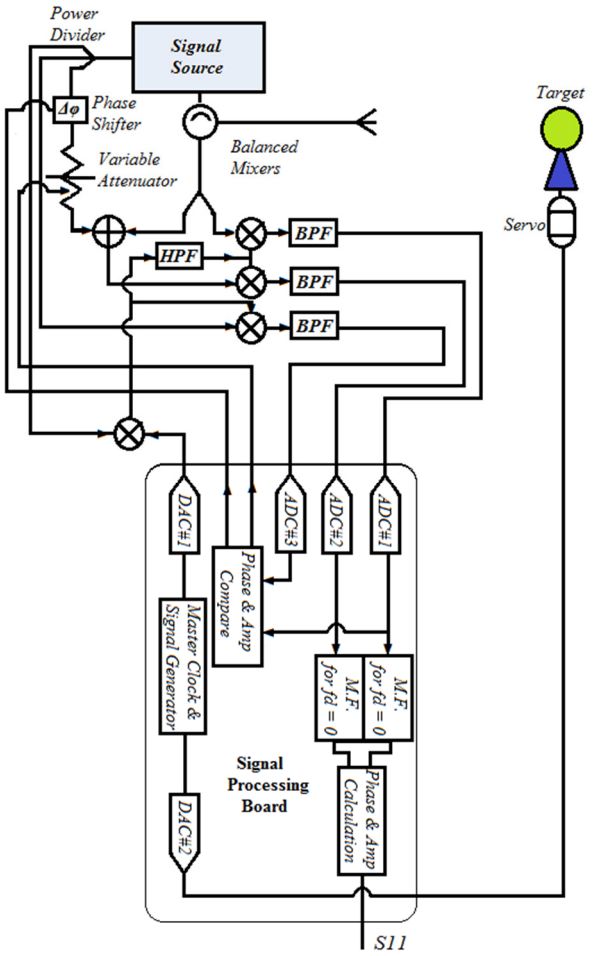

Fig. 2. System block diagram of Doppler frequency shift method.

A. Direct Path signal removal

As it can be seen in Fig. 2 signals of ADC #2 and ADC #3, are compared, and the subtraction of phases and amplitudes calculated, while target is placed at a fixed position. In this case, depending on gotten vector, direct path signal is attenuated and phase shifted and added to the signal received from the antenna. Ideally, one should get zero amplitude from the sum. However, in practice, because of some errors in the phase and amplitude estimation and also phase shifter and attenuator adjustment, the result is not zero. The errors in phase and amplitude estimation can be reduced by lengthening the observing interval and calculating long-term FFT. However, the errors in the phase shifter, attenuator adjustment, and time averaging still remain. If the first step of attenuator and phase shifter (which have least amount) are equal to Δa and $\Delta \varphi$,

respectively, then the output of collector is equal to,

$$x = \cos wt - \Delta a \cos(wt + \Delta\varphi)$$
$$x = (1 - \Delta a \cos \Delta\varphi) \cos wt + \Delta a \sin \Delta\varphi \sin wt = A \cos(wt + \psi) \quad . \tag{2}$$

Here A and ψ are equal to,

$$A = \sqrt{(1 - \Delta a \cos \Delta\varphi)^2 + \Delta a^2 (\sin \Delta\varphi)^2} = \sqrt{1 + \Delta a^2 - 2\Delta a \cos \Delta\varphi} \tag{3}$$

$$\psi = \tan^{-1}\left(\frac{\Delta a \sin \Delta\varphi}{1 - \Delta a \cos \Delta\varphi}\right). \tag{4}$$

The amplitude of the remained signal (i.e., A) related to the original signal is presented in Fig. 3. Figure 3 shows that for any value of Δa and small values of $\Delta\varphi$, the attenuation level tends to,

$$A = 1 - \Delta a. \tag{5}$$

Usually in practical systems, one cannot get Δa, to be less than 0.25 dB. Therefore referring to Fig. 3, direct path signal removal method attenuates clutter at most 30dB.

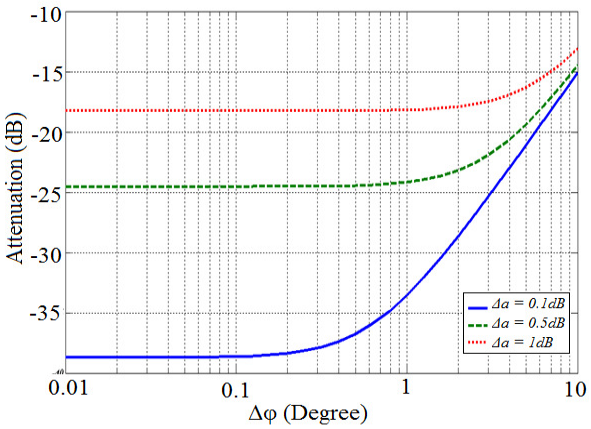

Fig. 3. Clutter removal level as a function of attenuation and phase shift steps.

B. Time gating clutter removal

In time gating method RCS measurement is done with different frequencies and at each frequency, phasor of scattered signal is obtained. However, it is shown in [27], with the use of inverse Fourier transform of these phasors, time domain profile is extracted and scattering from different points is decomposed. Actually if the number of frequencies equal to N and separation frequency equals ΔF, signals are mapped with resolution of $\frac{c}{2N\Delta F}$ meter between 0 to $\frac{c}{2\Delta F}$ meter. It means that clutter is divided into N parts and just one of them is equidistant to the target and that one will remain. Therefore, if we imagine that the clutter signal is homogenous then the method attenuates the clutter N times. However, if the clutter signal is not homogenous and no part of the signal is equidistant with the target to the radar, then the attenuation rate is more than that.

C. Doppler frequency shift effect

In Doppler frequency shift method, the target that is mounted on special pylons starts to move back and forth along the radar line-of-sight. The movement has a sinusoidal pattern with total displacement equals to 2Δx and angular frequency equals to ω_m. Then with $\Delta x \ll R$ (R is the mean distance of the target to antenna) the received signal is as follows,

$$S(t) = A_T \cos(w_c(t - \frac{\Delta x}{c} \cos \omega_m t)). \tag{6}$$

The signal is brought to the IF band, which is equal to,

$$S_{IF}(t) = A_T \cos\left(w_{IF} t - \frac{\Delta x . w_c}{c} \cos(\omega_m t)\right). \tag{7}$$

Scattered echo of stationary targets (i.e., clutter) in IF band is equal to,

$$S_c(t) = A_c \cos(w_{IF} t). \tag{8}$$

Now both target and clutter signals are passed through the filter that is matched to the echo of the moving target. The Impulse response of the matched filter equals,

$$h(t) = S_{IF}(T_s - t). \tag{9}$$

Here T_s is the total observation (sampling time). While passing through the matched filter, target echo will increase and the clutter signal is attenuated considerably. Figure 4 shows amplitude of the matched filter output for a target and a clutter with the same RCS. Here Δx equals 10 cm, f_m=10 Hz, and f_c=10 GHz.

It is easy to show that the clutter removal depends on $\Delta x/\lambda$, ω_m, T_s and maximum distance of the targets (maximum delay). However, it is not easy to extract a simple (closed form) equation for attenuation level, in Fig. 5, Monte-Carlo simulation method is used to find this attenuation level. In the simulations the chosen T_s equals to 10 second, τ_d=10 microsecond, $0.1 < \frac{\Delta x}{\lambda} < 10$ and ω_m =0.1 or 1 or 10.

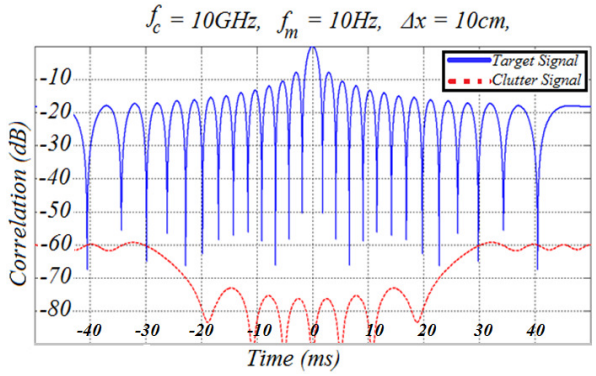

Fig. 4. The target and clutter signals at the output of matched filter (the target and the clutter have the same RCS).

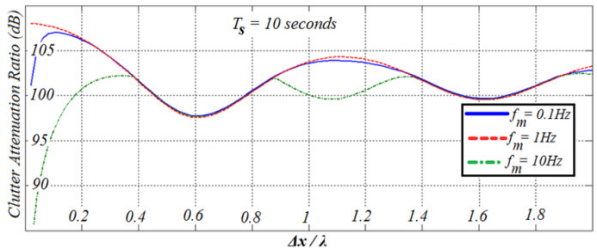

Fig. 5. Clutter removal level as a function of the frequency and the range of target movements (10 seconds signal integrations).

As it is seen in Fig. 5, the maximum target displacement should be at least one tenth of the wavelength. But the bigger Δx will not improve the attenuation level substantially, and the oscillation frequency does not have a great impact on the clutter removal performance of the system. The figure just shows that for Δx larger than one tenth of a wavelength, the clutter removal is about 100 dB.

In Fig. 6 the scenario is repeated with T_s = 1sec. It can be seen that 0.1 Hz oscillation frequency is not desirable anymore. Referring to this case if Δx almost equals two tenth of the wavelength, then the clutter removal level would be about 80 dB.

IV. SIMULATION RESULTS

In this section, the proposed Doppler processing method is simulated in some ideal and also practical cases. The results are compared against the theoretical values obtained in section III. In these simulations, 21 point-scatterers are assumed to be placed from 3 meters to 5 meters from the transmitting antenna. The RCS of these scatterers are assumed to be random valued with an exponential distribution. The mean RCS of each point scatterer equals 10^{-2} m^2. The target is also assumed to be a point scatterer with an RCS equals to 10^{-7} m^2. The distance between the target and the transmitting antenna is four meters, and the target vibrates about ±5 cm around this point in each 100 milliseconds.

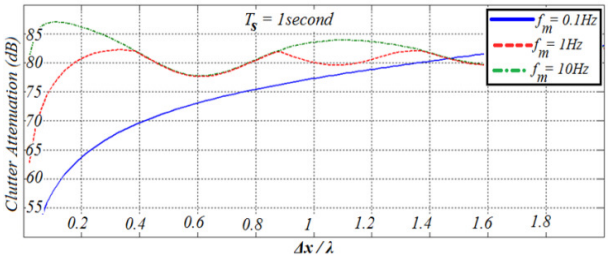

Fig. 6. Clutter removal level as a function of the frequency and the range of target movements (one second signal integrations).

The measurement system includes a frequency synthesizer operating from 8 GHz to 12 GHz (X-band), an antenna with 15 dBi gain, and a power amplifier that produces 1 milliwatt (0 dBm) at its output. The received signal is down converted to 1 kHz and is filtered with a narrow 100Hz band pass filter. The signal is sampled at 10 kilo-sample-per-second (ksps). The samples are collected for the duration of 10 seconds, then the proposed Doppler process in the previous section is carried out to extract target signal from that of the clutter.

In Fig. **7**, the power of the received signal at different frequencies is sketched before and after Doppler process. These two graphs are compared to the one that is obtained if just the target is under system illumination. As it is seen, before the process, the graph mainly represents the clutter's echo and there is no similarity between the power of the received signal and that of the right target. However, after Doppler processing there is a great coincidence between the processed signal and the true signal values. Based on Fig. 7, the clutter to signal power ratio (CSR) before and after Doppler processing is shown in Fig. 8. As it is observed, while in the raw signal the clutter is 50 dB more powerful than the target signal on average, after the process this ratio decreases roughly to -70 dB. This fact shows that the Doppler processing

method reduces the clutter signal at about 120 dB. The attenuation value is more than the one estimated in the previous section. This is because the clutter is just one point scatterer while in the simulations the clutter consists of 21 point scatterers.

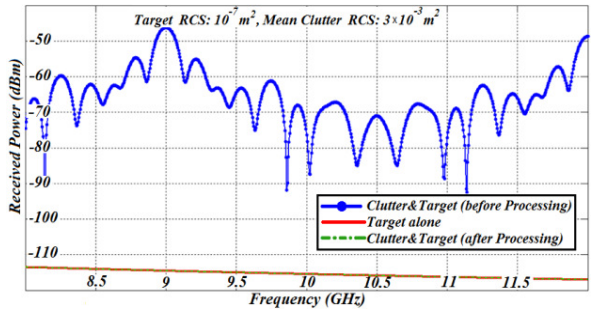

Fig. 7. Amplitude of received signal at different frequencies, before and after Doppler process (the Target alone (red) and the Clutter &Target after processing (green) curves have negligible differences and these curves are almost jugate).

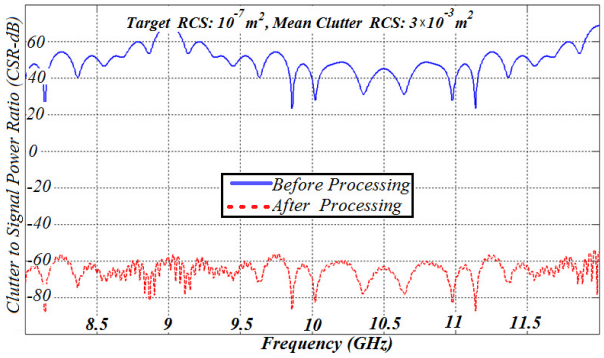

Fig. 8. Clutter to signal power ratio (CSR) before and after Doppler processing.

In the previous simulation an ideal receiver was assumed. However, in practical cases the system suffers from noise and impurities. In what follows the noise and impurity effects have been considered in order to evaluate the performance of the method under some more realistic conditions.

In Fig. 9 simulated model includes thermal noise effect. As it is observed, while at 20dB SNR value an error about 15dB may exist in the predicted received signal, for 30dB SNR, this error will be reduced to less than 5 dB. At 40dB SNR value, on average less than 1dB error will be observed.

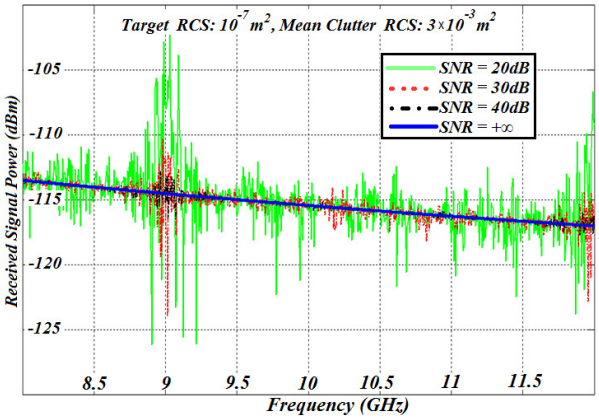

Fig. 9. Effect of input signal to noise ratio on the estimated target's received power.

In Fig. 10 the effect of quantization noise is simulated. Referring to this figure, the noise generated about 1dB error in the estimated signal's received power. It is amazing to observe that the average error is not strongly related to the total number of quantization bits.

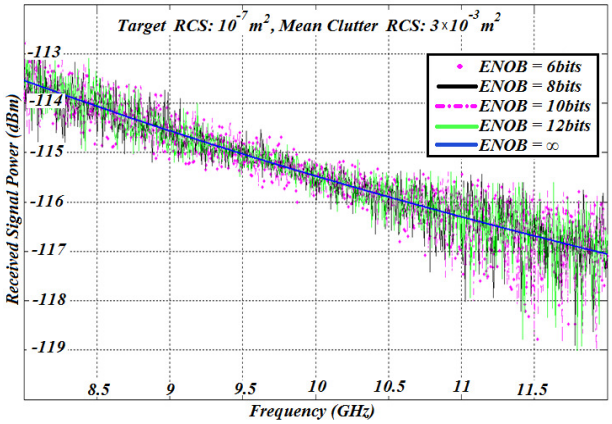

Fig. 10. Effect of quantization noise on the estimated target's received power.

Finally in Fig. 11, the effect of local oscillator impurity is simulated. As it is observed, while 10 degrees phase jitter produce a considerable error on the estimated targets received signal, the effect of impurity will become almost ignorable if the rms phase jitter is reduced to 1degree.

V. CONCOLUSION

In the paper, a new combined method for ultra-low RCS targets has been proposed. We see that with the help of direct path signal removal method, the clutter elimination is between 35 to 45 dB. In

addition, we see that Doppler frequency shift removed clutter between 80 dB to 100 dB. Clutter removal using time gating equals the number of the frequencies. If we have 100 to 1000 frequencies, then clutter attenuation is between 20 to 30 dB. Finally, by the use of the three methods together one can remove clutter 135 dB to 175 dB. This is much better than the previous methods. Of course, we should be aware that when this rate of clutter removal is used, problems like phase noise of oscillators and number of ADC bits will appear. By using simulations, it is shown that the effect of the thermal noise, quantization noise, etc., is so small that can be ignored.

It should be remembered that in our method the signal reflected from the moving part of the mount has the same Doppler nature as the target. So the new method cannot remove this part of the clutter. Regarding this fact, the moving part of the mount should be made of low RCS materials. Also direct signal removal can be used to omit this part of the clutter. However, for very low RCS measurement, more elaborated methods should be found to eliminate the deficiency of the method.

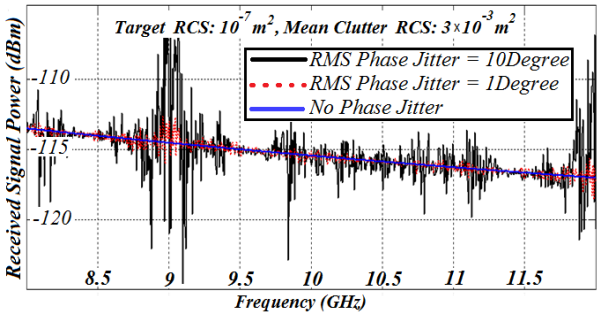

Fig. 11. Effect of local oscillator impurity on the estimated target's received power.

REFERENCES

[1] M. Skolnik, *Radar Handbook*, Third Edition, McGraw-Hill Professional, January 2008.

[2] M. O. Sadiku, *Numerical Techniques in Electromagnetics*, 2nd edition, CRC Press, 2000.

[3] C. A. Bennett, *Principles of Physical Optics*, first edition, Wiley, January 2008.

[4] C. G. Bachman, "Some recent developments in RCS measurement techniques," *Proceedings of The IEEE*, vol. 53, no. 8, pp. 962-974, August 1965.

[5] B. K. Chung, H. T. Chuah, and J. W. Bredod, "A microwave anechoic chamber for radar- cross section measurement," *IEEE Antennas and Propagation Magazine,* vol. 39, no. 3, pp. 21-26, June 1997.

[6] R. T. Lawner, P. F. Blanchard, and S. Gogineni, "Coherent FM-CW millimeter-wave radar systems for radar cross section measurements," *IEEE Transactions on Instrumentation and Measurement*, vol. 39, no. 1, pp. 208-211, February 1990.

[7] P. S. Kao, "Automated step frequency radar cross section measurements," *Antennas and Propagation Society International Symposium*, vol. 20, pp. 237-240, 1982.

[8] R. M. Polcrass, "Radar cross section measurements using target striping," *Telesystems Conference*, vol. 1, pp. 183-186, 1991.

[9] G. Schöne, S. Riegger, and E. Heidrich, "Wideband polarimetric radar cross section measurement," *Antennas and Propagation Society International Symposium*, vol. 2, pp. 537-540, 1988.

[10] B. M. Kent, "Comparative measurements of precision radar cross section (RCS) calibration targets," *IEEE Antennas and Propagation Society International Symposium*, vol. 4, pp. 412-415, 2001.

[11] B. M. Welsh and J. N. Link, "Accuracy criteria for radar cross section measurements of targets consisting of multiple independent scatterers," *IEEE Transactions on Antennas and Propagation*, vol. 36, no. 11, pp. 1587-1593, November 1988.

[12] T. E. Tice, "An overview of radar cross section measurement techniques," *IEEE Transactions on Instrumentation and Measurement*, vol. 39, no. 1, pp. 205-207, February 1990.

[13] K. Sarabandi and F. T. Ulaby, "A convenient technique for polarimetric calibration of single antenna radar system," *IEEE Transactions on Geoscience and Remote Sensing*, vol. 28, no. 6, pp. 1022-1033, November 1990.

[14] J. J. Ahne, K. Sarabandi,, and F. T. Ulaby, "Design and implementation of single antenna polarimetric active radar system," *Antennas And Propagation Society International Symposium*, vol. 3, pp. 1280-1283, 1993.

[15] L. A. Muth, "Nonlinear calibration of polarimetric radar cross section measurement systems," *IEEE Antennas and Propagation Magazine*, vol. 52, no. 3, pp. 187-192, June 2010.

[16] B. M. Welsh, B. M. Kent, and A. L. Buterbaugh, "Full polarimetric calibration for radar cross-section measurements performance analysis," *IEEE Transactions on Antennas and Propagation*, vol. 52, no. 9, pp. 2357-2365, September 2004.

[17] O. M. Bucci and M. D. Migliore, "Effective estimation of 2-D monostatic radar cross sections

from Near-Field measurements," *IEEE Transactions on Antennas and Propagation*, vol. 54, no. 2, pp. 750-752, February 2006.

[18] J. W. Odendaal and J. Joubert, "Radar cross section measurements using near-field radar imaging," *IEEE Transactions on Instrumentation and Measurement*, vol. 45, no. 6, pp. 948-954, December 1996.

[19] C. R. Birtcher, C. A. Balanis, and V. J. Vokurka, "RCS measurements, transformations, and comparisons under cylindrical and plane wave illumination," *IEEE Transactions on Antennas and Propagation*, vol. 42, no. 3, pp. 329-334, March 1994.

[20] A. Broquetas, J. Palau, L. Jofre, and A. Cardama, "Spherical wave near-field imaging and radar cross section measurement," *IEEE Transactions on Antennas and Propagation*, vol. 46, no. 5, pp. 730-735, May 1998.

[21] S. Hantscher, A. Reisenzahn, and C.G. Diskus, "Ultra-wide band radar noise reduction for target classification," *IET Radar Sonar and Navigation*, vol. 2, no. 4, pp. 315-322, 2008.

[22] L. A. Muth, C. M. Wang, and T. Conn, "Robust separation of background and target signals in radar cross-section measurements," *IEEE Transactions on Instrumentation and Measurement*, vol. 54, no. 6, pp. 2462-2468, December 2005.

[23] A. Broquetas, J. Palau, L. Jofre, and A. Cardama, "Spherical wave near-field imaging and radar cross-section measurement," *IEEE Transactions on Antennas and Propagation*, vol. 46, no. 5, pp. 730-735, May 1998.

[24] J. W. Burns and N. S. Subotic, "Reduction of clutter contamination in radar cross section measurements using independent components analysis," *IEEE Antennas and Propagation Society International Symposium*, vol. 1, pp. 731-734, 2004.

[25] A. Bati, T. Long, and H. Don, "Advanced radar cross section clutter removal algorithms", *Antennas and Propagation (EuCAP), 2010 Proceedings of the Fourth European Conference*, pp. 1-5, 2010.

[26] M. Miacci, I. Martin, and M. Rezende, "Radar cross section measurements of complex targets (missile parts) in C-band in anechoic chamber," *Microwave and Optoelectronics Conference, IMOC 2007. SBMO/IEEE MTT-S International*, pp. 401-405, 2007.

[27] N. Levanon and E. Mozeson, *Radar Signals*, first edition, Wiley-IEEEPress, July 2004.

Elham Sadat Kashani received the B.Sc. degree from Sharif University of Technology, Tehran, Iran, and the M.S. degree from the Amirkabir University of Technology, Tehran, Iran, both in electrical engineering. Her research interests include radar signal processing and modeling.

Yaser Norouzi (born in 1981) achieved his B.Sc, M.Sc, and PhD in Communication systems in 2001, 2003, and 2007, respectively all from Sharif University of Technology, Tehran, Iran. Currently he is with Department of electrical engineering at AmirKabir University of technology, Tehran, Iran. His fields of interest include analyzing of dynamic systems, Game Theory and Stochastic Processes.

Ahad Tavakoli was born in Tehran, Iran, on March 8, 1959. He received the B.S. and M.S. degrees from the University of Kansas, Lawrence, and the Ph.D. degree from the University of Michigan, Ann Arbor, all in electrical engineering, in 1982, 1984, and 1991, respectively. In 1991, he joined the Amirkabir University of Technology, Tehran, Iran, where he is currently a Professor in the Department of Electrical Engineering. His research interests include scattering of electromagnetic waves, electromagnetic compatibility, and microstrip antennas.

Parisa Dehkhoda received the B.S. degree from Tehran University, Tehran, Iran, and the M.S. and Ph.D. degrees from the Amirkabir University of Technology, Tehran, Iran, all in electrical engineering. She is currently an Assistant Professor in the Institute of Communications Technology and Applied Electromagnetics, Amirkabir University of Technology, Tehran, Iran. Her research interests include electromagnetic compatibility, specially shielding enclosures, scattering of electromagnetic waves and microstrip antennas.

Evaluation of Lightning Current and Ground Reflection Factor using Measured Electromagnetic Field

M. Izadi[1, 2], M. A. Ab Kadir[1], and M. Hajikhani[1, 3]

[1] Center for Electromagnetic and Lightning Protection Research (CELP),
Faculty of Engineering, University Putra Malaysia, UPM, Serdang, Selangor 43400, Malaysia
aryaphase@yahoo.com

[2] Department of Electrical, Firoozkooh Branch, Islamic Azad University, Firoozkooh, Iran

[3] Aryaphase Company, Tehran, Iran

***Abstract*—**In this paper, an inverse procedure algorithm is proposed to evaluate lightning return stroke current wave shapes at different heights along a lightning channel, as well as the ground reflection factor using measured electromagnetic fields at an observation point while the current model can be set for different models based on the general form of the engineering current models. In order to validate the proposed method, a set of measured electromagnetic fields are used as the input parameters for the proposed algorithm. Likewise, the evaluated channel base current is compared to the corresponding measured current and also the simulated fields at another observation point (based on the evaluated current) are compared to the corresponding measured fields and the results are discussed accordingly. The results show that the evaluated current and fields based on the proposed method are in good agreement with respect to the corresponding measured values.

Index Terms - Electromagnetic fields, ground reflection factor, lightning, and return stroke current.

I. INTRODUCTION

Lightning is an important natural phenomenon that can affect power systems, buildings, and humans while the lightning current wave shape plays an important role in studies into the effects of lightning [1-3]. Several studies have been undertaken to measure the lightning return stroke base current while the lightning current can be measured directly using the triggered lightning method or by installing current coils on the top of tall towers [4-7]. The main problem with these methods is the limited number of measured currents such as measurements cannot cover the wide range of lightning occurrences. In order to set an appropriate protection level for a power system and a building, only a limited number of lightning currents are available while some of the currents are not based on local information.

On the other hand, the lightning currents can be evaluated using measured electromagnetic fields by applying the inverse procedure algorithm where by the location of the lightning is usually determined by a lightning location system (LLS) [8-9]. This method can cover a greater number of lightning occurrences based on measured electromagnetic fields while the evaluated currents are based on local information. Several studies have been undertaken to evaluate lightning currents using measured electromagnetic fields in the time and frequency domains. However, a number of inverse procedure algorithms can only evaluate the lightning currents based on measured electromagnetic fields at far distances from a lightning channel using only the radiation component of the fields in the time domain [10]. However, the error due to ignoring the other field components will enter into the calculations, which have an inverse relationship with the radial distance with respect to the lightning channel. On the other hand, some other methods can evaluate the lightning current using all the field components in

Submitted On: Oct. 4, 2012
Accepted On: Jan. 26, 2014

the frequency domain but only for a restricted number of frequency samples[11, 12]. Moreover, the field sensors should be installed at fixed distances with respect to the lightning channel whilst in reality the striking point is not fully predictable. In addition, the ground reflection factor is ignored in previous methods whereby the ground reflection factor is due to the difference between the channel impedances and it is highly dependent on the ground impedance of the striking point. Therefore, additional reflected currents can enter into the channel, which can have an effect on the values of the associated electromagnetic fields. In this paper, an inverse procedure algorithm is proposed in the time domain to evaluate the full shape of the lightning currents at different heights along the channel whereby all the field components and the effect of the ground reflection factor on the calculations are considered. The proposed method can support different current models based on the general form of the engineering current models directly in the time domain without the need to apply any extra conversions. Moreover, in order to validate the proposed method, a set of measured electromagnetic fields from a triggered lightning experiment are used as input data and the evaluated current and fields at another observation point are compared to the corresponding measured current and fields, respectively. The proposed method can be used to prepare a lightning current data bank based on local information, which can be used for lightning studies. The basic assumptions in this study are listed below:

1- The lightning channel is a vertical channel to the surface of the ground.
2- The effect of lightning branches on the fields is ignored.
3- The ground conductivity is assumed to be infinite.
4- The surface of the ground is assumed to be flat.

II. RETURN STROKE CURRENT

The lightning return stroke current can be considered in two areas i.e., the channel base current at the striking point and at different heights along the lightning channel. The channel base current is usually simulated using a current function in the form of the sum of two Heidler functions [13-16], which are commonly used for the simulation due to the good agreement with the measured current. Equation (1) presents the sum of two Heidler functions. In this study, equation (1) is used as a general form of the channel base current with unknown constant parameters that will be evaluated based on the proposed inverse procedure algorithm as expressed in the next section,

$$i(0,t) = \left[\frac{i_{01}}{\eta_1}\frac{\left(\frac{t}{\Gamma_{11}}\right)^{n_{c1}}}{1+\left(\frac{t}{\Gamma_{11}}\right)^{n_{c1}}}\exp\left(\frac{-t}{\Gamma_{12}}\right) + \frac{i_{02}}{\eta_2}\frac{\left(\frac{t}{\Gamma_{21}}\right)^{n_{c2}}}{1+\left(\frac{t}{\Gamma_{21}}\right)^{n_{c2}}}\exp\left(\frac{-t}{\Gamma_{22}}\right)\right] \quad (1)$$

where i_{01}, i_{02} are the amplitudes of the channel base current, Γ_{11}, Γ_{12} are the front time constants, Γ_{21}, Γ_{22} are the decay- time constants, n_{c1}, n_{c2} are the exponents (2~10),

$$\eta_1 = \exp\left[-\left(\Gamma_{11}/\Gamma_{12}\right)\left(n_{c1}\frac{\Gamma_{12}}{\Gamma_{11}}\right)^{\frac{1}{n_{c1}}}\right],$$

$$\eta_2 = \exp\left[-\left(\Gamma_{21}/\Gamma_{22}\right)\left(n_{c2}\frac{\Gamma_{22}}{\Gamma_{21}}\right)^{\frac{1}{n_{c2}}}\right].$$

On the other hand, the current wave shapes at different heights along a lightning channel can be modelled using the general form of the engineering current models as expressed by equation (2) [17-19],

$$I(z',t) = \left[P(z')I\left(0, t-\frac{z'}{v}\right)\right]u\left(t-\frac{z'}{v_f}\right) \quad (2)$$

where z' is temporary charge height along lightning channel, I (z',t) is return stroke current at height of z' along lightning channel, I (0,t) is return stroke current at channel base, P (z') is attenuation height depend factor, v_f is return stoke front velocity, v is return stroke current velocity, u is Heaviside function. Equation (2) represents the current wave shapes as a function of the channel base current and an attenuation height dependent factor whereby the lightning channel is assumed to behave as a transmission line. Therefore, the different current models based on equation (2) can be a function of the attenuation height dependent factor and the return stroke current velocity along the lightning channel. The result of experimental work shows that the return stroke velocity at low heights of the lightning channel is beyond c/3 to 2c/3 where c is equal to the speed of light in free space [20]. However in reality, the velocity values along a lightning channel are variable but the velocity is

usually entered into calculations as an average value between c/3 to 2c/3 [20-22].

Table 1 shows the function of the attenuation height dependent factor and the return stroke velocity for a number of widely used current models where λ is a constant factor and H is the cloud height. Moreover, the return stroke current wave shape in the presence of the ground reflection factor can be expressed by equation (3) as follows,

$$i_{gr}(z',t) = [P(z')i\left(0,t-\frac{z'}{v}\right)+\rho_g\, i\left(0,t-\frac{z'}{c}\right)]U\left(t-\frac{z'}{v_f}\right) \quad (3)$$

where,

ρ_g is ground reflection coefficient equal to $\frac{z_{ch}-z_g}{z_{ch}+z_g}$, z_{ch} is surge impedance of return stroke channel, z_g is ground impedance, $i_{gr}(z',t)$ is return stoke current at different heights along channel in presence of ground reflection factor.

Table 1: The internal parameters of widely used current models [23].

Model	Return stroke current velocity	P(z')
Bruce and Golde model(BG)	∞	1
Transmission Line model (TL)	v	1
Traveling Current Source model (TCS)	-c	1
Modified Transmission Line with Exponential decay model (MTLE)	v	exp(-z'/λ)
Modified Transmission Line with Linear decay model (MTLL)	v	(1-z'/H)

In this paper, the current wave shapes at different heights along a lightning channel are modelled using equation (3) by selecting the MTLE model and the ground reflection factor, λ and v are assumed to be unknown parameters that will be evaluated using the proposed inverse procedure algorithm.

III. LIGHTNING ELECTROMAGNETIC FIELDS

The electromagnetic fields associated with a lightning channel in the presence of a ground reflection factor at an observation point above the surface of the ground can be can be evaluated by equations (4) to (6) based on the geometry of the problem as shown in Fig. 1 whereas the dipole method is applied [24-25]. Note that all electromagnetic field components in the time period less than or equal to R (z'=0)/c are zero,

$$\overrightarrow{B_\varphi}(r,z,t_n) = \sum_{i=1}^{n}\sum_{m=1}^{k+1}\{a_m F_{i,1}(r,z,t_n,h_{m,i}) - a'_m F_{i,1}(r,z,t_n,h'_{m,i})\} \quad (4)$$

$$\overrightarrow{E_r}(r,z,t_n) = \overrightarrow{E_r}(r,z,t_{n-1}) + \Delta t \times \sum_{i=1}^{n}\sum_{m=1}^{k+1}\{a_m F_{i,2}(r,z,t_n,h_{m,i}) - a'_m F_{i,2}(r,z,t_n,h'_{m,i})\}, \quad (5)$$

$$\overrightarrow{E_z}(r,z,t_n) = \overrightarrow{E_z}(r,z,t_{n-1}) + \Delta t \times \sum_{i=1}^{n}\sum_{m=1}^{k+1}\{a_m F_{i,3}(r,z,t_n,h_{m,i}) - a'_m F_{i,3}(r,z,t_n,h'_{m,i})\}, \quad (6)$$

where, $\overrightarrow{E_r}(r,z,t)$ is the horizontal electric field, $\overrightarrow{E_z}(r,z,t)$ is the vertical electric field, $\overrightarrow{B_\varphi}(r,z,t)$ is the magnetic flux density, z is height of observation point, r is radial distance from lightning channel, $\beta=v/c$, $\chi = \sqrt{\frac{1}{1-\beta^2}}$,

$$t_n = \frac{\sqrt{r^2+z^2}}{c} + (n-1)\Delta t$$

$$n = 1,2,\dots,n_{max}$$

$$\Delta h_i = \begin{cases} \beta\chi^2\{(ct_i - ct_{i-1}) - \sqrt{(\beta ct_i - z)^2 + (\frac{r}{\chi})^2} + \sqrt{(\beta ct_{i-1} - z)^2 + (\frac{r}{\chi})^2}\} \\ \beta\chi^2\left\{-(\beta z - ct_i) - \sqrt{(\beta ct_i - z)^2 + \left(\frac{r}{\chi}\right)^2}\right\} \quad \text{for } i = 1 \end{cases}$$

$$\Delta h'_i = \begin{cases} \beta\chi^2\{(ct_{i-1} - ct_i) + \sqrt{(\beta ct_i + z)^2 + (\frac{r}{\chi})^2} - \sqrt{(\beta ct_{i-1} + z)^2 + (\frac{r}{\chi})^2}\} \\ \beta\chi^2\left\{-(\beta z + ct_i) + \sqrt{(\beta ct_i + z)^2 + \left(\frac{r}{\chi}\right)^2}\right\} \quad \text{for } i = 1 \end{cases}$$

$$h_{m,i} = \begin{cases} \frac{(m-1)\times\Delta h_i}{k} + h_{m=k+1,i-1} \\ \frac{(m-1)\times\Delta h_i}{k} \quad \text{for } i = 1 \end{cases},$$

$$h'_{m,i} = \begin{cases} \frac{(m-1)\times\Delta h'_i}{k} + h'_{m=k+1,i-1} \\ \frac{(m-1)\times\Delta h'_i}{k} \quad \text{for } i = 1 \end{cases},$$

$$a_m = \begin{cases} \frac{\Delta h_i}{2\times k} & \text{for } m = 1 \text{ and } m = k+1 \\ \frac{\Delta h_i}{k} & \text{for others} \end{cases},$$

$$a'_m = \begin{cases} \frac{\Delta h'_i}{2\times k} & \text{for } m = 1 \text{ and } m = k+1 \\ \frac{\Delta h'_i}{k} & \text{for others} \end{cases},$$

$$R_m = \sqrt{r^2 + (z - h_{m,i})^2},$$

$$F_{i,1}(r, z, t_n, h_{m,i}) = \left(\frac{\mu_0}{4\pi}\right)\left\{\frac{r}{{R_m}^3} i_{gr}\left(h_{m,i}, t_n - \frac{R_m}{c}\right) + \frac{r}{c{R_m}^2}\frac{\partial i_{gr}\left(h_{m,i}, t_n - \frac{R_m}{c}\right)}{\partial t}\right\},$$

$$F_{i,2}(r, z, t_n, h_{m,i}) = \left(\frac{1}{4\pi\varepsilon_0}\right)\left\{\frac{3r(z-h_{m,i})}{{R_m}^5} \times i_{gr}\left(h_{m,i}, t_n - \frac{R_m}{c}\right) + \frac{3r(z-h_{m,i})}{c{R_m}^4} \times \frac{\partial i_{gr}\left(h_{m,i}, t_n - \frac{R_m}{c}\right)}{\partial t} + \frac{r(z-h_{m,i})}{c^2{R_m}^3} \times \frac{\partial^2 i_{gr}\left(h_{m,i}, t_n - \frac{R_m}{c}\right)}{\partial t^2}\right\},$$

$$F_{i,3}(r, z, t_n, h_{m,i}) = \left(\frac{1}{4\pi\varepsilon_0}\right)\left\{\frac{2(z-h_{m,i})^2 - r^2}{{R_m}^5} \times i_{gr}\left(h_{m,i}, t_n - \frac{R_m}{c}\right) + \frac{2(z-h_{m,i})^2 - r^2}{c{R_m}^4} \times \frac{\partial i_{gr}\left(h_{m,i}, t_n - \frac{R_m}{c}\right)}{\partial t} - \frac{r^2}{c^2{R_m}^3} \times \frac{\partial^2 i_{gr}\left(h_{m,i}, t_n - \frac{R_m}{c}\right)}{\partial t^2}\right\}.$$

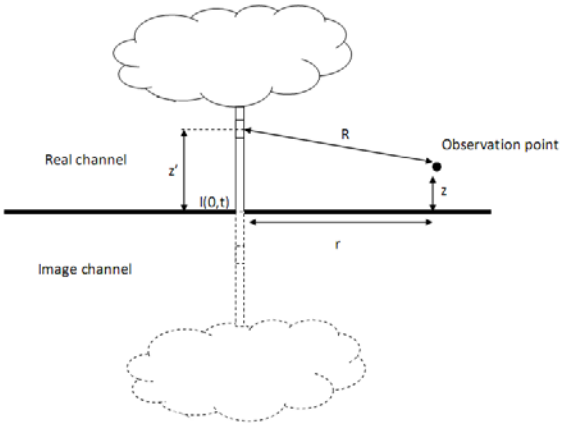

Fig. 1. The geometry of observation point with respect to lightning channel.

IV. INVERSE PROCEDURE ALGORITHM

The lightning return stroke current at different heights along a lightning channel can be evaluated using the proposed inverse procedure algorithm utilising the geometry of the required field sensors as illustrated in Fig. 2. As indicated, two field sensors (magnetic flux density and the vertical electric field) are installed at a radial distance equal to r_1 with respect to the lightning channel to use in the proposed algorithm as input data, while the channel base current and the electromagnetic fields are measured at another radial distance (r_2) to validate the evaluated currents that are obtained from proposed algorithm. Therefore, by extending equations (4) and (6) for an observation point on the surface of the ground, the electromagnetic fields expression can be prepared as a non-linear equation system as expressed by equation (7).

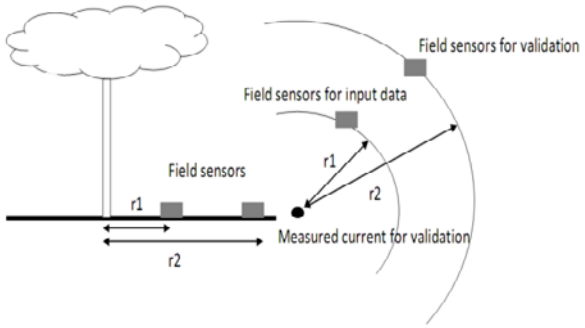

Fig. 2. The geometry of field sensors with respect to lightning channel.

$$\begin{cases} \vec{B}_{\varphi}(r, z=0, t_1) = \sum_{m=1}^{k+1}\{2a_m F_{i,1}(r, z=0, t_1, h_{m,i})\} \\ \vec{B}_{\varphi}(r, z=0, t_2) = \sum_{i=1}^{2}\sum_{m=1}^{k+1}\{2a_m F_{i,1}(r, z=0, t_2, h_{m,i})\} \\ \vdots \\ \vec{B}_{\varphi}(r, z=0, t_{n_{max}}) = \sum_{i=1}^{n_{max}}\sum_{m=1}^{k+1}\{2a_m F_{i,1}(r, z=0, t_{max}, h_{m,i})\} \\ \vec{E}_z(r, z=0, t_1) = \Delta t \times \sum_{m=1}^{k+1}\{2a_m F_{i,3}(r, z=0, t_1, h_{m,i})\} \\ \vec{E}_z(r, z=0, t_2) = E_z(r, z=0, t_1) + \Delta t \times \sum_{i=1}^{2}\sum_{m=1}^{k+1}\{2a_m F_{i,3}(r, z=0, t_2, h_{m,i})\} \\ \vdots \\ \vec{E}_z(r, z=0, t_{n_{max}}) = E_z(r, z=0, t_{max-1}) + \Delta t \times \sum_{i=1}^{n_{max}}\sum_{m=1}^{k+1}\{2a_m F_{i,3}(r, z=0, t_{max}, h_{m,i})\} \end{cases} . \quad (7)$$

Therefore, by substituting the measured fields in the left hand side of equation (7) and r_1 instead the r parameter into equation (7), the nonlinear equation system can be expressed by equation (8) as follows,

$$\begin{cases} \sum_{m=1}^{k+1}\{2a_m F_{i,1}(r_1, z=0, t_1, h_{m,i})\} - B_{\varphi}^{(m)}(r_1, z=0, t_1) = 0 \\ \sum_{i=1}^{2}\sum_{m=1}^{k+1}\{2a_m F_{i,1}(r_1, z=0, t_2, h_{m,i})\} - B_{\varphi}^{(m)}(r_1, z=0, t_2) = 0 \\ \vdots \\ \sum_{i=1}^{n_{max}}\sum_{m=1}^{k+1}\{2a_m F_{i,1}(r_1, z=0, t_{max}, h_{m,i})\} - B_{\varphi}^{(m)}(r_1, z=0, t_{n_{max}}) = 0 \\ \Delta t \times \sum_{m=1}^{k+1}\{2a_m F_{i,3}(r_1, z=0, t_1, h_{m,i})\} - E_z^{(m)}(r_1, z=0, t_1) = 0 \\ E_z(r_1, z=0, t_1) + \Delta t \times \sum_{i=1}^{2}\sum_{m=1}^{k+1}\{2a_m F_{i,3}(r_1, z=0, t_2, h_{m,i})\} - E_z^{(m)}(r_1, z=0, t_2) = 0 \\ \vdots \\ E_z(r_1, z=0, t_{max-1}) + \Delta t \times \sum_{i=1}^{n_{max}}\sum_{m=1}^{k+1}\{2a_m F_{i,3}(r_1, z=0, t_{max}, h_{m,i})\} - E_z^{(m)}(r_1, z=0, t_{n_{max}}) = 0 \end{cases} , \quad (8)$$

where, $B_{\varphi}^{(m)}(r_1, z=0, t_n)$ is the measured magnetic flux density at time equal to t_n, $E_z^{(m)}(r_1, z=0, t_n)$ is the measured vertical electric field at time equal to t_n. On the other hand, the current function and the current model (equations (1) and (3)) with unknown constant parameters can be entered into the $F_{i,1}$, $F_{i,3}$ terms. Therefore, the number of unknown parameters will be equal to eleven i.e., eight for the current function ($i_{01}, i_{02}, \tau_{11}, \tau_{12}, \tau_{21}, \tau_{22}, n_1, n_2$), plus the return stroke current velocity (v), the constant coefficient of the current model (λ) and the ground reflection factor (ρ_g). It should be noted that the MTLE model with unknown constant coefficients is used as a current model in this paper. The unknown parameters can be evaluated by solving equation (8) via different numerical methods. In this paper, the particle swarm optimization algorithm (PSO) is used to evaluate the roots of equation (8) whereby the value of each expression in equation (8) is minimized at roots [26-27]. The proposed method can evaluate the full shape of the lightning currents at different heights by considering all the field components and the ground reflection factor, unlike previous methods. Moreover, the proposed method is very flexible for different current functions and current models and the unknown constant parameters of the current expressions can be evaluated by the proposed algorithm. Further, the proposed method is directly in the time domain and there is no need to apply any extra conversions

compared to some of the previous methods. In the proposed method two field sensors are needed i.e., the vertical electric field sensor and the magnetic flux density sensor. It should be mentioned that the location of field sensors can be set at different points with respect to lightning channel whereas the values of radial distances between lightning channel and sensors are as input parameters of algorithm that can be obtained from lightning location systems and they can be entered into calculations by $F_{i,3}$ and $F_{i,3}$ terms in equation (8).

V. RESULTS AND DISCUSSION

In order to evaluate the proposed method, the measured electromagnetic fields at r_1 = 15 m obtained from a triggered lightning experiment are used as input data in equation (8). By applying the proposed method, the evaluated channel base current is compared to the corresponding measured current.

Moreover, the evaluated currents, ground reflection factor and return stroke current velocity are used for estimation of the magnetic flux density at another observation point with a value of r_2 of 30 m. The geometry of the field sensors with respect to the lightning channel is based on Fig. 2. Subsequently, the evaluated fields at the second observation point (field sensor at r_2) are compared to the corresponding measured fields. Figures 3 and 4 show the measured magnetic flux density and vertical electric fields at r_1 = 15 m, respectively, that are used as input data in the proposed inverse procedure algorithm. It is important to mention that the measured data are obtained from Florida triggered lightning campus whereas the specifications of experimental setup are presented as follow [28]:

i. The current was measured using current transformers (P 110A) and also the Meret fiber optic cable was used to transfer data to recorder. Likewise, the data were filtered using 3 dB bandwidth 20 MHz anti-aliasing filter and also they were digitized at 50 MHz.

ii. The vertical electric field was measured using a plate antenna (0.16 m^2) and also the Meret fiber optic cable was used to transfer data to recorder (with 35 MHz bandwidth) and they were filtered using 3 dB bandwidth 10 MHz low pass filter and they were digitized at 25 MHz.

iii. The rectangular loop antenna was used to measure magnetic flux density with the area about 0.56m^2 and also the Meret fiber optic cable was used to transfer data to recorder (with 35 MHz bandwidth). Moreover, they were filtered using a 10 MHz, 3 dB anti-aliasing filter before the signals were digitized in 25 MHz.

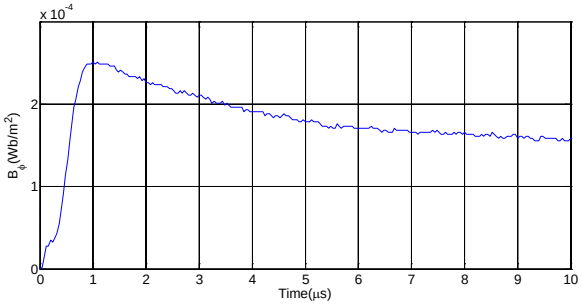

Fig. 3. Measured magnetic flux density at r_1= 15 m based on geometry of problem that is illustrated in Fig. 2.

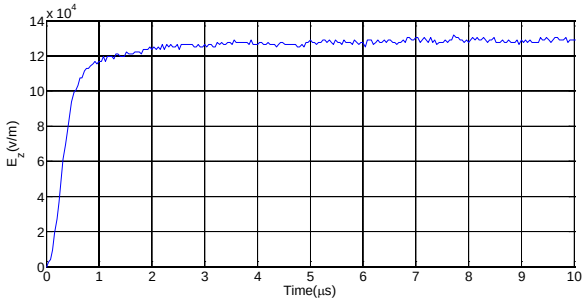

Fig. 4. Measured vertical electric field at r_1= 15 m based on geometry of problem that is illustrated in Fig. 2.

The evaluated values of the current parameters are listed in Table 2 using the current function and current model set on the double Heidler function and the MTLE model, respectively.

Table 2: The evaluated values of current parameters using inverse procedure algorithm.

i_{01} (kA)	i_{02}(kA)	τ_{11} (μs)	τ_{12} (μs)	τ_{21}(μs)
17.568	9.0103	0.2722	3.8723	4.7035
τ_{22} (μs)	n_1	n_2	Λ (m)	V (m/s)
53.3559	2	2	1716	1.71x10^8

Figure 5 shows a comparison between the evaluated channel base current and the corresponding measured current. It illustrates that the evaluated current is in good agreement with respect to the corresponding measured values.

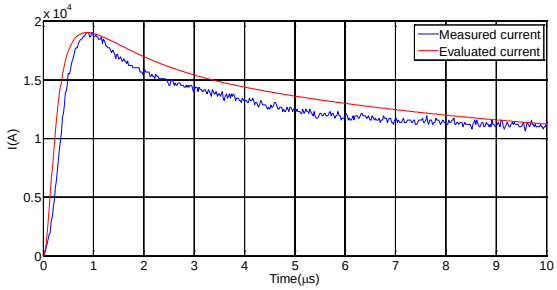

Fig. 5. Comparison between evaluated channel base current and the corresponding measured current.

Moreover, the magnetic flux density at r_2= 30 m is estimated based on the evaluated values of the current parameters from the inverse procedure algorithm as shown in Fig. 6 as compared to the corresponding measured field and the other simulated field based on $\rho_g = 0$. Figure 6 shows that by considering the ground reflector factor, the evaluated field is in good agreement with the corresponding measured field, unlike other methods of simulating the field.

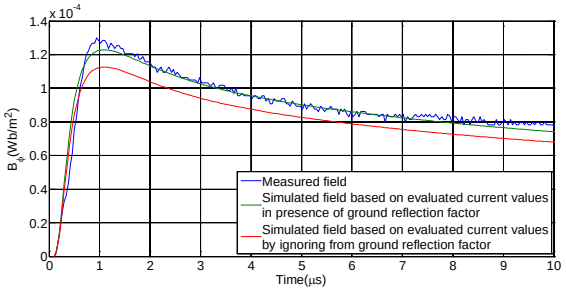

Fig. 6. Comparison between simulated magnetic flux densities and the corresponding measured field at r_2= 30 m.

The simulated vertical electric fields at r_2 = 30 m are compared to the corresponding measured fields. The simulated fields are evaluated based on the current parameters using the proposed method. The results show that the simulated field in the presence of the ground reflection factor is in better agreement with the corresponding measured field compared to other methods of simulating the field.

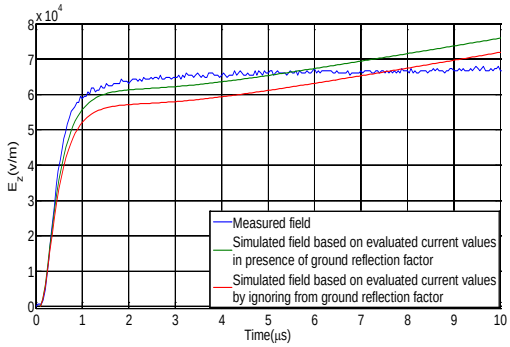

Fig. 7. Comparison between simulated vertical electric fields and the corresponding measured field at r_2= 30 m.

Figures 6 and 7 demonstrate that the ground reflection factor has a direct effect on the values of the electromagnetic fields due to the lightning channel and the additional reflected currents act as new sources along the lightning channel to create the electromagnetic fields. Therefore, by ignoring the ground reflection factor, an error will be entered into calculations. The proposed method can evaluate the full shape of the lightning return stroke currents using the measured electromagnetic field directly in the time domain while all field components and ground reflection factor are taken into consideration compared to previous methods. Likewise, the ground resistivity parameter can be entered into account by using equation (9) that considers on the relation between the ground impedance and ground resistivity [29]. It should be mentioned that $\rho_g = \frac{z_{ch}-z_g}{z_{ch}+z_g}$ [30, 31],

$$z_g = \frac{\rho}{2\pi l}\ln\left(\frac{4l}{r} - 1\right) \qquad (9)$$

where, ρ is ground resistivity, l is the depth of rod (connection point), r is the radius of rod (connection point).

The proposed algorithm can be used to prepare a lightning current data bank, which can be used for studies into the effects of lightning on power systems, buildings and humans and for setting an appropriate protection level for a power system. Moreover, the method can consider a wide range of lightning occurrences using local measured electromagnetic fields and LLS compared to direct measuring methods that can consider only limited occurrences.

VI. CONCLUSION

In this paper, an inverse procedure algorithm is proposed to evaluate the full shape of lightning return stroke currents at different heights along a lightning channel in the time domain and it considers the all electromagnetic field components and the effect of the ground reflection factor on the fields. Moreover, the proposed algorithm is applied to a set of measured electromagnetic fields that have been obtained from a triggered lightning experiment and the results discussed accordingly. The proposed method can be used for preparing a lightning current data bank that can be very useful for studies into the effects of lightning on power systems and for setting the appropriate protection level for power systems and buildings.

REFERENCES

[1] C. A. Nucci, F. Rachidi, M. Ianoz, and C. Mazzetti, "Lightning-induced voltages on overhead lines," *IEEE Transactions on Electromagnetic Compatibility*, vol. 35, pp. 75-86, 1993.

[2] H. M. Ren, B. H. Zhou, V. A. Rakov, L. H. Shi, C. Gao, and J. H. Yang, "Analysis of lightning-induced voltages on overhead lines using a 2-D FDTD method and Agrawal coupling model," *IEEE Transactions on E lectromagnetic Compatibility*, vol. 50, pp. 651-659, 2008.

[3] V. A. Rakov and M. A. Uman, *Lightning Physics and Effects*, Cambridge University Press, 2003.

[4] V. Rakov, M. Uman, and K. Rambo, "A review of ten years of triggered-lightning experiments at camp blanding, Florida," *Atmospheric Research*, vol. 76, pp. 503-517, 2005.

[5] V. Rakov, "Lightning discharges triggered using rocket-and wire techniques," *Geophysics*, vol. 2, pp. 141-171, 1999.

[6] A. Hussein, W. Janischewskyj, M. Milewski, V. Shostak, W. Chisholm, and J. Chang, "Current waveform parameters of CN tower lightning return strokes," *Journal of Electrostatics*, vol. 60, pp. 149-162, 2004.

[7] A. Hussein, M. Milewski, W. Janischewskyj, F. Noor, and F. Jabbar, "Characteristics of lightning flashes striking the CN tower below its tip," *Journal of Electrostatics*, vol. 65, pp. 307-315, 2007.

[8] A. Andreotti, D. Assante, S. Falco, and L. Verolino, "An improved procedure for the return stroke current identification," *IEEE Transactions on Magnetics*, vol. 41, pp. 1872-1875, 2005.

[9] A. Andreotti, F. Delfino, P. Girdinio, and L. Verolino, "A field-based inverse algorithm for the identification of different height lightning return strokes," *The International Journal for Computation and Mathematics in Electrical and Electronic Engineering (COMPEL)*, vol. 20, pp. 724-731, 2001.

[10] A. Shoory, F. Rachidi, M. Rubinstein, R. Moini, and S. H. Hesamedin Sadeghi, "Analytical expressions for zero-crossing times in lightning return-stroke engineering models," *IEEE Transactions on Electromagnetic Compatibility*, vol. 51, pp. 963-974, 2009.

[11] F. Delfino, R. Procopio, A. Andreotti, and L. Verolino, "Lightning return stroke current identification via field measurements," *Electrical Engineering (Archiv fur Elektrotechnik)*, vol. 84, pp. 41-50, 2002.

[12] A. Andreotti, U. De Martinis, and L. Verolino, "An inverse procedure for the return stroke current identification," *IEEE Transactions on Electromagnetic Compatibility*, vol. 43, pp. 155-160, 2002.

[13] F. Heidler, "Analytische Blitzstromfunktion zur LEMP- Berechnung," *presented at the 18th ICLP*, Munich, Germany, 1985.

[14] M. Izadi, M. Z. Ab Kadir, C. Gomes, and W. Wan Ahmad, "Evaluation of electromagnetic fields due to lightning channel with respect to the striking angle," *International Review of Electrical Engineering (IREE)*, vol. 6, pp. 1013-1023, 2011.

[15] M. Izadi, A. Kadir, M. Z. Abidin, and C. Gomes, "Evaluation of electromagnetic fields associated with inclined lightning channel using second order FDTD-hybrid methods," *Progress In Electromagnetics Research*, vol. 117, pp. 209-236, 2011.

[16] M. Izadi, M. Z. Ab Kadir, C. Gomes, and W. F. H. W. Ahmad, "Analytical expressions for electromagnetic fields associated with the inclined lightning channels in the time domain," *Electric Power Components and Systems*, vol. 40, pp. 414-438, 2012.

[17] M. Izadi, M. Kadir, C. Gomes, and W. Wan Ahmad, "An analytical second-FDTD method for evaluation of electric and magnetic fields at intermediate distances from lightning channel," *Progress In Electromagnetic Research (PIER)*, vol. 110, pp. 329-352, 2010.

[18] M. Izadi and M. Kadir, "New algorithm for evaluation of electric fields due to indirect lightning strike," *CMES: Computer Modeling in Engineering and Sciences*, vol. 67, pp. 1-12, 2010.

[19] V. Rakov and A. Dulzon, "A modified transmission line model for lightning return stroke field calculations," *Proc. 9th Int. Zurich Symposium on Electromagnetic Compatibility*, Zurich, Switzerland, pp. 229-235, 1991.

[20] V. Rakov, "Lightning return stroke speed," *Journal of Lightning Research*, vol. 1, 2007.
[21] R. Olsen, D. Jordan, V. Rakov, M. Uman, and N. Grimes, "Observed two-dimensional return stroke propagation speeds in the bottom 170m of rocket-triggered lightning channel," *Journal of Geophysical Research*, vol. 31, 2004.
[22] D. Wang, V. Rakov, and M. Uman, "Observed leader and return-stroke propagation characteristics in the bottom 400 m of a rocket-triggered Iightning channel," *Journal of Geophysical Research*, vol. 104, pp. 14,369-14,376, 1999.
[23] M. Izadi, M. Kadir, C. Gomes, and W. Ahmad, "Numerical expressions in time domain for electromagnetic fields due to lightning channels," *International Journal of Applied Electromagnetics and Mechanics*, vol. 37, pp. 275-289, 2011.
[24] R. Thottappillil and V. Rakov, "Review of three equivalent approaches for computing electromagnetic fields from an extending lightning discharge," *Journal of Lightning Research*, vol. 1, pp. 90-110, 2007.
[25] O. Sadiku and N. Matthew, *Numerical Technique in Electromagnetics*, CRC Press, LLC, 2001.
[26] J. Robinson and Y. Rahmat-Samii, "Particle swarm optimization in electromagnetics," *IEEE Transactions on Antennas and Propagation*, vol. 52, pp. 397-407, 2004.
[27] M. Clerc, *Particle Swarm Optimization*, Wiley-ISTE, 2006.
[28] M. Izadi, M. Ab Kadir, M. Askari, and M. Hajikhani, "Evaluation of lightning current using inverse procedure algorithm," *International Journal of Applied Electromagnetics and Mechanics*, vol. 41, pp. 267-278, 2013.
[29] IEEE Guide for Measuring Earth Resistivity, Ground Impedance, and Earth Surface Potentials of a Ground System, ANSI/IEEE Std 81-1983.
[30] M. Izadi, M. Ab Kadir, and M. Hajikhani, "Evaluation of electromagnetic fields due to inclined lightning channel in presence of ground reflection," *Progress In Electromagnetic Research (PIER)*, vol. 135, pp. 677-694, 2013.
[31] M. Izadi, M. Ab Kadir, and M. Hajikhani, "The analytical field expressions associated with lightning channel in presence of ground reflection at striking point," *International Journal of Applied Electromagnetics and Mechanics*, vol. 42, pp. 303-317, 2013.

Mahdi Izadi was born in Tehran, Iran, at 1977. He received B.Sc. in Electrical Power Engineering from Azad University, Iran at 1999 and obtained M.Sc. and PhD degrees in Electrical Power Engineering from University Putra Malaysia (UPM), Malaysia at 2010 and 2012, respectively. Currently, he is a research fellow in the CELP, Department of Electrical and Electronics Engineering, Faculty of Engineering, University Putra Malaysia. He has authored and co-authored more than 50 scientific papers published in journals and conferences. His research interests include lightning effects on the power systems and lightning electromagnetic fields and protection of power systems.

M. Z. A. Ab Kadir graduated with B.Eng degree in Electrical and Electronic from University Putra Malaysia in 2000 and obtained his PhD from the University of Manchester, United Kingdom in 2006 in High Voltage Engineering. Currently, he is a Professor in the Department of Electrical and Electronics Engineering, Faculty of Engineering, University Putra Malaysia. To date he has authored and co-authored over 100 technical papers comprising of national and international conferences proceedings and citation indexed journals. His research interests include high voltage engineering, insulation coordination, lightning protection, EMC/EMI, kerauna-medicine and power system transients.

Maryam Hajikhani was born in Tehran, Iran in 1978. She graduated with B.Sc. and M.Sc. in Computer Engineering from Azad University, Iran and MMU University, Malaysia in 2003 and 2011, respectively. She is currently pursuing her PhD in UPM and she has authored and co-authored more than 6 scientific papers published in journals and conferences. Her interests include algorithms and computer coding.